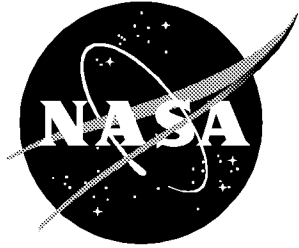


NASA/CR-1999-209115



# Crack Growth Simulation and Residual Strength Prediction in Airplane Fuselages

*Chuin-Shan Chen, Paul A. Wawrzynek, and Anthony R. Ingraffea  
Cornell University, Ithaca, New York*

---

March 1999

## The NASA STI Program Office . . . in Profile

Since its founding, NASA has been dedicated to the advancement of aeronautics and space science. The NASA Scientific and Technical Information (STI) Program Office plays a key part in helping NASA maintain this important role.

The NASA STI Program Office is operated by Langley Research Center, the lead center for NASA's scientific and technical information. The NASA STI Program Office provides access to the NASA STI Database, the largest collection of aeronautical and space science STI in the world. The Program Office is also NASA's institutional mechanism for disseminating the results of its research and development activities. These results are published by NASA in the NASA STI Report Series, which includes the following report types:

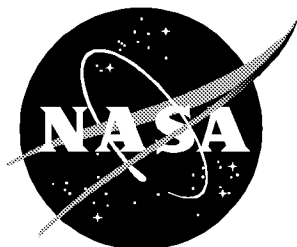
- TECHNICAL PUBLICATION. Reports of completed research or a major significant phase of research that present the results of NASA programs and include extensive data or theoretical analysis. Includes compilations of significant scientific and technical data and information deemed to be of continuing reference value. NASA counterpart or peer-reviewed formal professional papers, but having less stringent limitations on manuscript length and extent of graphic presentations.
- TECHNICAL MEMORANDUM. Scientific and technical findings that are preliminary or of specialized interest, e.g., quick release reports, working papers, and bibliographies that contain minimal annotation. Does not contain extensive analysis.
- CONTRACTOR REPORT. Scientific and technical findings by NASA-sponsored contractors and grantees.
- CONFERENCE PUBLICATION. Collected papers from scientific and technical conferences, symposia, seminars, or other meetings sponsored or co-sponsored by NASA.
- SPECIAL PUBLICATION. Scientific, technical, or historical information from NASA programs, projects, and missions, often concerned with subjects having substantial public interest.
- TECHNICAL TRANSLATION. English-language translations of foreign scientific and technical material pertinent to NASA's mission.

Specialized services that complement the STI Program Office's diverse offerings include creating custom thesauri, building customized databases, organizing and publishing research results . . . even providing videos.

For more information about the NASA STI Program Office, see the following:

- Access the NASA STI Program Home Page at <http://www.sti.nasa.gov>
- Email your question via the Internet to [help@sti.nasa.gov](mailto:help@sti.nasa.gov)
- Fax your question to the NASA STI Help Desk at (301) 621-0134
- Telephone the NASA STI Help Desk at (301) 621-0390
- Write to:  
NASA STI Help Desk  
NASA Center for AeroSpace Information  
7121 Standard Drive  
Hanover, MD 21076-1320

NASA/CR-1999-209115



# Crack Growth Simulation and Residual Strength Prediction in Airplane Fuselages

*Chuin-Shan Chen, Paul A. Wawrzynek, and Anthony R. Ingraffea*  
*Cornell University, Ithaca, New York*

National Aeronautics and  
Space Administration

Langley Research Center  
Hampton, Virginia 23681-2199

Prepared for Langley Research Center  
under Grant NAG1-1184

---

March 1999

---

Available from:

NASA Center for AeroSpace Information (CASI)  
7121 Standard Drive  
Hanover, MD 21076-1320  
(301) 621-0390

National Technical Information Service (NTIS)  
5285 Port Royal Road  
Springfield, VA 22161-2171  
(703) 605-6000



# Acknowledgements

This work was performed with financial support from the NASA Aircraft Structural Integrity Program under contract NAG-1-1184. The authors would like to express their deepest gratitude to Dr. James C. Newman, Jr. and Dr. David S. Dawicke in the Mechanics of Materials Branch at the NASA Langley Research Center, for their advice, support, and encouragement during the progress of this research. In addition, the advice from Dr. Charles C. Rankin at Lockheed-Martin's Advanced Technology Center and Dr. Richard D. Young in the Structural Mechanics Branch at the NASA Langley Research Center is highly appreciated.

Helpful discussions with Mr. Keith E. Wilkins and Mr. Michael L. Gruber of the Boeing Commercial Airplane Group in Seattle, Dr. Jin Yu, Dr. Cong Duong, and Mr. Richard G. Pettit of the Boeing Commercial Airplane Group in Long Beach, and Mr. Dale Cope of the Boeing Defense and Space Group in Wichita is also acknowledged.

# Table of Contents

<b>1</b>	<b>Introduction</b>	<b>1</b>
1.1	Overview . . . . .	1
1.2	Background 1: Structural Integrity of Fuselage Structures . . . . .	3
1.2.1	WFD in Fuselage Structures . . . . .	3
1.2.2	Crack Growth in Thin Sheet Metals . . . . .	5
1.2.3	Bulging in Pressurized Thin Shell Structures . . . . .	5
1.3	Background 2: Computational Issues for Crack Growth Simulation .	6
1.4	FRANC3D/STAGS Software Environment . . . . .	7
1.5	Organization of the Dissertation . . . . .	8
<b>2</b>	<b>Theory for CTOA-Driven Elastic-Plastic Crack Growth and Residual Strength Analysis</b>	<b>11</b>
2.1	Introduction . . . . .	11
2.2	Evaluation of Fracture Mechanics Methods . . . . .	12
2.3	CTOA Fracture Criterion . . . . .	14
2.4	Elastic-Plastic Crack Growth . . . . .	15
2.5	Link-up and Residual Strength Analysis with CTOA Fracture Criterion . . . . .	17
2.6	Guidelines for Using the CTOA Fracture Criterion . . . . .	19
2.7	Summary . . . . .	20
<b>3</b>	<b>Residual Strength Analysis of a Flat Panel with Self-Similar Elastic-Plastic Crack Growth</b>	<b>21</b>
3.1	Introduction . . . . .	21
3.2	Experimental Procedures and Test Configurations . . . . .	24
3.3	Numerical Simulations of MT Specimens . . . . .	26
3.3.1	Numerical Results . . . . .	27
3.3.2	Discussion . . . . .	29
3.4	Numerical Simulations of Specimens with Multiple Cracks . . . . .	33
3.4.1	Numerical Results and Discussion . . . . .	33
3.5	Summary . . . . .	35

<b>4</b>	<b>Residual Strength Analysis of Fuselage Structures with Self-Similar Crack Growth</b>	<b>38</b>
4.1	Demonstration Example: A Generic Narrow Body Fuselage Panel . . .	38
4.1.1	Numerical Model . . . . .	39
4.1.2	Numerical Results and Discussion . . . . .	45
4.2	Validation Example: A Generic Wide Body Fuselage Panel . . . . .	45
4.2.1	Full-Scale Fuselage Panel Testing . . . . .	49
4.2.2	Numerical Model . . . . .	54
4.2.3	Determination of $CTOA_c$ . . . . .	57
4.2.4	Numerical Results: Comparison with Strain Gage . . . . .	59
4.2.5	Numerical Results: Stable Crack Growth and Residual Strength Analyses . . . . .	69
4.3	Summary . . . . .	83
<b>5</b>	<b>Theory for Curvilinear Crack Growth in Planar and Thin Shell Structures</b>	<b>85</b>
5.1	Introduction . . . . .	85
5.2	Crack Tip Fields in Two Dimensions and Thin Plates . . . . .	88
5.3	Crack Growth Direction Criterion Based on Maximum Tangential Stress Theory . . . . .	92
5.3.1	Crack Path Stability under Pure Mode I Conditions . . . . .	93
5.3.2	Determine Crack Propagation Angle under General Mixed-Mode Problems . . . . .	94
5.3.3	Discussion: The Critical Distance $r_c$ . . . . .	96
5.3.4	Anisotropic Problems . . . . .	97
5.4	Discussion: Crack Growth Direction Criterion for Geometrically and Materially Nonlinear Problems . . . . .	98
5.4.1	Geometrically Nonlinear Problems . . . . .	100
5.4.2	Materially Nonlinear Problems . . . . .	101
5.5	Summary . . . . .	105
<b>6</b>	<b>Numerical Evaluation of <math>T</math>-Stress</b>	<b>106</b>
6.1	Introduction . . . . .	106
6.1.1	Outline for Numerical Assessment of $T$ -stress Computation Using a p-version Finite Element Method . . . . .	107
6.2	Path Independent Integral For $T$ -Stress Computation . . . . .	107
6.2.1	Construction of Path Independent Integral for $T$ -Stress Using Betti-Rayleigh Reciprocal Theorem . . . . .	108
6.2.2	Construction of Path Independent Integral for $T$ -Stress Using Eshelby's Energy Momentum Tensor . . . . .	110
6.2.3	Analytical Equivalence between Betti's Reciprocal and Eshelby Integrals . . . . .	112
6.3	$T$ -Stress Evaluation Using Finite Element Analyses . . . . .	113
6.3.1	Equivalent Domain Integral . . . . .	113

6.3.2	Hierarchical p-version Finite Element Method . . . . .	114
6.3.3	Error Analysis and Accuracy Assessment . . . . .	115
6.4	Numerical Results . . . . .	117
6.4.1	A Simple Benchmark Example . . . . .	117
6.4.2	Fracture Specimens . . . . .	119
6.4.3	Discussion: Numerical Assessment of $T$ -stress Computation Using a p-version Finite Element Method . . . . .	123
6.5	FRANC3D/STAGS Results . . . . .	127
6.5.1	Two-Dimensional Problems . . . . .	127
6.5.2	Thin Shell Problems . . . . .	128
6.6	Summary . . . . .	128
<b>7</b>	<b>Curvilinear Crack Growth Simulations</b>	<b>130</b>
7.1	Curvilinear Crack Growth Simulations For DCB Fracture Specimens	130
7.1.1	Description of Experiment . . . . .	130
7.1.2	Description of Simulation . . . . .	132
7.1.3	Numerical Results . . . . .	133
7.1.4	Concluding Remarks for Curvilinear Crack Growth Simula- tion in DCB Specimen . . . . .	137
7.2	Curvilinear Crack Growth Simulations For Fuselage Structures . . .	139
7.2.1	Description of Experiment . . . . .	139
7.2.2	Numerical Model . . . . .	140
7.2.3	Fracture Parameter Evaluation . . . . .	140
7.2.4	Numerical Results . . . . .	141
7.2.5	Comparisons with Previous Studies . . . . .	147
7.2.6	Concluding Remarks for Curvilinear Crack Growth Simula- tion in Narrow Body Fuselage Panel . . . . .	148
7.3	Discussion: Elastic-Plastic Curvilinear Crack Growth and Residual Strength Prediction . . . . .	151
7.4	Summary . . . . .	151
<b>8</b>	<b>Summary, Conclusions, and Recommendations for Future Work</b>	<b>152</b>
8.1	Part One: Elastic-Plastic Crack Growth Simulation and Residual Strength Prediction . . . . .	153
8.1.1	Chapter 2: Theory for CTOA-Driven Elastic-Plastic Crack Growth and Residual Strength Analysis . . . . .	153
8.1.2	Chapter 3: Residual Strength Analysis of a Flat Panel with Self-Similar Elastic-Plastic Crack Growth . . . . .	153
8.1.3	Chapter 4: Residual Strength Analysis of Fuselage Struc- tures with Self-Similar Crack Growth . . . . .	154
8.1.4	Recommendations for Future Work . . . . .	155
8.2	Part Two: Curvilinear Crack Growth Simulation . . . . .	156
8.2.1	Chapter 5: Theory for Curvilinear Crack Growth in Planar and Thin Shell Structures . . . . .	156

8.2.2	Chapter 6: Numerical Evaluation of $T$ -Stress . . . . .	157
8.2.3	Chapter 7: Curvilinear Crack Growth Simulations . . . . .	158
8.2.4	Recommendations for Future Work . . . . .	159
<b>Bibliography</b>		<b>160</b>

# List of Tables

3.1	Comparisons of Residual Strength Predictions of MT Specimens (unit: ksi) . . . . .	32
4.1	Test Matrix for MT Specimens (after [49]) . . . . .	58
4.2	Predicted and Observed Pressure Loading for Stable Tearing Initiation . . . . .	76
6.1	Numerical Path Independence of $J$ , $K_I$ , and $T$ for $p = 6$ and $K_I/T = 1$ for Benchmark Example . . . . .	119
6.2	Relative Error of $K_I$ and $T$ Computed at Integration Domain on First Layer Away From Crack Tip and Relative Error in Energy Norm for Benchmark Example . . . . .	120
6.3	Computed Values of $K_I$ , $T$ , and $B$ for the DCB Specimen . . . . .	123
6.4	Computed Values of $K_I$ , $T$ , and $B$ for MT, SENT, and SENB Specimens . . . . .	126
7.1	Test Matrix for DCB Specimens . . . . .	131

# List of Figures

1.1	1988 Aloha Airlines accident (aircraft after landing). . . . .	2
1.2	1988 Aloha Airlines accident—the shaded area illustrates the part of fuselage lost at cruising altitude. . . . .	2
1.3	Illustration of effect of WFD on residual strength and critical crack size. . . . .	4
1.4	Illustration of typical life of aircraft structures. . . . .	5
1.5	Illustration of the sequence of operations on databases and processes involved in each crack growth increment. . . . .	7
1.6	The FRANC3D/STAGS software components, their primary functions, and their interactions necessary to perform arbitrary crack growth simulation (modified after [106]). . . . .	9
2.1	Specimen configurations tested and analyzed in ASTM round robin (after [91]). . . . .	13
2.2	Illustration of CTOA definition. . . . .	15
2.3	Illustration of crack growth in nonlinear elastic and elastic-plastic materials. . . . .	16
2.4	Illustration of plastic wake effect caused by crack growth. . . . .	17
2.5	Residual strength diagram under load control. . . . .	18
2.6	Residual strength diagram under displacement control. . . . .	18
3.1	Schematic of fracture surface indicating transition from a flat to a slant crack plane (after [93]). . . . .	23
3.2	Schematic of the plane strain core. . . . .	24
3.3	Test configurations of MT specimens. . . . .	25
3.4	Test configurations of 12 inch wide specimens with multiple cracks. . . . .	25
3.5	Surface measurements of CTOA <sub>c</sub> (after [29]). . . . .	26
3.6	Piecewise linear representation of the uniaxial stress-strain curve for 2024-T3 aluminum. . . . .	27
3.7	Finite element mesh for 24 inch wide MT specimen and detail along crack path. . . . .	28
3.8	Convergence study: predicted crack growth and predicted residual strength for 24 inch wide panel with different crack tip element sizes. . . . .	28

3.9	Crack opening profiles and $CTOA_a$ after the first crack growth increment and after reaching the residual strength for 24 inch wide panels. . . . .	29
3.10	Comparisons between experimental measurements and numerical predictions of applied stress versus half crack extension for various sizes of specimens. . . . .	30
3.11	Numerical predictions of plastic zone for various sizes of specimens reaching their residual strength. . . . .	31
3.12	Predicted results of thin shell, plane strain, plane stress with a plane strain core, and 3D analyses compared with experimental measurements. . . . .	32
3.13	Finite element mesh for the test configuration b (12 inch wide specimen with two cracks). . . . .	34
3.14	Predicted applied stress versus crack extension for test configuration b and d. . . . .	34
3.15	Crack opening profile(s) and plastic zone evolution of test configuration b during crack growth: (1) at the first increment, (2) before link-up, (3) after link-up, and (4) reaching the residual strength. . . . .	35
3.16	Relative difference of residual strength and link-up load between predicted results and experimental measurements for specimens with multiple cracks. . . . .	36
3.17	Loss of residual strength due to the presence of small cracks. . . . .	36
4.1	Dimensions of generic narrow body panel for demonstration example. . . . .	39
4.2	Detailed rivet spacing for demonstration example. . . . .	40
4.3	Dimensions of stringer and frame for demonstration example (dimensions in inches, modified after [25]). . . . .	40
4.4	Demonstration example: piecewise linear representation of the uni-axial stress-strain curve for 2024-T3 aluminum. . . . .	41
4.5	Demonstration example: piecewise linear representation of the uni-axial stress-strain curve for 7075-T6 aluminum. . . . .	41
4.6	Demonstration example: rivet shear stiffness and strength. . . . .	42
4.7	Crack configurations with a 10-inch initial lead crack and MSD (external view). . . . .	43
4.8	Finite element mesh for demonstration example. . . . .	44
4.9	Detailed mesh around crack path for demonstration example. . . . .	44
4.10	Predicted operating pressure versus total crack extension for the demonstration example: (a) 7.14-inch initial lead crack, (b) 7.14-inch initial lead crack with corrosion damage, (c) 10-inch initial lead crack, and (d) 10-inch initial lead crack with corrosion damage. . . . .	46
4.11	Predicted residual strength versus initial lead crack length. . . . .	47
4.12	Deformed shape of the demonstration example (pressure = 15.3 psi, magnification factor = 5.0). . . . .	47



4.13	Predicted plastic zones for 10-inch initial lead crack without MSD (pressure = 15.3 psi, magnification factor = 5.0). . . . .	48
4.14	Predicted plastic zones for 10-inch initial lead crack with 0.025 inch MSD (pressure = 11.3 psi, magnification factor = 5.0). . . . .	48
4.15	Generic narrow and wide body test fixtures (after [82]). . . . .	49
4.16	Validation example: test panel dimensions. . . . .	50
4.17	Validation example: detailed panel dimensions (after [49]). . . . .	51
4.18	Validation example: detailed rivet spacing (after [49]). . . . .	52
4.19	Validation example: dimensions of frame and stringer clip (dimensions in inches). . . . .	53
4.20	Validation example: dimensions of stringer (dimensions in inches). . . . .	53
4.21	Global and local finite element models. . . . .	55
4.22	Validation example: piecewise linear representation of the uniaxial stress-strain curve for 2024-T3 aluminum. . . . .	56
4.23	Validation example: piecewise linear representation of the uniaxial stress-strain curve for 7075-T6 aluminum. . . . .	56
4.24	Validation example: shear stiffness and strength of rivet spring. . . . .	56
4.25	Validation example: shear stiffness and strength of adhesive spring. . . . .	57
4.26	Finite element mesh for a quarter of 48 inch wide MT specimen. . . . .	58
4.27	Predicted applied stress versus stable crack growth for 48 inch wide MT specimen (half plane strain core height = 0.08 inch). . . . .	59
4.28	Effect of plane strain core height on predicted stable crack growth for 48 inch wide MT specimen. . . . .	60
4.29	Strain gage locations on the skin and tear strap. . . . .	61
4.30	Deformed structures of the validation example at global and local modeling levels (pressure = 9.4 psi, crack length = 38.2 inch, magnification factor = 5.0). . . . .	62
4.31	Three mesh discretizations at the global modeling level. . . . .	63
4.32	Global convergence study: comparison between computed and measured hoop stresses for strain gage 1-4 (pressure = 9.4 psi; crack length = 38.2 in.; frame cut; No MSD). . . . .	64
4.33	Global convergence study: comparison between computed and measured hoop stresses for strain gage 5 (pressure = 9.4 psi; crack length = 38.2 in.; frame cut; No MSD). . . . .	65
4.34	Two mesh discretizations at the local modeling level. . . . .	66
4.35	Global and local model study: comparison between computed and measured hoop stresses for strain gage 1-4 (pressure = 9.4 psi; crack length = 38.2 in.; frame cut; No MSD). . . . .	67
4.36	Global and local model study: comparison between computed and measured hoop stresses for strain gage 5 (pressure = 9.4 psi; crack length = 38.2 in.; frame cut; No MSD). . . . .	68
4.37	Illustration of distributed connection that connects fastener node to surrounding shell nodes . . . . .	69

4.38	Effects of distributed rivet connection: comparison between computed and measured hoop stresses for strain gage 1-4 (pressure = 9.4 psi; crack length = 38.2 in.; frame cut; No MSD). . . . .	70
4.39	Effects of distributed rivet connection: comparison between computed and measured hoop stresses for strain gage 5 (pressure = 9.4 psi; crack length = 38.2 in.; frame cut; No MSD). . . . .	71
4.40	Comparison between the predicted stable crack growth and experimental measurements: (a) case without MSD, and (b) case with MSD. . . . .	72
4.41	Predicted crack-opening and crack-closure pressure under cyclic loading (cyclic pressure = 8.6 psi, No MSD). . . . .	74
4.42	Predicted crack opening profiles of outer skin at initial tearing crack tip: (a) case without fatigue crack closure, and (b) case with 0.32 inch fatigue crack closure (no stable crack growth, magnification factor = 2.0). . . . .	75
4.43	Predicted crack-opening and crack-closure pressure under cyclic loading (cyclic pressure = 7.0 psi, MSD). . . . .	76
4.44	Comparison between predicted stable crack growth with fatigue closure effects and experimental measurements: (a) case without MSD, and (b) case with MSD. . . . .	77
4.45	Predicted effective stress distribution (pressure = 9.86 psi, $da = 0.5$ inch, $CTOA_c = 5.5^\circ$ ). . . . .	78
4.46	Predicted effective stress distribution of inner tear strap with rivet holes (pressure = 9.86 psi, $da = 0.5$ inch, $CTOA_c = 5.5^\circ$ ). . . . .	79
4.47	Illustration of broken inner tear strap. . . . .	79
4.48	Comparison between predicted stable crack growth with broken tear strap and experimental measurements: (a) case without MSD, and (b) case with MSD. . . . .	80
4.49	Comparison between predicted results with tear strap failure at various stages during stable crack growth and experimental measurements (No MSD, $CTOA_c = 4.5^\circ$ ). . . . .	81
4.50	Comparison between predicted stable crack growth and experimental measurements (broken tear strap, reduced plastic wake, No MSD). . . . .	82
4.51	Illustration of crack propagation near rivet: (a) lead crack approaching rivet, (b) lead crack growing into rivet hole, and (c) new crack initiating out of rivet hole. . . . .	83
5.1	Flapping phenomenon in pressurized fuselage due to curvilinear crack growth (after [82]). . . . .	86
5.2	Comparison of elastic mixity parameters versus predicted crack growth angles. . . . .	87
5.3	Local crack tip coordinates. . . . .	88
5.4	Local crack tip coordinates for a through crack in a plate (after [57]). . . . .	92

5.5	The tangential stress $\sigma_{\theta\theta}$ distributions for different values of critical distance $r_c$ under pure Mode I conditions ( $T > 0$ ). . . . .	94
5.6	Predicted propagation angle from maximum tangential stress theory (Equation (5.17)). . . . .	95
5.7	Predicted propagation angle for the angled crack problem. . . . .	96
5.8	Elliptical representation of anisotropic fracture toughness. . . . .	98
5.9	Effects of fracture orthotropy ratio on predicted propagation angle. . . . .	99
5.10	Effects of material orientation on predicted propagation angle. . . . .	99
5.11	Comparison of elastic mixity parameters versus predicted crack growth angles for different strain hardening exponents (after [124]). . . . .	102
5.12	Illustration of main and kinked crack relationship for CTOD-based crack growth directional criterion. . . . .	103
5.13	Comparison of predicted propagation angles for the angled crack problem. . . . .	104
6.1	A closed contour in the neighborhood of a crack tip. . . . .	109
6.2	Point force applied at crack tip. . . . .	111
6.3	An equivalent domain integral. . . . .	114
6.4	Postprocessing meshes for domain integral. . . . .	115
6.5	Benchmark example for $T$ -stress computation: (a) numerical model and (b) mesh with 6 layers of refinement (only 2 visible as shown) . . . . .	117
6.6	Convergence of $T$ -stress and energy norm for the benchmark example. $T$ -stress values are computed on the first layer ( $L1$ , $r_1 = 7.59375 \times 10^{-5}$ ) and the second layer ( $L2$ , $r_1 = 5.0625 \times 10^{-4}$ ) of elements outside the crack tip. . . . .	121
6.7	Accuracy assessment with p-extension for the benchmark example: (a) the relative error of calculated $T$ -stress, $e_{rel}^T$ , versus dimensionless parameter $K_I/(T\sqrt{r_1})$ , and (b) the ratio of $e_{rel}^T$ over $K_I/(T\sqrt{r_1})$ versus the polynomial degree of the shape functions, p. . . . .	122
6.8	(a) Double cantilever beam (DCB) specimen configuration, and (b) a hp-version finite element model for DCB specimen with 6 layer refinement (only 2 visible). . . . .	124
6.9	Convergence of normalized $K_I$ for p-extension for the DCB specimen. . . . .	125
6.10	Convergence of normalized $T$ -stress for p-extension for the DCB specimen. . . . .	125
6.11	Various fracture specimen configurations used for $T$ -stress computation. . . . .	127
6.12	A focused finite element mesh used in FRANC3D/STAGS. . . . .	128
7.1	The DCB specimen configuration. . . . .	131
7.2	(a) Stable tearing (2024LT-4) and (b) fatigue crack growth (2024LT-6) in the L-T orientation observed in DCB specimens (after [101]). . . . .	132

7.3	Predicted and measured crack trajectories for DCB specimen under stable crack growth: (a) overall crack trajectories, and (b) crack paths in the focused region (Equation (5.17) with various magnitudes of $r_c$ ; $\Delta a = 0.2$ in.). . . . .	134
7.4	Computed deformed shapes and the corresponding finite element meshes used in the curvilinear crack growth simulations in DCB specimens (isotropic case with $r_c = 0.09$ inch). . . . .	135
7.5	Predicted and measured crack trajectories for DCB specimen under fatigue crack growth (Equation (5.17) with various magnitudes of $r_c$ ; $\Delta a = 0.2$ in.). . . . .	136
7.6	Predicted and measured crack trajectories for DCB specimen under stable crack growth: effect of the length of crack growth increment (Equation (5.17) with $r_c = 0.09$ inch). . . . .	137
7.7	Predicted and measured crack trajectories for DCB specimen under stable crack growth: effect of the fracture toughness orthotropy (Equation (5.24) with $r_c = 0.09$ inch; $\frac{K_c(T)}{K_c(L)} = 1.1$ ; $\Delta a = 0.2$ in.). . . . .	138
7.8	Structural features of a narrow body fuselage panel (modified after [85]). . . . .	139
7.9	Finite element model for the narrow body fuselage panel. . . . .	140
7.10	Comparisons between predicted and measured crack trajectories (isotropic directional criterion with various magnitudes of $r_c$ ). . . . .	142
7.11	Computed deformed shapes during curvilinear crack growth (isotropic case with $r_c = 0.09$ inch, magnification factor = 2.0). . . . .	143
7.12	Computed stress intensity factors and $T$ -stress versus half crack extension. The hollow and solid markers denote the computed fracture parameters for the isotropic case with $r_c = 0$ and $r_c = 0.09$ inch, respectively. . . . .	144
7.13	Comparisons between predicted and measured crack trajectories (isotropic and orthotropic cases with $r_c = 0.09$ inch). . . . .	145
7.14	Comparisons between predicted and measured crack trajectories (isotropic directional criterion with various magnitudes of $r_c$ ). . . . .	148
7.15	Computed stress intensity factors versus half crack extension. The hollow and solid markers denote the computed stress intensity factors from the current isotropic prediction with $r_c = 0$ and those from Chen <i>et al.</i> [21], respectively. . . . .	149
7.16	Computed stress intensity factors versus half crack extension. The hollow and solid markers denote the computed stress intensity factors from the current isotropic prediction with $r_c = 0$ and those from Potyondy <i>et al.</i> [106, 108], respectively. . . . .	150
8.1	Illustration of <i>mixed modeling</i> of thin shell and 3D solids. . . . .	156

# Chapter 1

## Introduction

This is the final report for the NASA funded project NAG-1-1184 entitled “Crack Growth Prediction Methodology for Multi-Site Damage.” The primary objective of the project was to create a capability to simulate curvilinear fatigue crack growth and ductile tearing in aircraft fuselages subjected to widespread fatigue damage. The second objective was to validate the capability by way of comparisons to experimental results. Both objectives have been achieved and the results are detailed herein. The body of this report is derived primarily from the Ph.D. thesis of the first author [19].

### 1.1 Overview

Modern aircraft structures are designed using a damage tolerance philosophy. This design philosophy envisions sufficient strength and structural integrity of the aircraft to sustain major damage and to avoid catastrophic failure. However, structural aging of the aircraft may significantly reduce the strength below an acceptable level; this raises many important safety issues.

Concerns about aging aircraft are reinforced by the in-flight structural failure of an Aloha Airlines Boeing 737 on April 28, 1988 [97]. The failure precipitated from the link-up of small fatigue cracks extending from adjacent rivet holes in a fuselage lap-splice joint. This caused approximately 18 feet of the upper crown skin and structure to separate from the fuselage (see Figures 1.1 and 1.2). The 1988 Aloha Airlines accident created a revolution in the aircraft community. The problems associated with aging aircraft have to be quantified and the methodology to ensure the structural integrity of airplanes has to be reassessed [5].

One of the most notable problems in aging aircraft is widespread fatigue damage (WFD) defined in [139] as “the simultaneous presence of fatigue cracks at multiple structural details that are of sufficient size and density whereby the structure will no longer meet its damage tolerance requirement.” In response to such aging aircraft problems, the National Aeronautics and Space Administration (NASA) initiated an Airframe Structural Integrity Program (ASIP) [52, 95, 53, 54] to develop

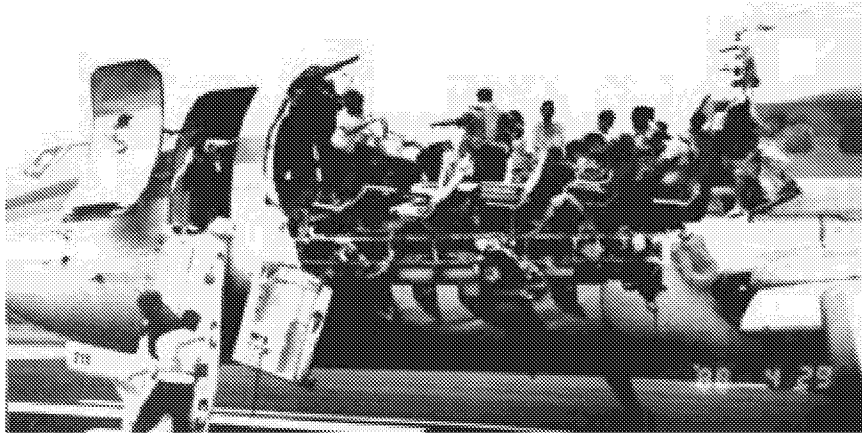


Figure 1.1: 1988 Aloha Airlines accident (aircraft after landing).

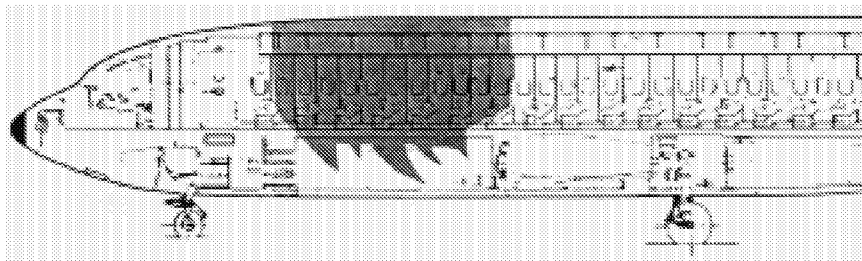


Figure 1.2: 1988 Aloha Airlines accident—the shaded area illustrates the part of fuselage lost at cruising altitude.

an advanced analysis methodology for predicting structural integrity and residual strength<sup>1</sup> of fuselage structures with WFD. The analysis methodology would allow engineers to maintain the aging fleet economically while insuring continuous airworthiness.

The work described in this thesis is part of the ASIP program. The main objective of this work is to develop a computational analysis methodology to simulate realistic crack growth and to predict remaining life and residual strength of complex built-up structures. While the methodology developed is generic in nature, the particular focus is on fuselage structural integrity where WFD is likely to occur as the fleet grows older. The analysis methodology will help to determine service inspection intervals, quantitatively evaluate inspection findings, and design and certify damage-tolerant structural repairs. Thus, the outcome will improve the technology to support the safe operation of the current fleet and the design of more damage-tolerant aircraft for the next-generation fleet.

## 1.2 Background 1: Structural Integrity of Fuselage Structures

A general overview of the structural integrity of a pressurized fuselage with cracks is provided as background material for the thesis. In particular, the following issues are discussed:

- concerns about WFD related to the loss of residual strength,
- the characterization of WFD in riveted fuselage structures,
- typical life of aircraft structures and the dominant behavior of cracks, and finally
- the analysis methodology described in this thesis to evaluate the structural integrity of damaged structures.

### 1.2.1 WFD in Fuselage Structures

The philosophy of damage tolerance presumes that any damage initiated by fatigue, accident, or corrosion will be found before catastrophic failure [138]. The safety of the aircraft heavily depends upon finding cracks before they reach a critical length. The occurrence of WFD, however, drastically reduces the residual strength or decreases the critical crack size as illustrated in Figure 1.3. The loss of residual strength in the presence of WFD has raised great safety concerns for aging aircraft.

---

<sup>1</sup>Residual strength is the maximum load carrying capacity of a damaged structure.

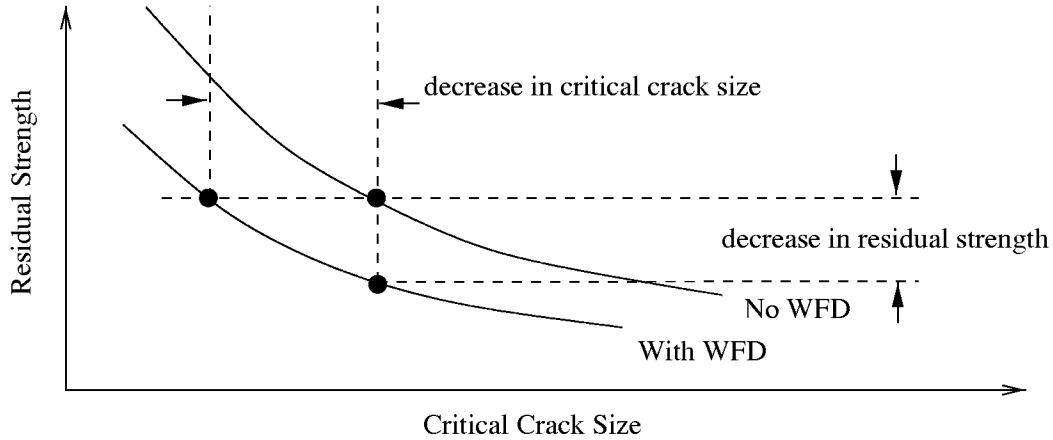


Figure 1.3: Illustration of effect of WFD on residual strength and critical crack size.

To establish the characteristics of WFD in fuselage riveted structures, Piascik *et al.* [105] and Harris *et al.* [54] conducted teardown fractographic examinations of aircraft components. A four bay section of a Boeing 747 fuselage containing a longitudinal lap splice joint was examined after conducting a full-scale fatigue test with 60,000 full pressurization cycles; this is about three times the original economic design life of the aircraft. Several observations were made from detailed non-destructive and destructive examinations of each rivet hole:

1. crack initiation mechanisms included high local stresses, fretting along mating surfaces, and manufacturing defects created during the riveting process;
2. fatigue cracks were present at virtually every rivet hole in the upper row of the lap joint;
3. the lengths of all of the fatigue cracks at link-up were approximately the same.

The last observation implies that as long as the crack has extended a considerable distance from the rivet head, the crack growth behavior is somewhat independent of the initiating mechanism. Thus, the typical life of aircraft structures can be subdivided into the nucleation and crack growth periods as shown in Figure 1.4. The nucleation period heavily depends on micro-structural details of the material. The microscopic studies provide fundamental understanding and phenomenological criteria for fatigue and fracture used in macro-scale applications. Regardless of the initiation mechanism, fracture mechanics is adequate to describe the macrocrack behavior for practical problems. The methodology developed herein is intended for the macro-scale and it is the crack growth period that is of primary interest.



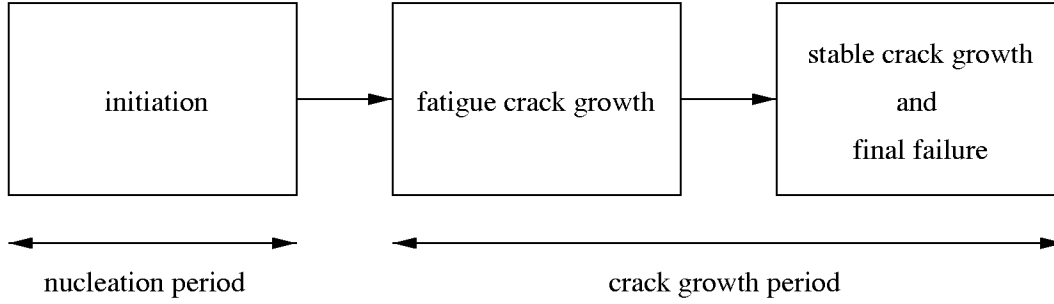


Figure 1.4: Illustration of typical life of aircraft structures.

### 1.2.2 Crack Growth in Thin Sheet Metals

In general, crack growth in thin, ductile materials used in aircraft fuselages is likely to experience fatigue and stable crack growth before the occurrence of fast fracture and final failure. Fatigue is a process of cumulative damage that is caused by repeated fluctuating loads. Fatigue crack propagation can be characterized by a crack growth-rate model that predicts the number of loading cycles required to propagate a fatigue crack to a critical size. Stress intensity factors (SIFs) under fatigue loading are below the critical value for quasi-static or unstable crack propagation. Under such circumstance, linear elastic fracture mechanics (LEFM) suffices to characterize the crack growth-rate model. Stable crack growth and final failure generally occur at the very last loading cycle of the life of aircraft. Crack propagation at this stage involves elastic-plastic stable tearing followed by fast-fracture. Since crack growth is no longer under small-scale yielding conditions, elastic-plastic fracture mechanics (EPFM) is needed to characterize the fracture behavior and to predict the residual strength.

### 1.2.3 Bulging in Pressurized Thin Shell Structures

For cracks in a pressurized fuselage, the out-of-plane deformation or bulging at crack edges is an essential characteristic feature of the displacement fields. Following Potyondy *et al.* [108], the dominant factors that affect the behavior of through-cracks in the skin of pressurized fuselages are:

1. a geometrically nonlinear stiffening effect that restricts the crack edge bulging,
2. the presence of stiffening elements that alter the stress distribution in the skin,
3. the internal pressure and the mechanical loads that act on the structure, and
4. plasticity effects.

All the factors described above are taken into consideration in developing the analysis methodology in this work. The following general guidelines are used to characterize crack growth and to evaluate fuselage structural integrity:

- For fatigue crack growth, use thin shell analyses with geometric nonlinearity to evaluate SIFs for shells under membrane and bending loading. The SIFs are then used to evaluate crack growth-rate.
- For stable crack growth, use thin shell analyses with geometric and material nonlinearity to evaluate crack tip opening angle (CTOA). The critical CTOA is then used to control the crack advancement. Structural integrity and residual strength are then evaluated based on the predicted results of elastic-plastic crack growth simulations.

### 1.3 Background 2: Computational Issues for Crack Growth Simulation

To simulate realistic crack growth where crack trajectories are not known *a priori*, continual updating of the geometry is required. This feature makes conventional programs for computational solid mechanics difficult to use, if used alone. In this section, a brief overview of the main computational issues for arbitrary, discrete crack growth simulations is provided. Key aspects of the high-level description of the implementation to make the crack growth simulations efficient are presented<sup>2</sup>.

Discrete crack growth simulation is an incremental process, where a series of steps is repeated for a progression of models. The process continues until a suitable termination condition is reached. Results of such a simulation might include one or more of the following: a final crack geometry, a loading versus crack size history, a crack opening profile, or a history of the crack-front fracture parameters. In general, each increment in the process relies on previously computed results and represents one crack configuration. Following Carter *et al.* [17, 18], data in each crack growth increment can be divided into: representation database ( $\mathbf{R}_i$ , where the subscript denotes the increment number), analysis database ( $\mathbf{A}_i$ ), equilibrium database ( $\mathbf{E}_i$ ), and fracture parameter database ( $\mathbf{F}_i$ ). Each simulation of crack growth increment involves three major processes, a discretization process ( $\mathbf{D}$ ), a solution process ( $\mathbf{S}$ ), and an update process ( $\mathbf{U}$ ). The sequence of operations is illustrated in Figure 1.5. A discretization process,  $\mathbf{D}$ , primarily consisting of a meshing function,  $\mathbf{M}$ , transforms a representational description of a cracked body to a discrete model suitable for stress analysis. A solution process,  $\mathbf{S}$ , computes unknown field variables,  $\mathbf{E}_i$ , and fracture parameters,  $\mathbf{F}_i$ . An update process,  $\mathbf{U}$ , takes the equilibrium state field variables and the existing representation, using a function that predicts crack shape evolution,  $\mathbf{C}$ , creates a new representational database. The major problem in using conventional programs alone to simulate

---

<sup>2</sup>It is not the intent of the author to describe details of computational issues about arbitrary crack growth, but instead present a broad background and a departure point to introduce the software written and developed as part of this thesis. The readers are referred to [143, 17, 18] for more detailed and in-depth discussion.

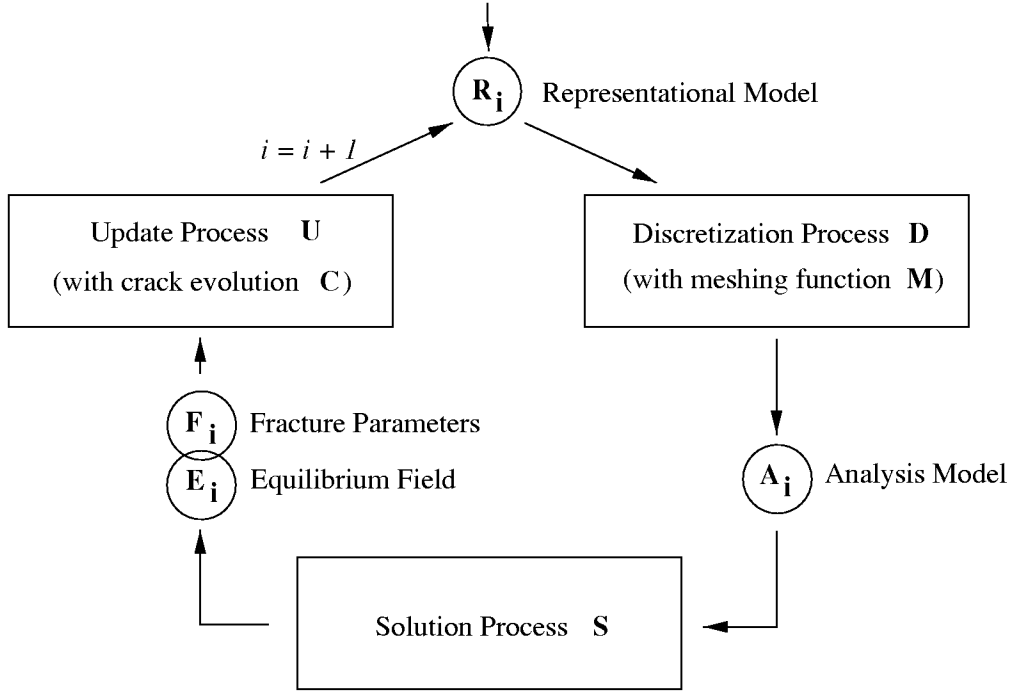


Figure 1.5: Illustration of the sequence of operations on databases and processes involved in each crack growth increment.

discrete crack growth is that they are ill-suited for tracking geometry changes that accompany crack growth unless the growth is constrained to be along existing element edges or faces. For general cases, where crack trajectories are not known *a priori*, a general representational model provides the key to efficiently handle crack growth simulations.

## 1.4 FRANC3D/STAGS Software Environment

A software system FRANC3D/STAGS that incorporates the conceptual crack growth model described above to support the analysis methodology in evaluating structural integrity of aging aircraft is developed. The system combines a topology based program, FRANC3D (FRacture ANalysis Code for 3D solids and shells), and a general nonlinear shell finite element program, STAGS (STructural Analysis of General Shells). FRANC3D has been under development by the Cornell Fracture Group since the late 1980s. The aim is a systematic representational model for arbitrary crack growth analysis. The key concepts embodied in FRANC3D are:

- solid modeling tools,
- a topological data structure that separates topology from geometry,
- the association of model attributes with topological entities, and

- a hierarchy of topological models to organize and guide the discretization process.

The representational model in FRANC3D is well-suited for tracking the geometry changes that accompany crack growth. The task of updating the representational model and generating a sequence of analysis models is separated from the task of performing an analysis on a particular model. For the FRANC3D/STAGS software, the analyses are performed by the STAGS code.

STAGS is a finite element code for general-purpose analysis of shell structures developed by Lockheed-Martin's Advanced Technology Center [113]. The main analysis capabilities in STAGS are:

- linear elastic stress analysis,
- geometrically and materially nonlinear stress analysis,
- linear bifurcation buckling analysis, and
- transient response analysis.

The FRANC3D/STAGS software first developed by Potyondy [106] is further modified by the author to support the evolving analysis methodology for evaluating structural integrity of aircraft structures.

The software components of FRANC3D/STAGS necessary to perform arbitrary crack growth simulation are illustrated in Figure 1.6. The FRANC3D code controls the entire process, allowing the analyst to compute the equilibrium states for a series of structural configurations. The STAGS code performs the stress analysis. Finally, an interface program is written to facilitate the data communication between the two codes.

## 1.5 Organization of the Dissertation

The primary objective of the dissertation is to develop an accurate structural analysis methodology and a useful and usable software program for predicting the structural integrity and residual strength of fuselage structures. The dissertation is divided into two parts: (1) elastic-plastic crack growth analyses and residual strength prediction with self-similar crack growth, Chapters 2–4; and (2) crack trajectory prediction with non-self-similar, curvilinear crack growth, Chapters 5–7.

Chapter 2 reviews and critiques various fracture mechanics methods for simulating elastic-plastic crack growth and predicting residual strength of thin-sheet metallic structures. Among the methods, the CTOA fracture criterion is found to be superior due to its relative independence of the geometry of the structure, the length of the crack, and the presence of multiple cracks. The concepts and formulations of the CTOA criterion are presented. Elastic-plastic crack growth,

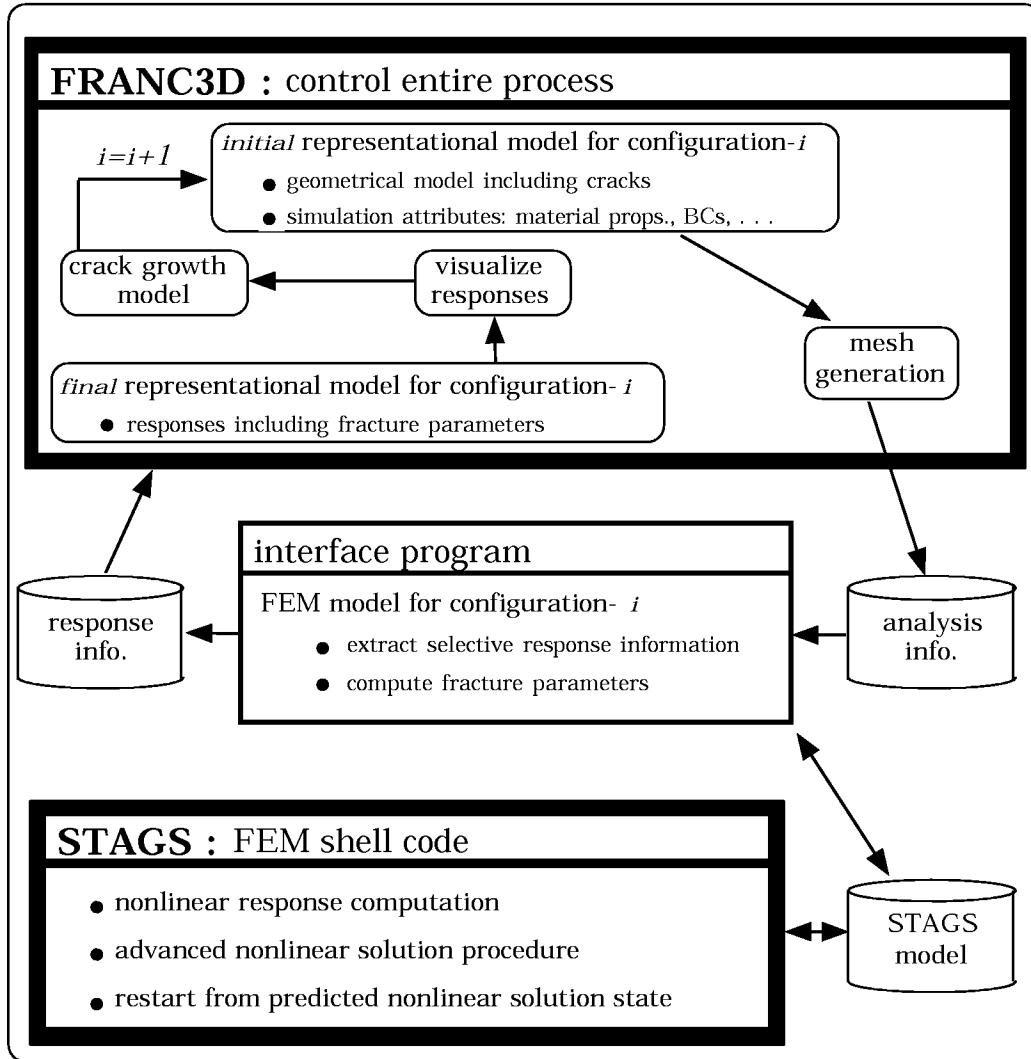


Figure 1.6: The FRANC3D/STAGS software components, their primary functions, and their interactions necessary to perform arbitrary crack growth simulation (modified after [106]).

link-up of multiple cracks, and residual strength analyses using the CTOA fracture criterion are discussed.

Chapters 3 and 4 describe finite element analyses of fracture tests using the CTOA fracture criterion. Elastic-plastic crack growth simulations and residual strength prediction of fracture coupon tests and full-scale fuselage panel tests are presented. In Chapter 3, fracture behavior in coupon tests including middle-crack tension (MT) and multiple crack specimens is analyzed. In Chapter 4, fracture behavior in full-scale narrow body and wide body panel tests is analyzed. Possible scenarios that can occur in pressurized fuselages are examined, including lead crack growth, multi-site damage, multiple crack interaction, plastic wake from fatigue crack growth, tear strap failure, and corrosion damage.

Chapters 5 through 7, the second part of the dissertation, consist of material related to crack trajectory prediction. An evolving methodology to improve structural integrity of aircraft structures using the crack turning phenomenon is discussed.

Chapter 5 reviews and critiques various crack growth directional criteria for crack trajectory prediction. A directional criterion based on the maximum tangential stress theory, but taking into account the effect of  $T$ -stress and fracture toughness orthotropy is developed. In Chapter 6, the path independent contour integral method for  $T$ -stress evaluation is presented. The numerical accuracy using the path independent integral is assessed by highly accurate two-dimensional p- and hp-version adaptive finite element analyses. Chapter 7 analyzes curvilinear crack growth in coupon tests and in full-scale narrow body fuselage panel tests. The  $T$ -stress and fracture toughness orthotropy effect on crack trajectory prediction is examined.

The final chapter summarizes the contributions of this thesis, draws conclusions, and where appropriate, provides recommendations for future work.

# Chapter 2

## Theory for CTOA-Driven Elastic-Plastic Crack Growth and Residual Strength Analysis

This chapter together with Chapters 3 and 4 gives a comprehensive treatise on using the crack tip opening angle (CTOA) fracture criterion to predict elastic-plastic crack growth and residual strength of thin-sheet metallic structures. Theories, concepts, and formulations related to the CTOA-driven fracture criterion are given in this chapter. Elastic-plastic crack growth simulations and residual strength prediction of coupon tests and full-scale fuselage panel tests are presented in the next two chapters.

### 2.1 Introduction

To predict successfully fracture behavior and residual strength of aircraft fuselage structures subjected to widespread fatigue damage (WFD), a fracture criterion independent of the geometry of the structure, the length of the crack, and the presence of multi-site damage (MSD) is required [29]. In this chapter, a brief evaluation of various fracture mechanics methods to simulate elastic-plastic crack growth and to predict residual strength of damaged structures is given. The evaluation focuses on the applicability to thin-sheet metallic structures with single and multiple cracks where plastic flow makes a substantial contribution to crack growth resistance.

Among the fracture methods, the superior nature of the CTOA fracture criterion to characterize elastic-plastic crack growth in thin-sheet metals is revealed after review of two recent evaluations [91, 28]. Theories for simulating the CTOA-driven crack growth are discussed and guidelines for using the CTOA fracture criterion to predict residual strength of aircraft structures are presented.

## 2.2 Evaluation of Fracture Mechanics Methods

Thin sheet metallic structures in ductile states generally undergo stable crack growth before the occurrence of fast fracture. To have an accurate and reliable prediction of residual strength for such structures, a fracture criterion that can characterize stable crack growth under conditions of general yielding is needed. Various fracture mechanics methods have been developed over the past several decades. However, for materials exhibiting a large amount of plasticity and stable crack growth prior to failure, there is no consensus on the most satisfactory method [116, 91]. To evaluate various methods in assessing crack growth resistance and predicting failure of flawed structures, an experimental and predictive round robin was conducted in 1979-1980 by the ASTM Committee E-24 on Fracture Testing [91]. The fracture analysis methods used in the round robin included:

1. linear elastic fracture mechanics (LEFM) corrected for size effects or for plastic yielding [91],
2. equivalent energy [148],
3. the two-parameter fracture criterion,  $K_F$  and  $m$  [87],
4. the deformation plasticity failure assessment diagram based on deformation plasticity, a  $J$ -integral estimation scheme, and a solution from the *Plastic Handbook* [10, 75],
5. the theory of ductile fracture [11],
6. the  $K_R$ -curve with the Dugdale model [37],
7. the effective  $K_R$ -curve [79],
8. a two-dimensional (2D) finite element analysis using the CTOA criterion with stable crack growth [90], and
9. a three-dimensional (3D) finite element analysis using a crack-front singularity parameter with a stationary crack [81].

Fracture tests were conducted on compact tension specimens (CT), middle-crack tension specimens (MT), and three-hole-crack tension specimens (THCT) as shown in Figure 2.1. Three materials tested were 7075-T651 aluminum alloy, 2024-T351 aluminum alloy, and 304 stainless steel. The accuracy of the prediction methods was judged by the failure loads obtained from experiments. For 7075-T651 aluminum alloy, the best methods were the effective  $K_R$ -curve, a 2D finite element analysis using CTOA with stable crack growth, and the  $K_R$ -curve with the Dugdale model. For 2024-T351 aluminum alloy, the best methods were the two-parameter fracture criterion, a 2D finite element analysis using CTOA with stable crack growth, the  $K_R$ -curve with the Dugdale model, the effective  $K_R$ -curve,



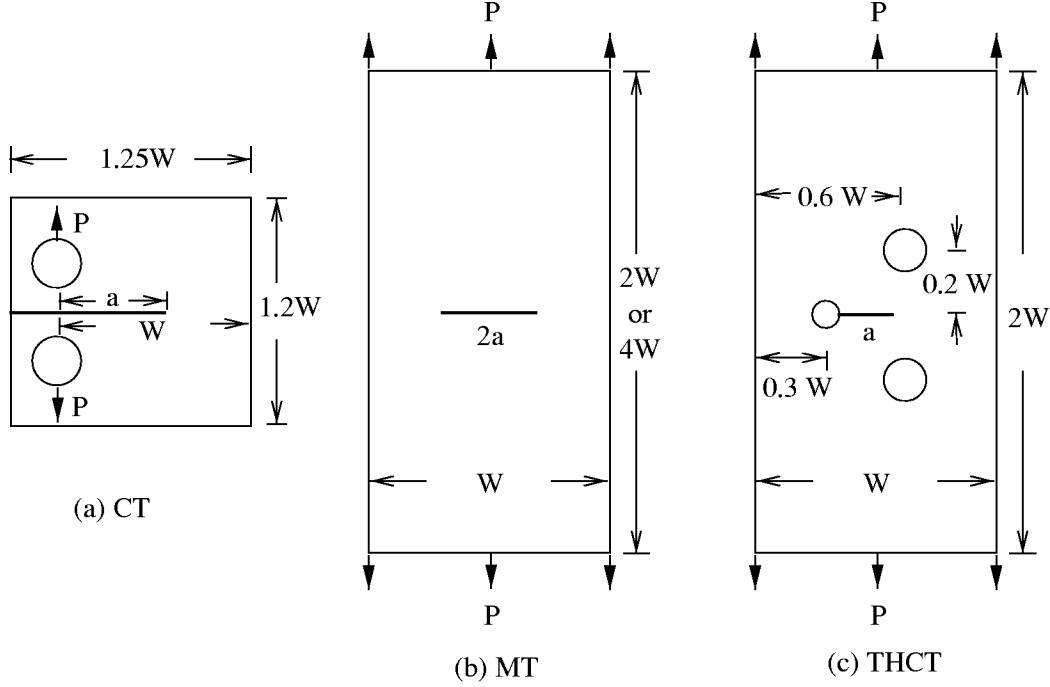


Figure 2.1: Specimen configurations tested and analyzed in ASTM round robin (after [91]).

and the deformation plasticity failure assessment diagram. For 304 stainless steel, the best methods were the effective  $K_R$ -curve, a 2D finite element analysis using CTOA with stable crack growth, the two-parameter fracture criterion, and the deformation plasticity failure assessment diagram.

These tests were conducted using specimens with a single crack configuration. Recently, fracture tests were conducted on a 0.09 inch thick, 2024-T3 aluminum alloy using CT, MT, and MSD specimens [28]. Several fracture mechanics methods were again evaluated including the effective  $K_R$ -curve [79, 3], the  $J$ -integral resistance curve ( $J_R$ ) [92], the crack-opening resistance curve ( $\delta_R$ ) [55], the  $T^*$ -integral resistance curve ( $T_R^*$ ) [4], the plastic-zone link-up criterion [139], and the critical CTOA fracture criterion using a 3D finite element analysis [29]. The study concluded that the plastic-zone link-up criterion had limited use in predicting fracture behavior of specimens. The effective  $K_R$ ,  $J_R$ ,  $T_R^*$ , and  $\delta_R$  fracture criteria could predict MSD fracture behavior of some larger specimens based on small specimen tests, but were limited to a certain size of specimens. The critical CTOA fracture criterion using a 3D, elastic-plastic finite element analysis was able to predict the fracture behavior for all specimen sizes.

Based on the above evaluations, the CTOA-driven, elastic-plastic stable crack growth simulation appears to be a plausible fracture analysis method to assess crack growth resistance and to predict residual strength of thin-sheet metallic structures.

## 2.3 CTOA Fracture Criterion

The CTOA fracture criterion is essentially an integration of the near-tip strains. It evolves from the critical crack tip opening displacement (CTOD) concept proposed by Wells [144]. Since the CTOD has a limiting value of zero at the crack tip, the local slope of the crack tip opening profile, or CTOA, was suggested to characterize the crack growth behavior [2, 36]. Newman [90], Rice and Sorensen [121], and Kanninen and Popelar [64] further defined the CTOA as the crack tip opening angle measured at a fixed distance behind the moving crack tip.

The CTOA fracture criterion asserts that the angle maintains a constant value during stable crack growth for a given thickness of a metallic material. This phenomenon has been observed in numerous experiments for a wide range of metals [66, 63, 65, 90, 34, 94], indirectly supported from slip-line field solutions [121, 118], and verified by numerical simulations [36, 90, 64, 93, 35, 30, 27, 29, 28, 20, 23, 22]. Tests on aluminum alloys as well as steels [65, 90] have confirmed that the CTOA is essentially constant after a certain transitional period of stable crack growth. A larger critical CTOA during the initiation of stable tearing rapidly decreases to a constant value. The amount of crack growth to reach the constant CTOA is approximately equal to the specimen thickness [34]. Based on a fatigue marker load technique and scanning electron microscope observations, Dawicke and Sutton [34] concluded that the non-constant CTOA region is associated with severe tunneling during the initiation of stable crack growth.

Asymptotic solutions of a growing crack provide indirect support for using the critical CTOA criterion. Rice *et al.* [118], extending the work of Rice and Sorensen [121], obtained Prandtl slip-line field solutions for a Mode I, plane-strain growing crack in a nonhardening elastic-plastic solid. Based on the asymptotic solutions, they proposed that a similar geometric profile of crack opening very near the tip is maintained during crack growth. The criterion for continuing crack growth in [121, 118] is:

$$\frac{\delta_c}{d} = \frac{\alpha}{\sigma_0} \frac{dJ}{da} + \beta \frac{\sigma_0}{E} \ln \frac{eR}{d} \quad (2.1)$$

where  $\delta_c$  is the critical CTOD measured at a small characteristic distance  $d$  behind the growing crack tip<sup>1</sup>. The  $dJ/da$  represents the rate of external applied loading during crack growth. The  $\sigma_0$ ,  $E$ , and  $e$  in Equation (2.1) are the yield stress, the elastic modulus, and the natural logarithm base, respectively. The length parameter  $R$  and material parameters  $\alpha$  and  $\beta$  are to be determined by tests or numerical analyses. This asymptotic field crack growth criterion is equivalent to the CTOA fracture criterion.

The ability of the CTOA fracture criterion to simulate elastic-plastic crack growth has been verified by many numerical analyses. de Koning [36] and Anderson [2] were among the first to demonstrate that CTOA can be used to characterize

---

<sup>1</sup>The characteristic distance is called  $\Delta l$  and  $r_m$  in [121] and [118], respectively.

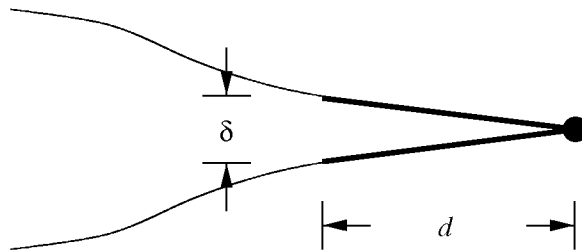


Figure 2.2: Illustration of CTOA definition.

stable crack growth. Newman [90, 91], using a 2D elastic-plastic finite element analysis, was able to simulate stable crack growth and predict residual strength within 10% for the test configurations shown in Figure 2.1.

Recently, the CTOA fracture criterion has been extensively verified through tests and analyses for various loading, geometry, and crack configurations<sup>2</sup>. Tests on aluminum alloys [34, 94], 2D [93, 35, 30, 33], thin-shell [20, 23, 22], and 3D [27, 29, 28] elastic-plastic crack growth analyses have been conducted to assess the CTOA fracture criterion for aging aircraft applications. These studies will be discussed in Chapter 3.

The CTOA fracture criterion is used in this study to characterize stable crack growth in thin-sheet metallic materials. The definition of CTOA as suggested by Newman [90] is adopted. For Mode-I only deformations, it is defined as (Figure 2.2):

$$\text{CTOA} = 2 \tan^{-1} \frac{\delta}{2d} \quad (2.2)$$

where  $\delta$  is the CTOD measured at a specific distance,  $d$ , behind the crack tip. For mixed-mode problems, the opening angle is obtained from the cross product of two vectors:

$$\text{CTOA} = \sin^{-1} \frac{\|\mathbf{a} \times \mathbf{b}\|}{\|\mathbf{a}\| \|\mathbf{b}\|} \quad (2.3)$$

where  $\mathbf{a}$  and  $\mathbf{b}$  are the vectors from the crack tip to crack edges at a specific distance,  $d$ , behind the crack tip.

## 2.4 Elastic-Plastic Crack Growth

Stable crack growth seems to be an inherent feature of elastic-plastic materials because of the occurrence of permanent plastic deformations during unloading [115]. This effect can be demonstrated by global energy dissipation or by the local residual plastic deformations. The energy dissipation effect on stable crack growth is illustrated by considering the example used in [115]. Suppose two materials have

---

<sup>2</sup>Most of the test data are available from the Internet at [irwin.larc.nasa.gov](http://irwin.larc.nasa.gov).

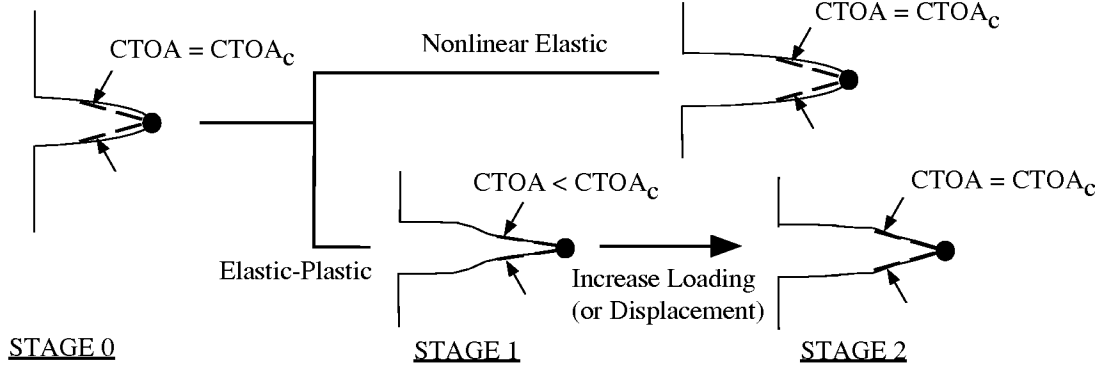


Figure 2.3: Illustration of crack growth in nonlinear elastic and elastic-plastic materials.

the same uniaxial stress-strain curves; one is an idealized nonlinear elastic material and the other is an elastic-plastic material. For cases without crack growth, the same CTOA and strain concentration will occur in the two materials as illustrated in Figure 2.3, STAGE 0. As the crack propagates in the nonlinear elastic material, deformation fields need to be readjusted and the same crack tip opening profile would occur for the new crack tip location [115]. This is not the case for the elastic-plastic material because a large part of the energy is consumed by plastic dissipation with far less strain recovered during unloading. Thus, a smaller CTOA is obtained after crack growth (STAGE 1). Further increase of the applied loading is needed to open the crack (STAGE 2) and causes stable crack growth in the elastic-plastic material. Fracture instability will occur as the crack reaches a steady-state condition in which the crack continually advances without further increase in load. If the analysis is performed under displacement control, then a reduction in applied load is required to maintain a constant CTOA for continuous crack growth. Hereafter,  $CTOA_a$  is the crack tip opening angle measured immediately after propagation, STAGE 1.  $CTOA_b$  is denoted as the increase in crack tip opening angle required to reach the critical value ( $CTOA_c$ ). Thus,

$$CTOA_a + CTOA_b = CTOA_c \quad (2.4)$$

satisfies the fracture criterion for crack propagation, and the condition

$$CTOA_a = CTOA_c \quad (2.5)$$

indicates the occurrence of fracture instability for the analysis under load control.

Another related factor for stable crack growth is the plastic wake effect caused by the residual plastic deformations [90]. As the crack grows, the plastic zone behind the crack tip unloads to an elastic state leaving the appropriate plastic wake behind the advancing crack tip. This effect results in resistance to crack tip opening as illustrated in Figure 2.4. The dashed curves in the plastic wake

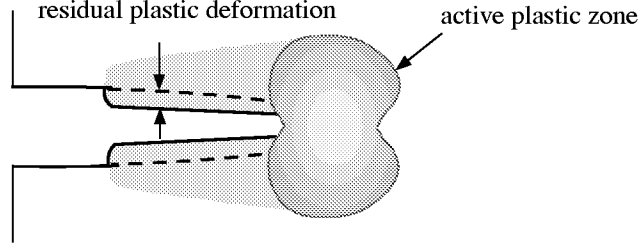


Figure 2.4: Illustration of plastic wake effect caused by crack growth.

region show what the crack opening profile would have been if residual plastic deformations had not been retained in the material behind the advancing crack tip. This phenomenon is also essential for simulating the initiation of stable crack growth associated with high fatigue stress prior to tearing [30].

It is of interest to note that a different density of residual plastic deformation would develop as the crack propagates under plane stress compared to plane strain conditions. Based on the Prandtl field together with an elastic sector following the centered fan, Rice *et al.* [118, 117] have shown that asymptotic plastic strains for quasi-static crack growth under plane strain conditions in elastic-perfectly plastic materials are:

$$\epsilon_{\alpha\beta}^P = F_{\alpha\beta}(\theta) \ln\left(\frac{1}{r}\right) \quad r \rightarrow 0 \quad (2.6)$$

where  $(r, \theta)$  is a local polar coordinate system with the origin at the crack tip and  $F_{\alpha\beta}(\theta)$  are functions determined from an asymptotic angular integration of the plastic strain rate. No complete asymptotic solutions are available for plane stress conditions, but only two types of plastic sectors can exist near the crack tip; one is the centered fan and the other is constant stress [117, 86]. For the case with the center fan sectors, Rice [115] shows that plastic strains under plane stress conditions are:

$$\epsilon_{ij}^P = G_{ij}(\theta) \ln^2\left(\frac{1}{r}\right) \quad \theta = 0 \quad r \rightarrow 0 \quad (2.7)$$

where  $G_{ij}$  are scalars from solutions with a centered fan on the  $\theta = 0$  ray. By comparing Equations (2.6) and (2.7), one finds that plastic strains on the  $\theta = 0$  ray have a stronger singularity in plane stress than in plane strain. This observation gives a preliminary indication that higher residual plastic deformations may occur under plane stress conditions leading to higher resistance to the opening of a growing crack.

## 2.5 Link-up and Residual Strength Analysis with CTOA Fracture Criterion

Since analyses based on the CTOA fracture criterion are direct simulations of realistic crack growth, multiple crack growth interaction and link-up are automatically

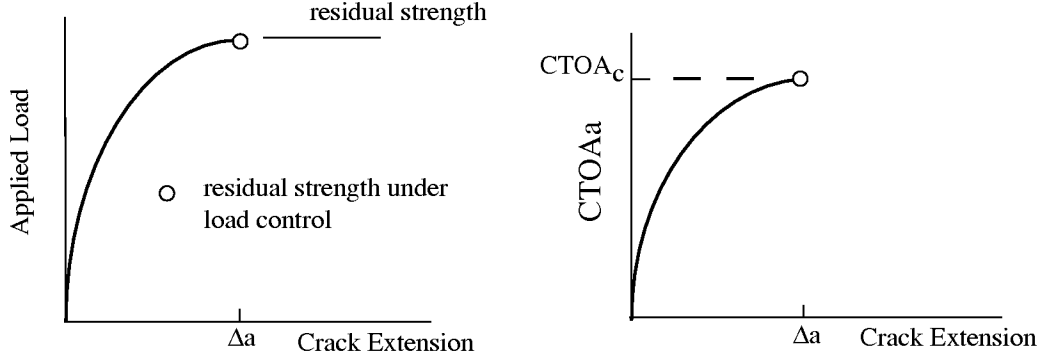


Figure 2.5: Residual strength diagram under load control.

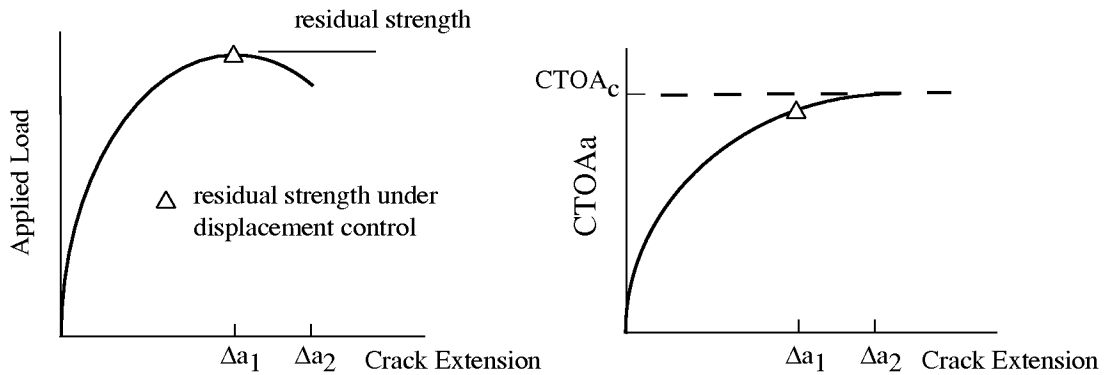


Figure 2.6: Residual strength diagram under displacement control.

captured as the crack propagates. Residual strength of a damaged structure is also obtained directly from the crack growth data. For tests conducted under load control with the plastic zone well-confined by the elastic region, fracture instability is reached when no further increase of the applied load is required to maintain quasi-static crack extension. For tests under displacement control, the maximum load carrying capacity of a structure occurs followed by a reduction in load during continued crack growth. The residual strength diagrams corresponding to load control and displacement control are illustrated in Figures 2.5 and 2.6, respectively. Note that under displacement control, the load instability occurs before Equation (2.5) is satisfied. By comparing Figures 2.5 and 2.6, one finds that the load-crack extension curve up to residual strength is obtained under load control. On the other hand, the curve after residual strength can be obtained from the displacement-control technique.

## 2.6 Guidelines for Using the CTOA Fracture Criterion

Guidelines for using the CTOA criterion to predict fracture behavior and residual strength of built-up aircraft fuselages are presented below<sup>3</sup> for future reference. The guidelines focus on (1) how to obtain a valid CTOA value from laboratory fracture tests for a given thickness of thin-sheet metallic material, and (2) how to correlate or *fine-tune* numerical analyses based on laboratory tests to predict the fracture behavior and residual strength of complex structures.

1. Conduct tension tests to accurately describe the stress-strain behavior of the material.
2. Conduct fracture tests on coupon specimens. Measure the  $CTOA_c$  and record crack growth data during stable tearing. The experimental  $CTOA_c$  measurements typically have a scatter band of  $\pm 0.5^\circ$  to  $\pm 1.0^\circ$ . The material of the specimen should be the same alloy, temper, and thickness as the material of the complex structure. The specimen should be large enough to allow significant crack growth prior to reaching residual strength.
3. Use thin-shell elastic-plastic finite element analyses accounting for 3D constraint effects developed at the crack tip<sup>4</sup> to simulate fracture behavior. Compare the predicted load versus crack growth to the experimental data and determine the value of  $CTOA_c$  that best correlates the experimental data and numerical results. Note that:
  - The characteristic distance,  $d$ , used in analyses should be the same as the one used in experimental measurements.
  - Agreement of the  $CTOA_c$  values obtained independently from experimental measurements and numerical analyses would greatly increase the confidence in the chosen  $CTOA_c$  value.
4. Create a finite element model for the structure to be analyzed. Use the previously determined  $CTOA_c$  value to predict the fracture behavior. The model should have the same size and type of crack tip elements as the one used in the coupon test correlation.

The validity of these guidelines as applied to fuselage structures will be examined extensively through Chapters 3 and 4.

---

<sup>3</sup>These guidelines follow closely the recommendations made in [33, 29].

<sup>4</sup>One way to consider the 3D constraint effects in a thin shell analysis is to use the plane strain core concept (see Figure 3.2).

## 2.7 Summary

Various LEFM and EPFM versions of fracture mechanics methods to characterize fracturing processes in thin-sheet metals were reviewed and critiqued in Section 2.2. Among them, the CTOA fracture criterion with a 3D elastic-plastic analysis was found to be a superior one because of its relative independence of the geometry of the structure, the length of the crack, and the presence of multiple cracks.

Previous experimental, analytical, and numerical studies for the CTOA fracture criterion were reviewed in Section 2.3. The definition of the CTOA was given in Equation (2.2) for Mode-I only deformations and in Equation (2.3) for general mixed-mode problems.

The CTOA-driven elastic-plastic crack growth was studied in Section 2.4. The inherent feature of stable crack growth in elastic-plastic materials was discussed using the energy dissipation and residual plastic deformation. Residual plastic strains from elastic-plastic crack growth under plane stress and plane strain conditions were studied using the Prandtl field. Higher residual plastic deformations were found under plane stress conditions. As a result, a higher fracture resistance of a growing crack may occur under plane stress conditions. This behavior will be further examined numerically in Chapter 3.

Analyses of link-up of multiple cracks and residual strength of damaged structures using the CTOA fracture criterion were discussed in Section 2.5. Finally, guidelines for using the CTOA criterion calibrated from coupon tests to predict fracture behavior of built-up aircraft fuselages were presented in Section 2.6.



## Chapter 3

# Residual Strength Analysis of a Flat Panel with Self-Similar Elastic-Plastic Crack Growth

Elastic-plastic crack growth simulations and residual strength prediction of flat panel coupon tests are studied in this chapter. The purposes of this chapter are to:

1. further review and discuss some recent activities of using the crack tip opening angle (CTOA) fracture criterion for aging aircraft applications,
2. model the fracturing processes in middle-crack tension (MT) specimens using elastic-plastic, thin shell finite element analyses,
3. explore the need to incorporate the three-dimensional constraint effect to characterize fracture behavior of thin-sheet metals, and
4. model the fracturing processes in thin-sheet specimens with multi-site damage (MSD).

### 3.1 Introduction

Tests and numerical simulations have been performed to assess the CTOA fracture criterion for predicting residual strength of aging aircraft. Laboratory tests were conducted on flat panels made of aluminum alloys [34, 94]. Numerical simulations were conducted using two-dimensional (2D) [93, 35, 94, 30, 33], thin-shell [20, 23, 22], and three-dimensional (3D) [27, 29, 28] finite element elastic-plastic crack growth analyses. We review these activities in a somewhat chronological order and highlight the important findings of these studies below. The latest results are used as a starting point for subsequent simulations in this study.

A series of fracture tests have been conducted using a 2024-T3 aluminum alloy for MT, CT, blunt notch, THCT and MSD specimens. Newman *et al.* [93]

conducted tests on 0.05, 0.07, and 0.09 inch thick, 3.0 and 11.8 inch wide MT and blunt notch specimens as well as 0.09 inch thick, 10 inch wide THCT specimens. The blunt-notch specimen is similar to the MT specimen except that a small hole is drilled at both ends of the saw cut. It is intended to assess the suitability of elastic-plastic finite element analyses with the small-strain assumption to model large-scale plasticity deformations. A good agreement between predicted and measured load versus notch-tip displacements substantiates the assumption.

The critical values of CTOA ( $CTOA_c$ ) were measured for the MT and THCT specimens to assert the specimen configuration independence of the fracture criterion. The THCT specimen has a stress intensity factor solution like that of a cracked, stiffened panel [91]. The measured  $CTOA_c$  values showed higher angles at crack initiation, but reached the same constant value after a small transition period of crack growth. The agreement of  $CTOA_c$  between MT and THCT specimens indicates that the CTOA fracture criterion is independent of specimen configuration; this was further confirmed by a follow-up study with measurements from CT specimens [35].

A 2D elastic-plastic finite element code, ZIP2D [88], and a 6.1 degree  $CTOA_c$ , computed at 0.01875 inch behind the crack tip, were used to simulate fracture behavior of the MT specimens [93]. To model fatigue pre-cracking, cyclic loading simulation was conducted prior to stable tearing analyses. Experimental and predicted results showed that a higher applied stress during the fatigue tests increased the resistance of stable crack growth initiation. Predicted residual strengths under plane stress conditions were within 4% of experimental results for 3.0 and 11.8 inch wide MT specimens. Yet the plane stress analyses over-predicted crack extensions prior to limit load while the plane strain analyses under-predicted crack extensions.

The above studies raised two important questions:

1. What is the governing mechanism that causes higher  $CTOA_c$  values during crack initiation?
2. What is the governing mechanism that causes the discrepancy between 2D predictions and test results?

Dawicke and Sutton [30] examined the higher values of measured  $CTOA_c$  observed during crack initiation, *i.e.*, question 1. Two independent techniques, optical microscopy (OM) and digital image correlation (DIC) were used to measure surface  $CTOA_c$  during crack growth. The results of the two methods agreed very well. Fatigue marker loads and a scanning electron microscope were used to examine the fracture morphology and sequences of crack front profiles. For specimens under low magnitude of fatigue stress prior to tearing, crack surfaces underwent a transition from flat-to-slant crack growth. A schematic of the transition is shown in Figure 3.1. During the transition period, the  $CTOA_c$  values were high and significant tunneling occurred. After an amount of crack growth equal to about the specimen thickness,  $CTOA_c$  reached a constant value. After crack growth equal to about twice the thickness, crack tunneling stabilized. For specimens that were

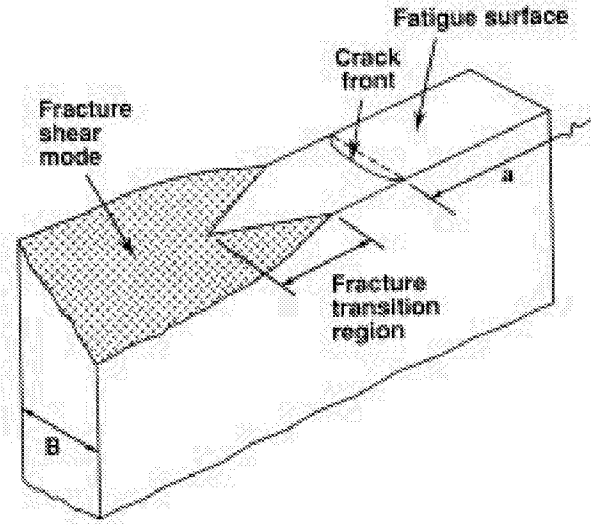


Figure 3.1: Schematic of fracture surface indicating transition from a flat to a slant crack plane (after [93]).

pre-cracked under a high magnitude of fatigue stress, a 45-degree, slant, through-thickness initial crack was formed prior to tearing. During the crack initiation period, the  $CTOA_c$  values of specimens with high fatigue stress were lower than the ones with low fatigue stress. But the same constant  $CTOA_c$  value was observed after crack growth equal to about the specimen thickness.

The discrepancy between 2D predictions and test results, *i.e.*, question 2, was thought to be related to the 3D constraint effect. Although thin-sheet structures behave essentially in plane stress, the constraint due to the finite thickness of the specimens can cause the regions local to the crack tip to approach plane strain conditions [56].

To investigate the constraint effect, 2D and 3D analyses were conducted. In the 2D analyses, a *core* of elements above and below the crack path were assigned as plane strain while all other elements were assigned as plane stress. The plane strain core concept is illustrated in Figure 3.2.

In their early attempt, Dawicke *et al.* [35, 94] used 2D finite element analyses with a 6.0 degree  $CTOA_c$  computed at 0.02 inch behind the crack tip and a plane strain core height equal to 0.2 inch to simulate fracture behavior with the constraint effect. They showed that the use of a plane strain core was essential to accurately model crack growth. The predicted residual strengths were within 2% for 3 and 12 inch wide, 0.09 inch thick MT specimens and within 4% for 6 inch wide, 0.09 inch CT specimens. For 20 inch wide, 0.04 inch thick MSD specimens, 2D analyses with a 5.1 degree  $CTOA_c$  showed excellent agreement of link-up and residual strength between predictions [94] and test results [13].

Dawicke *et al.* [27, 29] further studied the constraint effect using 3D finite element analyses with a 5.25 degree  $CTOA_c$  computed at 0.04 inch behind the

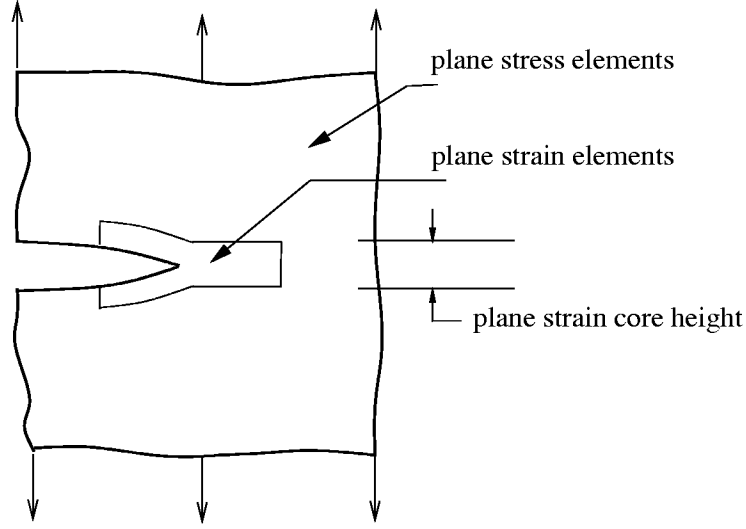


Figure 3.2: Schematic of the plane strain core.

crack tip. The 3D analyses successfully simulated fracture behavior of 2.0, 4.0, 6.0, and 8.0 inch wide CT specimens, 1.2, 3.0, 6.0, 12.0, 24.0, and 60.0 inch wide MT specimens, and 12.0 inch wide MSD specimens made of 0.09 inch thick, 2024-T3 aluminum alloy. A plane strain core height of 0.12 inch was required for 2D analyses to match the measured results and the 3D fracture predictions.

In the following, the MT and MSD tests are studied. The FRANC3D/STAGS program is used to simulate fracture behavior and predict residual strength using the guidelines derived from the above 2D and 3D studies.

## 3.2 Experimental Procedures and Test Configurations

Fracture tests of MT specimens were conducted by the Mechanics of Materials Branch at NASA Langley Research Center [34, 27, 29]. The test specimens were made of 0.09 inch thick 2024-T3 aluminum alloy. All specimens were fatigue pre-cracked in the L-T orientation with a low stress level that results in a stress intensity factor range of  $\Delta K = 7 \text{ ksi}\sqrt{\text{inch}}$ . For specimens with a single crack, different widths of panels equal to 3 inch, 12 inch, and 24 inch with a crack-length to width ratio equal to 1/3 were tested (Figure 3.3). For cases with multiple cracks, only the 12 inch wide specimens with two to five near collinear cracks as illustrated in Figure 3.4 were tested. All tests were conducted under displacement control with guide plates to prevent out-of-plane buckling. Both OM and DIC techniques were used to measure the  $\text{CTOA}_c$  during stable crack growth [34]. Results for MT and CT specimens are shown in Figure 3.5. The  $\text{CTOA}_c$  rapidly reaches a constant value with a scatter band about  $\pm 1.0^\circ$ .

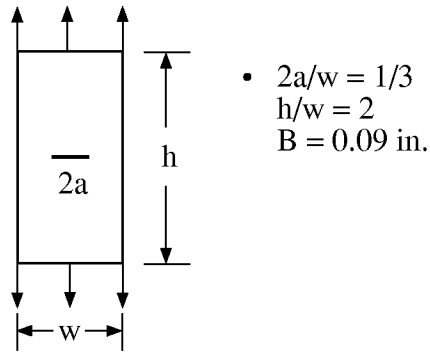


Figure 3.3: Test configurations of MT specimens.

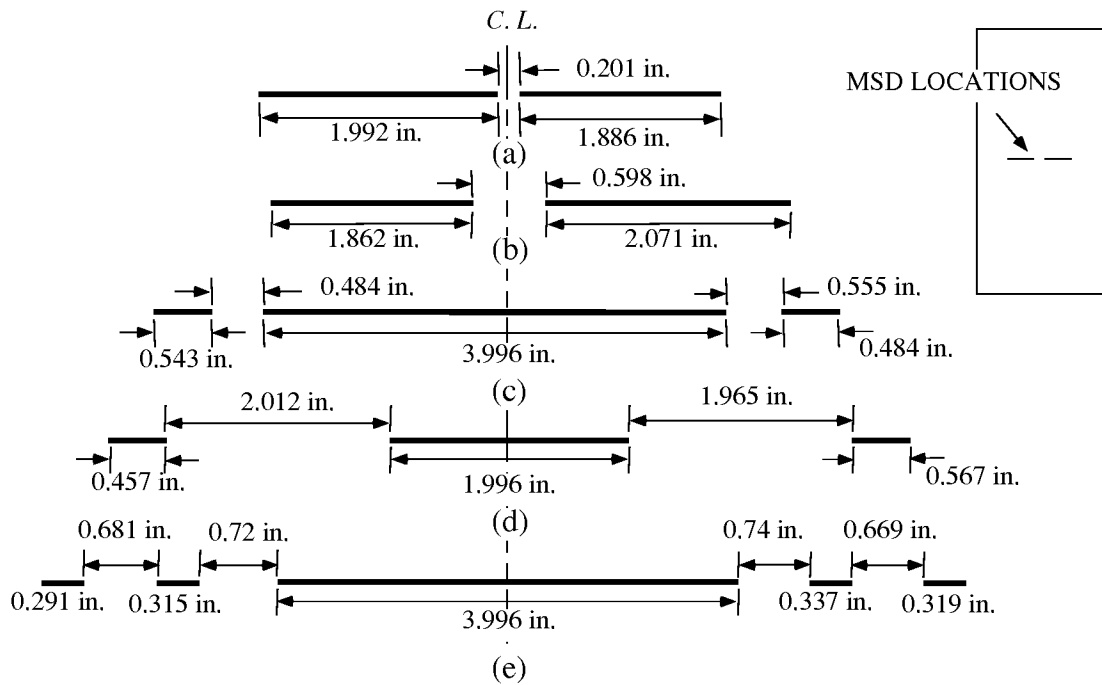


Figure 3.4: Test configurations of 12 inch wide specimens with multiple cracks.

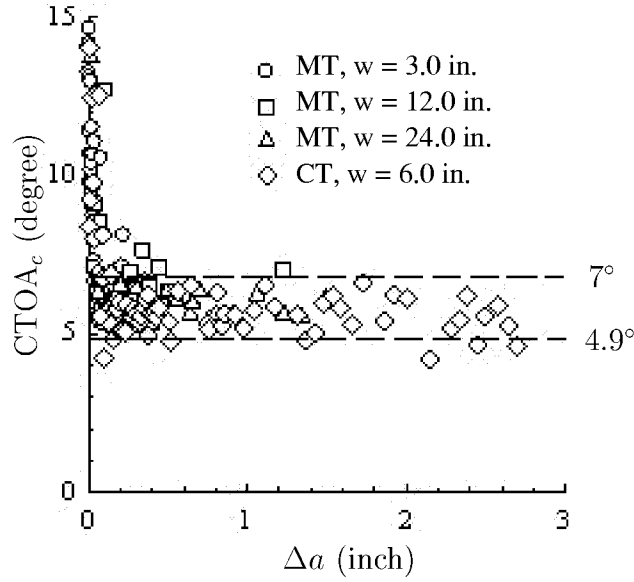


Figure 3.5: Surface measurements of  $CTOA_c$  (after [29]).

### 3.3 Numerical Simulations of MT Specimens

Fracture processes of MT specimens were simulated first. To investigate panel size effects, numerical simulations of 60 inch wide panels with the same crack-length-to-width ratio were also performed. Elastic-plastic finite element analyses based on incremental flow theory with the von Mises yield criterion and the small strain assumption were used to capture the active plastic zone and the plastic wake during stable crack propagation. A piecewise linear representation was used for the uniaxial stress-strain curve for 2024-T3 aluminum (Figure 3.6). The  $CTOA_c$  used in this study was 5.25 degrees measured 0.04 inch behind the crack tip. This particular  $CTOA$  value was provided by Dawicke and Newman [27, 29] based on 3D simulations of CT specimens<sup>1</sup>. Upon satisfaction of the fracture criterion, nodal release and load (or displacement) relaxation techniques were employed to propagate the crack. Because of the double symmetry of the geometry and loading, only one quarter of the specimen with imposed symmetry boundary conditions was modeled. Out-of-plane displacements were suppressed. Displacement-based four-noded and five-noded quadrilateral shell elements having  $C^1$  continuity were used [112]. These elements are intended to model thin shell structures for which transverse shear deformation is not important. Each node of the element has six degrees of freedom including three translations and three rotations. A special five-noded shell element, formulated by combining two four-noded elements and using linear constraint along the edge to eliminate the dependent node, was used to

<sup>1</sup>As noted by Dawicke and Newman [29], the fracture behavior of the CT specimen is more sensitive to small changes in  $CTOA_c$  than the MT specimen; thus the CT specimen is more suitable to correlate predicted and measured results.

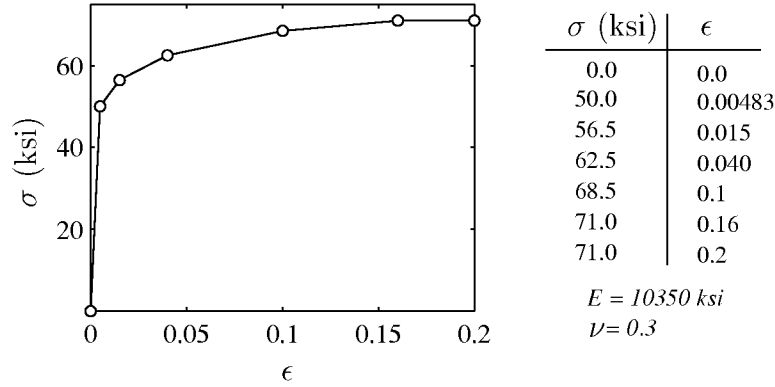


Figure 3.6: Piecewise linear representation of the uniaxial stress-strain curve for 2024-T3 aluminum.

transition from locally refined zones around the crack path to a coarse mesh away from the crack.

A convergence study was conducted to determine the sensitivity of the predicted residual strength to the element size along the crack extension path. Three meshes for the 24 inch wide panel were created with crack tip element sizes of 0.04 inch, 0.02 inch, and 0.01 inch. For all crack growth and residual strength analyses, the CTOA was evaluated at 0.04 inch behind the crack tip to be consistent with experimental measurements. A finite element mesh with 0.04 inch square crack tip elements for the 24 inch wide panel is shown in Figure 3.7. Predicted crack growth results for cases with 0.04 inch and 0.02 inch crack tip elements as well as predicted residual strengths for all three cases are shown in Figure 3.8. Although some discrepancy was observed at the early stage of stable tearing, the predicted results exhibited little influence of mesh size after a relatively small amount of stable crack growth. More importantly, the predicted residual strength was very insensitive to crack tip element size. Thus, all the remaining meshes used in this study had 0.04 inch crack tip elements.

### 3.3.1 Numerical Results

Figure 3.9 shows two predicted crack opening profiles for the 24 inch wide panel. The angles were computed immediately after propagation (*i.e.*,  $CTOA_a$ , see Figure 2.3) with relaxation procedures completed and before increasing the applied displacement. The two  $CTOA_a$  values correspond to (1) the angle after the first increment of crack growth, and (2) the angle after the specimen reaches its residual strength. As shown in the figure,  $CTOA_a$  is much smaller than the critical angle after the first crack growth increment. This clearly demonstrates the permanent plastic deformation effects on stable crack growth in the elastic-plastic material (*cf.* section 2.4). As the crack propagates,  $CTOA_a$  increases. Since the analyses were conducted under displacement control, the  $CTOA_a$  at residual strength is less

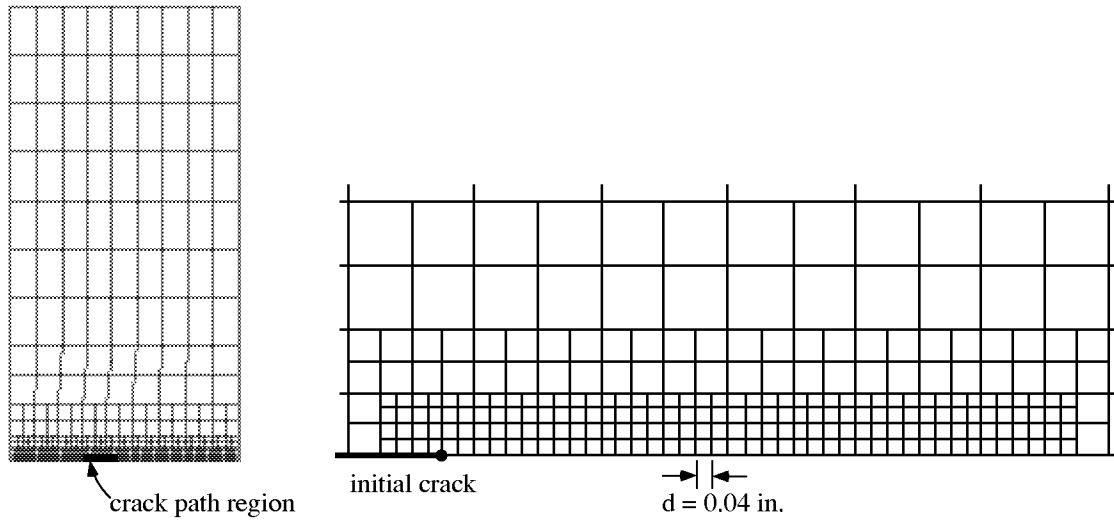


Figure 3.7: Finite element mesh for 24 inch wide MT specimen and detail along crack path.

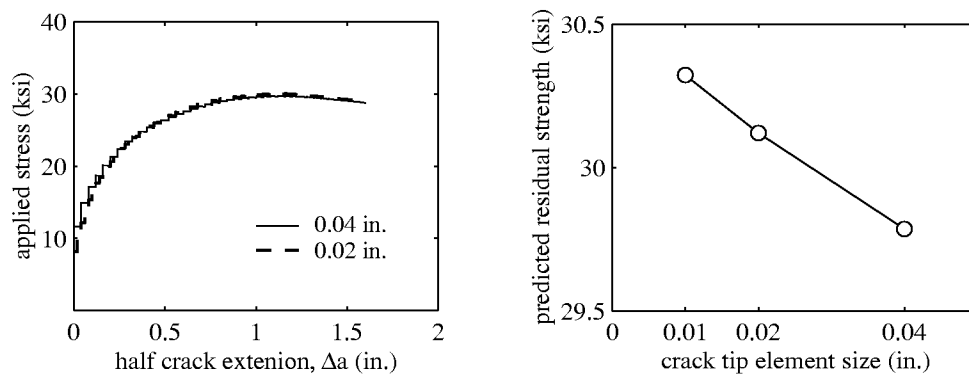


Figure 3.8: Convergence study: predicted crack growth and predicted residual strength for 24 inch wide panel with different crack tip element sizes.



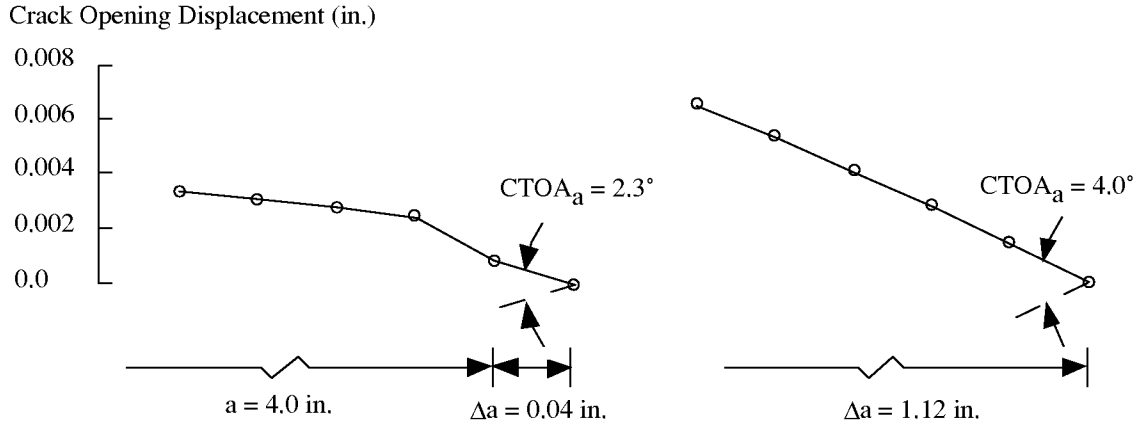


Figure 3.9: Crack opening profiles and  $CTOA_a$  after the first crack growth increment and after reaching the residual strength for 24 inch wide panels.

than, but approaching its critical value.

Comparisons between numerical results and experimental measurements for the applied stress versus half crack extension are shown in Figure 3.10. Results of predicted residual strength are comparable to experimental measurements, but as the width of the panel increases, the relative difference between experimental measurements and numerical predictions increases. Figure 3.11 depicts the predicted plastic zone as the specimens reach their ultimate strength. Two distinct phenomena are observed. For small specimens, plastic zones reach the free edge and the limit load is attained due to net section yielding. In contrast, for large specimens, plastic zones are well-confined by the elastic region and residual strength is reached near the fracture instability of the specimens.

### 3.3.2 Discussion

As shown in Figure 3.10, the relative difference in residual strength between experimental and numerical results increases as the width of the panel increases. This discrepancy is believed to be due to the three-dimensional nature of the stresses around the crack tip, a result of constraint effects due to the finite thickness of the panels [56, 31]. Numerical results using plane strain, plane stress with a plane strain core height (see Figure 3.2) equal to 0.12 inch, and three-dimensional finite element analyses obtained from [27, 29] were studied to further demonstrate constraint effects on residual strength predictions. Predicted results shown in Table 3.1 and Figure 3.12 suggest that:

- thin shell finite element analysis, behaving essentially in plane stress, tends to over-predict the residual strength as the width of the panel increases;
- plane strain analysis over-predicts the residual strength of small specimens, but under-estimates it for large specimens;

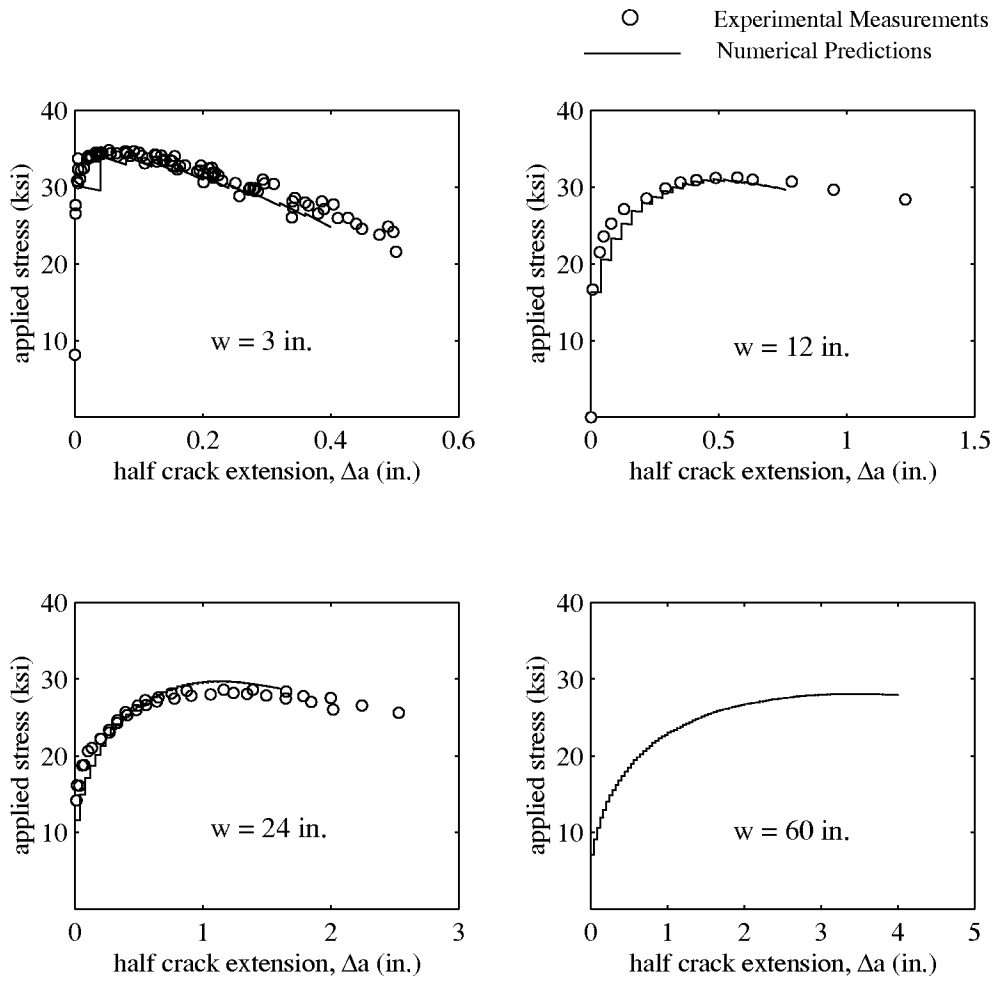


Figure 3.10: Comparisons between experimental measurements and numerical predictions of applied stress versus half crack extension for various sizes of specimens.

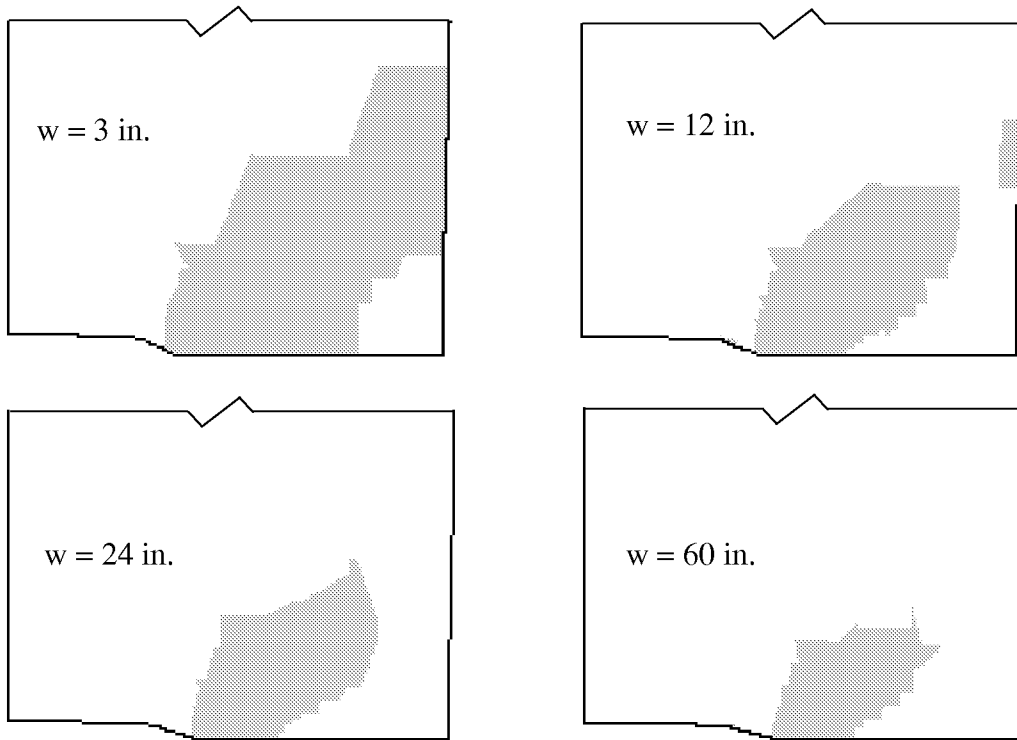


Figure 3.11: Numerical predictions of plastic zone for various sizes of specimens reaching their residual strength.

Table 3.1: Comparisons of Residual Strength Predictions of MT Specimens (unit: ksi)

plate width	thin shell	plane $\epsilon$	plane $\epsilon$ core	3D	exp.
3 in.		34.0	38.0	33.6	34.3
12 in.		30.7	32.7	30.7	31.3
24 in.		29.6	26.3	29.1	28.4
60 in.		28.1	16.6	26.7	N/A

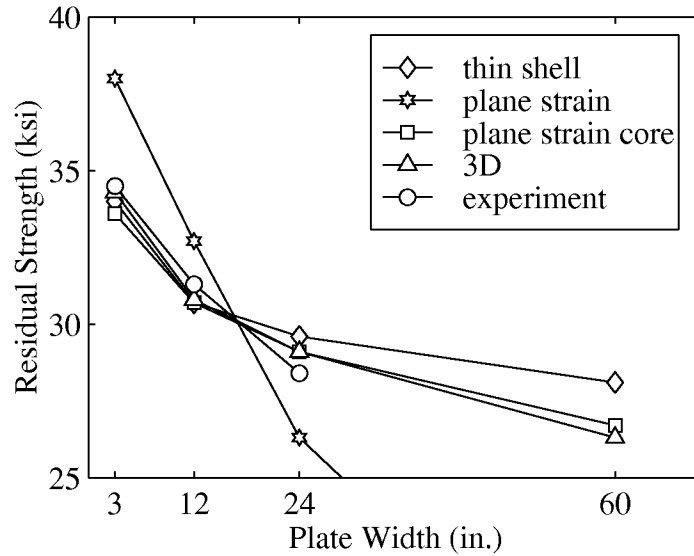


Figure 3.12: Predicted results of thin shell, plane strain, plane stress with a plane strain core, and 3D analyses compared with experimental measurements.

- 2D plane stress analysis with a plane strain core and 3D analysis properly account for constraint effects. The predicted results follow the trend of experimental measurements even for wide panels.

The *cross over* between plane stress and plane strain in predicting residual strength as the specimen size increases is an interesting topic. Based on the predicted plasticity distribution in Figure 3.11, the net section yielding mechanism seems to dominate the residual strength prediction of small specimens. This may explain why the plane strain analysis predicts a higher residual strength for small specimens because the effective yield stress in plane strain is larger than that in plane stress. Thus, a further increase of remote stresses under plane strain conditions is needed for specimens to reach the point of net section yielding. For larger specimens, residual strength is governed by stable crack growth and fracture. As one would expect from the thickness effects on  $K_c$  in LEFM [9], materials

in plane stress have higher fracture toughness than materials in plane strain. Recent micromechanics-based, 3D analysis of ductile crack growth in a thin plate with a Gurson-type model also showed that, although the crack growth resistance at first increases with increasing plate thickness, the resistance to crack growth decreases after a small amount of crack extension [84].

For CTOA-driven ductile crack growth, stresses and strains under plane stress and plane strain conditions have not been studied in sufficient detail to clarify the issue. A possible cause of higher crack growth resistance in plane stress may be related to the residual plastic deformation effects. Based on asymptotic solutions for cracks growing in an incompressible elastic-perfectly plastic material under Mode I loading (Equations (2.6) and (2.7)), larger residual plastic deformations would occur under plane stress than plane strain conditions leading to higher crack growth resistance.

### 3.4 Numerical Simulations of Specimens with Multiple Cracks

Numerical simulations of tests with multiple cracks using the CTOA fracture criterion are straightforward extensions of single crack specimen simulations. The same fracture criterion ( $CTOA_c = 5.25$  degrees measured 0.04 inch behind the crack tip) was used to simulate stable crack growth and the link-up of multiple cracks, and to predict the residual strength. No supplementary criterion is needed. Multiple crack test configurations as shown in Figure 3.4 were modeled and the fracture processes were simulated. Note that the symmetry conditions along the vertical central line of the specimens (see Figure 3.4) are no longer valid due to the various lengths of fatigue pre-cracks; thus, at least one half of the specimen needs to be modeled. A finite element mesh for test configuration b is shown in Figure 3.13. Mesh patterns around the multiple cracks are similar to those of the single crack models.

#### 3.4.1 Numerical Results and Discussion

Numerical results and experimental measurements for the applied stress versus half crack extension for test configuration b and d are shown in Figure 3.14. Two distinct applied load versus crack growth history curves are predicted. For test configuration a, b, and c, link-up of cracks happens before the specimens reach their residual strength. For test configurations d and e, the limit load is attained before link-up. These numerical predictions agree with observations from the fracture tests.

Again, plastic deformation plays an important role in the fracture process. Figure 3.15 shows the plastic zone evolution of test configuration b during stable crack growth. The inherent residual plastic deformations during crack growth are clearly demonstrated through the deformed shapes. Figure 3.16 summarizes the

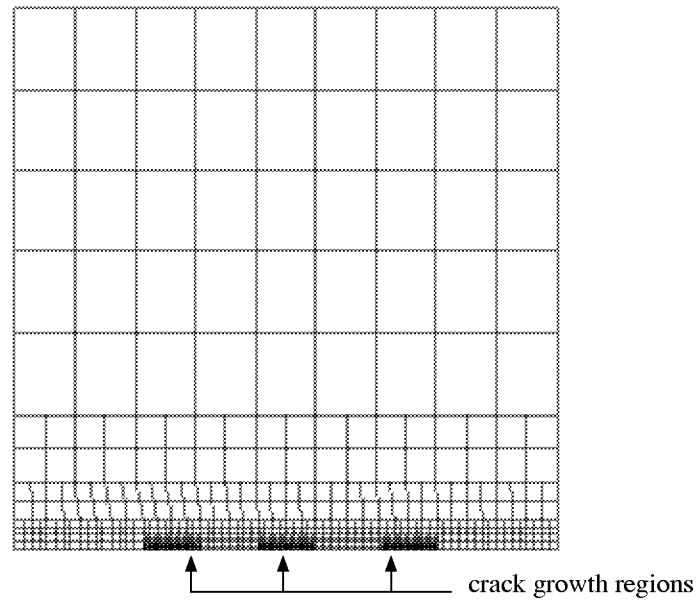


Figure 3.13: Finite element mesh for the test configuration b (12 inch wide specimen with two cracks).

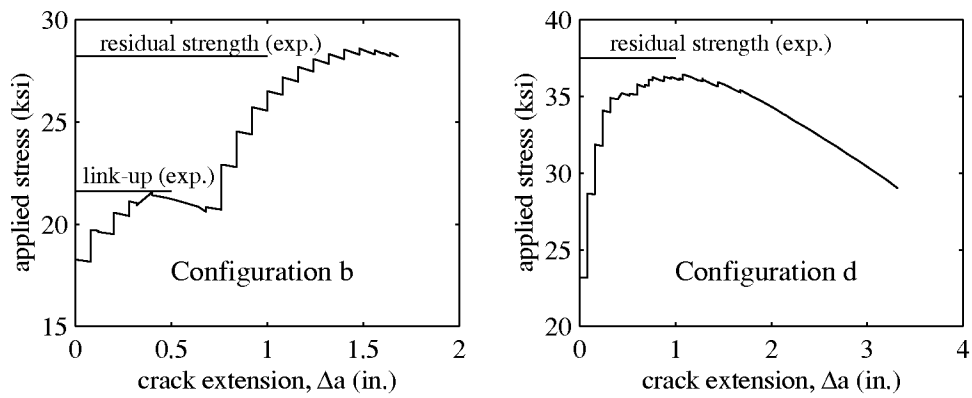


Figure 3.14: Predicted applied stress versus crack extension for test configuration b and d.

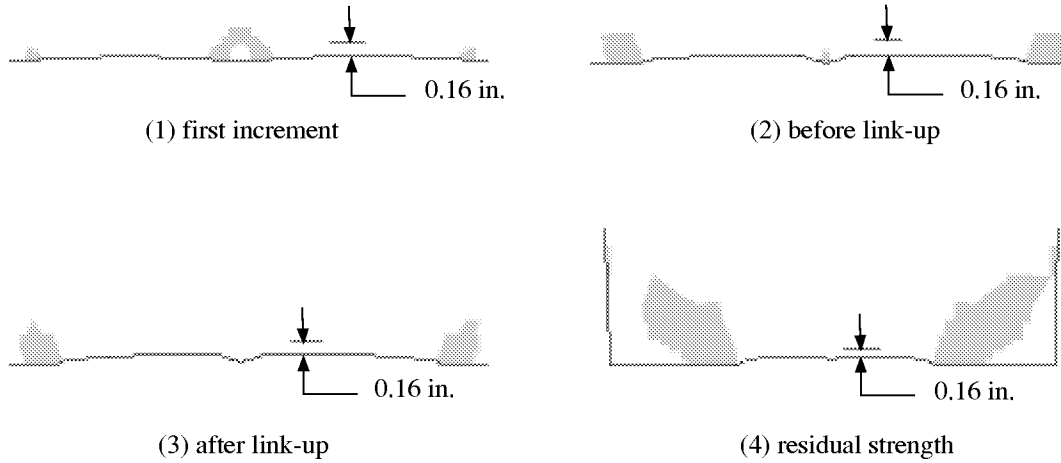


Figure 3.15: Crack opening profile(s) and plastic zone evolution of test configuration b during crack growth: (1) at the first increment, (2) before link-up, (3) after link-up, and (4) reaching the residual strength.

relative difference between predicted results and experimental measurements. The predicted residual strength of all five MSD simulations agrees very well (within 3%) with experimental data. The predicted link-up load is comparable to experimental measurements, but the difference is larger than that for the residual strength. Reasons for the discrepancy may be related to the difficulty in measuring link-up load during the fracture tests.

It is of practical importance to characterize the reduction in residual strength caused by MSD [50]. Figure 3.17 plots numerical predictions of residual strength versus lead crack length for cases with and without small cracks. A loss of residual strength due to the presence of multiple small cracks is observed.

### 3.5 Summary

Stable crack growth and residual strength prediction for the flat panel tests were performed. The CTOA criterion was used to characterize the elastic-plastic crack growth in thin-sheet metals. The major findings of the flat panel study are:

1. Two distinct failure mechanisms are observed for MT specimens. For small specimens, plastic zones reach the free boundary and the limit load is attained due to net section yielding. For large specimens, plastic zones are well-confined by the elastic region and residual strength is reached due to the fracture instability of the specimens.
2. Constraint effects caused by the finite thickness of the plates provide a reasonable explanation for the increase of the relative difference between predicted residual strength from thin shell analyses and experimental measurements as the panel size increases.

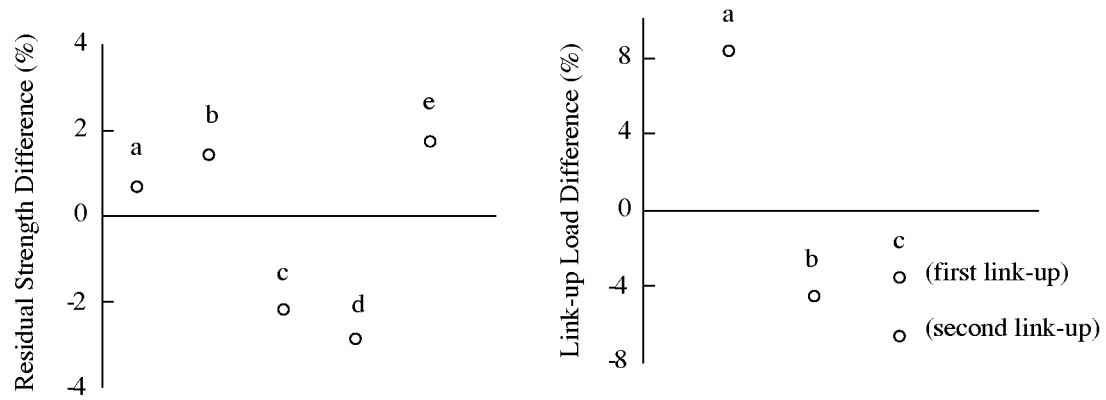


Figure 3.16: Relative difference of residual strength and link-up load between predicted results and experimental measurements for specimens with multiple cracks.

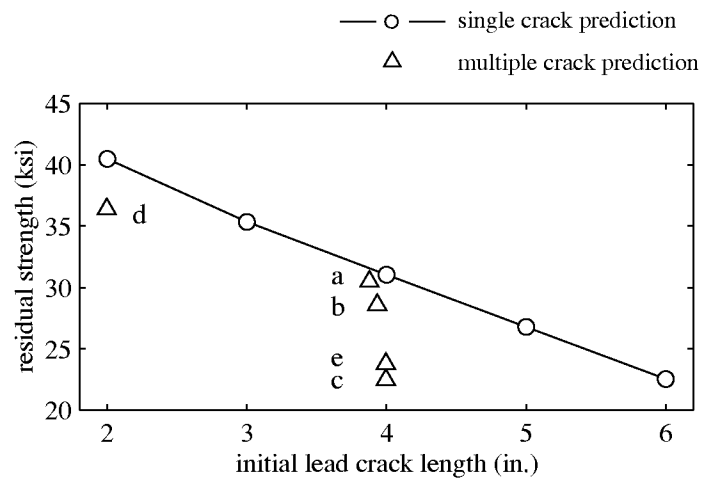


Figure 3.17: Loss of residual strength due to the presence of small cracks.



3. Predicted link-up load and residual strength are in good agreement with experimental measurements for the panels with multiple cracks. A loss of residual strength due to the presence of multiple small cracks is observed.
4. The CTOA fracture criterion, combined with elastic-plastic shell finite element analyses, proves to be a rational and rigorous simulation tool to characterize stable crack growth and to predict the residual strength of flat panels with single and multiple cracks.

## Chapter 4

# Residual Strength Analysis of Fuselage Structures with Self-Similar Crack Growth

In this chapter, the crack tip opening angle (CTOA) fracture criterion obtained from coupon tests is used to predict fracture behavior and residual strength of built-up aircraft fuselages that are subjected to widespread fatigue damage (WFD). Two fuselage models are investigated. The first example is a generic narrow body, lap-jointed fuselage with stringers and frames but without tear straps. This relatively simple, built-up configuration is used to demonstrate the ability of the FRANC3D/STAGS system to predict residual strength of fuselage structures subjected to WFD. The second example is a detailed analysis of a wide body, lap-jointed fuselage panel with tear straps, stringers, stringer clips, and frames. The analyses focus on simulations of single crack growth and multi-site damage (MSD) in a fuselage panel conducted in a full-scale, wide body, pressure test fixture [49, 50]. This example is intended to validate the analysis methodology by directly comparing numerical predictions with experimental measurements on actual fuselage structures.

### 4.1 Demonstration Example: A Generic Narrow Body Fuselage Panel

A relatively simple built-up narrow body fuselage configuration was modeled. The example demonstrates the analysis capability to predict the residual strength of a pressurized fuselage, subjected to WFD and corrosion damage [25, 24]. The problem chosen for analysis was a three stringer wide, three frame long fuselage panel. The panel section had a radius of curvature of 72 inches. It contained a lap joint at the central stringer. The lap joint was a typical three row configuration with 3/16 inch diameter countersunk-head rivets. The other two stringers were spot-welded to the skin. The upper and lower skins were made of 0.04 inch thick, 2024-T3

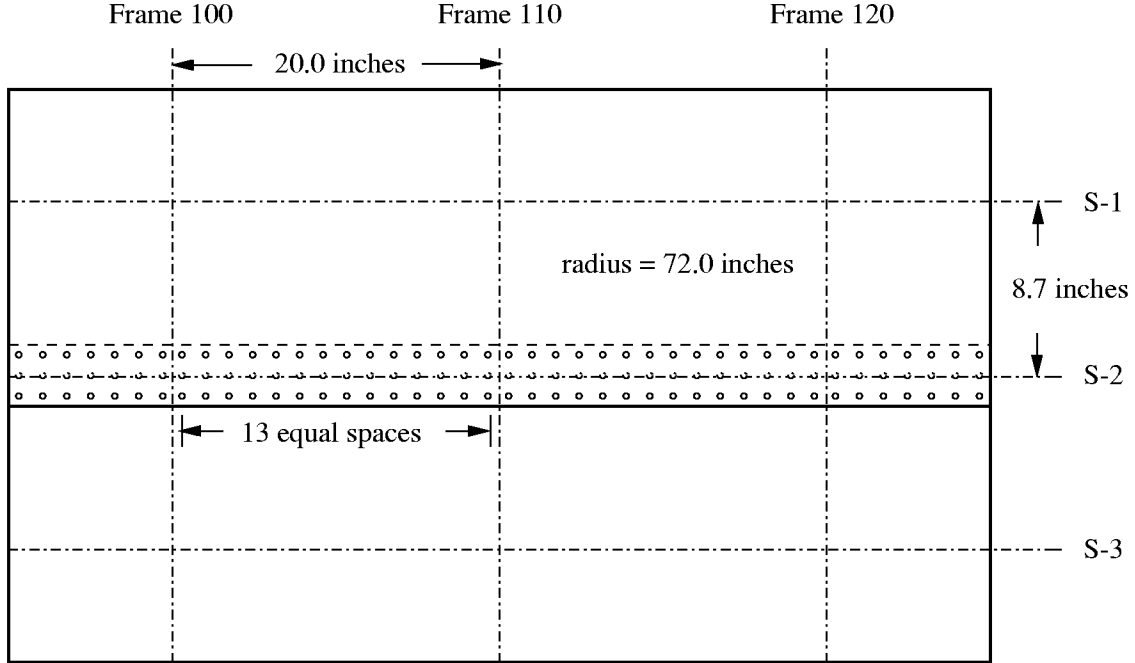


Figure 4.1: Dimensions of generic narrow body panel for demonstration example.

aluminum alloy. The stringers and frames were made of 7075-T6 aluminum alloy. Frames were simply connected to stringers by rivets. The panel configurations are shown in Figures 4.1 and 4.2. The frame and stringer dimensions are shown in Figure 4.3.

#### 4.1.1 Numerical Model

All structural components including skins, stringers, and frames were modeled by shell elements. Each node of a shell element has six degrees of freedom. A piecewise linear representation was used for the uniaxial stress-strain curves for 2024-T3 and 7075-T6 aluminum alloys (see Figures 4.4 and 4.5). Symmetric boundary conditions were imposed on all the boundary edges to simulate a cylinder-like fuselage structure. Pressure loading was applied on all the external skins.

Both geometric and material nonlinearities were included in the analysis. The former captures the out-of-plane bulging deformation and the latter captures the active plastic zone and the plastic wake during stable crack propagation. The nonlinear solution algorithm consists of Newton's method. Large rotations were included in the nonlinear solution by a co-rotation algorithm applied at the element level [96]. The Riks arc-length path following method was used to trace a solution past the limit points of a nonlinear response [122, 113].

Rivets were modeled by elastic-plastic spring elements that connect finite element nodes in the upper and lower skins. Each rivet was modeled with six degrees of freedom, corresponding to extension, shearing, bending and twisting of the rivet.

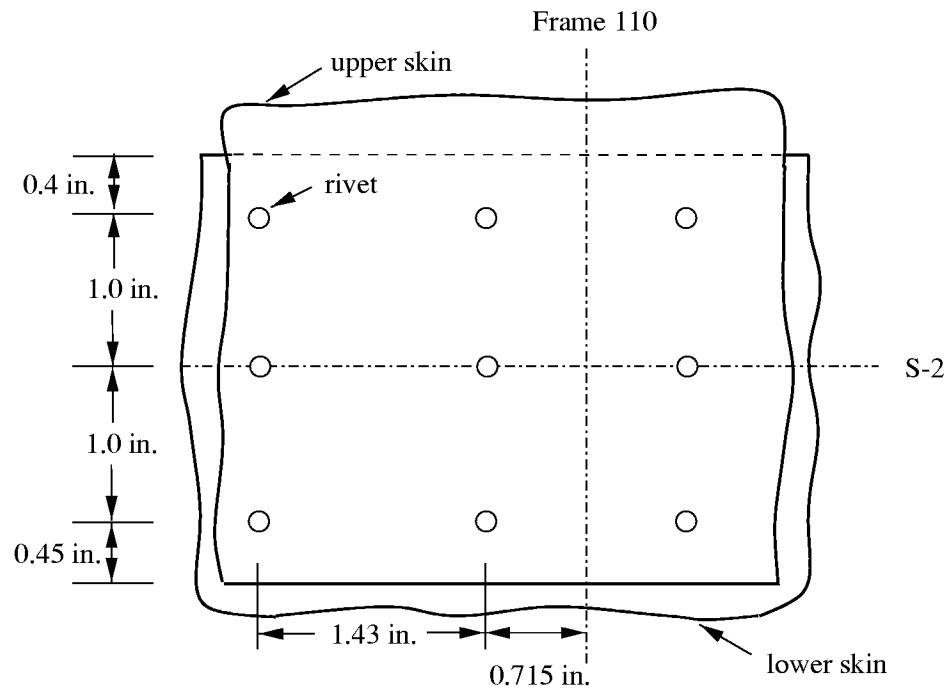


Figure 4.2: Detailed rivet spacing for demonstration example.

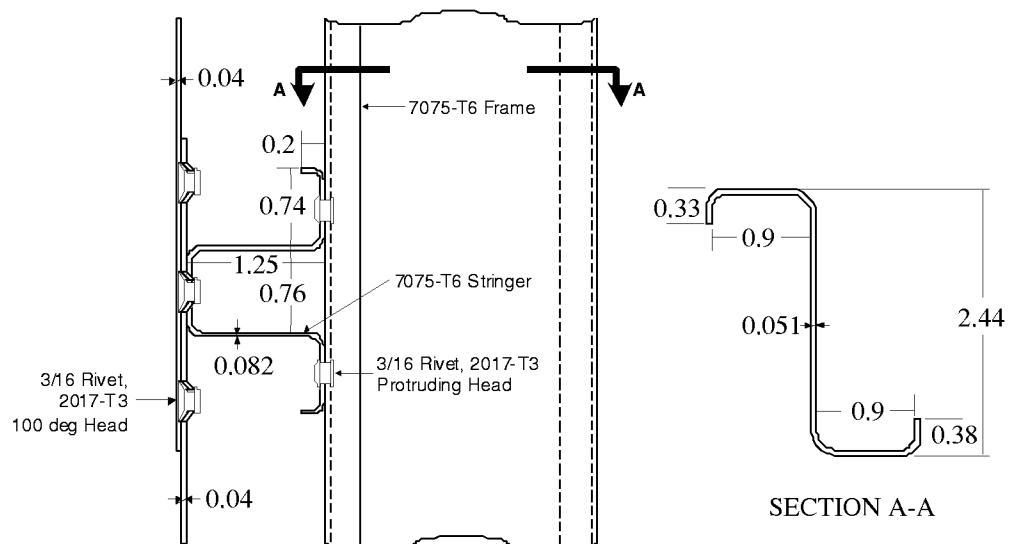


Figure 4.3: Dimensions of stringer and frame for demonstration example (dimensions in inches, modified after [25]).

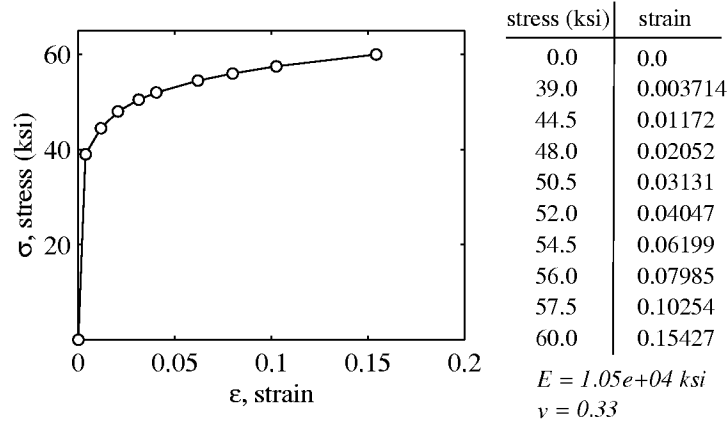


Figure 4.4: Demonstration example: piecewise linear representation of the uniaxial stress-strain curve for 2024-T3 aluminum.

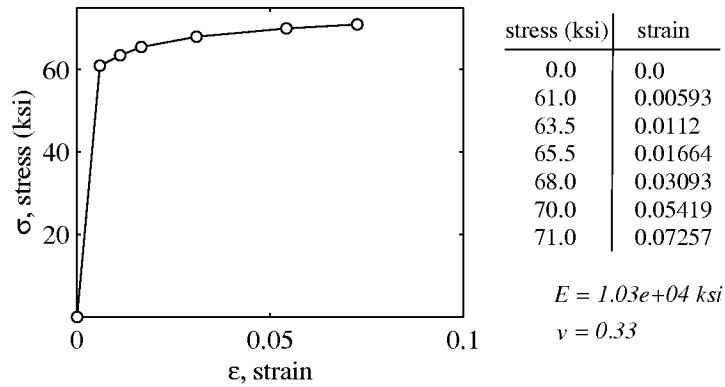


Figure 4.5: Demonstration example: piecewise linear representation of the uniaxial stress-strain curve for 7075-T6 aluminum.

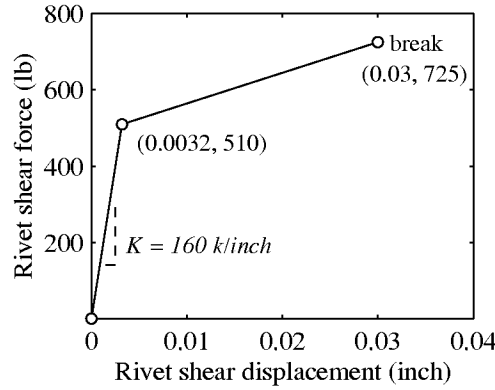


Figure 4.6: Demonstration example: rivet shear stiffness and strength.

The stiffness of each degree of freedom was defined by prescribing a force-deflection curve. The axial, flexural, and torsional stiffnesses of the spring element were computed by assuming that the rivet behaves like a simple elastic rod with a diameter of 3/16 inch. The elastic shear stiffness of the rivet was computed by the following empirical relation developed by Swift [136]:

$$K_{rivet} = \frac{ED}{[A + C(D/t_1 + D/t_2)]} \quad (4.1)$$

where  $E$  is the elastic modulus of the sheet material,  $D$  is the rivet diameter,  $t_1$  and  $t_2$  are the thicknesses of the joined sheets, and  $A = 5.0$  and  $C = 0.8$  for aluminum rivets. The initial shear yielding and ultimate shear strength of the rivets were assumed to occur at load levels of 510 lb and 725 lb, respectively. Once a rivet reaches its ultimate strength, it will *break* and lose its load carrying capacity. The force-deflection curve shown in Figure 4.6 for shearing is intended to represent empirically the net shear stiffness of a rivet-joined sheet connection, accounting for bearing deformations and local yielding around the rivet [136, 150].

The critical crack tip opening angle ( $CTOA_c$ ) was used to characterize elastic-plastic crack growth and to predict residual strength. The  $CTOA_c$  used in this example was 5.7 degrees measured 0.04 inch behind the crack tip with a plane strain core height equal to 0.08 inch<sup>1</sup>. Six different crack configurations with various lengths of lead and MSD cracks were studied. The initial configurations prior to crack growth were:

1. a 7.14-inch lead crack,
2. a 7.14-inch lead crack with 0.025 inch MSD cracks emanating from both sides of a fastener hole,

---

<sup>1</sup>Since no experimental crack growth data were available, this particular  $CTOA_c$  value was estimated based on the 5.25 degrees used in 0.09 inch thick, 2024-T3 bare material in Chapter 3. The plane strain core height was assumed to be twice the sheet thickness.

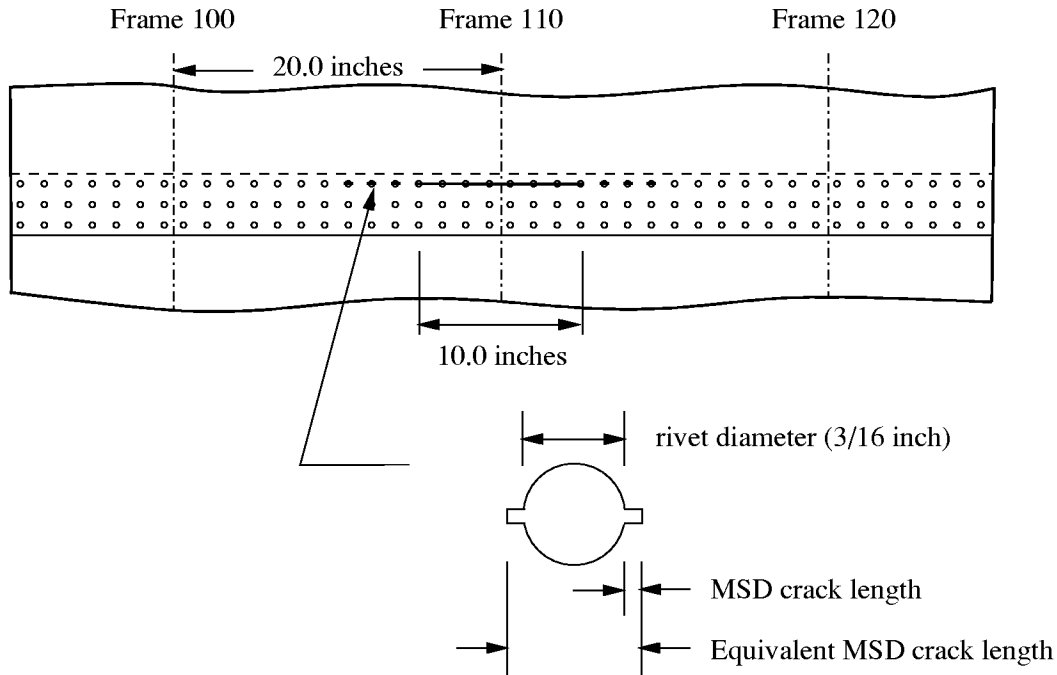


Figure 4.7: Crack configurations with a 10-inch initial lead crack and MSD (external view).

3. a 7.14-inch lead crack with 0.046 inch MSD cracks emanating from both sides of a fastener hole,
4. a 10-inch lead crack,
5. a 10-inch lead crack with 0.025 inch MSD cracks emanating from both sides of a fastener hole, and
6. a 10-inch lead crack with 0.046 inch MSD cracks emanating from both sides of a fastener hole.

The lead crack was located symmetrically about the central frame line. The MSD pattern was symmetric about the lead crack at the 3 rivets in front of the lead crack. The lead and MSD cracks were located along the upper rivet row in the upper skin of the joint. The crack configurations with a 10-inch initial lead crack are shown in Figure 4.7. Since rivet holes were not modeled explicitly in the finite element model, a small crack with a length equal to the rivet diameter plus the MSD length was used to model the MSD crack.

A mesh pattern with 0.04 inch crack tip elements was used. This pattern is similar to the one used in the flat panel simulation (*cf.* Figure 3.7). A finite element mesh for the model is shown in Figures 4.8 and 4.9. In addition to the effects of WFD, material thinning due to corrosion damage was also studied. The effect of material thinning was modeled by a uniform reduction in thickness of the upper skin at the lap joint in the two center bays.

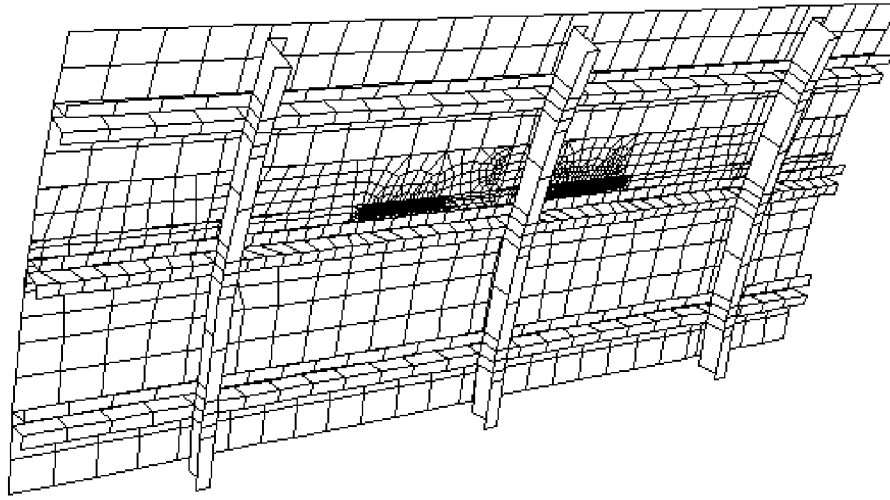


Figure 4.8: Finite element mesh for demonstration example.

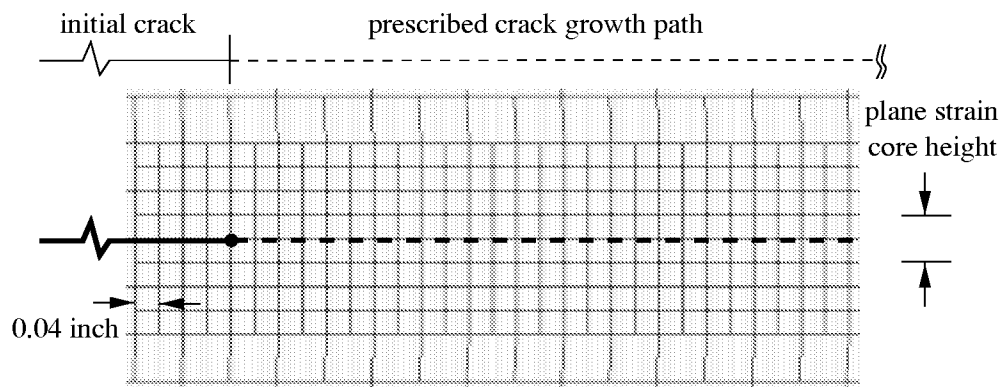


Figure 4.9: Detailed mesh around crack path for demonstration example.



### 4.1.2 Numerical Results and Discussion

Figure 4.10 shows the predicted results of the operating pressure loading versus the total crack extension for all the cases conducted in this study. Predicted residual strengths summarized in Figure 4.11 indicate:

- The MSD cracks significantly reduce the residual strength of the fuselage panel. A 21.8 to 28.0% loss of residual strength due to the presence of small MSD is observed.
- A 10% uniform thickness degradation due to corrosion damage reduces the residual strength by 3.4 to 9.0%. The coupling of WFD and corrosion damage leads to the most severe damage scenario.
- In general, increasing the lead and MSD crack lengths reduces the residual strengths. However, for the cases with a 10-inch initial lead crack, residual strength seems to be relatively insensitive to the MSD crack sizes.

The deformed structure at residual strength for the case with a 10-inch initial lead crack but without MSD and corrosion damage is shown in Figure 4.12. Out-of-plane bulging is observed in the skin crack edges. Because of the stiffness of the stringer, the bulging at the lower crack edge is much smaller than the opposing edge. The unsymmetric out-of-plane bulging thus leads to an anti-symmetric bending deformation field at the crack tips [108].

Figures 4.13 and 4.14 depict the predicted plastic zones for the cases with a 10-inch initial lead crack as the panel reaches its residual strength. As shown in Figure 4.13, the evolving plastic zones are well-confined by the elastic regions within the frames. For the case without MSD, dominant plastic zones accompanying the lead crack tips are observed. For the case with MSD, plastic zones are developed at the multiple crack tips. The plasticity distributions are highly influenced by the multiple crack interactions.

## 4.2 Validation Example: A Generic Wide Body Fuselage Panel

Full-scale pressurized panel tests described in [49, 50] were simulated. The tests, funded by the Federal Aviation Administration (FAA), and performed by the Boeing Commercial Airplane Group, were intended to characterize crack growth in a generic wide body, lap-jointed fuselage configuration, subjected to WFD. Detailed analyses using the FRANC3D/STAGS program were conducted to validate the analysis methodology. Stress distributions were compared with strain gage readings. Predicted stable crack growth and residual strength results were compared with experimental measurements.

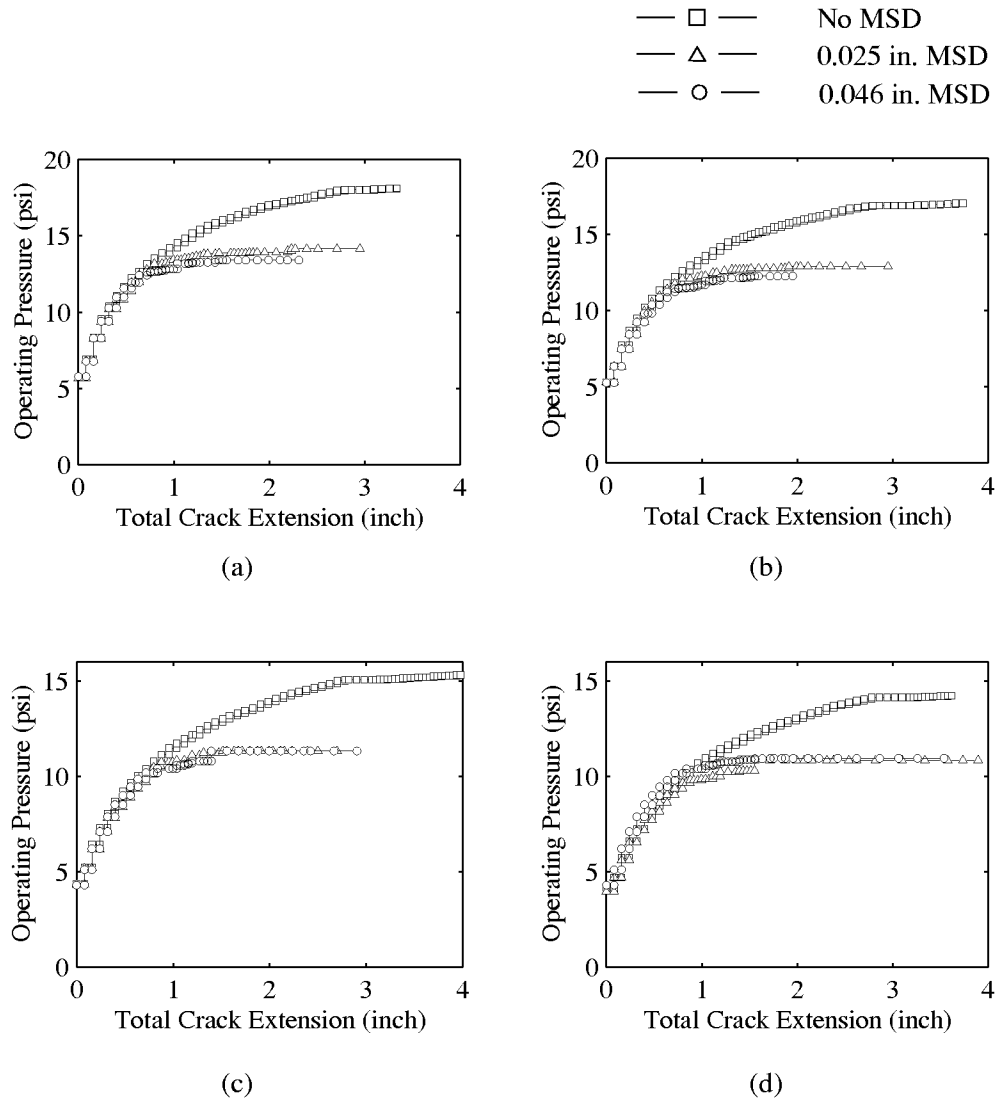


Figure 4.10: Predicted operating pressure versus total crack extension for the demonstration example: (a) 7.14-inch initial lead crack, (b) 7.14-inch initial lead crack with corrosion damage, (c) 10-inch initial lead crack, and (d) 10-inch initial lead crack with corrosion damage.

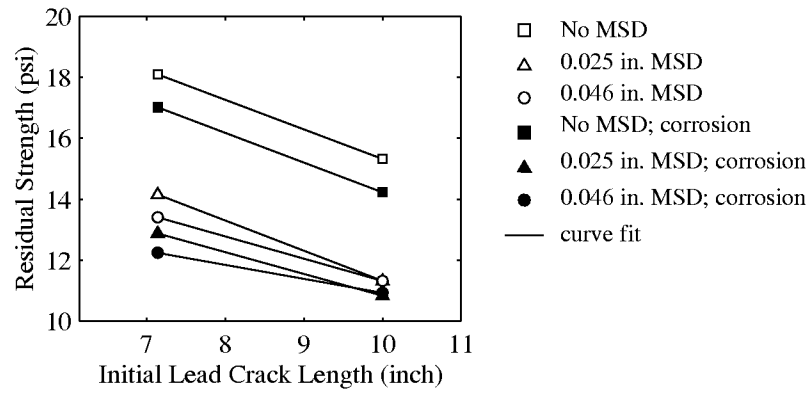


Figure 4.11: Predicted residual strength versus initial lead crack length.

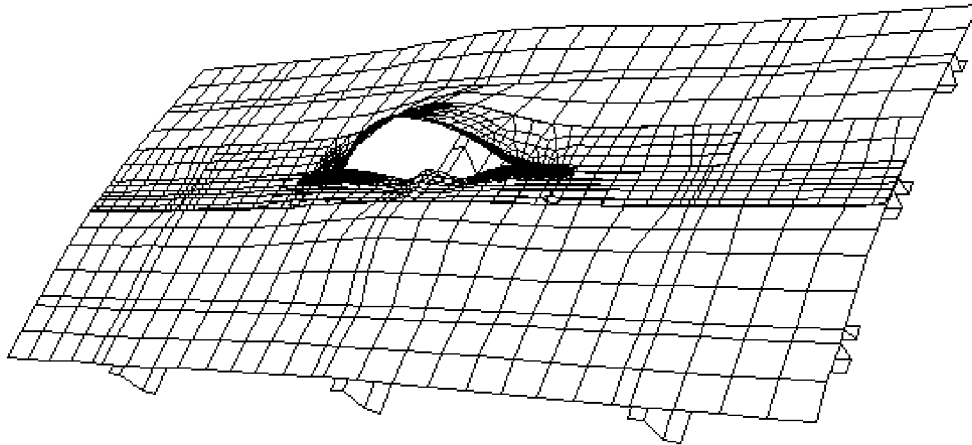


Figure 4.12: Deformed shape of the demonstration example (pressure = 15.3 psi, magnification factor = 5.0).

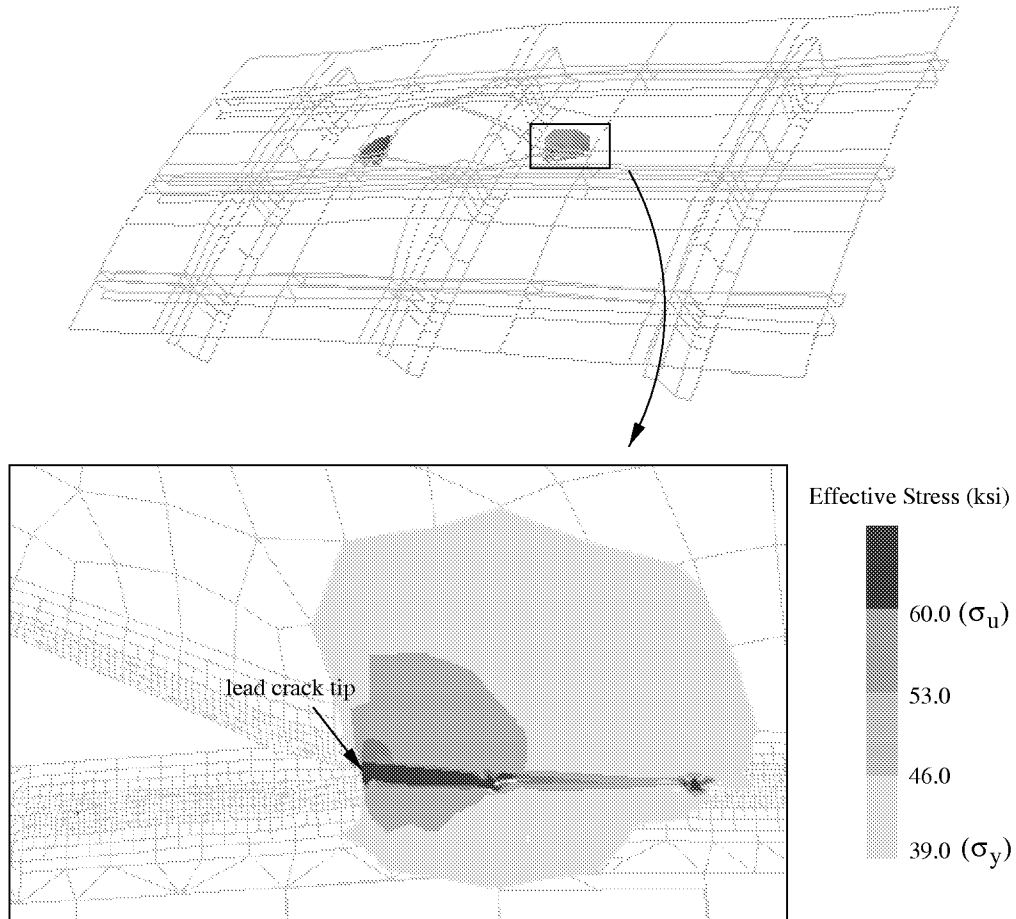


Figure 4.13: Predicted plastic zones for 10-inch initial lead crack without MSD (pressure = 15.3 psi, magnification factor = 5.0).

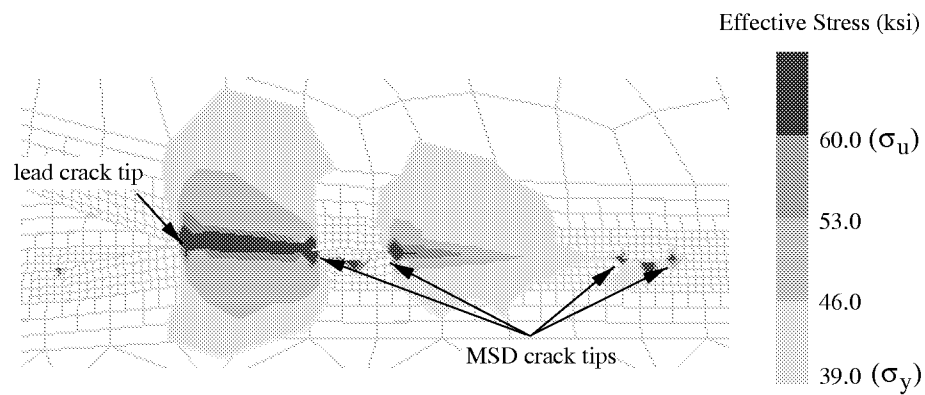


Figure 4.14: Predicted plastic zones for 10-inch initial lead crack with 0.025 inch MSD (pressure = 11.3 psi, magnification factor = 5.0).

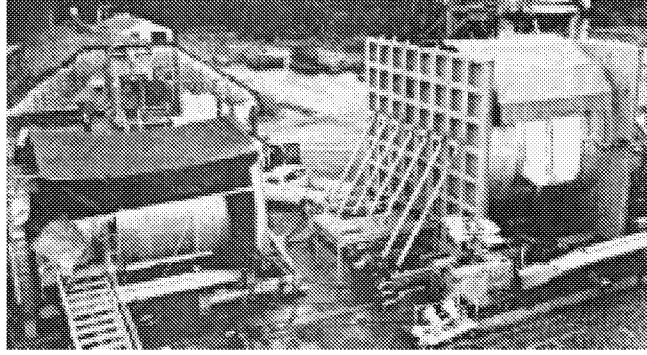


Figure 4.15: Generic narrow and wide body test fixtures (after [82]).

#### 4.2.1 Full-Scale Fuselage Panel Testing

Two generic pressure test fixtures were fabricated by the Boeing Commercial Airplane Group. One fixture had a radius of curvature of 74 inches to match narrow body airplanes and the other had a radius of curvature of 127 inches to match wide body airplanes. The test fixtures are shown in Figure 4.15. One end of each fixture was mounted in a rigid framework and the other on rollers to allow longitudinal displacement. Removable test sections were inserted in cutouts in the fixtures. Tests were conducted under pressure loading only, using air as the pressurizing medium. The full-scale fuselage panel tests investigated in this section were performed on the wide body pressure test fixture. A brief overview of the panel tests is described below. More information about the fixtures and tests can be found in [82, 85, 49, 50].

Two identical curved lap-jointed panels were fabricated. The test panels were designed to simulate typical wide body fuselage crown structures consisting of bonded tear straps and floating frames connected to hat section stringers with stringer clips. Skins and tear straps were made of 0.063 inch thick, 2024-T3 clad aluminum alloy. Stringers, frames, and stringer clips were made of 7075-T6 clad aluminum alloy. The skins were joined by the lap joints. The joint was a typical three row configuration assembled using standard 3/16 inch diameter, 100° countersunk-head rivets. The tear straps were hot-bonded to the skins at each frame station. The outer and inner tear straps were overlapped above the lap joint. The dimensions of the panels are shown in Figures 4.16, 4.17, and 4.18. The dimensions of frames, stringers, and stringer clips are shown in Figures 4.19 and 4.20.

A five-inch initial saw cut was inserted along the upper rivet row in the outer skin. For the panel with MSD cracks, small sawcuts were inserted in the outer skin after the rivet holes had been drilled, but prior to the application of the fay sealant and rivet installation. The panels were subjected to pressure cycling until the length of the crack reached about two frame bays. The central frame was then cut and the residual strength tests were conducted. Rosette strain gages were installed back-to-back on the skins and tear straps in the vicinity of the lap joint.

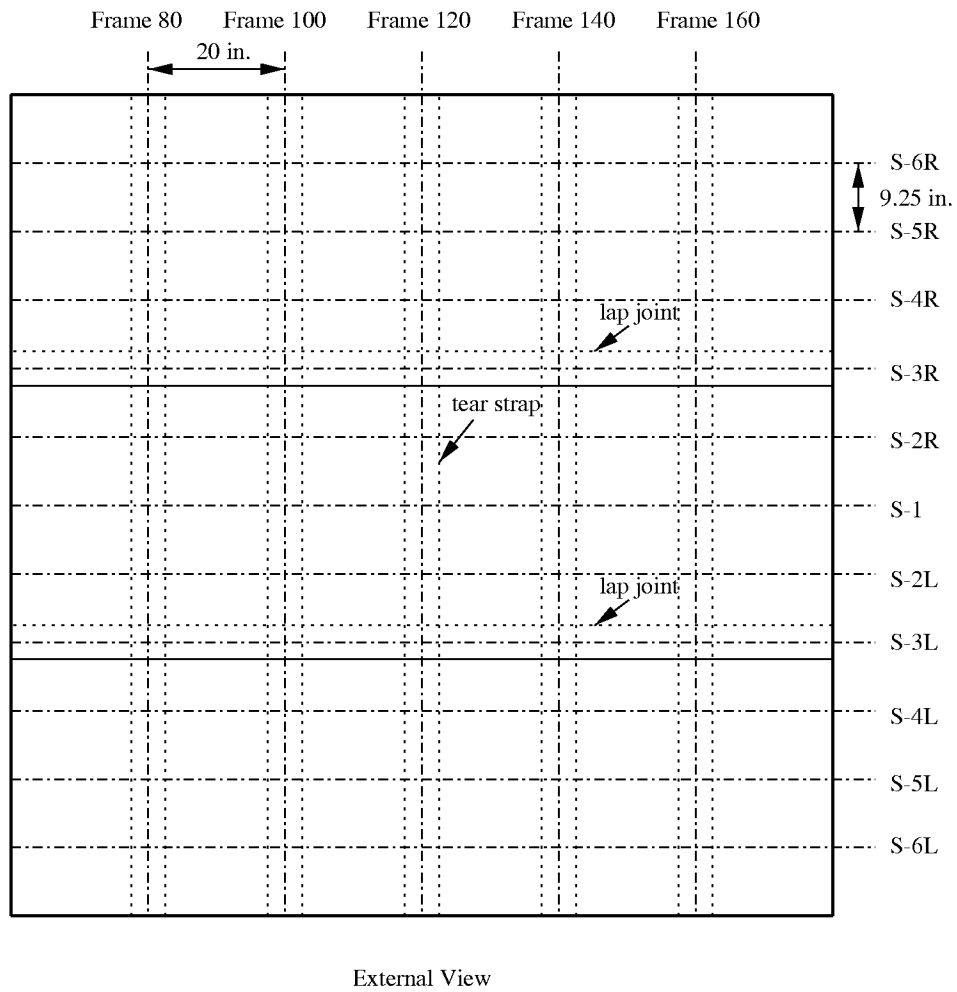


Figure 4.16: Validation example: test panel dimensions.

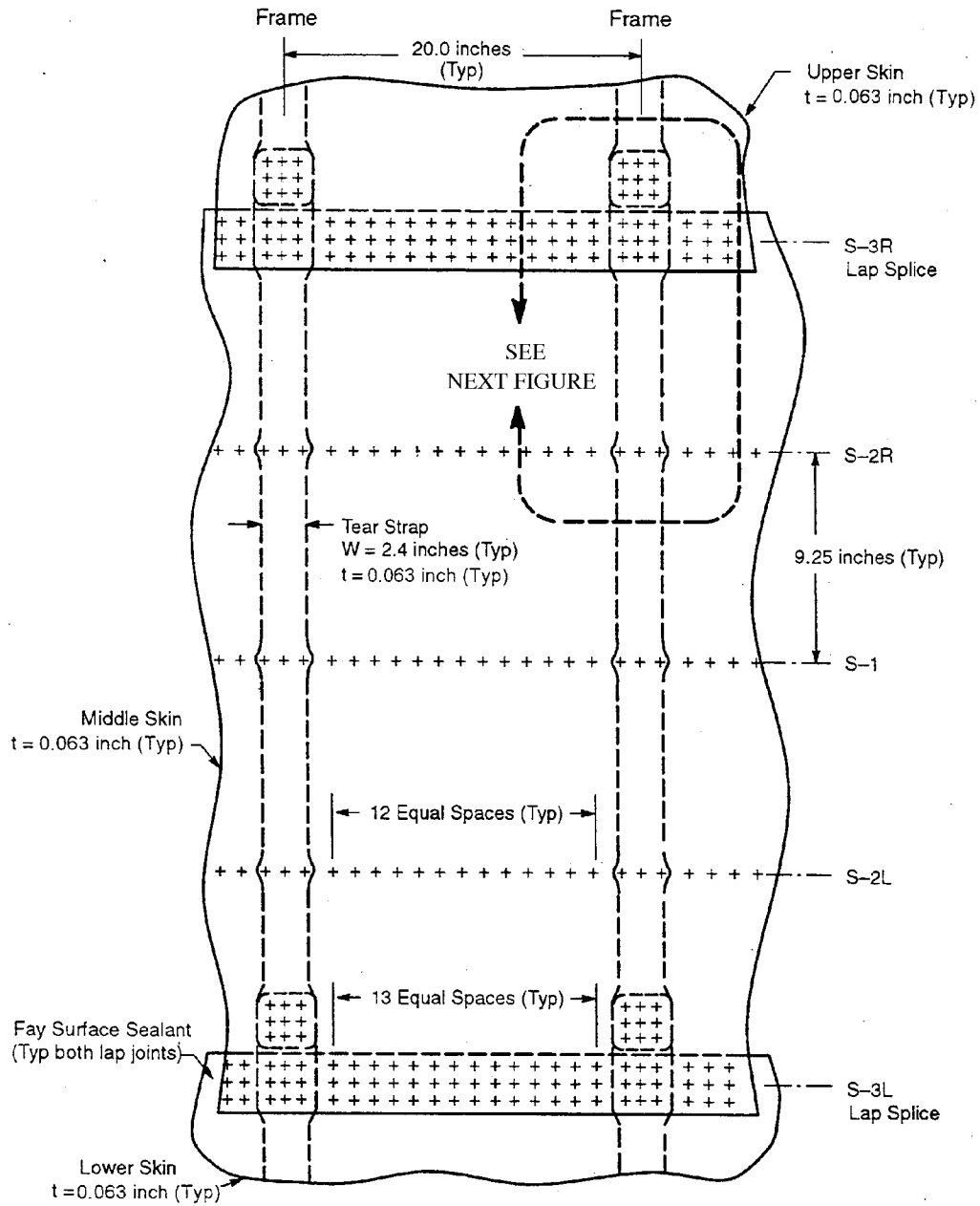


Figure 4.17: Validation example: detailed panel dimensions (after [49]).

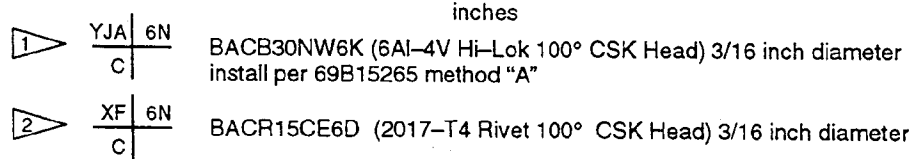


Figure 4.18: Validation example: detailed rivet spacing (after [49]).



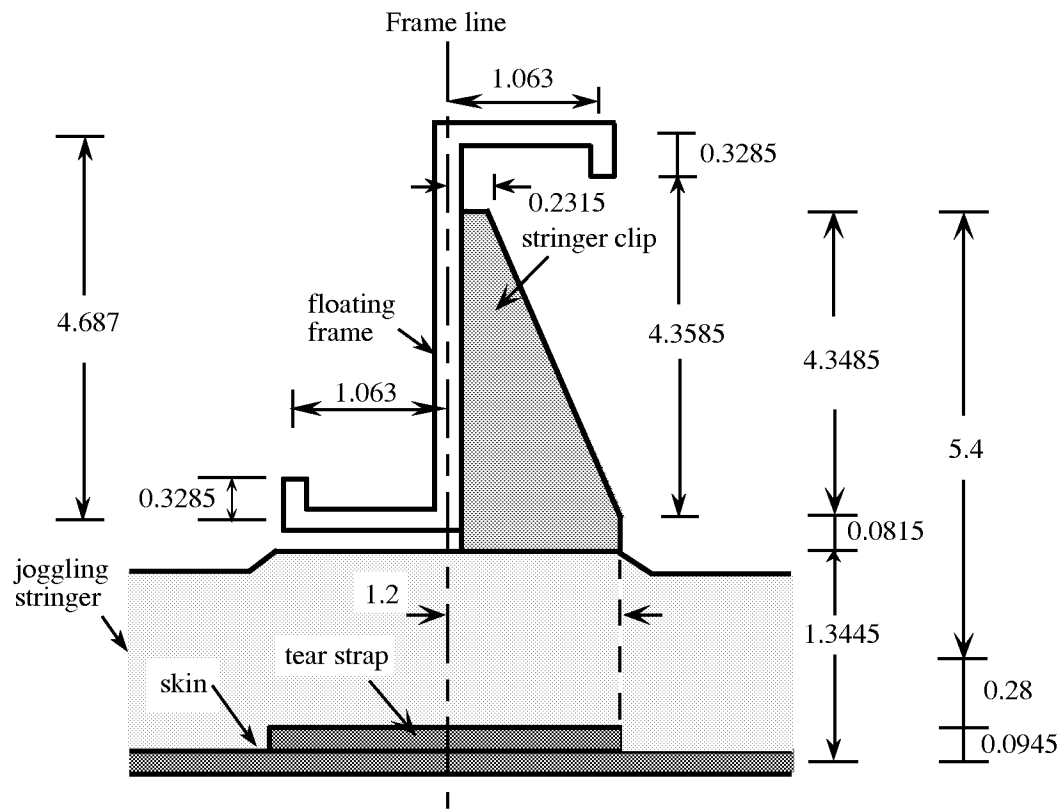


Figure 4.19: Validation example: dimensions of frame and stringer clip (dimensions in inches).

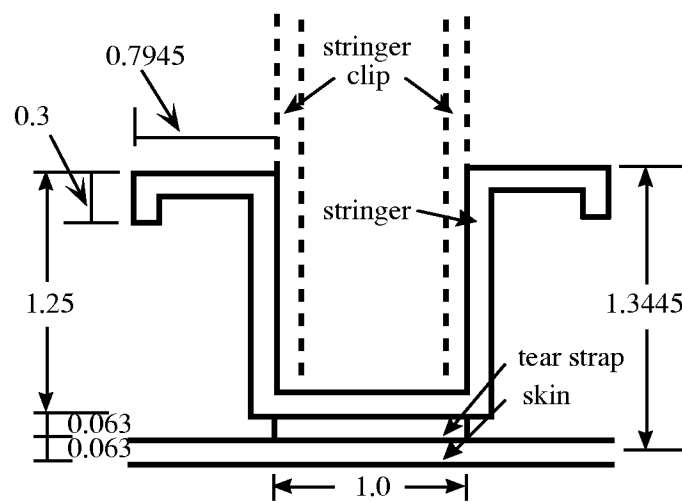


Figure 4.20: Validation example: dimensions of stringer (dimensions in inches).

### 4.2.2 Numerical Model

All structural components including skins, stringers, and frames were modeled by displacement-based four-noded or five-noded quadrilateral shell elements [113, 112]. To analyze the panel tests with reasonable computer resources and sufficient accuracy, a global-local approach was used. Figure 4.21 shows the typical finite element meshes for the two hierarchical modeling levels employed in the simulations. A 12-stringer-bay wide and 5-frame-bay long panel, which is about the size of the test panel, was modeled at the global level. A 1x1 bay stiffened panel was modeled at the local level. The local model differed from the global model in the finite element mesh density and the detailed geometric modeling of the cross sectional shapes of stringers and frames.

Pressure loading was applied on all the external skins. Symmetric boundary conditions were imposed on all the boundary edges of the global model to simulate a cylinder-like fuselage structure. Uniform axial expansion was allowed at one longitudinal end. On this boundary edge, an axial force equal to  $(PR/2) \cdot L$  was assigned where  $P$  is the applied pressure,  $R$  is the radius of the panel, and  $L$  is the arc-length of the edge. The kinematic boundary conditions (displacements and rotations) applied along the boundaries of the local model were extracted from the global model results. In addition to these kinematic constraints, the local model was also subjected to internal pressure.

A piecewise linear representation was used for the uniaxial stress-strain curves for 2024-T3 and 7075-T6 aluminum alloys (see Figures 4.22 and 4.23). Similar to the demonstration example, rivets were modeled by elastic-plastic spring elements. The shear force-deflection curve for the rivet is shown in Figure 4.24. Since no special adhesive elements were available in the STAGS element library, the adhesive bond between skin and tear strap was also modeled with spring elements. The shear stiffness for the springs was computed based on an *effective* area of the adhesive with [128]:

$$K_{adhesive} = \frac{A_{eff}}{t_a/G_a + (3/8)(t_1/G + t_2/G)} \quad (4.2)$$

where  $A_{eff}$  is the bond area being lumped at the finite element nodal connection,  $G$  is the elastic shear modulus of the sheet material,  $G_a$  is the elastic shear modulus of the adhesive,  $t_1$  and  $t_2$  are the thicknesses of the bonded sheets, and  $t_a$  is the thickness of the adhesive bond. Because no adhesive tests were conducted, the material properties of adhesive,  $G_a$  and  $t_a$ , were obtained from the experimental results in [135]. The maximum shear deflection of the adhesive bond was assumed to be 0.001 inch. Similar to the rivet spring, once the adhesive spring reaches its ultimate strength, it will *break* and lose its load carrying capacity. The force-deflection curve for shearing is shown in Figure 4.25. The axial stiffness of the adhesive spring was derived from the shear stiffness. The torsional and flexural stiffnesses of adhesive were assumed to be negligible.

Both geometric and material nonlinearities were used in the analysis at the

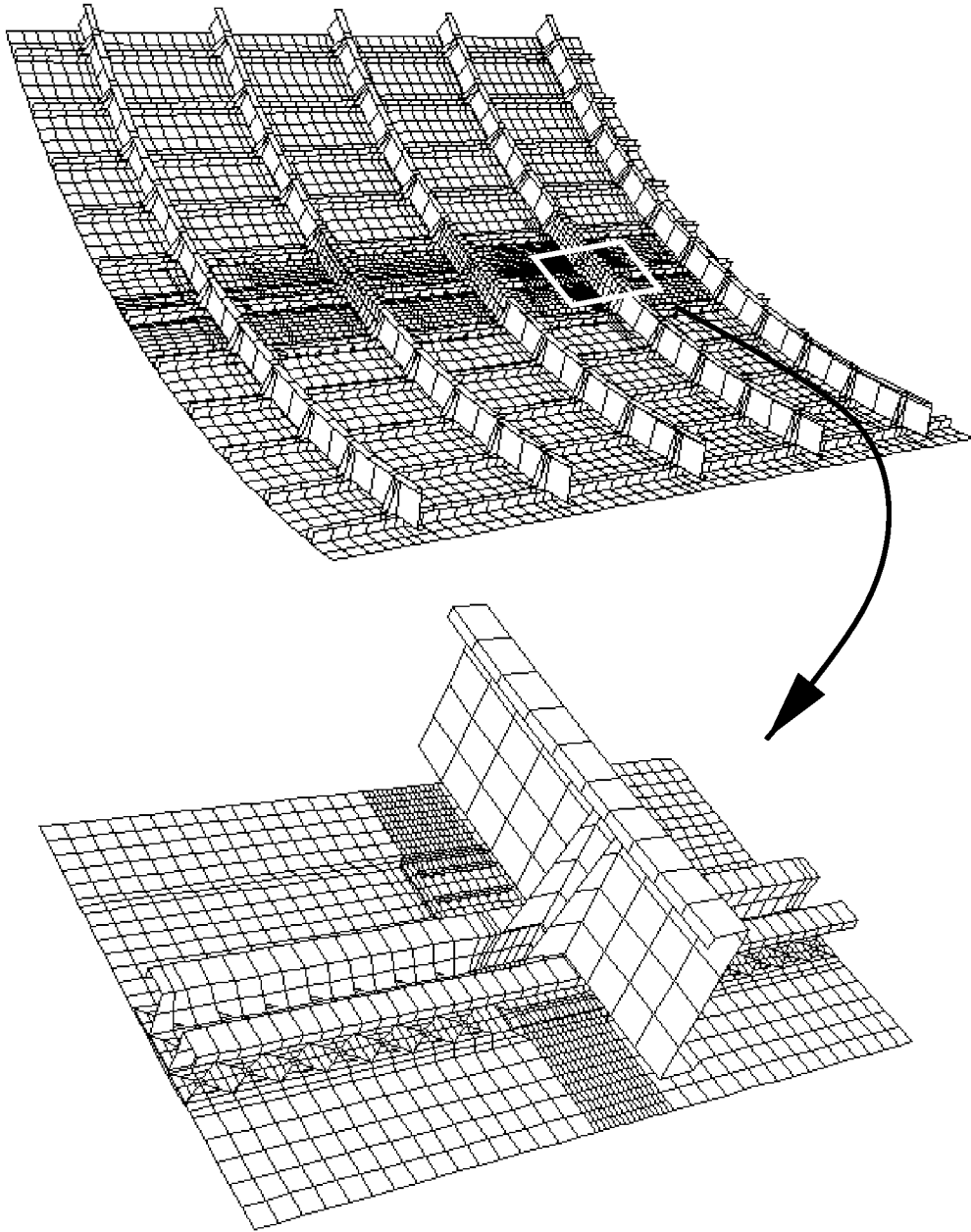


Figure 4.21: Global and local finite element models.

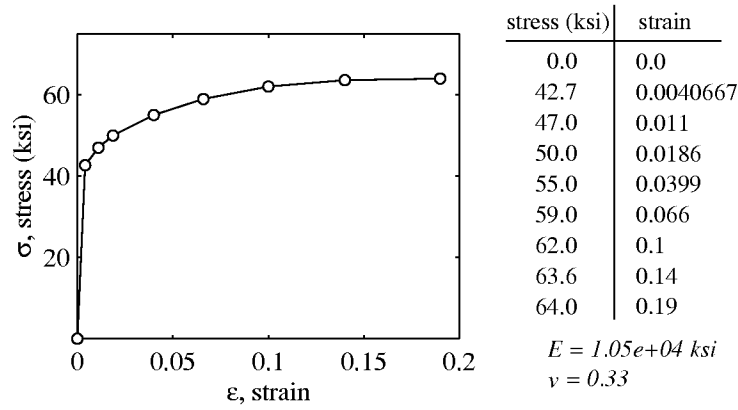


Figure 4.22: Validation example: piecewise linear representation of the uniaxial stress-strain curve for 2024-T3 aluminum.

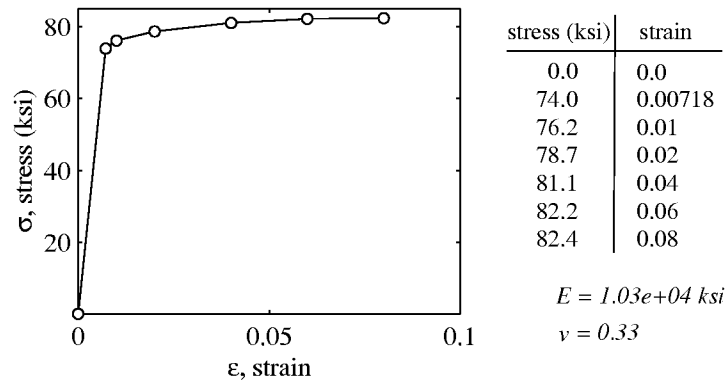


Figure 4.23: Validation example: piecewise linear representation of the uniaxial stress-strain curve for 7075-T6 aluminum.

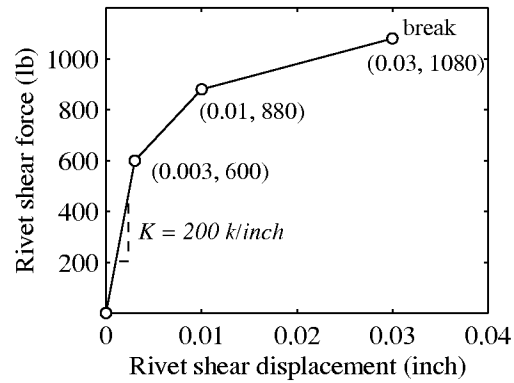


Figure 4.24: Validation example: shear stiffness and strength of rivet spring.

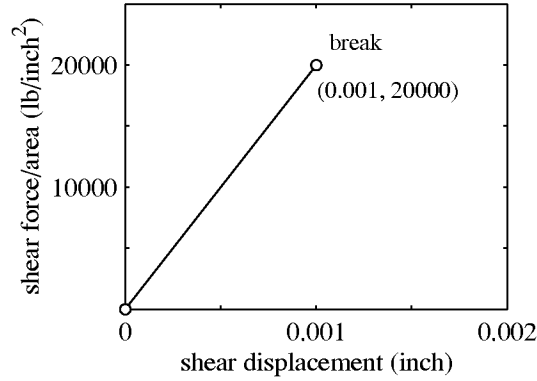


Figure 4.25: Validation example: shear stiffness and strength of adhesive spring.

global and local modeling levels. The global shell model captures the overall non-linear response of the stiffened, curved, pressurized structure. The local shell model provides the detailed deformation and stress field near the crack tips to compute the fracture parameters (*e.g.*, CTOA) that control stable crack growth.

### 4.2.3 Determination of $CTOA_c$

Flat panel tests were conducted by the Boeing Commercial Airplane Group to obtain material properties for fatigue and fracture analysis of the curved fuselage panels. Four, 48 inch wide, 80 inch long, 0.063 inch thick middle crack tension (MT) specimens were tested. The flat panel specimens were made from the same aluminum sheet used for the skin of the curved fuselage panels. A constant amplitude cyclic loading was applied to propagate an initial sawcut. After the fatigue crack growth, a residual strength test was conducted under a monotonically increasing load. The test matrix prior to the residual strength test is summarized in Table 4.1. Visual crack extension measurements were taken. Surface  $CTOA_c$  was measured for Specimen 2024\_FAA\_TL3 during the residual strength test. Nine values were obtained and the mean of the measured critical angles was about 5.5 degrees with a scatter band about  $\pm 1.0^\circ$ .

The value of  $CTOA_c$  used in the residual strength analysis of the fuselage panels was determined by finding an angle within the scatter band of the  $CTOA_c$  measurements that best correlates with the observed stable crack growth and residual strength of the coupon tests. The FRANC3D/STAGS program was used to simulate fracture behavior of the MT specimens. A finite element mesh modeling a quarter of the specimen with a crack tip element size of 0.04 inch and a half plane strain core height equal to 0.08 inch is shown in Figure 4.26. The plane strain core was used to capture the three-dimensional (3D) constraint effects developed at the local crack tip [94, 31, 56]. The half core height was about the thickness of the specimen.

Table 4.1: Test Matrix for MT Specimens (after [49])

Specimen ID	half initial crack (inch)	half final fatigue crack (inch)	$\sigma_{fatigue}$ (ksi)	R
2024_FAA_TL3	2.0	8.0	8.0	0.1
2024_FAA_TL4	2.0	5.5	16.0	0.1
	5.5	8.0	8.0	
2024_FAA_TL5	5.0	12.0	12.0	0.1
2024_FAA_TL6	2.0	8.0	7.0	0.5

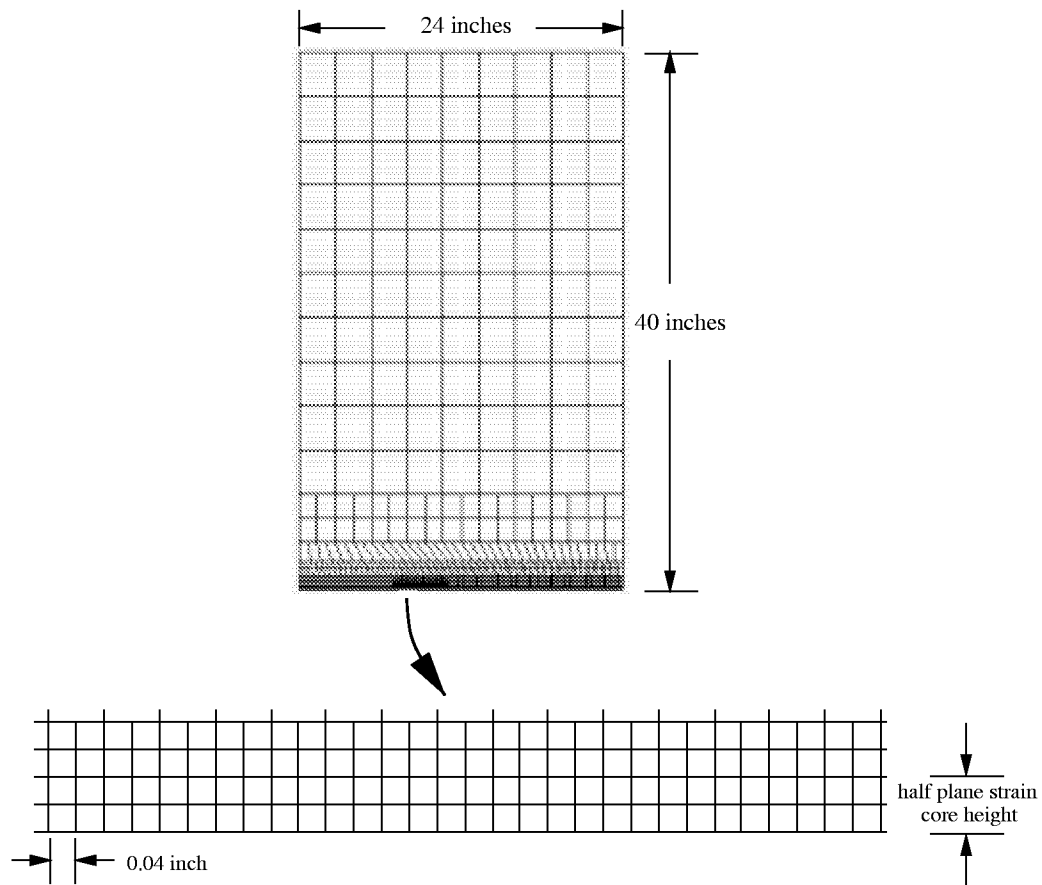


Figure 4.26: Finite element mesh for a quarter of 48 inch wide MT specimen.

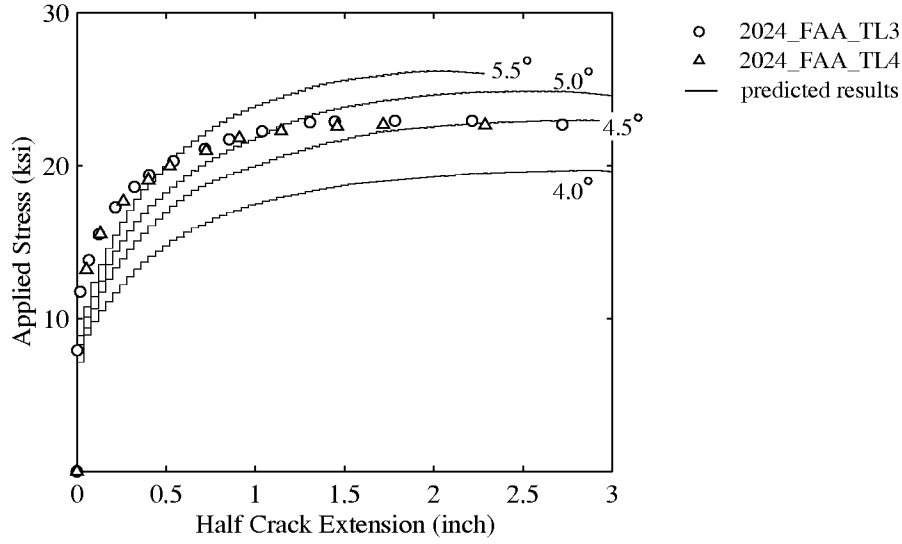


Figure 4.27: Predicted applied stress versus stable crack growth for 48 inch wide MT specimen (half plane strain core height = 0.08 inch).

Figure 4.27 compares the predicted stable crack growth results to the experimental measurements. The  $CTOA_c$  of 4.5 degrees best correlates the predicted and measured residual strengths. However, it under-estimates the applied stress at the early stage of stable crack growth. The 5 and 5.5 degree critical angles give a better correlation for the early stable crack growth, but over-predict the residual strength by 8.5% and 14.3%, respectively.

The effect of the 3D constraint zone, *i.e.*, the height of the plane strain core, on stable crack growth and residual strength prediction was further investigated. Note that in general, a change of the plane strain core height requires a different value of  $CTOA_c$  to correlate the predicted and measured residual strengths. Figure 4.28 shows the core height effects on the stable crack growth prediction. A slightly better correlation for the early growth is observed by increasing the plane strain core height.

The discrepancy between predicted and measured stable crack growth at the early stage of tearing might relate to the residual plastic deformation left by the fatigue crack growth. This effectively increases the crack opening resistance during early stable crack growth [30]. The plastic wake effect on stable crack growth and residual strength analysis is further discussed in Section 4.2.5.

#### 4.2.4 Numerical Results: Comparison with Strain Gage

Strain gage comparisons were made to verify predicted stress distributions. The strain gage readings were recorded during fatigue and residual strength tests. The records as the panels reach their residual strengths are of primary interest in this study. The corresponding damage configurations are:

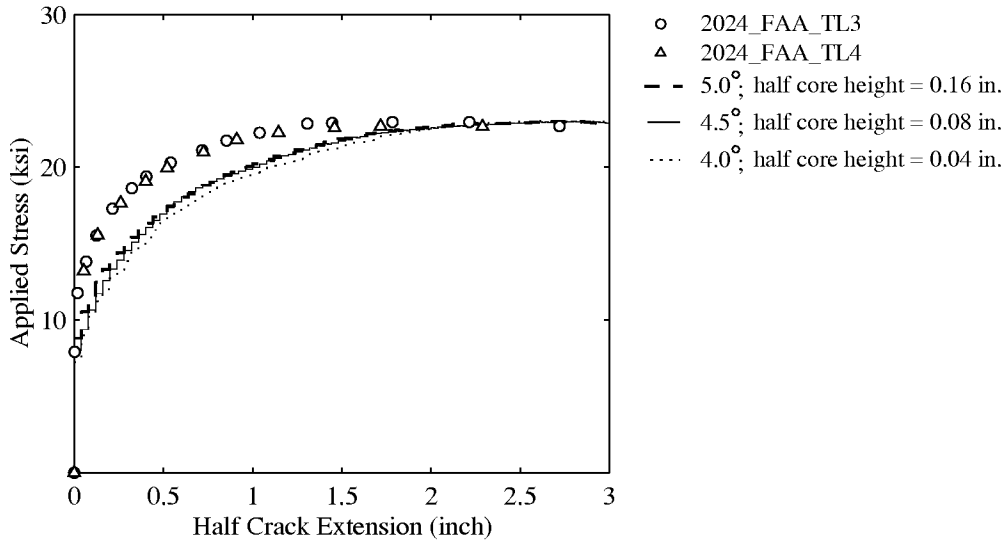


Figure 4.28: Effect of plane strain core height on predicted stable crack growth for 48 inch wide MT specimen.

1. a 38.2 inch long crack with a severed central frame for the panel without MSD cracks, and
2. a 41.7 inch long crack with a severed central frame for the panel with MSD cracks.

The ultimate pressure loadings are 9.4 psi and 7.5 psi, respectively. The locations of strain gages and the damage configurations are illustrated in Figure 4.29. Five back-to-back strain gage rosettes are numbered for the purpose of comparison. Because similar trends for stress distributions were observed for both damage configurations, only detailed strain gage comparisons for the panel without MSD cracks are described below.

Nonlinear stress analyses at the global and local modeling levels were performed. Figure 4.30 shows the overall deformed structures at both levels. Convergence studies were conducted to ensure accuracy of deformations and stress distributions. Figure 4.31 shows three finite element discretizations, G1, G2, and G3, used at the global modeling level. The mesh density around the gage locations was progressively refined from global model G1 to G3. The predicted hoop stress distributions compared to strain gage readings are shown in Figures 4.32 and 4.33; the predicted results converge quickly. The predicted membrane hoop stresses agreed well with experimental measurements. The predicted bending hoop stresses were comparable to experimental measurements as one refined the finite element meshes.

Two discretizations, L1 and L2, were performed at the local modeling level (Figure 4.34). The mesh density in the local model L1 was about the same as the corresponding region in the global model G3. The purpose is to ensure transition



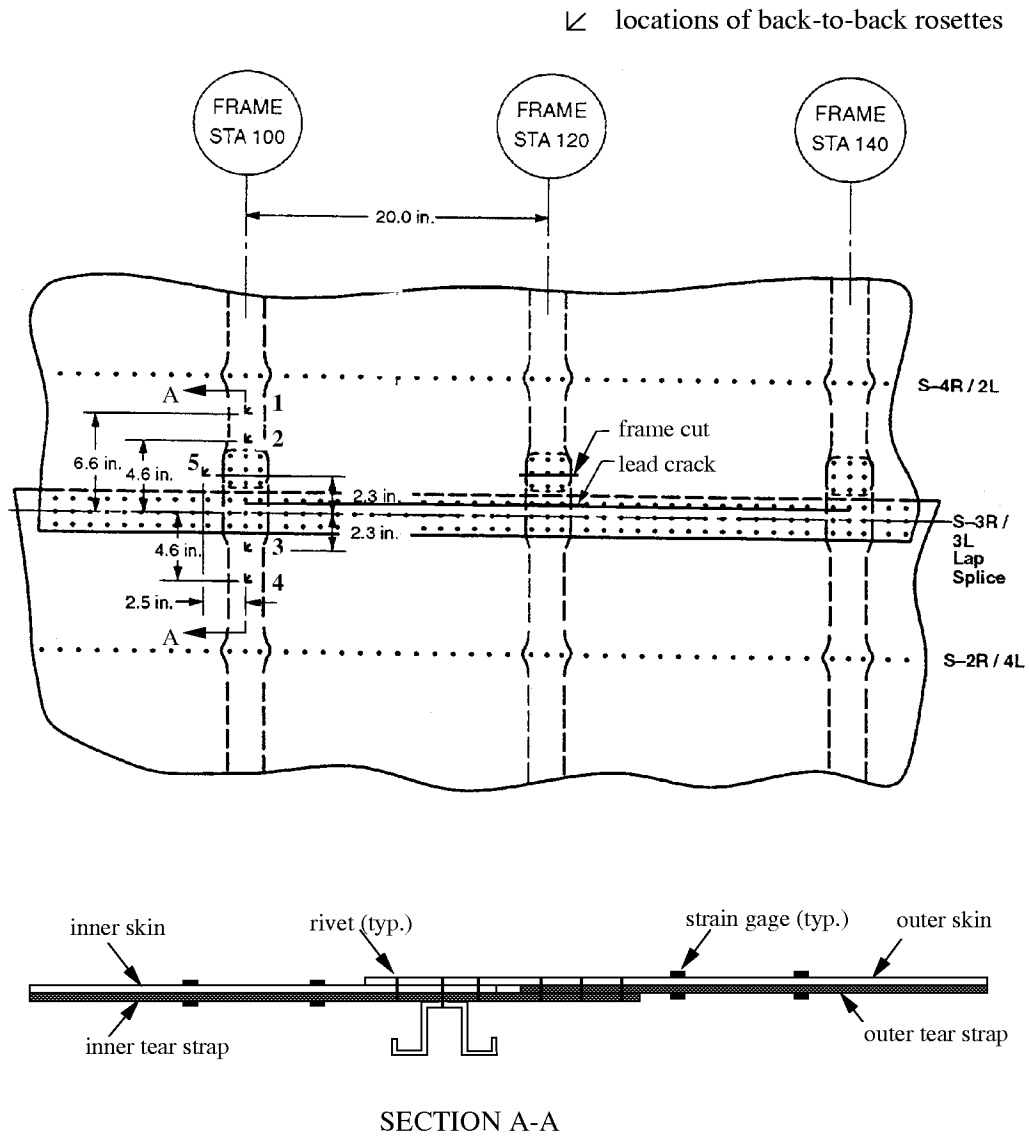


Figure 4.29: Strain gage locations on the skin and tear strap.

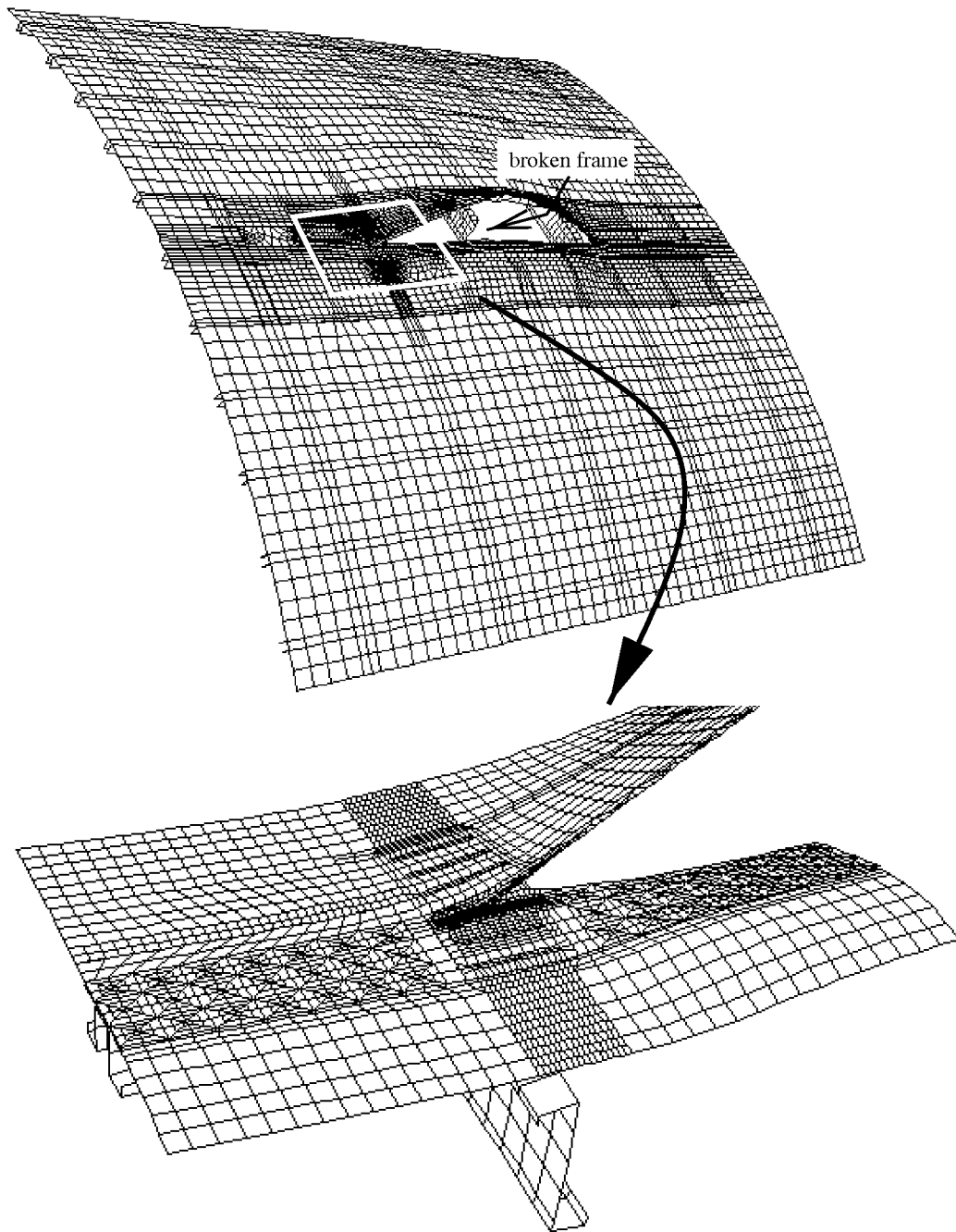


Figure 4.30: Deformed structures of the validation example at global and local modeling levels (pressure = 9.4 psi, crack length = 38.2 inch, magnification factor = 5.0).

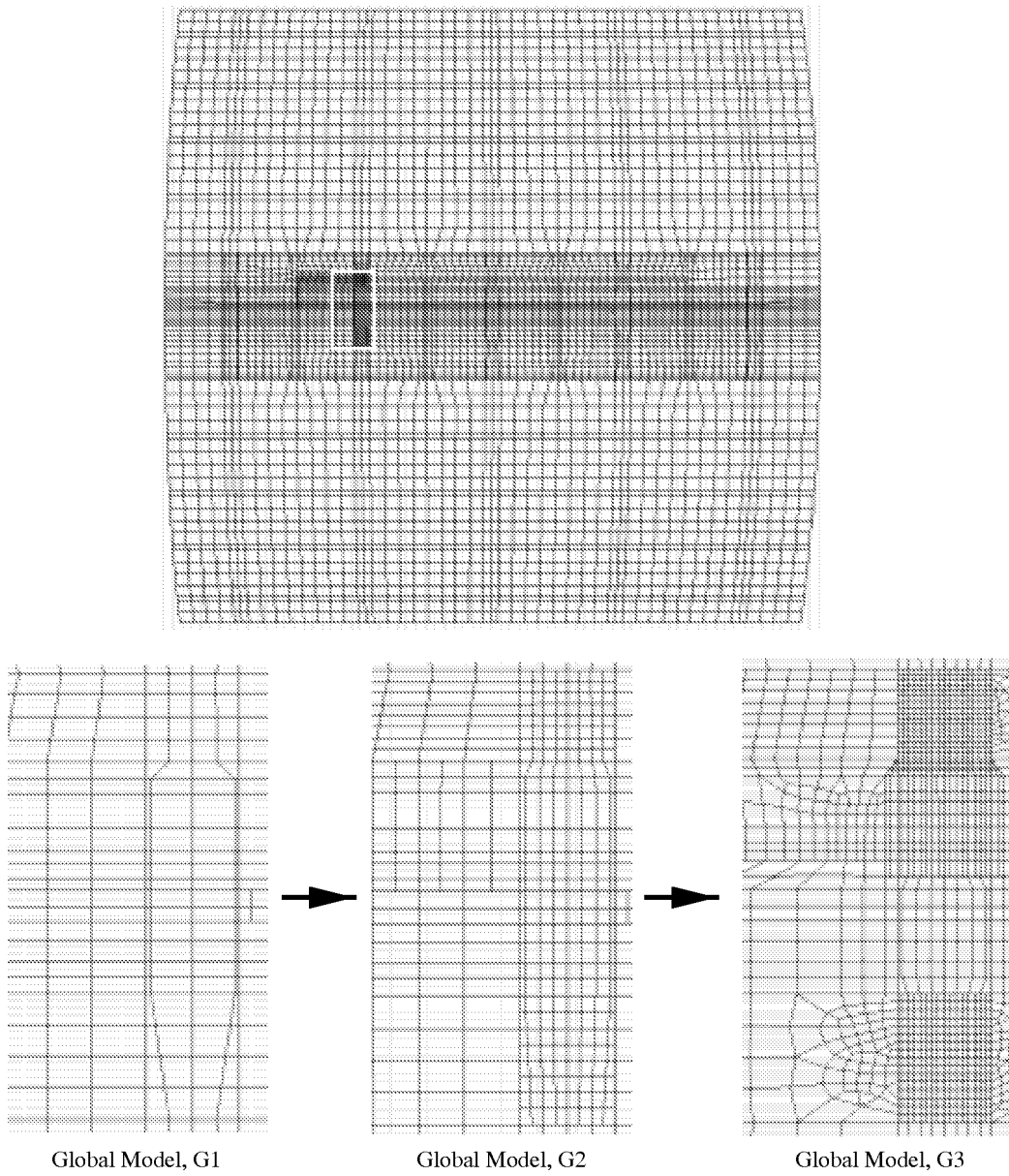


Figure 4.31: Three mesh discretizations at the global modeling level.

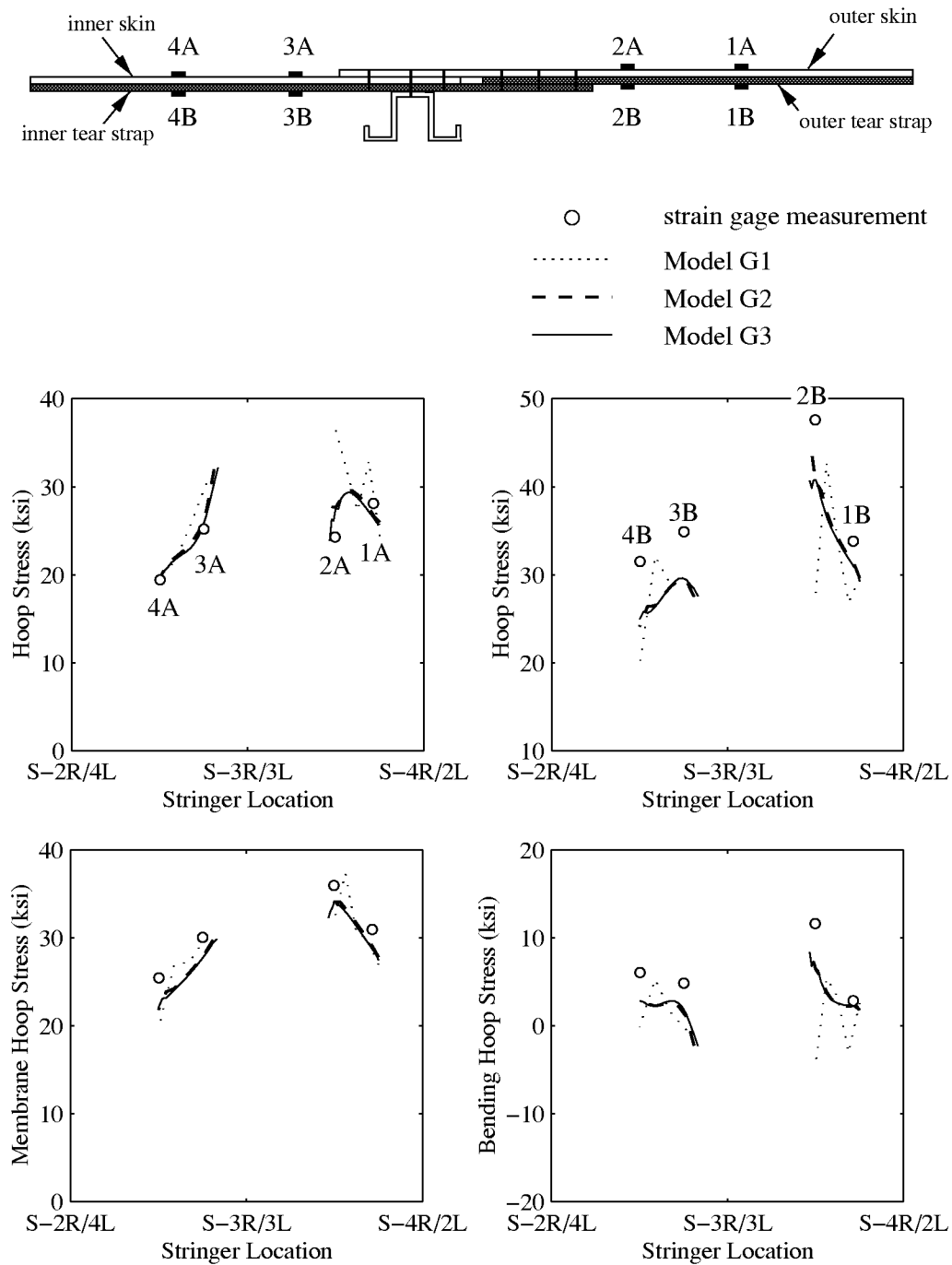


Figure 4.32: Global convergence study: comparison between computed and measured hoop stresses for strain gage 1-4 (pressure = 9.4 psi; crack length = 38.2 in.; frame cut; No MSD).

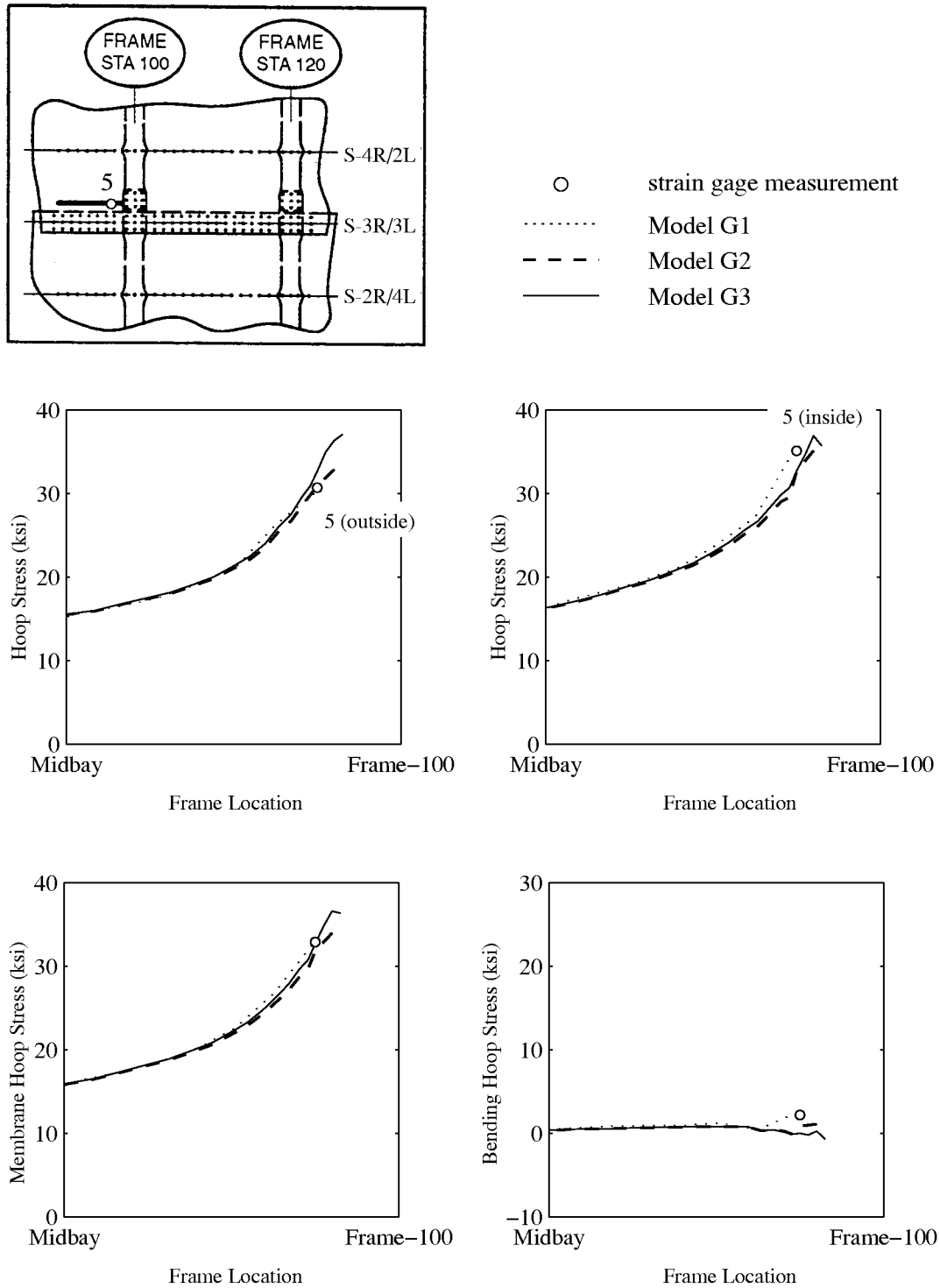


Figure 4.33: Global convergence study: comparison between computed and measured hoop stresses for strain gage 5 (pressure = 9.4 psi; crack length = 38.2 in.; frame cut; No MSD).

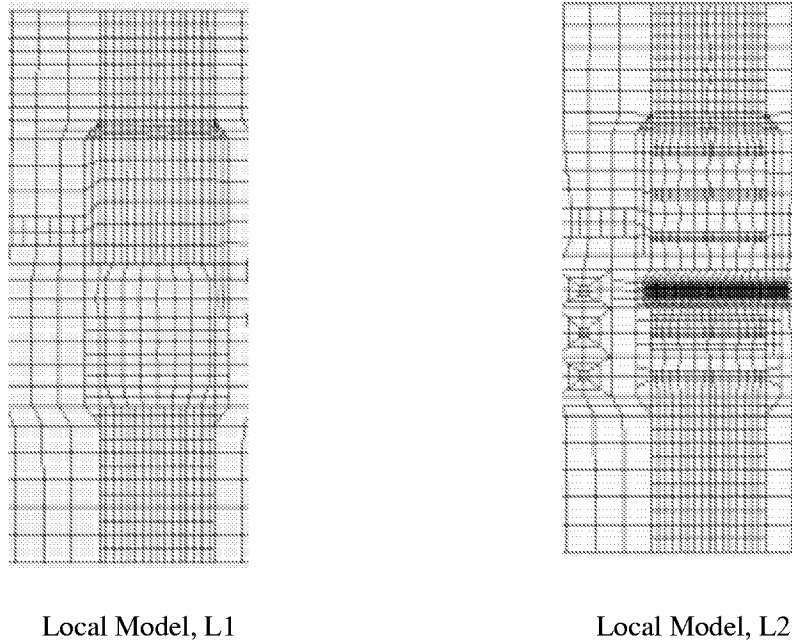


Figure 4.34: Two mesh discretizations at the local modeling level.

accuracy of the hierarchical modeling. Predicted hoop stress distributions from local model L1 agreed well with global model predictions and experimental measurements (Figures 4.35 and 4.36). The other discretization, local model L2, had a much higher mesh density, which is suitable for stable crack growth analyses. The results from local model L2 disagreed with the rest of numerical predictions and experimental measurements (Figures 4.35 and 4.36). In particular, the predicted membrane hoop stresses were much lower than those observed.

The discrepancy is related to the idealized representation of the two-noded spring element for the rivet connection in the finite element model [150, 141]. The single point connection results in unrealistic distortion of the surrounding shell elements. The local distortion causes premature yielding of the shell elements and reduces the load transfer from sheet to rivet. This artificial distortion of the shell elements is discretization-dependent [141, pp. 318–327]. Refining the mesh captures the local artificial distortion better, but makes the comparison to strain gage readings worse [150].

Two modeling idealizations are proposed to avoid this artificial effect. One is to faithfully represent the geometry of the rivets and their interference with the sheets. This will considerably increase the required computational resources and may not be simple to implement in thin-shell elastic-plastic crack growth analyses. The other approach is to generate distributed connections between the two-noded spring element and the surrounding shell elements [150]. The load distribution can be accomplished by defining rigid links, stiff spring elements, or least-squares loading conditions that connect the rivet-spring node to the surrounding shell-element nodes. Care must be taken while defining the area in the shell elements

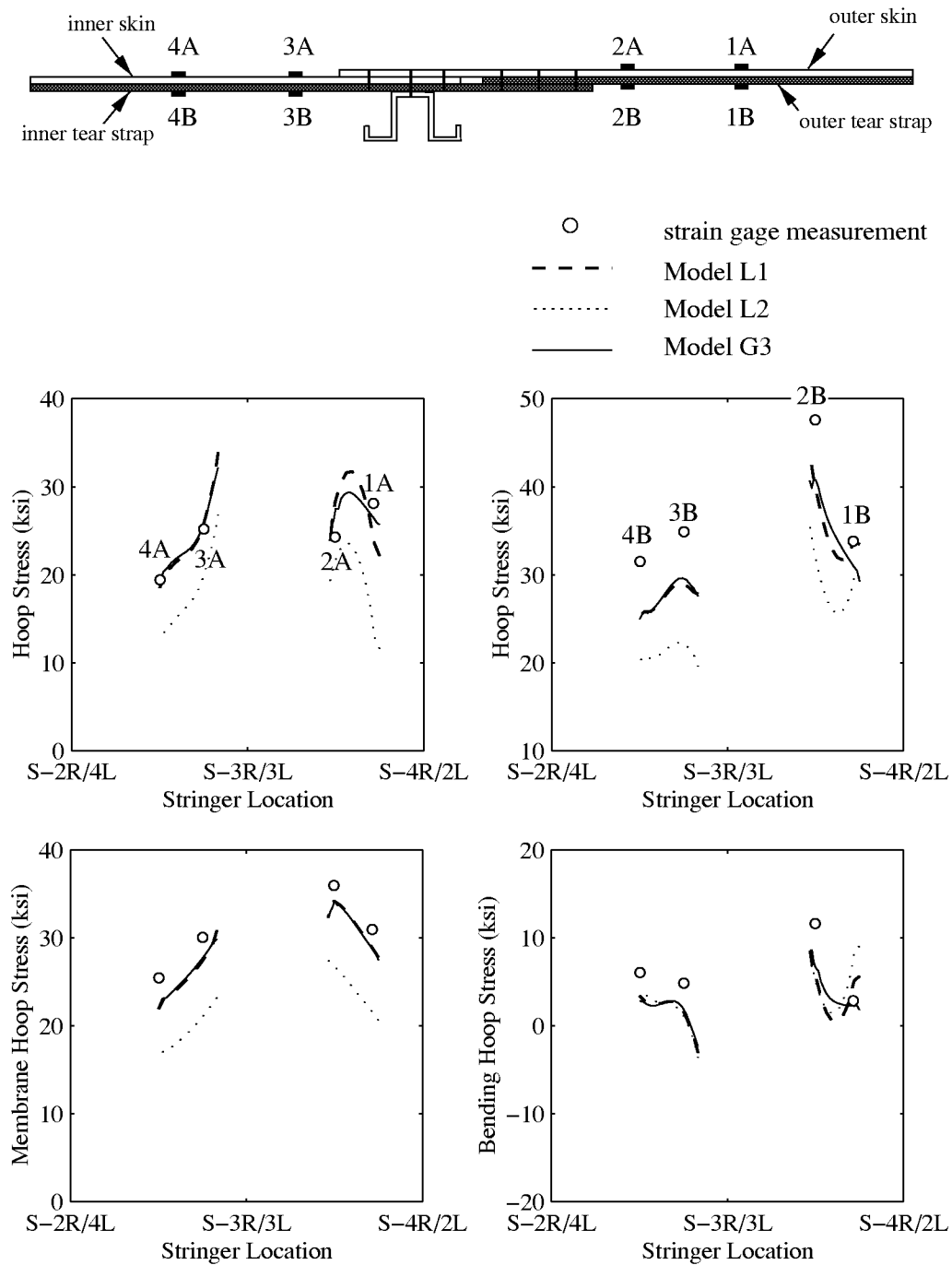


Figure 4.35: Global and local model study: comparison between computed and measured hoop stresses for strain gage 1-4 (pressure = 9.4 psi; crack length = 38.2 in.; frame cut; No MSD).

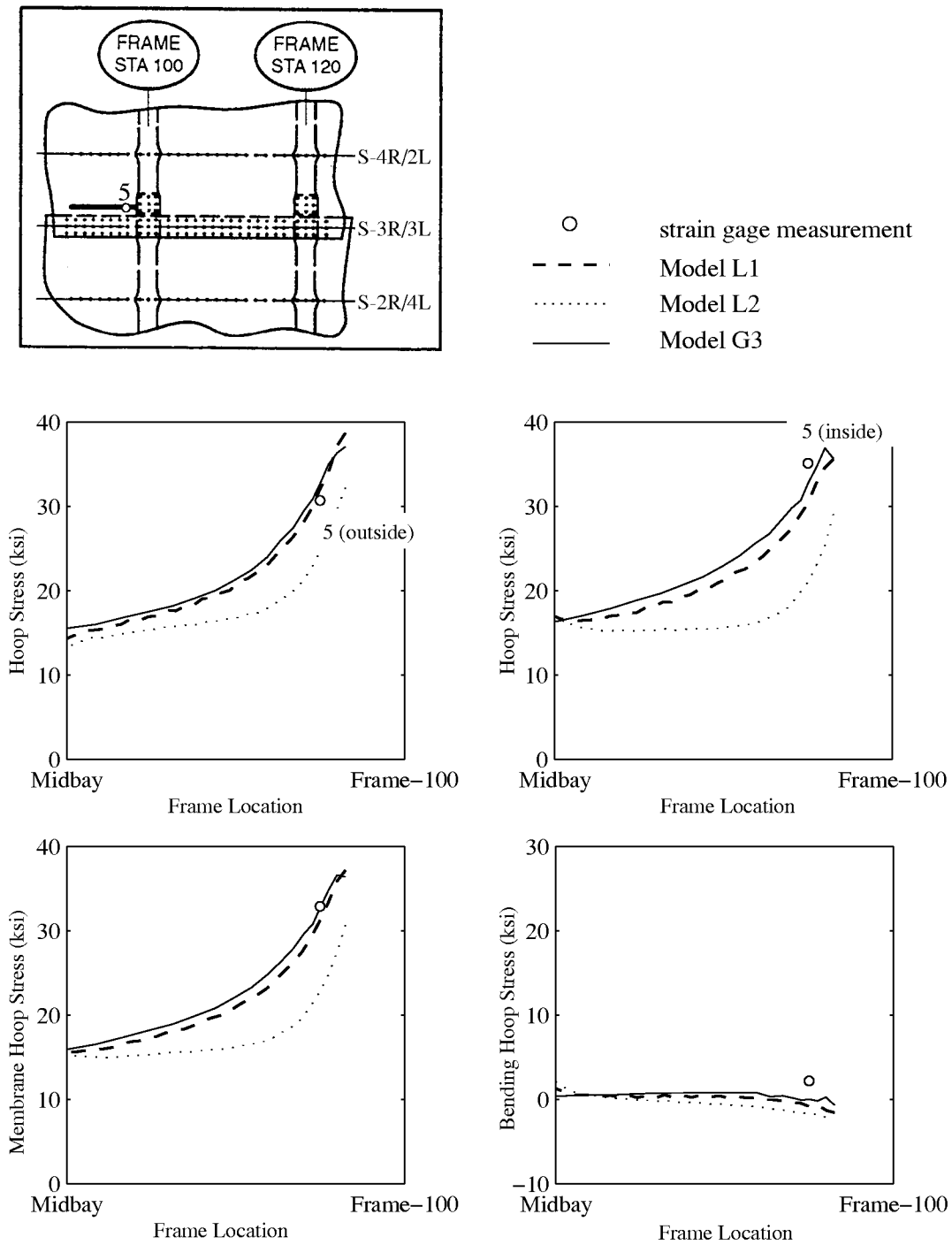


Figure 4.36: Global and local model study: comparison between computed and measured hoop stresses for strain gage 5 (pressure = 9.4 psi; crack length = 38.2 in.; frame cut; No MSD).



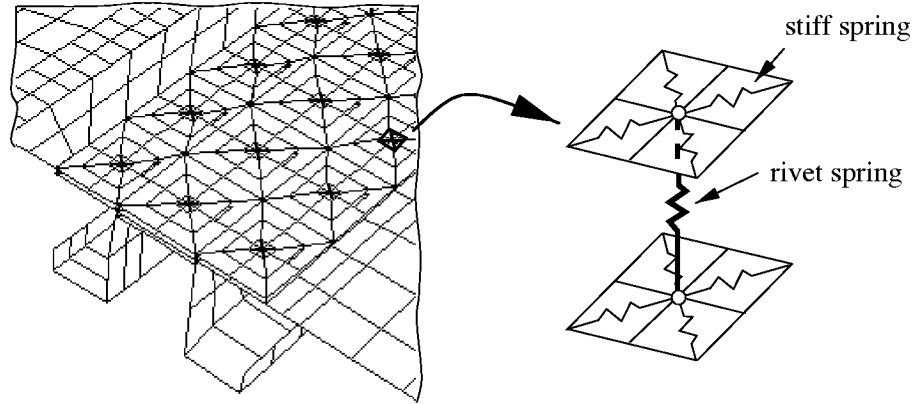


Figure 4.37: Illustration of distributed connection that connects fastener node to surrounding shell nodes

over which the rivet load is distributed. The area should be of the order of the rivet cross-sectional area, since distributing the load over a larger area may inadvertently stiffen the shell elements.

Figure 4.37 illustrates simulation of the distributed connection using stiff spring elements. The stiff spring elements with an order of magnitude stiffer than the rivet spring element were used to distribute the rivet load. For a rivet located on a prescribed tearing path, it is expected that the rivet stays intact on only one side of the crack as the crack propagates through the rivet. Thus, only the shell elements on this side of the crack were used to model the distributed rivet connection. Figures 4.38 and 4.39 show the predicted hoop stress distributions with distributed connection simulations; a much better prediction is observed. The local mesh model, taking into consideration the distributed rivet connection, was used for stable crack growth and residual strength analyses.

#### 4.2.5 Numerical Results: Stable Crack Growth and Residual Strength Analyses

Elastic-plastic crack growth and residual strength analyses were conducted using the local model. Both 4.5 and 5.5 degree critical angles computed at 0.04 inch behind the growing crack tip were used to investigate the sensitivity of  $CTOA_c$  on stable crack growth and residual strength prediction. The 4.5°  $CTOA_c$  was the angle that best correlates the predicted and observed residual strengths of the MT tests. The 5.5° angle was the mean from the surface  $CTOA_c$  measurements in the MT tests. The plane strain core height was 0.16 inch along the prescribed tearing path.

Figure 4.40 shows predicted results from the first attempt for stable crack growth analyses. The change of the  $CTOA_c$  from 4.5° to 5.5° increases predicted residual strength by about 33% and 22% for the cases without and with MSD cracks, respectively.

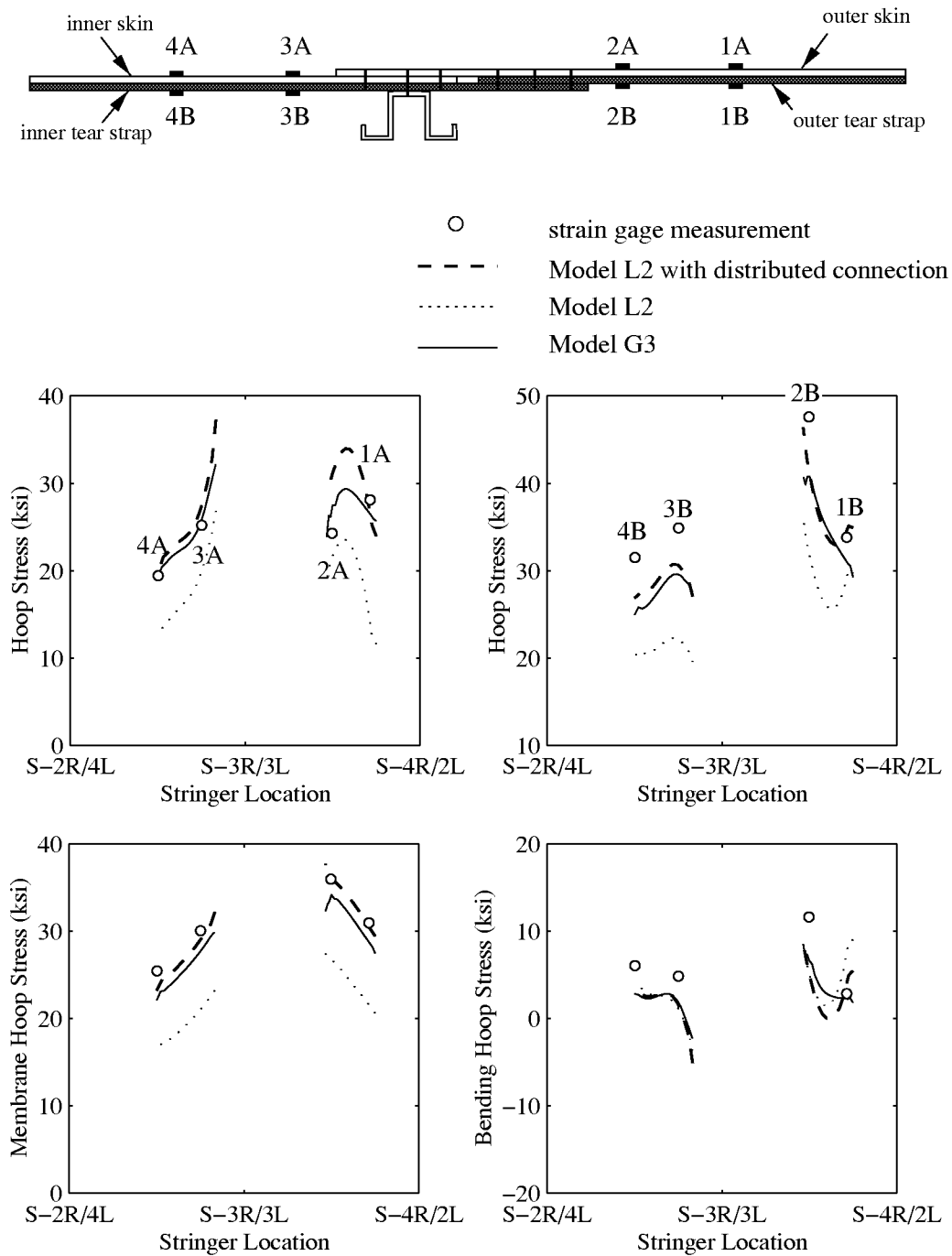


Figure 4.38: Effects of distributed rivet connection: comparison between computed and measured hoop stresses for strain gage 1-4 (pressure = 9.4 psi; crack length = 38.2 in.; frame cut; No MSD).

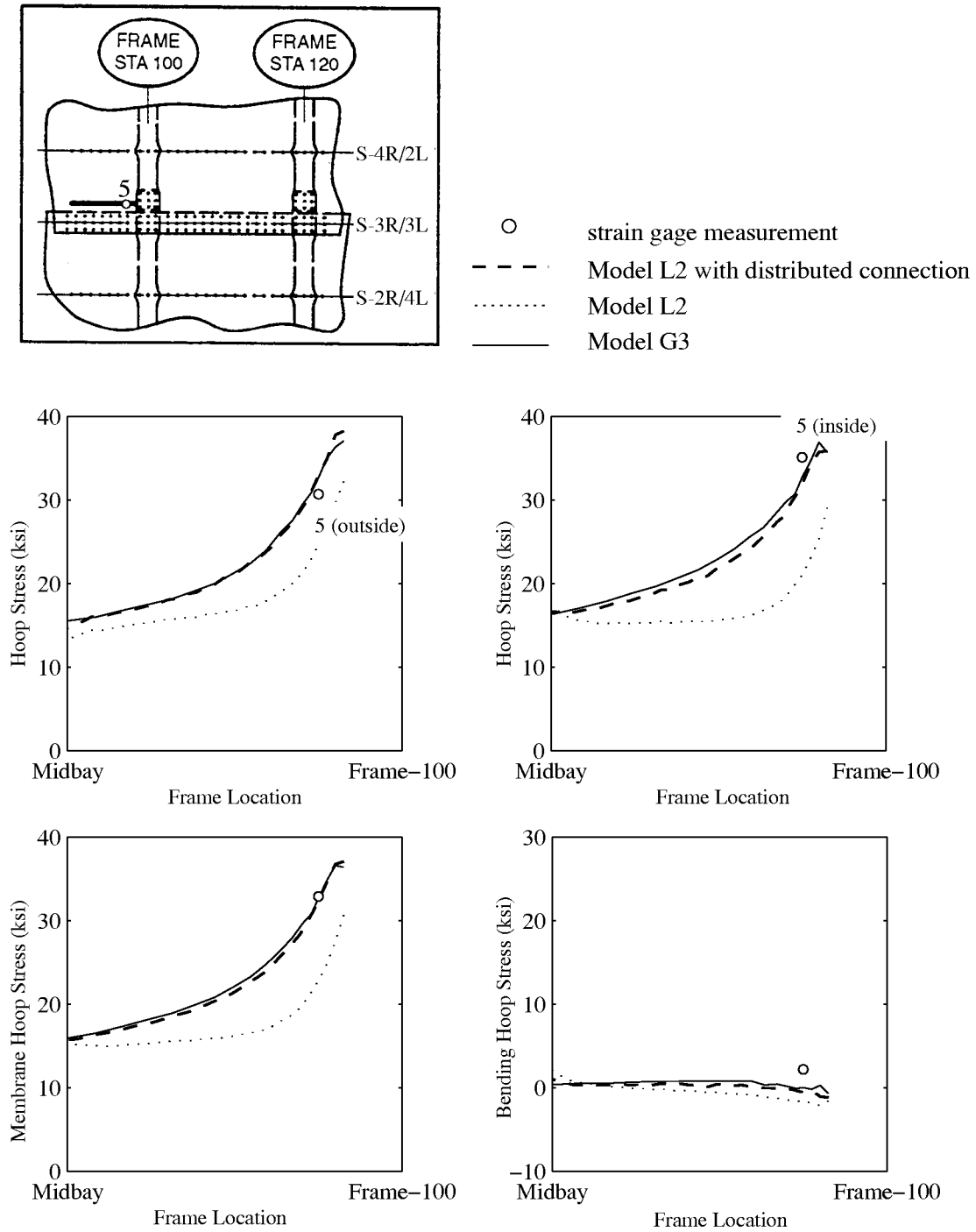


Figure 4.39: Effects of distributed rivet connection: comparison between computed and measured hoop stresses for strain gage 5 (pressure = 9.4 psi; crack length = 38.2 in.; frame cut; No MSD).

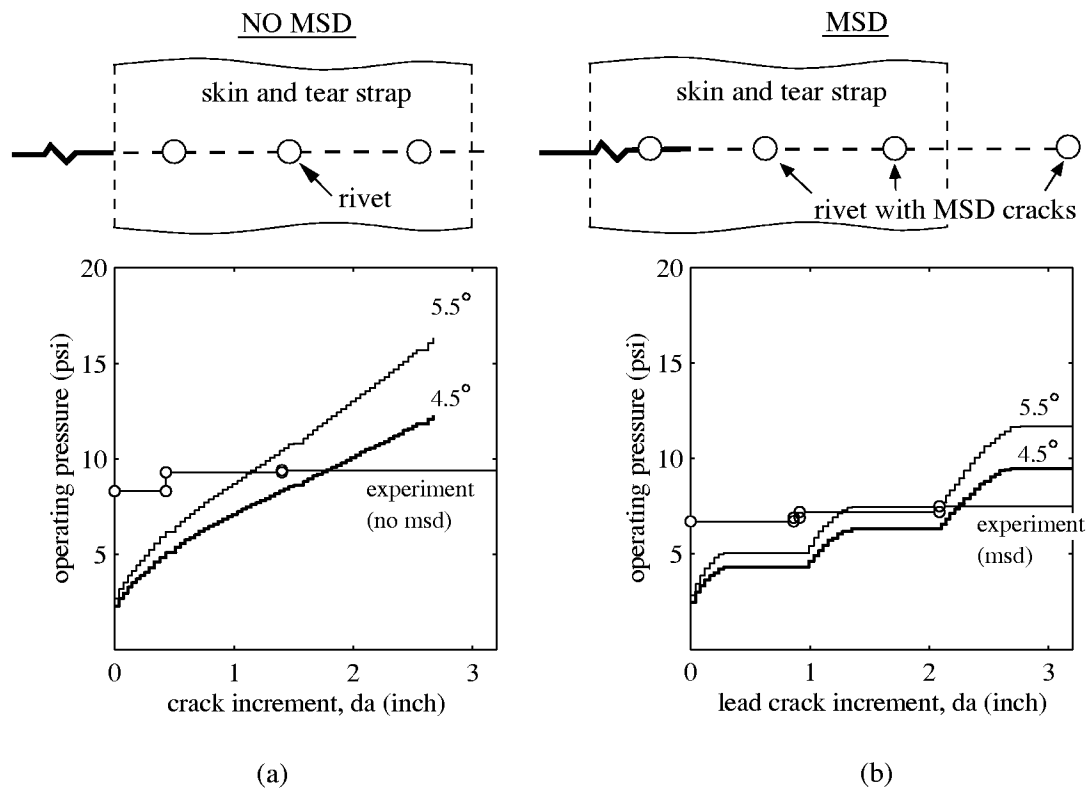


Figure 4.40: Comparison between the predicted stable crack growth and experimental measurements: (a) case without MSD, and (b) case with MSD.

Although analysis results in Figure 4.40 clearly demonstrate the loss of residual strength due to the presence of MSD, all the predicted results (i) under-estimate the pressure loading to initiate the stable crack growth, and (ii) over-estimate the residual strength.

The much lower predicted pressure for tearing initiation is mainly caused by residual plastic deformation left by the fatigue crack growth. A possible cause for the lower residual strengths observed in the test may be related to the occurrence of tear strap failure. Both effects are discussed below.

#### 4.2.5.1 Residual Plastic Deformation Effects

The test panels were subjected to pressure cycling prior to the residual strength test. To incorporate the residual plastic deformations due to the cyclic loading, the residual strength analyses were re-performed using an elastic-plastic cyclic loading simulation suggested by Newman [89]. The procedure consists of the following steps:

- step 1** *Close* an appropriate length of fatigue crack.
- step 2** Load the fuselage model up to the maximum pressure loading conducted in fatigue tests.
- step 3** Release the crack tip node and unload the model.
- step 4** Repeat steps 2 and 3 until the crack tip reaches the initial position for stable tearing.

This procedure implies that the fatigue crack only propagates at the maximum pressure during the cyclic loading simulation. For Mode-I only deformations under constant-amplitude load cycling, crack surfaces close at a positive applied load (*i.e.*, step 3). The contact stresses cause the material to yield in compression. Crack face contact and compressive yielding were not modeled in the current simulations.

In subsequent analyses, the fuselage model is brought to the operating pressure level during fatigue tests without allowing the crack to advance. The crack is then allowed to advance one element, and the load is returned to zero. Figure 4.41 illustrates results for a 0.32 inch *length* of fatigue crack closure used in the analysis for the case without MSD cracks. The crack-opening and crack-closure pressures in the fuselage panel simulations follow similar trends observed in the MT flat panel simulations [89]. After two cycles of simulation, the crack-opening and crack-closure pressures quickly stabilize to 7.2 psi and 5.3 psi, respectively.

Figure 4.42 shows two predicted crack opening profiles with and without fatigue crack closure effect when the pressure loading reaches 8.6 psi (no growth). The effects of residual plastic deformations on the crack opening profile and consequently, the CTOA prediction, are clearly observed.

The 7.2 psi crack-opening pressure shown in Figure 4.41 seems to be too high in comparison with 2D plane stress results [89] and laboratory observations [39, 40].

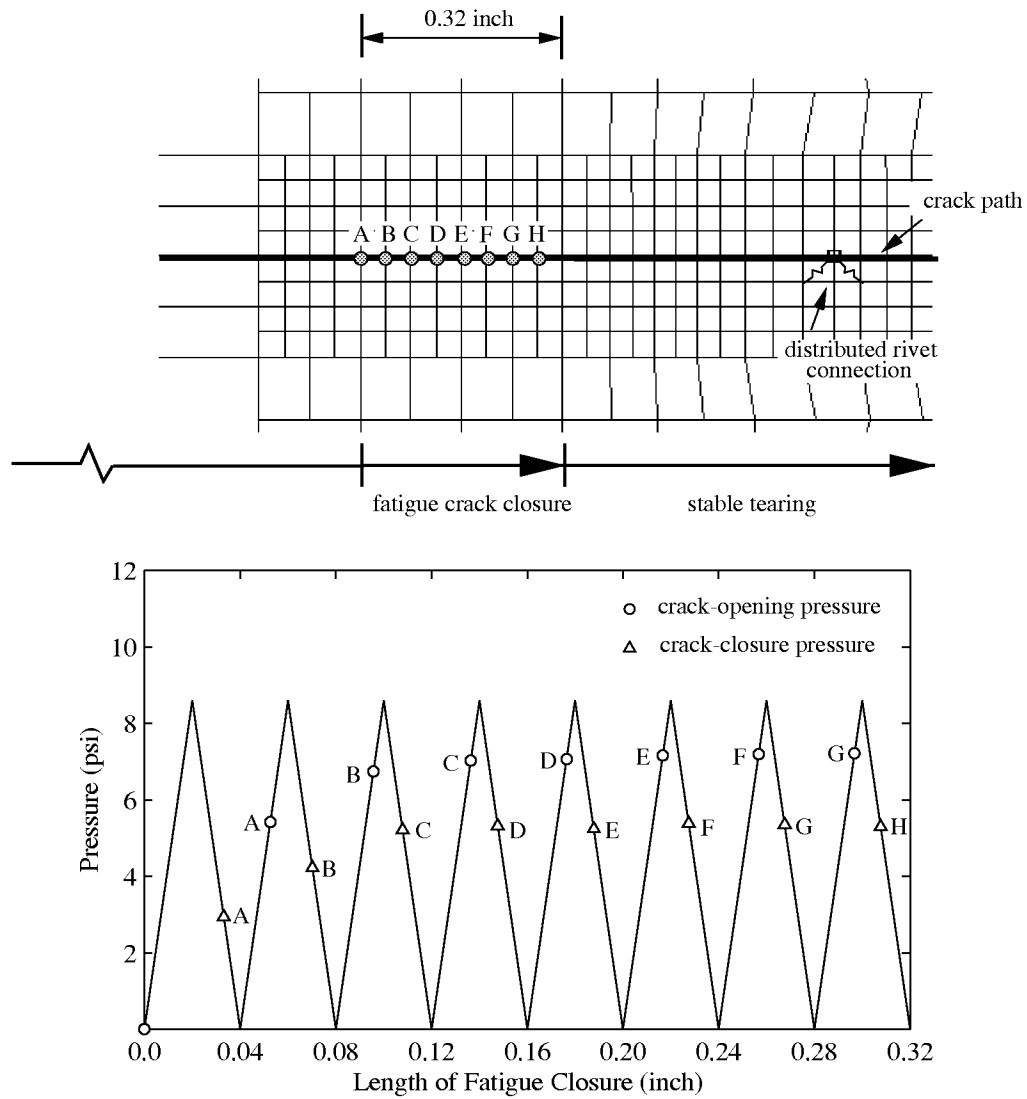


Figure 4.41: Predicted crack-opening and crack-closure pressure under cyclic loading (cyclic pressure = 8.6 psi, No MSD).

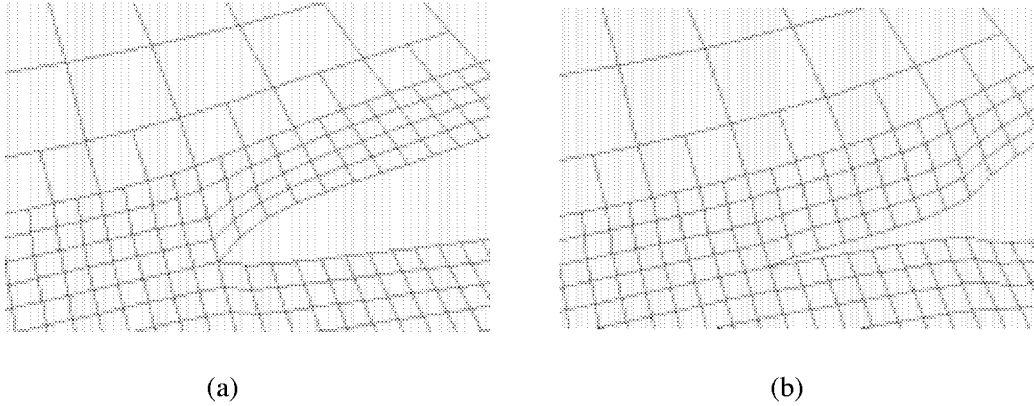


Figure 4.42: Predicted crack opening profiles of outer skin at initial tearing crack tip: (a) case without fatigue crack closure, and (b) case with 0.32 inch fatigue crack closure (no stable crack growth, magnification factor = 2.0).

This may be due to the lack of modeling of contact conditions when the crack closes. That is, the crack faces pass each other so no compressive yielding is developed in the unloaded state. The compressive yielding stress will reduce residual tensile plastic deformation thus leading to a lower crack-opening pressure [89].

Figure 4.43 shows the predicted results for a 0.08 inch *length* of fatigue crack closure used for the case with MSD cracks. During cyclic loading simulation, the lead and MSD crack tips are released simultaneously. The crack-opening and crack-closure pressures at the second loading cycle for the lead crack are about 4.7 psi and 3.3 psi, respectively. We note that the *length* of fatigue crack closure is restrained by the *length* of MSD cracks. Further amount of fatigue crack closure simulation is possible, but leads to somewhat ambiguous MSD fatigue crack propagation. The results after two cycles of simulation, however, are believed to essentially capture the residual plastic deformation effects. This assertion is based on observations from the case without MSD cracks (Figure 4.41).

Figure 4.44 shows predicted stable crack growth incorporating the closure effects. Table 4.2 summarizes the predicted and observed starting pressure to initiate stable crack growth. The plasticity-induced closure increases the initiation pressure by about 150% to 210%. The predicted crack initiation loads are within 6% of experimental measurements for the cases that incorporate prior plastic residual deformations due to fatigue crack growth. However, the predicted residual strengths are still higher than those observed.

#### 4.2.5.2 Effects of Tear Strap Failure

A possible cause for the lower residual strengths observed in the test is the occurrence of failure of other structural elements. Figure 4.45 shows the predicted effective stress distribution in the outer skin, inner skin, outer tear strap, and inner

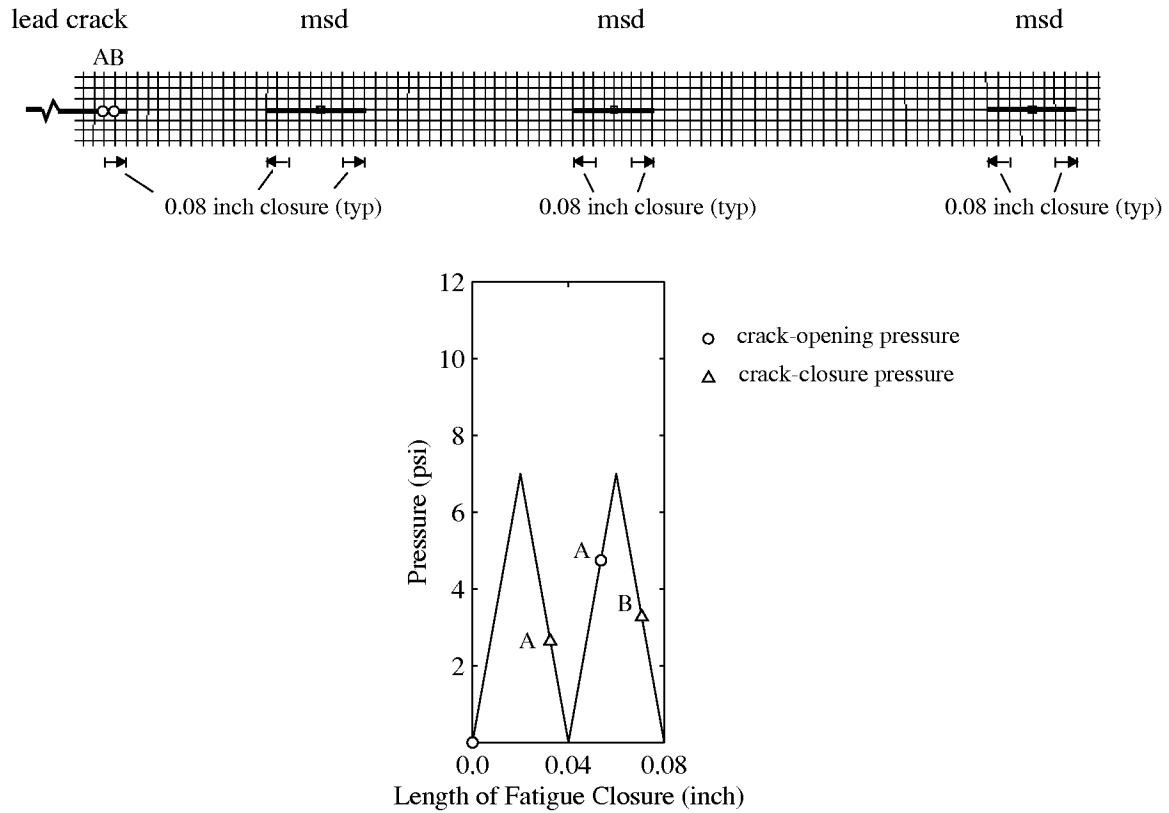


Figure 4.43: Predicted crack-opening and crack-closure pressure under cyclic loading (cyclic pressure = 7.0 psi, MSD).

Table 4.2: Predicted and Observed Pressure Loading for Stable Tearing Initiation

	predicted (psi)		observed (psi)
	$CTOA_c = 4.5^\circ$	$CTOA_c = 5.5^\circ$	
No MSD	2.3	2.7	8.3
No MSD (0.32 inch closure)	8.3	8.4	
MSD	2.5	2.8	6.7
MSD (0.08 inch closure)	6.3	6.5	



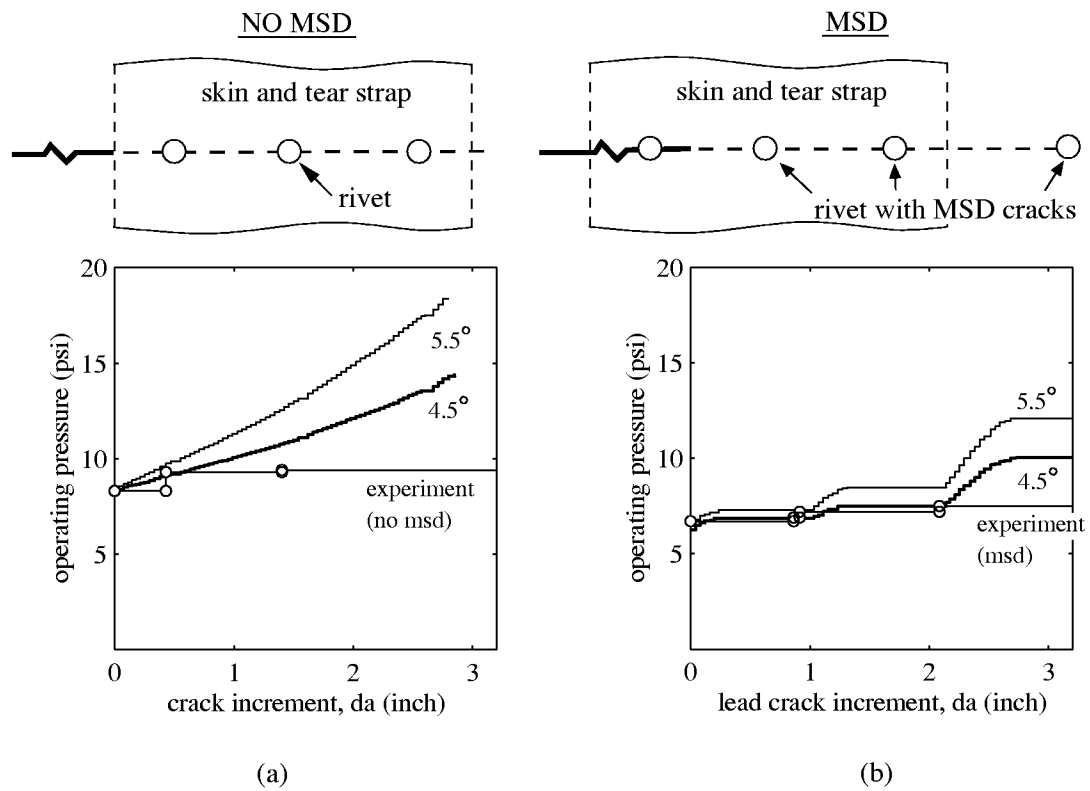


Figure 4.44: Comparison between predicted stable crack growth with fatigue closure effects and experimental measurements: (a) case without MSD, and (b) case with MSD.

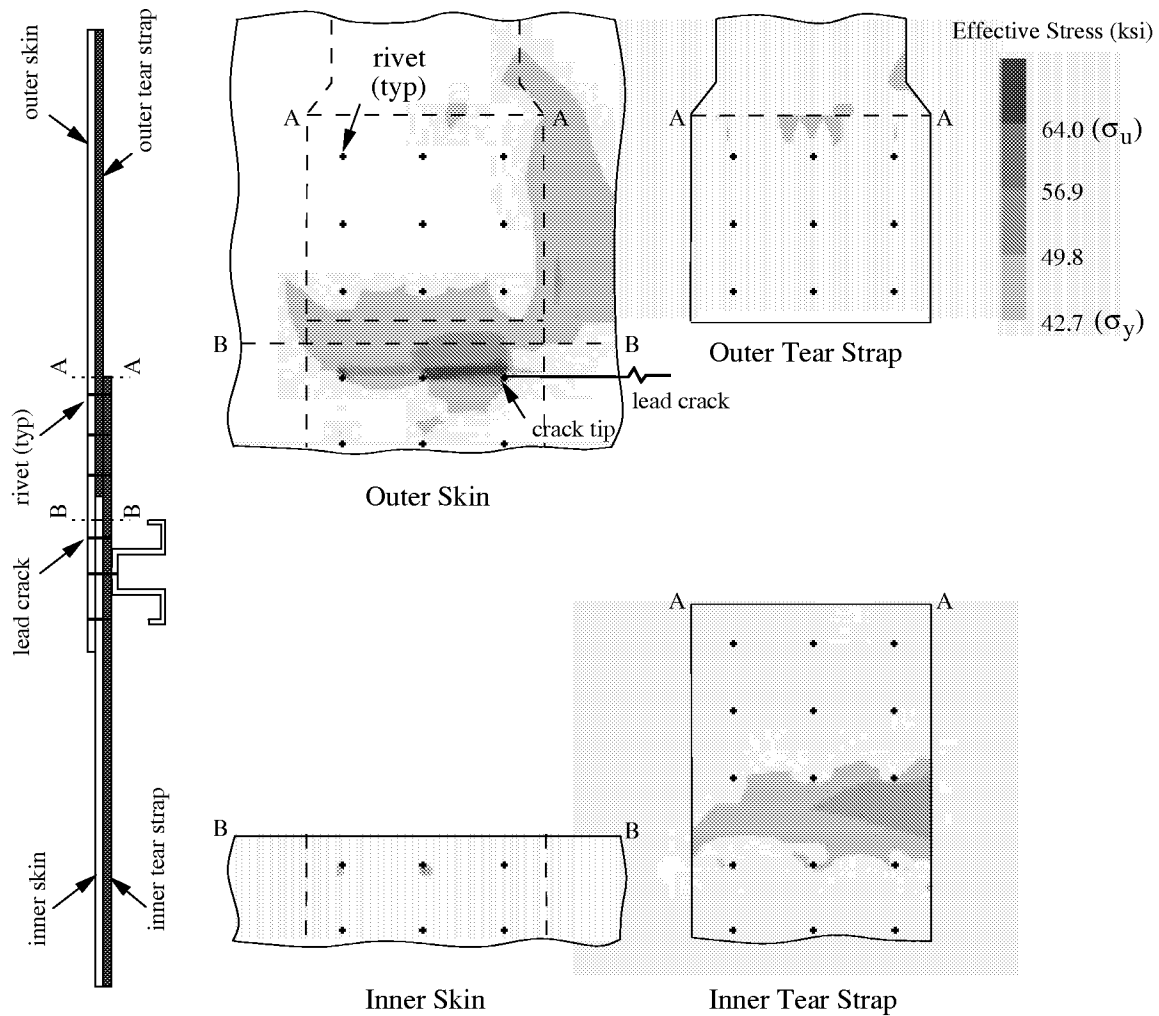


Figure 4.45: Predicted effective stress distribution (pressure = 9.86 psi,  $da = 0.5$  inch,  $CTOA_c = 5.5^\circ$ ).

tear strap as the stable crack growth analysis reaches 9.86 psi pressure loading for the case without MSD cracks. Net section yielding is clearly shown in the inner tear strap.

The possible breakage of the inner tear strap during the residual strength test was also reported in [49]. To further investigate this damage scenario, a tear strap with rivet holes was modeled. By taking the kinematic boundary conditions from the local fuselage model, a stress concentration around the holes is observed (Figure 4.46). It is then postulated that the high stress concentration is likely to initiate new cracks from the rivet holes thus leading to breakage of the inner tear strap.

To incorporate the tear strap damage scenario into the crack growth analysis, the inner tear strap is cut prior to fatigue crack closure and stable crack growth analyses as illustrated in Figure 4.47. The predicted crack-opening pressures of

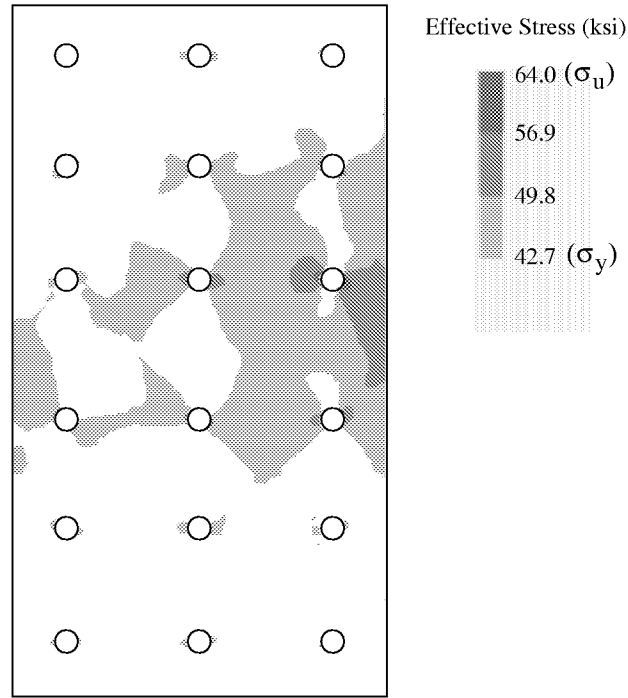


Figure 4.46: Predicted effective stress distribution of inner tear strap with rivet holes (pressure = 9.86 psi,  $d_a = 0.5$  inch,  $CTOA_c = 5.5^\circ$ ).

the broken tear strap models with 0.32 and 0.08 inch fatigue crack closure are 7.0 psi and 3.1 psi for the cases without and with MSD cracks, respectively (*cf.* 7.2 psi and 4.7 psi for the models with the intact tear strap).

Figure 4.48 shows the predicted stable crack growth and residual strength for the fuselage models with a broken inner tear strap. The predicted residual strength using  $4.5^\circ$   $CTOA_c$  is within 13% of the experimental observation for the case without MSD cracks and within 1% of the experimental observation for the case with MSD cracks.

We further examine several damage scenarios with the possible occurrence of the tear strap failure at various stages of stable crack growth. In subsequent analyses, the inner tear strap stays intact until it reaches a certain amount of stable

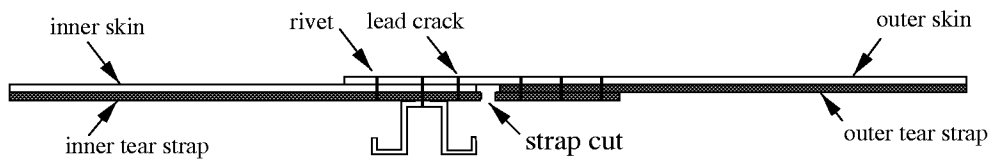


Figure 4.47: Illustration of broken inner tear strap.

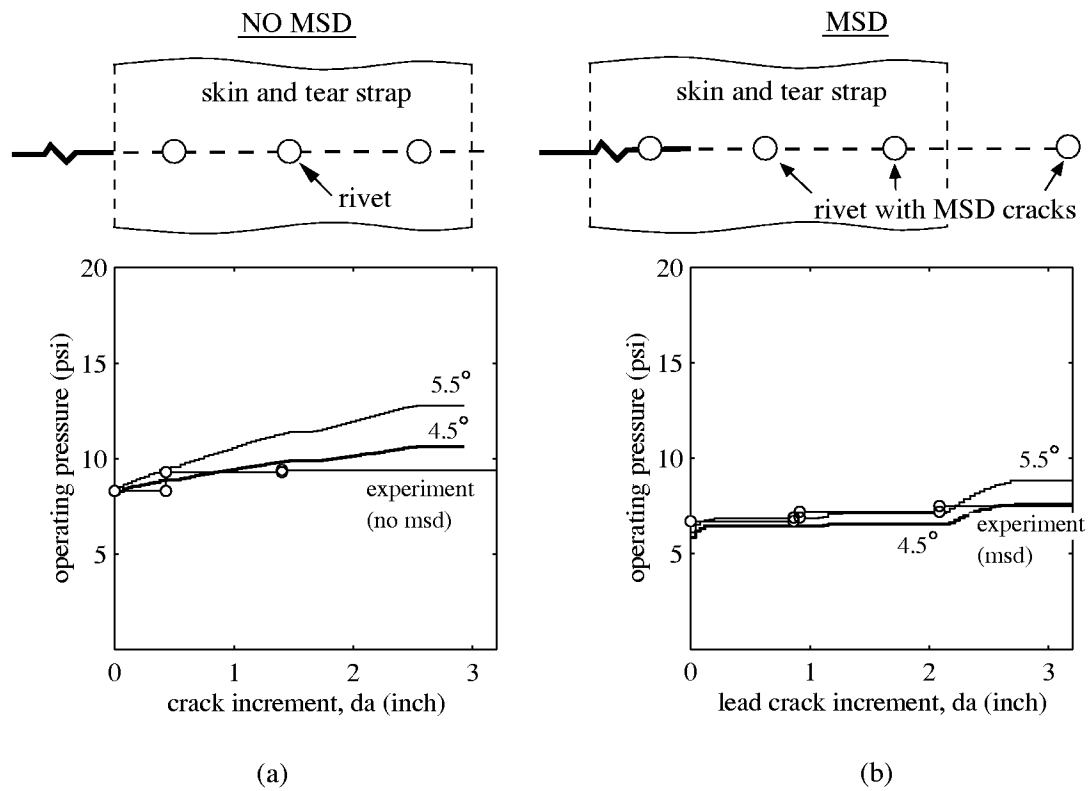


Figure 4.48: Comparison between predicted stable crack growth with broken tear strap and experimental measurements: (a) case without MSD, and (b) case with MSD.

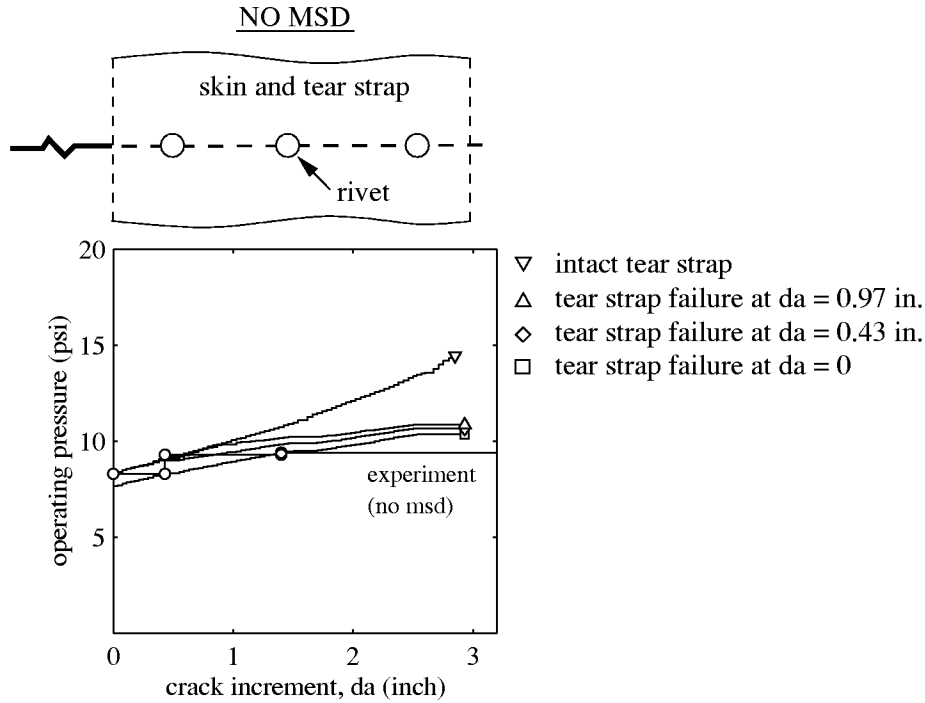


Figure 4.49: Comparison between predicted results with tear strap failure at various stages during stable crack growth and experimental measurements (No MSD,  $CTOA_c = 4.5^\circ$ ).

crack growth. The analysis is continued until the residual strength is reached. Figure 4.49 shows the predicted stable crack growth and residual strength using  $4.5^\circ$   $CTOA_c$  for the fuselage models without MSD cracks. For comparison, the predicted results with an intact tear strap shown in Figure 4.44 are also plotted. The influence of the tear strap failure on residual strength prediction is again observed. The occurrence of the tear strap failure at various stages of stable crack growth affects the predicted crack growth resistance. But this scenario has a very mild influence on residual strength prediction, as long as there is a sufficient amount of tearing before the structure reaches its residual strength.

#### 4.2.5.3 Discussion

The difference between predicted and observed residual strengths for the case without MSD cracks may be due to the simulated excess residual plastic deformation prior to tearing. One way to *reduce* the plastic wake is to grow the crack at *one half* the actual fatigue load. The corresponding crack-opening pressure with 0.32 inch of fatigue crack closure for the case without MSD is 3.2 psi. This, in conjunction with the tear strap damage scenario and  $4.5^\circ$   $CTOA_c$ , predicts 9.34 psi residual strength for the case without MSD (Figure 4.50). The result is within 1% of the experimental observation. However, the crack tearing now initiates at loads much

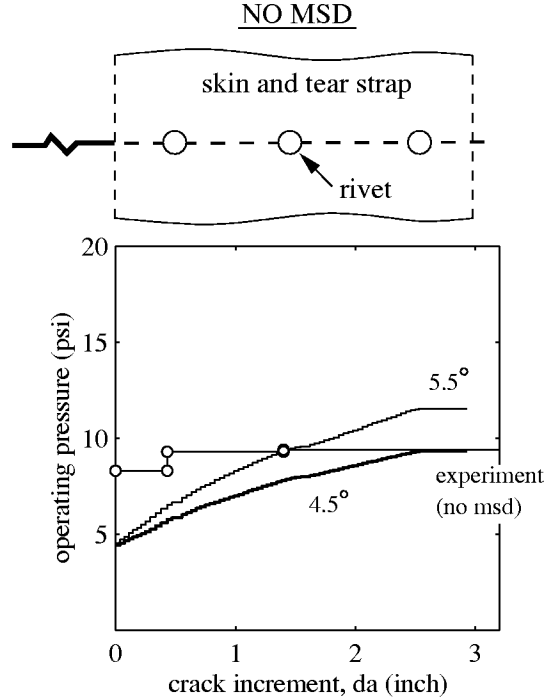


Figure 4.50: Comparison between predicted stable crack growth and experimental measurements (broken tear strap, reduced plastic wake, No MSD).

lower than those seen in the experiment, indicating that this correlation may only be coincidental.

Another possibility of higher predicted residual strength for the case without MSD may be related to the fact that the current model does not faithfully model fracturing processes in the vicinity of rivets. In the panel test, the lead crack propagated into and re-initiated from a rivet hole as illustrated in Figure 4.51. Apparently, neither the CTOA fracture criterion for the lead crack propagation nor the idealized distributed rivet representation have sufficient accuracy in capturing this phenomenon. Further investigation is needed to quantify its effect on residual strength prediction.

#### 4.2.5.4 Major Observations

Several observations are made from stable crack growth and residual strength analyses conducted in this section:

- For all the scenarios simulated, the loss of residual strength due to the presence of small MSD cracks is consistently observed. The reduction in residual strength caused by MSD varies from 28% to 47%.
- The residual strength prediction is sensitive to changes in  $CTOA_c$ . Altering the  $CTOA_c$  from  $4.5^\circ$  to  $5.5^\circ$  changes the predicted residual strength by 17%

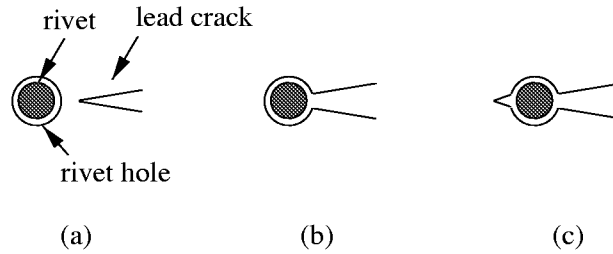


Figure 4.51: Illustration of crack propagation near rivet: (a) lead crack approaching rivet, (b) lead crack growing into rivet hole, and (c) new crack initiating out of rivet hole.

to 33% for all the analyses conducted in the damage configuration without MSD cracks. It changes the predicted residual strength by 12% to 22% for the case with MSD.

- The residual plastic deformation or the plastic wake from fatigue crack growth has a strong effect on stable crack initiation and a mild effect on residual strength prediction. For stable crack growth initiation, it is essential to incorporate the plastic wake to accurately predict the starting pressure loading. Neglecting plastic wake effect leads to a totally erroneous prediction of early stable crack growth. For all the residual strength analyses conducted, the plastic wake increases the predicted residual strength by 3% to 9%.
- The breakage of the inner tear strap, categorized as possible failure of other structural elements during stable crack growth, is crucial to residual strength prediction. For all the analyses conducted, the occurrence of the broken tear strap reduces the predicted residual strength by 24% to 30%. Cutting the tear strap prior to or during stable crack growth analysis is a preliminary approach to model this damage scenario. A better approach would be to incorporate proper mechanics to initiate and propagate the damage directly in the crack growth analysis. Also, dynamic effects resulting from the failure of the tear strap could be simulated, and may not be negligible [130].

### 4.3 Summary

The crack tip opening angle (CTOA) fracture criterion obtained from coupon tests is used to predict fracture behavior and residual strength of built-up aircraft fuselages that are subjected to widespread fatigue damage (WFD). In the process, the feasibility and validity of the analysis methodology are assessed. The major findings of the fuselage panel study are:

1. The occurrence of small MSD cracks substantially reduces the residual strength of pressurized fuselages.

2. Modeling fatigue crack closure is essential to capture the fracture behavior during early stable crack growth.
3. Possible damage of other structural elements during stable crack growth, *e.g.*, tear strap failure, substantially reduces the residual strength of pressurized fuselages.
4. The distributed rivet load treatment of fasteners is crucial for the local crack growth model to accurately predict the stress distribution.
5. It is apparent that more full-scale fuselage tests need to be conducted to fully verify the analysis methodology. However, the CTOA fracture criterion together with the FRANC3D/STAGS program proves to be an effective tool to simulate: (1) lead crack growth, (2) MSD crack growth, (3) multiple crack interaction, (4) plastic wake from fatigue crack growth, (5) tear strap failure, and (6) corrosion damage in pressurized fuselages.



# Chapter 5

## Theory for Curvilinear Crack Growth in Planar and Thin Shell Structures

Theories and simulations presented in the previous chapters mainly deal with *self-similar* elastic-plastic crack growth where crack trajectories are known *a priori*. However, a crack in a shell-like structural component under combined loading will likely propagate in a *non-self-similar* fashion. Curvilinear crack growth can lead to the so-called flapping phenomenon observed in pressurized fuselages [137, 82] (Figure 5.1). Flapping can produce a controlled opening in the fuselage that causes a “safe” decompression and can prevent catastrophic failure of the structure.

As discussed in the previous chapters, stress intensity factors (SIFs) and the crack tip opening angle (CTOA) serve well to explain fatigue and elastic-plastic crack advancement in thin-sheet metallic structures. In addition to these crack growth criteria, a criterion for predicting the direction of propagation is needed to simulate curvilinear crack growth.

This chapter together with next two chapters examines some relevant issues about curvilinear crack growth simulations. Theories for curvilinear crack growth in planar and thin shell structures are discussed in this chapter. In Chapter 6, computational methods used to evaluate the  $T$ -stress term that is known to have a significant effect on crack trajectory prediction are discussed. Curvilinear crack growth simulations of coupon tests and full-scale fuselage panel tests are presented in Chapter 7.

### 5.1 Introduction

In general, a crack in planar and thin shell structures under mixed-mode loading will propagate in a curved fashion. This so-called *non-self-similar* crack growth where crack trajectories are not known *a priori* requires a direction criterion to predict the impending angle of crack propagation. For crack growth in ideally

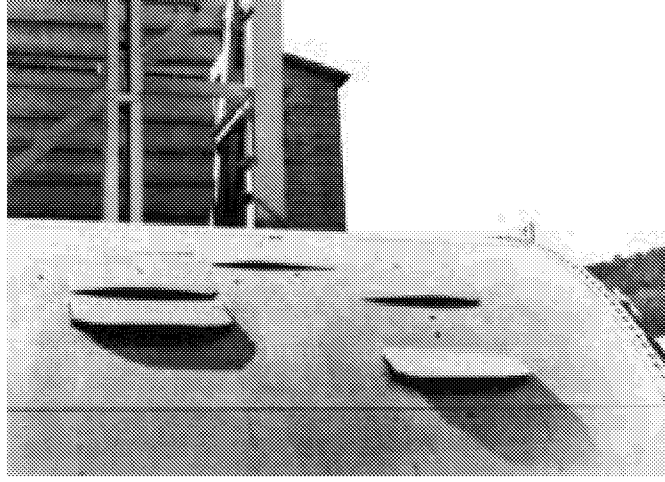


Figure 5.1: Flapping phenomenon in pressurized fuselage due to curvilinear crack growth (after [82]).

brittle isotropic material, the three most common theories for predicting the crack propagation angle are:

1. the maximum tangential stress theory ( $\sigma_{\theta\theta_{max}}$ ) [41],
2. the maximum energy release rate theory ( $G(\theta)_{max}$ ) [58], and
3. the minimum strain energy density theory ( $S(\theta)_{min}$ ) [126].

There is no consensus on the most satisfactory theory to predict crack growth direction. A convenient way to compare the predicted crack growth angles from various mixed-mode theories is through introducing a mixed-mode parameter,  $\Psi$ :

$$\Psi = \frac{2}{\pi} \tan^{-1} \left| \frac{K_I}{K_{II}} \right| \quad (5.1)$$

that characterizes the elastic loading mixity [124]. Comparisons of the elastic mixity parameter,  $\Psi$ , versus the predicted crack growth angle,  $\theta_c$ , from the three mixed-mode theories are plotted in Figure 5.2. For small values of  $\Psi$  where  $K_{II}$  is dominant, the three theories predict different crack propagation angles. For large values of  $\Psi$  where  $K_I$  is dominant, the three theories predict similar results. In the present study, the maximum tangential stress theory is used as a starting point to evaluate the direction of crack growth.

The theory in its original form used only the singular stress fields near the crack tip to evaluate the maximum tangential stress [41]. Subsequent studies [145, 46] suggested that the non-singular stress fields can have a significant effect on crack growth direction and crack path stability. Recent studies [152, 72, 103] further indicated that the non-singular stress fields play an important role in predicting crack turning and flapping in fuselage structures.

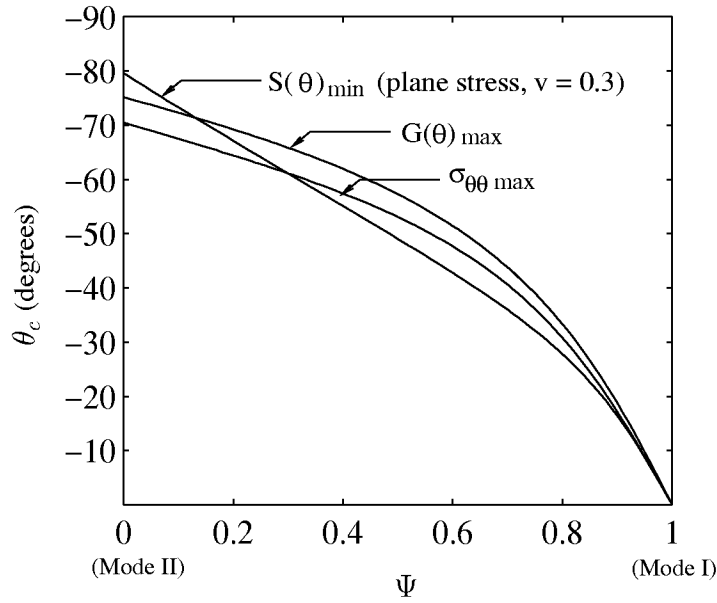


Figure 5.2: Comparison of elastic mixity parameters versus predicted crack growth angles.

The maximum tangential stress theory was originally proposed to predict the direction of crack propagation in ideally isotropic brittle material under plane stress or plane strain conditions [41]. It has been extended to include the effects of elastic and fracture anisotropy [14, 12, 21, 104]. Boone *et al.* [12], using the theory proposed by Buczek and Herakovich [14], showed that both elastic and fracture orthotropy can affect the direction of crack propagation, but the fracture orthotropy was found to be a much more dominant factor. Chen *et al.* [21] found that the fracture orthotropy has a strong influence on predicted crack trajectories in narrow body fuselages. The theory has recently been extended to include the non-singular stress contributions [104].

All the above theories were developed for two-dimensional, linear elastic fracture mechanics (LEFM) problems. As discussed in Section 1.2.2, for pressurized thin shell structures a geometrically nonlinear analysis is required to capture the crack tip deformations. The fracture parameters developed under the linear elastic framework have been extended to handle geometrically nonlinear problems with finite elastic deformations. Eshelby [43], using the energy-momentum tensor, developed a Lagrangian framework for LEFM problems. The counterpart fracture parameters in the Lagrangian formulation are able to characterize the crack tip fields for deformations of arbitrary magnitude [43, 119, 125].

The maximum tangential stress theory originally developed under small-scale yielding conditions has been extended to the elastic-plastic range. Shih [124] studied mixed-mode, plane strain problems using the deformation plasticity and near-field singularity dominated by Hutchinson-Rice-Rosengren (HRR) fields [60, 120,

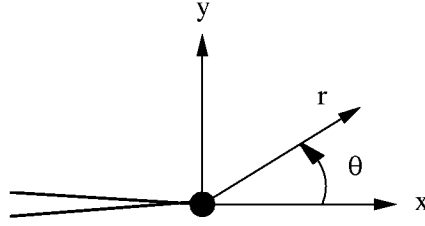


Figure 5.3: Local crack tip coordinates.

59]. He concluded that the crack propagation angle depends not only on the elastic mixity parameter,  $\Psi$ , but also on the strain hardening exponent of materials. Maccagno and Knott [80] as well as Pawliska *et al.* [100] using Shih's approach, further showed the applicability of the maximum tangential stress criterion for elastic-plastic materials. Recent studies [134, 51, 133] indicated that an additional directional criterion related to *shear type fracture* is needed for Mode-II dominated crack propagation in metals. These authors, however, agreed that the maximum tangential stress criterion suffices for Mode-I dominated crack propagation.

## 5.2 Crack Tip Fields in Two Dimensions and Thin Plates

The crack tip stress and displacement fields in two dimensions [146] as well as in thin plates subjected to bending and twisting [147, 57] are outlined below.

Let  $(x, y)$  be the local Cartesian coordinates and  $(r, \theta)$  be the local polar coordinates centered at the crack tip (Figure 5.3). For two-dimensional elastic crack problems, Williams [146] derived a set of solutions for stresses and displacements that would satisfy equilibrium and compatibility equations in the neighborhood of a crack tip:

$$\sigma_{ij} = \sum_{\lambda=-\infty}^{+\infty} A_{\lambda} r^{\frac{\lambda}{2}} f_{ij}^{\lambda}(\theta) \quad (5.2)$$

$$u_i = \sum_{\lambda=-\infty}^{+\infty} B_{\lambda} r^{\frac{\lambda}{2}+1} g_i^{\lambda}(\theta) \quad (5.3)$$

where  $\frac{\lambda}{2}$  is the eigenvalue of the problem and  $A_{\lambda}$  and  $B_{\lambda}$  are coefficients of expansions.

With the physical argument that the total strain energy should be bounded at the crack tip, stress expansions from Equation (5.2) in terms of the local Cartesian

coordinates are:

$$\begin{aligned}
\sigma_{xx} = & \frac{K_I}{\sqrt{2\pi r}} \cos \frac{\theta}{2} (1 - \sin \frac{\theta}{2} \sin \frac{3\theta}{2}) \\
& + T \\
& + \sum_{n=3}^{\infty} (A_{In} \frac{n}{2}) r^{\frac{1}{2}n-1} \times \left[ \left( 2 + (-1)^n + \frac{1}{2}n \right) \cos(\frac{1}{2}n - 1)\theta \right. \\
& \left. - (\frac{1}{2}n - 1) \cos(\frac{1}{2}n - 3)\theta \right] \\
& + \frac{K_{II}}{\sqrt{2\pi r}} (-\sin \frac{\theta}{2}) (2 + \cos \frac{\theta}{2} \cos \frac{3\theta}{2}) \\
& - \sum_{n=3}^{\infty} (A_{IIn} \frac{n}{2}) r^{\frac{1}{2}n-1} \times \left[ \left( 2 - (-1)^n + \frac{1}{2}n \right) \sin(\frac{1}{2}n - 1)\theta \right. \\
& \left. - (\frac{1}{2}n - 1) \sin(\frac{1}{2}n - 3)\theta \right] \tag{5.4}
\end{aligned}$$

$$\begin{aligned}
\sigma_{yy} = & \frac{K_I}{\sqrt{2\pi r}} \cos \frac{\theta}{2} (1 + \sin \frac{\theta}{2} \sin \frac{3\theta}{2}) \\
& + \sum_{n=3}^{\infty} (A_{In} \frac{n}{2}) r^{\frac{1}{2}n-1} \times \left[ \left( 2 - (-1)^n - \frac{1}{2}n \right) \cos(\frac{1}{2}n - 1)\theta \right. \\
& \left. + (\frac{1}{2}n - 1) \cos(\frac{1}{2}n - 3)\theta \right] \\
& + \frac{K_{II}}{\sqrt{2\pi r}} \sin \frac{\theta}{2} \cos \frac{\theta}{2} \cos \frac{3\theta}{2} \\
& - \sum_{n=3}^{\infty} (A_{IIn} \frac{n}{2}) r^{\frac{1}{2}n-1} \times \left[ \left( 2 + (-1)^n - \frac{1}{2}n \right) \sin(\frac{1}{2}n - 1)\theta \right. \\
& \left. + (\frac{1}{2}n - 1) \sin(\frac{1}{2}n - 3)\theta \right] \tag{5.5}
\end{aligned}$$

$$\begin{aligned}
\sigma_{xy} = & \frac{K_I}{\sqrt{2\pi r}} \sin \frac{\theta}{2} \cos \frac{\theta}{2} \cos \frac{3\theta}{2} \\
& + \sum_{n=3}^{\infty} (A_{In} \frac{n}{2}) r^{\frac{1}{2}n-1} \times \left[ - \left( (-1)^n + \frac{1}{2}n \right) \sin(\frac{1}{2}n - 1)\theta \right. \\
& \left. + (\frac{1}{2}n - 1) \sin(\frac{1}{2}n - 3)\theta \right] \\
& + \frac{K_{II}}{\sqrt{2\pi r}} \cos \frac{\theta}{2} (1 - \sin \frac{\theta}{2} \sin \frac{3\theta}{2}) \\
& - \sum_{n=3}^{\infty} (A_{II n} \frac{n}{2}) r^{\frac{1}{2}n-1} \times \left[ - \left( (-1)^n - \frac{1}{2}n \right) \cos(\frac{1}{2}n - 1)\theta \right. \\
& \left. - (\frac{1}{2}n - 1) \cos(\frac{1}{2}n - 3)\theta \right] \tag{5.6}
\end{aligned}$$

where  $K_I$  and  $K_{II}$  are Mode I and Mode II stress intensity factors,  $T$  is the constant non-singular stress term that appears only in the  $\sigma_{xx}$  component, and  $A_{In}$  and  $A_{II n}$  are Mode I and Mode II coefficients of higher order terms.

Similarly, displacements from Equation (5.3) can be expressed as:

$$\begin{aligned}
u_x = & \frac{K_I}{4G} \sqrt{\frac{r}{2\pi}} \left[ (2\kappa - 1) \cos \frac{\theta}{2} - \cos \frac{3\theta}{2} \right] \\
& + \frac{Tr}{\widetilde{E}} (\cos \theta) \\
& + \sum_{n=3}^{\infty} \frac{(A_{In})}{2G} r^{\frac{n}{2}} \times \left[ \kappa \cos \frac{n\theta}{2} - \frac{n}{2} \cos(\frac{n}{2} - 2)\theta \right. \\
& \left. + \left( \frac{n}{2} + (-1)^n \right) \cos \frac{n\theta}{2} \right] \\
& + \frac{K_{II}}{4G} \sqrt{\frac{r}{2\pi}} \left[ (2\kappa + 3) \sin \frac{\theta}{2} + \sin \frac{3\theta}{2} \right] \\
& - \sum_{n=3}^{\infty} \frac{(A_{II n})}{2G} r^{\frac{n}{2}} \times \left[ \kappa \sin \frac{n\theta}{2} - \frac{n}{2} \sin(\frac{n}{2} - 2)\theta \right. \\
& \left. + \left( \frac{n}{2} + (-1)^n \right) \sin \frac{n\theta}{2} \right] \tag{5.7}
\end{aligned}$$

$$\begin{aligned}
u_y = & \frac{K_I}{4G} \sqrt{\frac{r}{2\pi}} \left[ (2\kappa + 1) \sin \frac{\theta}{2} - \sin \frac{3\theta}{2} \right] \\
& - \tilde{\nu} \frac{Tr}{\tilde{E}} \sin \theta \\
& + \sum_{n=3}^{\infty} \frac{(A_{In})}{2G} r^{\frac{n}{2}} \times \left[ \kappa \sin \frac{n\theta}{2} + \frac{n}{2} \sin\left(\frac{n}{2} - 2\right)\theta \right. \\
& \left. - \left(\frac{n}{2} + (-1)^n\right) \sin \frac{n\theta}{2} \right] \\
& - \frac{K_{II}}{4G} \sqrt{\frac{r}{2\pi}} \left[ (2\kappa - 3) \cos \frac{\theta}{2} + \cos \frac{3\theta}{2} \right] \\
& - \sum_{n=3}^{\infty} \frac{(A_{II n})}{2G} r^{\frac{n}{2}} \times \left[ \kappa \cos \frac{n\theta}{2} - \frac{n}{2} \cos\left(\frac{n}{2} - 2\right)\theta \right. \\
& \left. + \left(\frac{n}{2} + (-1)^n\right) \cos \frac{n\theta}{2} \right] \tag{5.8}
\end{aligned}$$

where  $E$  is the Young's modulus,  $G$  is the elastic shear modulus, and  $\nu$  is the Poisson ratio. For plane stress problems,  $\kappa = (3 - \nu)/(1 + \nu)$ ,  $\tilde{E} = E$ , and  $\tilde{\nu} = \nu$ . For plane strain problems,  $\kappa = (3 - 4\nu)$ ,  $\tilde{E} = E/(1 - \nu^2)$ , and  $\tilde{\nu} = \nu/(1 - \nu)$ .

In addition to the above two-dimensional fields, Williams [147] and Hui and Zehnder [57] further derived an asymptotic field for bending in elastic thin plates. The bending stress and displacement fields near the crack tip in the context of Kirchhoff plate theory are:

$$\begin{aligned}
\begin{pmatrix} \sigma_{rr}^b \\ \sigma_{r\theta}^b \\ \sigma_{\theta\theta}^b \end{pmatrix} = & \frac{k_1}{(3 + \nu)\sqrt{2r}} \frac{z}{2t} \begin{pmatrix} (3 + 5\nu) \cos \frac{\theta}{2} - (7 + \nu) \cos \frac{3\theta}{2} \\ -(1 - \nu) \sin \frac{\theta}{2} + (7 + \nu) \sin \frac{3\theta}{2} \\ (5 + 3\nu) \cos \frac{\theta}{2} + (7 + \nu) \cos \frac{3\theta}{2} \end{pmatrix} \\
& + \frac{k_2}{(3 + \nu)\sqrt{2r}} \frac{z}{2t} \begin{pmatrix} (3 - 5\nu) \sin \frac{\theta}{2} + (5 + 3\nu) \sin \frac{3\theta}{2} \\ -(1 - \nu) \cos \frac{\theta}{2} + (5 + 3\nu) \cos \frac{3\theta}{2} \\ -2(5 + 3\nu) \cos \frac{\theta}{2} \sin \theta \end{pmatrix} \tag{5.9}
\end{aligned}$$

$$\begin{pmatrix} \sigma_{rz}^b \\ \sigma_{\theta z}^b \end{pmatrix} = \frac{(1 - (\frac{2z}{t})^2)}{(3 + \nu)(2r)^{\frac{3}{2}}} \frac{t}{2} \begin{pmatrix} -k_1 \cos \frac{\theta}{2} + k_2 \sin \frac{\theta}{2} \\ -k_1 \sin \frac{\theta}{2} - k_2 \cos \frac{\theta}{2} \end{pmatrix} \tag{5.10}$$

$$\sigma_{zz}^b = 0$$

$$w^b = \frac{(2r)^{3/2}}{2Gt(3 + \nu)} \left( k_1 \left[ \frac{1}{3} \frac{(7 + \nu)}{(1 - \nu)} \cos \frac{3\theta}{2} - \cos \frac{\theta}{2} \right] + k_2 \left[ \frac{1}{3} \frac{(5 + 3\nu)}{(1 - \nu)} \sin \frac{3\theta}{2} - \sin \frac{\theta}{2} \right] \right) \tag{5.11}$$

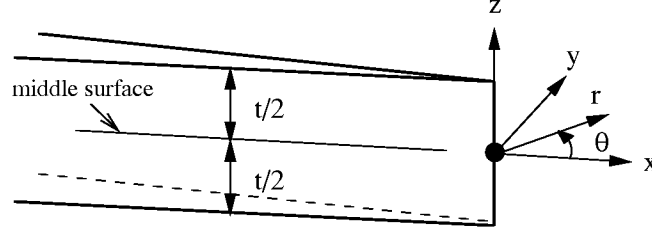


Figure 5.4: Local crack tip coordinates for a through crack in a plate (after [57]).

$$\begin{pmatrix} u^b \\ v^b \end{pmatrix} = -z \begin{pmatrix} \frac{\partial w^b}{\partial x} \\ \frac{\partial w^b}{\partial y} \end{pmatrix} \quad (5.12)$$

where  $(r, \theta, z)$  are the polar cylindrical coordinates centered at the crack tip (Figure 5.4),  $t$  is the plate thickness, and  $k_1, k_2$  are the Kirchhoff theory stress intensity factors.

For elastic curvilinear crack growth in thin shell structures, the local crack tip fields are assumed to be sufficiently characterized by the two-dimensional plane stress and the Kirchhoff plate fields [57, 108]. For points on a shell midsurface (*i.e.*,  $z = 0$ ),  $k_1$  and  $k_2$  stress intensity factors make no contributions to the displacement and stress fields. We thus will directly extend the two-dimensional crack growth direction criterion to handle thin shell LEFM problems.

### 5.3 Crack Growth Direction Criterion Based on Maximum Tangential Stress Theory

In their work on predicting the direction of crack growth, Erdogan and Sih stated [41]:

“... (There are) two commonly recognized hypotheses for the extension of cracks in a brittle material under slowly applied plane loads:

- (a) The crack extension starts at its tip in radial direction.
- (b) The crack extension starts in the plane perpendicular to the direction of greatest tension.

These hypotheses imply that the crack will start to grow from the tip in the direction along which the tangential stress  $\sigma_{\theta\theta}$ , is maximum ...”

The tangential stress  $\sigma_{\theta\theta}$  near the crack tip can be derived from the local Cartesian stresses (Equations (5.4), (5.5), and (5.6)) with coordinate transformations. For two dimensional mixed-mode problems,  $\sigma_{\theta\theta}$  up to the order of the  $T$ -stress term is:

$$\sigma_{\theta\theta} = \frac{1}{\sqrt{2\pi r}} \cos \frac{\theta}{2} \left( K_I \cos^2 \frac{\theta}{2} - \frac{3}{2} K_{II} \sin \theta \right) + T \sin^2 \theta \quad (5.13)$$



Based on the hypotheses that crack extension would take place in the direction along which  $\sigma_{\theta\theta}$  possesses a maximum value, we have:

$$\frac{\partial \sigma_{\theta\theta}}{\partial \theta} = 0 \quad \text{and} \quad \frac{\partial^2 \sigma_{\theta\theta}}{\partial \theta^2} < 0 \quad (5.14)$$

Taking the derivative of  $\sigma_{\theta\theta}$  with respect to  $\theta$ , we have:

$$\frac{\partial \sigma_{\theta\theta}}{\partial \theta} = \frac{1}{\sqrt{2\pi r}} \left( -\frac{3}{4} \cos \frac{\theta}{2} \right) (K_I \sin \theta + K_{II} (3 \cos \theta - 1)) + 2 T \sin \theta \cos \theta \quad (5.15)$$

Taking the second derivative, we have:

$$\frac{\partial^2 \sigma_{\theta\theta}}{\partial \theta^2} = \frac{1}{\sqrt{2\pi r}} \left( -\frac{3}{8} (3 \cos \theta - 1) \right) \left( K_I \cos \frac{\theta}{2} - K_{II} \sin \frac{\theta}{2} \right) + 2 T \cos 2\theta \quad (5.16)$$

Thus,  $\sigma_{\theta\theta}$  is a relative maximum if the following conditions are satisfied:

$$\begin{cases} \frac{1}{\sqrt{2\pi r_c}} \left( -\frac{3}{4} \cos \frac{\theta_c}{2} \right) (K_I \sin \theta_c + K_{II} (3 \cos \theta_c - 1)) + 2 T \sin \theta_c \cos \theta_c = 0 \\ \frac{1}{\sqrt{2\pi r_c}} \left( -\frac{3}{8} (3 \cos \theta_c - 1) \right) (K_I \cos \frac{\theta_c}{2} - K_{II} \sin \frac{\theta_c}{2}) + 2 T \cos 2\theta_c < 0 \end{cases} \quad (5.17)$$

where  $r_c$  is a critical distance away from the crack tip and  $\theta_c$  is the corresponding crack propagation angle. We note that this directional criterion is the same as the one proposed by Williams and Ewing [145] and later corrected by Finnie and Saith [46]. The above equation reduces to the classical Erdogan and Sih directional criterion [41] if  $T = 0$  or  $r_c = 0$ , *i.e.*,

$$K_I \sin \theta_c + K_{II} (3 \cos \theta_c - 1) = 0 \quad (5.18)$$

By comparing Equation (5.17) with Equation (5.18), one finds that a length parameter,  $r_c$ , is needed to incorporate  $T$ -stress into the crack growth directional criterion. We will further discuss the physical meaning of  $r_c$  in Section 5.3.3.

### 5.3.1 Crack Path Stability under Pure Mode I Conditions

Using Equation (5.17), crack path instability in pure Mode I conditions is predicted for certain circumstances under positive  $T$ -stress. For pure Mode I problems where  $K_{II} = 0$ , we have closed-form solutions for Equation (5.17) [152]:

$$\theta_c = 0 \quad (5.19)$$

or

$$\theta_c = 2 \cos^{-1} \left[ s_F \pm \sqrt{\frac{1}{2} + s_F^2} \right] \quad (5.20)$$

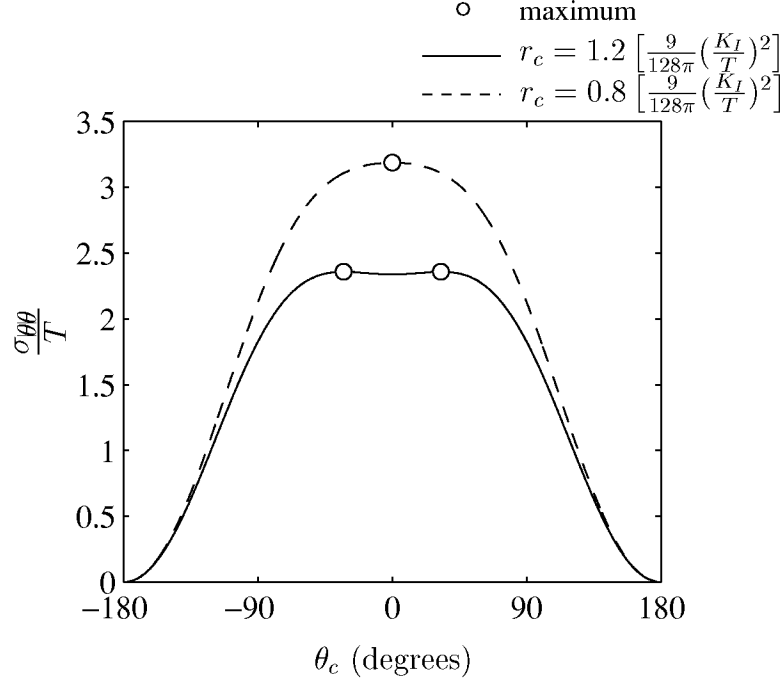


Figure 5.5: The tangential stress  $\sigma_{\theta\theta}$  distributions for different values of critical distance  $r_c$  under pure Mode I conditions ( $T > 0$ ).

in which  $s_F \equiv (3K_I)/(32T\sqrt{2\pi r_c})$ . For  $\theta_c = 0$ , the second derivative of  $\sigma_{\theta\theta}$  with respect to  $\theta$  is:

$$\frac{\partial^2 \sigma_{\theta\theta}}{\partial \theta^2} = -\frac{3}{4} \frac{K_I}{\sqrt{2\pi r_c}} + 2T \quad (5.21)$$

Thus, under a negative  $T$ -stress environment,  $\partial^2 \sigma_{\theta\theta} / \partial \theta^2$  is always smaller than zero. This implies that  $\sigma_{\theta\theta}$  at  $\theta_c = 0$  is a relative maximum and the crack will grow in a straight (*i.e.*, *self-similar*) manner. For positive  $T$ -stress, the crack will propagate in a *self-similar* fashion only if:

$$r_c < \frac{9}{128\pi} \left( \frac{K_I}{T} \right)^2 \quad (5.22)$$

For  $r_c > (9K_I^2)/(128\pi T^2)$ ,  $\sigma_{\theta\theta}$  at  $\theta_c = 0$  is a relative minimum and a crack will grow in the direction predicted by Equation (5.20). Figure 5.5 illustrates the  $\sigma_{\theta\theta}$  distribution for different values of  $r_c$  and the relative maximum and minimum.

### 5.3.2 Determine Crack Propagation Angle under General Mixed-Mode Problems

For general two-dimensional mixed-mode problems, the crack propagation angle can be solved from Equation (5.17) for given  $r_c$ ,  $K_I$ ,  $K_{II}$ , and  $T$ . Figure 5.6 plots

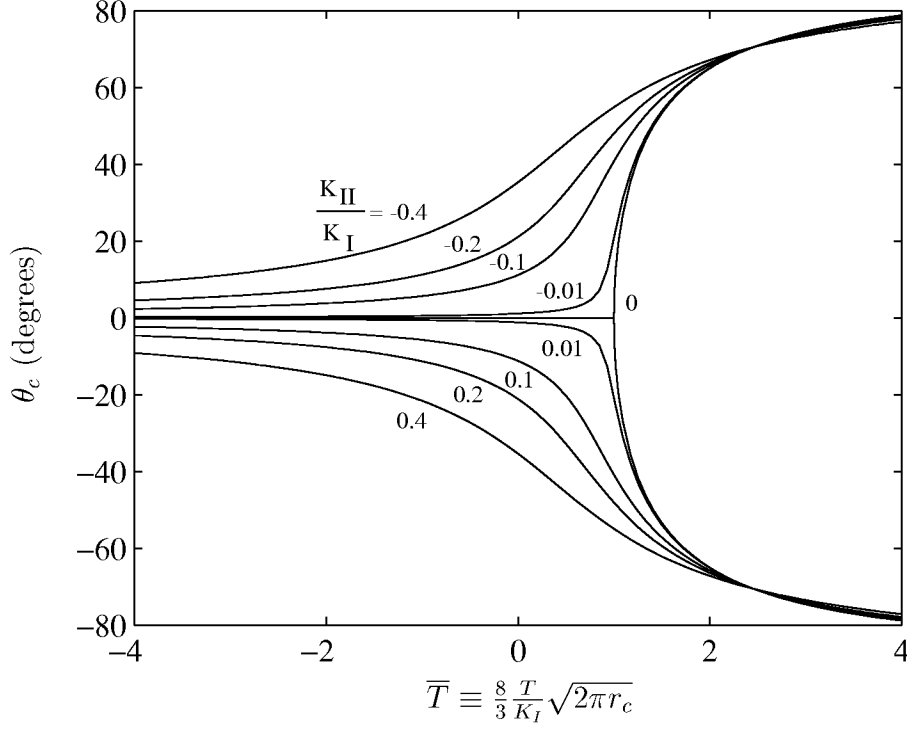


Figure 5.6: Predicted propagation angle from maximum tangential stress theory (Equation (5.17)).

the predicted propagation angle  $\theta_c$  versus a dimensionless parameter  $\bar{T}$  [104]:

$$\bar{T} \equiv \frac{8}{3} \frac{T}{K_I} \sqrt{2\pi r_c} \quad (5.23)$$

for various ratios of  $K_{II}/K_I$ .

The parameter  $r_c$  is assumed to be a material constant and will be further discussed in next section.  $K_I$  and  $K_{II}$  for two-dimensional problems can be accurately computed from the path independent  $M$ -integral [149] or from symmetric and anti-symmetric parts of the  $J$ -integral [15]. For thin shell problems, membrane and bending stress intensity factors can be obtained from an extension of the modified crack closure integral method [106, 142]. How to obtain an accurate  $T$ -stress numerically is not obvious from the literature. We will further discuss this issue in Chapter 6.

It is of historical interest to consider a specific angled crack problem shown in Figure 5.7. For this special case, we have [41, 46]:

$$K_I = \sigma \sqrt{\pi a} \sin^2 \beta \quad K_{II} = \sigma \sqrt{\pi a} \sin \beta \cos \beta \quad T = \sigma (\cos^2 \beta - \sin^2 \beta)$$

The predicted propagation angle  $\theta_c$  can be solved by applying Equation (5.17). In Figure 5.7, the predicted propagation angles  $\theta_c$  from Equation (5.18) (or from Erdogan and Sih [41]) are compared with those of  $\sqrt{2r_c/a} = 0.1$  from Equation (5.17) (or from Finnie and Saith [46]). Some results are observed:

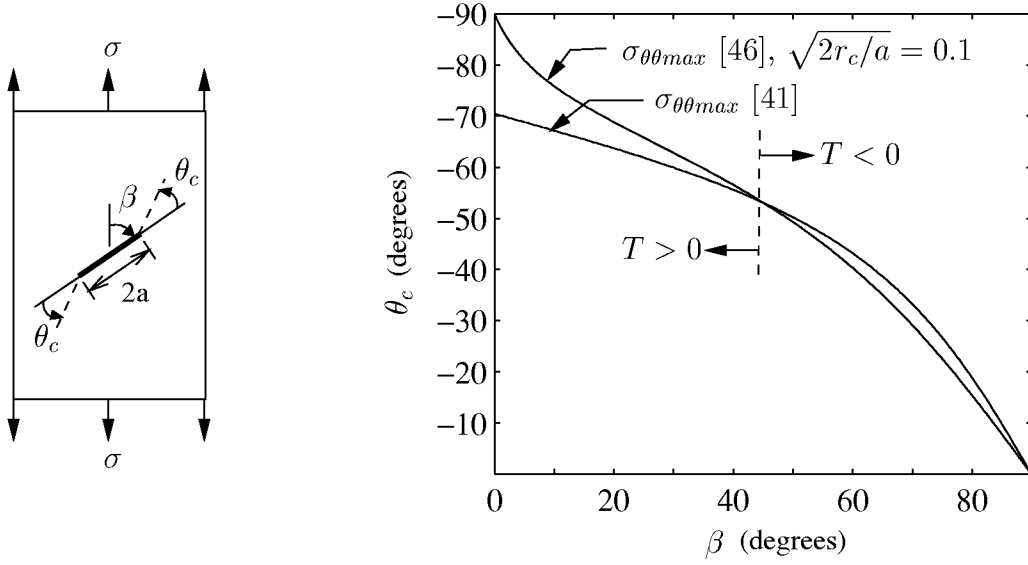


Figure 5.7: Predicted propagation angle for the angled crack problem.

- Two curves intersect at  $\beta = 45^\circ$  in which  $T = 0$ .
- The incorporation of the  $T$ -stress predicts a larger propagation angle under positive  $T$ -stress conditions. It predicts a smaller angle under negative  $T$ -stress conditions.

### 5.3.3 Discussion: The Critical Distance $r_c$

As shown in Figures 5.5 and 5.6, the critical distance ahead of the crack tip,  $r_c$ , plays an important role in predicting crack path stability and crack growth direction. Earlier studies by Williams and Ewing [145] and Finnie and Saith [46] assumed that  $r_c/a$  is a constant value (*cf.*  $2r_c/a = 0.1$  in Figure 5.7). Streit and Finnie [132] further postulated that  $r_c$  is a critical distance in front of the crack tip where fracture would occur. A photoelastic and experimental study of Mode I crack extension was conducted. The ratio  $K_I/T$  was determined by analyzing the isochromatic-fringe geometry in the photoelastic experiments. The critical distance  $r_c$  was determined by simply observing the onset of crack turning where  $r_c = (9K_I^2)/(128\pi T^2)$  at this instance. They concluded that for 7075-T651 aluminum plate,  $r_c = 0.005$  inch for side-grooved specimens and  $r_c = 0.01$  inch for the ungrooved, L-T specimens. These values seem to be too small in comparing with subsequent experimental studies [110, 103].

Ramulu and Kobayashi [110] extended the method of Streit and Finnie [132] and measured  $r_c$  for a dynamically growing crack. They observed that  $r_c$  is a constant value for specimens under various mixed-mode conditions. Based on the dynamic photoelastic experiments, they concluded that  $r_c$  is about 0.05 inch for

Homalite-100. Recent studies by Kobayashi and his associates [71, 72, 73] further estimated that  $r_c$  is about 0.04–0.06 inch for 7075-T6 and 2024-T3 thin-sheet fracture specimens.

Pettit *et al.* [103] determined the magnitude of  $r_c$  by analyzing crack turning in 2024-T3, double cantilever beam (DCB) specimens. They estimated that the value of  $r_c$  is about 0.05 inch for stable tearing under a monotonically increasing load. For slow fatigue crack growth under a low stress level of cyclic loading,  $r_c$  is assumed to be negligible. Recent ongoing research [102] further suggested that the magnitude of  $r_c$  for stable tearing in 2024-T3 specimens is about 0.04–0.09 inch.

In this study, we simply assume that  $r_c$  is a material constant that can be determined from fracture coupon tests. The effect of  $r_c$  on crack trajectory prediction will be extensively examined in Chapter 7.

### 5.3.4 Anisotropic Problems

Material grain structure variations and other micro-structural factors from different forms of material processing can influence fracture toughness variation with direction and, therefore, the crack growth trajectory. Taking a rolled sheet made of 2024-T3 aluminum alloy for example, the direction perpendicular to the rolling direction could have a 5 to 20% higher toughness than that of the rolling direction [47, 44, 99].

In general, crack propagation in anisotropic media is considerably more complicated than the isotropic case [12]. In the present work, a simple extrapolation of the maximum tangential stress theory to materials with orthotropic toughness proposed by Buczek and Herakovich [14] is used. The tangential stress is normalized with respect to the directional strength of the material. Crack propagation is assumed to be in the direction of maximum normalized stress, such that:

$$\text{Maximum} \left[ \frac{\sigma_{\theta\theta}(K_I, K_{II}, T, r_c, \theta)}{K_c(\alpha)} \right] = \left( \frac{\sigma_{\theta\theta}}{K_c} \right)_{critical} \quad \text{at} \quad \theta = \theta_c \quad (5.24)$$

where  $\alpha$  is the angle characterizing the material grain orientation,  $K_c(\alpha)$  is the strength parameter characterizing the material fracture resistance, and  $\theta_c$  is the angle of impending crack propagation.

A simple elliptical function is used in this study to characterize the anisotropic fracture toughness,  $K_c(\alpha)$  [14, 68]. The equation of the ellipse with fracture toughness  $K_c(0^\circ)$  along the material longitudinal ( $\tilde{x}$ ) direction and  $K_c(90^\circ)$  along the transverse ( $\tilde{y}$ ) direction is (Figure 5.8):

$$\frac{\tilde{x}^2}{[K_c(0^\circ)]^2} + \frac{\tilde{y}^2}{[K_c(90^\circ)]^2} = 1 \quad (5.25)$$

Substituting  $\tilde{x} = K_c(\alpha) \cos \alpha$  and  $\tilde{y} = K_c(\alpha) \sin \alpha$  into Equation (5.25), we have:

$$K_c(\alpha)^2 \left( \frac{\cos^2 \alpha}{K_c(0^\circ)^2} + \frac{\sin^2 \alpha}{K_c(90^\circ)^2} \right) = 1 \quad (5.26)$$

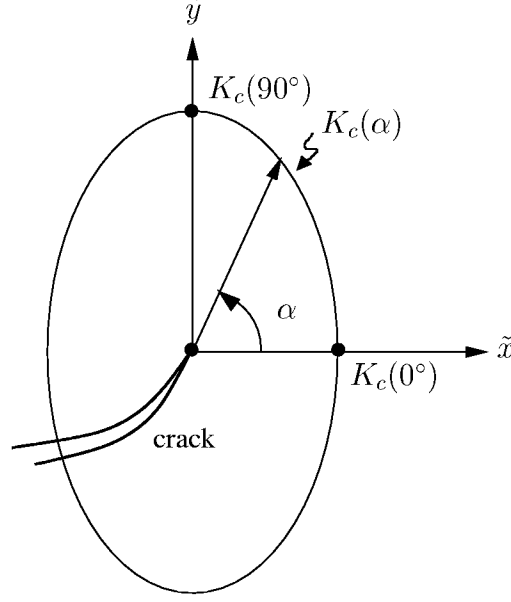


Figure 5.8: Elliptical representation of anisotropic fracture toughness.

Thus, the anisotropic fracture toughness  $K_c(\alpha)$  can be expressed as [104]:

$$K_c(\alpha) = \sqrt{\frac{1}{\cos^2 \alpha + (1/\bar{K}_m)^2 \sin^2 \alpha}} \quad (5.27)$$

where  $\bar{K}_m$  is the fracture orthotropy ratio defined as  $\bar{K}_m \equiv K_c(90^\circ)/K_c(0^\circ)$ .

Both the fracture orthotropy ratio,  $\bar{K}_m$ , and the material orientation angle,  $\alpha$ , can affect the predicted angle of impending fracture propagation,  $\theta_c$ , as demonstrated in Figure 5.9 and 5.10.

We note that Equation (5.26) can be generalized to the  $n$ -th order:

$$K_c(\alpha)^n \left( \frac{\cos^2 \alpha}{K_c(0^\circ)^n} + \frac{\sin^2 \alpha}{K_c(90^\circ)^n} \right) = 1 \quad (5.28)$$

and  $n = -1$  was used in [14, 12].

## 5.4 Discussion: Crack Growth Direction Criterion for Geometrically and Materially Nonlinear Problems

Possible extensions of the above crack growth directional criteria developed under the LEFM framework to handle geometrically and materially nonlinear shell problems are discussed below.

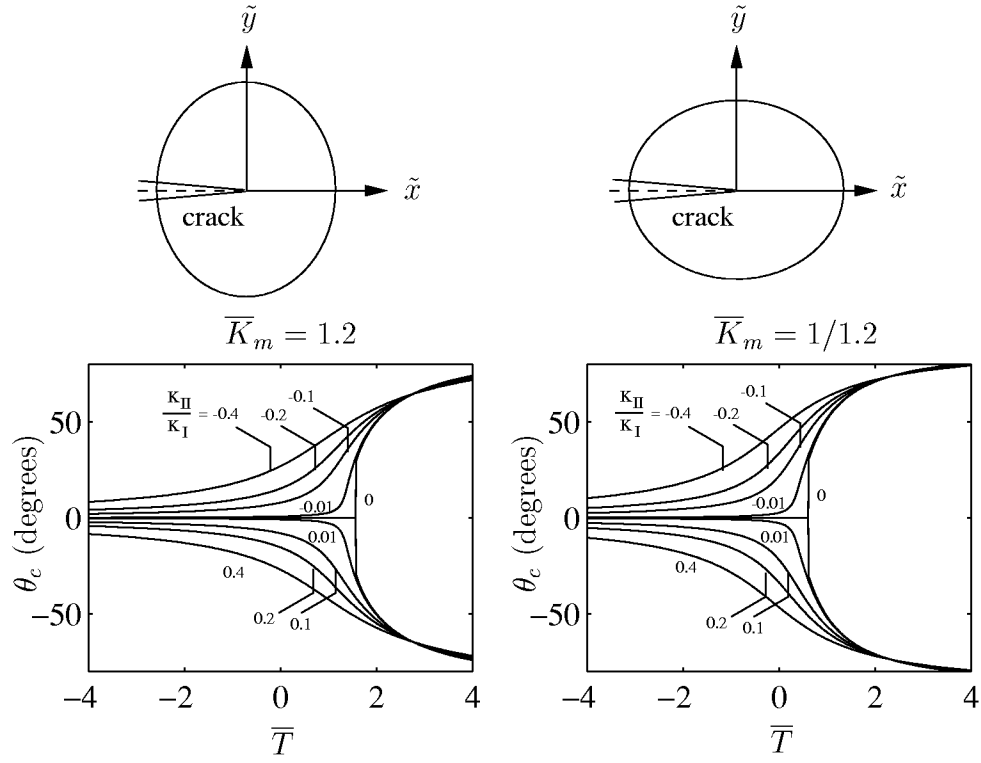


Figure 5.9: Effects of fracture orthotropy ratio on predicted propagation angle.

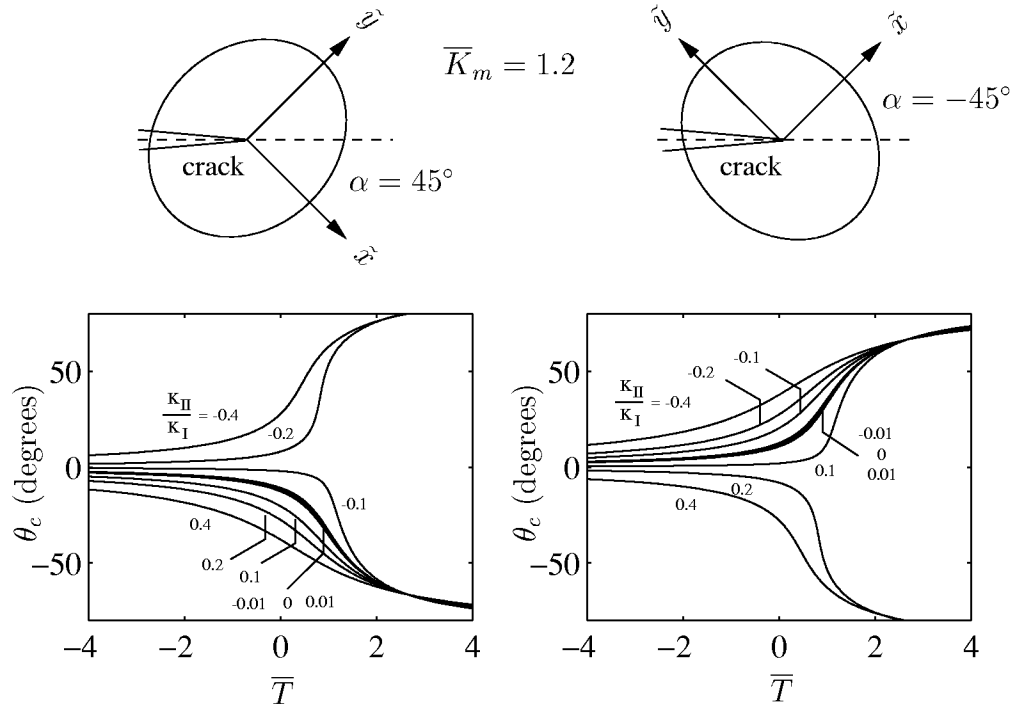


Figure 5.10: Effects of material orientation on predicted propagation angle.

### 5.4.1 Geometrically Nonlinear Problems

To compute stress intensity factors and  $T$ -stress with elastic deformations of arbitrary magnitude, one can simply evaluate the fracture parameters based on the computed quantities in the current deformed equilibrium configuration. This so-called Eulerian approach together with the modified crack closure integral method has been used successfully to compute the membrane and bending stress intensity factors for geometrically nonlinear shell problems [106, 142].

It is often desirable to use the path independent integral to evaluate the fracture parameters. However, the integral is difficult to be directly applied in the Eulerian framework [43]. Taking the deformed structure shown in Figure 4.30 for example, it is conceptually difficult to evaluate a rigorous path independent integral at the deformed configuration with the occurrence of severe bulging.

An alternative way is to evaluate the path independent integral in the Lagrangian framework [43, 70]. The derivations rely on finding the counterparts of conservative (*i.e.*, path independent) integrals, well-defined under elastic states with infinitesimal deformations, in the context of finite elastic deformations. The fracture parameters (for example, stress intensity factors) are then related to these conservative integrals.

The well known conservative  $J$ -integral in two dimensions, for example, is given by:

$$J = \oint_{\Gamma} \left[ W \delta_{xj} - \sigma_{ij} \frac{\partial u_i}{\partial x} \right] n_j d, \quad (5.29)$$

where  $\Gamma$  is an arbitrary counter-clockwise contour around the tip of a crack,  $W$  is the strain energy density,  $\delta_{xj}$  is the Kronecker delta,  $\sigma_{ij}$  are components of the Cauchy stress tensor,  $u_i$  are components of the displacement vector, and  $n_j$  are components of the normal vector along the contour  $\Gamma$ .

The counterpart of the  $J$ -integral under finite elastic deformations can be derived in a relatively straightforward manner in Lagrangian coordinates,  $\mathbf{X}$ . With re-interpretation of the field quantities with reference to the undeformed configuration, the  $J$ -integral for geometrically nonlinear problems can be expressed as [43, 70]:

$$J_{GN} = \oint_C \left[ W \delta_{Xj} - p_{ij} \frac{\partial u_i}{\partial X} \right] N_j dC \quad (5.30)$$

where  $C$  and  $N_j$  are evaluated in the undeformed configuration,  $W$  is interpreted as the strain energy per unit undeformed volume, and  $p_{ij}$  are components of the nominal stress tensor (transpose of the first Piola-Kirchhoff stress tensor).

The  $J$  in linearized and  $J_{GN}$  in finite elastic states both characterize the energy release per unit crack advance [43]. Under Mode-I, plane stress conditions, we thus have:

$$K_I = \sqrt{EJ} \quad (5.31)$$



and equivalently,

$$(K_I)_{GN} = \sqrt{EJ_{GN}} \quad (5.32)$$

Similarly, other fracture parameters can be related to their finite deformation counterparts. As a result, crack propagation and direction criteria derived under LEFM can be extended to handle geometrically nonlinear problems.

However, we note that the Lagrangian counterparts of conservative integrals to characterize the stress intensity factors and  $T$ -stress for geometrically nonlinear shell problems are yet to be derived. In this study, we will simply use the modified crack closure integral method to compute the membrane and bending stress intensity factors [106, 142] and the displacement correlation method to evaluate the  $T$ -stress for geometrically nonlinear shell problems [69, 134, 104].

### 5.4.2 Materially Nonlinear Problems

The crack growth directional criteria developed above are strictly valid only for small-scale yielding problems. The criteria may be sufficient for curvilinear crack growth under fatigue loading (*cf.* Section 1.2.2). For stable crack growth, directional criteria need to be extended to the elastic-plastic range.

In an early attempt, Shih [124], using HRR fields, extended the maximum tangential stress theory to the elastic-plastic range under plane strain conditions. Figure 5.11 shows the predicted crack propagation angle,  $\theta_c$ , versus the elastic load mixity,  $\Psi$  (Equation (5.1)). The results indicate that the crack propagation angle,  $\theta_c$ , depends not only on the elastic mixity parameter,  $\Psi$ , but also on the strain hardening exponent of materials,  $n$ .

For  $n = 1$  (*i.e.*, linear elastic material), the criterion reduces to the maximum tangential stress theory of Erdogan and Sih [41]. Thus, the theory will not capture the crack path instability under the pure Mode-I conditions caused by  $T$ -stress. And more importantly, the theory is based on the HRR fields. The fields are no longer valid to characterize the elastic-plastic crack tip fields after a sufficient amount of stable crack growth. These two main disadvantages prohibit direct application of the above theory to predict the direction of stable crack growth in fuselage structures.

Recently, a simple crack growth directional criterion based on the crack tip opening displacement (CTOD) concept has been proposed by Sutton *et al.* [133]. The criterion is motivated by the laboratory observations of recent Arcan specimen tests conducted by Amstutz *et al.* [1, 32]. The test results show that there is a sharp transition of crack growth behavior from predominantly Mode I type to Mode II type fracture for 2024-T3 thin sheet materials. Since the crack growth direction prediction based on the maximum tangential stress theory is mainly for Mode I dominated fracture, Sutton *et al.* [133] proposed a general CTOD-based criterion to overcome this disadvantage.

The CTOD-based crack growth directional criterion considers a *kinked* crack departing from a *main* crack as shown in Figure 5.12. The criterion postulates

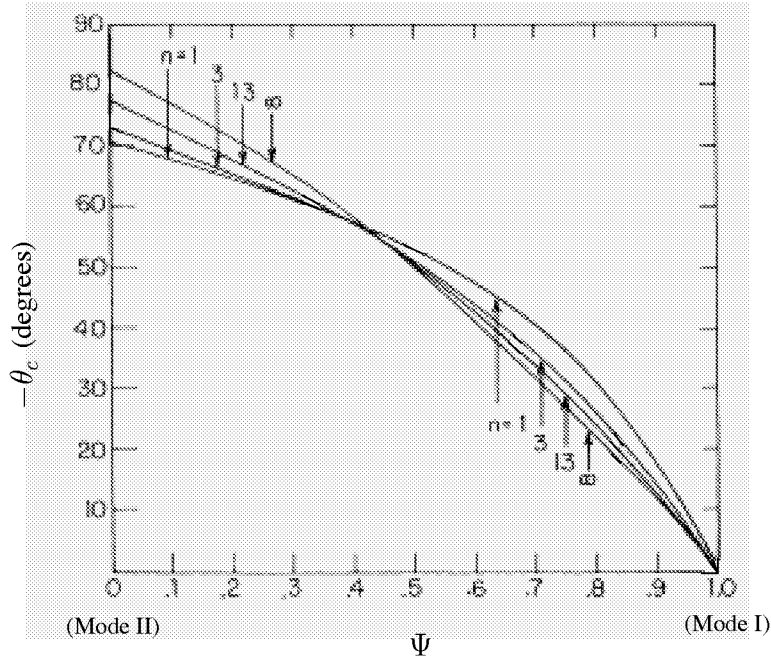


Figure 5.11: Comparison of elastic mixity parameters versus predicted crack growth angles for different strain hardening exponents (after [124]).

that crack growth direction of a *kinked* crack would likely follow a path that gives the maximum CTOD of the kinked crack (*i.e.*,  $\delta$ ). The following steps outline the procedure to incorporate the directional criterion into the elastic-plastic crack advancement controlled by the CTOA criterion [133]:

- step 1** Apply the load monotonically until  $D$  (or CTOD) at a specified distance  $L$  behind the main crack tip, or equivalently CTOA, reaches its critical value.
- step 2** Release the main crack tip node and extend the crack along every possible ray from the crack tip.
- step 3** Compute  $\delta$  of all possible kinked cracks.
- step 4** Determine the crack propagation angle  $\theta_c$  by finding the path that gives the maximum  $\delta$ .
- step 5** Continue stable crack growth simulation controlled by the CTOA criterion.

The CTOD-based directional criterion predicts both Mode I and Mode II type crack growth observed in Arcan specimens [133]. The directional criterion, however, suffers from its computational inefficiency since  $\delta$  must be evaluated for a large number of rays to determine the propagation angle.

To overcome the drawback, Sutton [133] further assumed that there exists a unique relationship between  $\delta$  (CTOD of the kinked crack) and  $D$  (CTOD of the

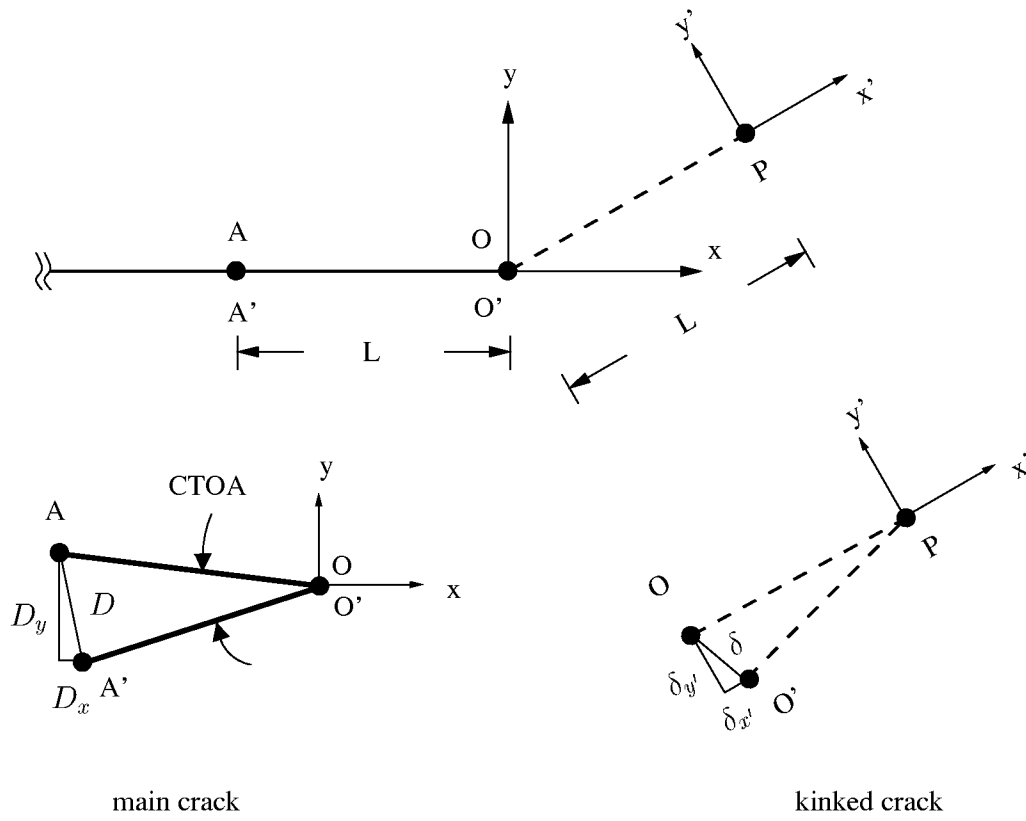


Figure 5.12: Illustration of main and kinked crack relationship for CTOD-based crack growth directional criterion.

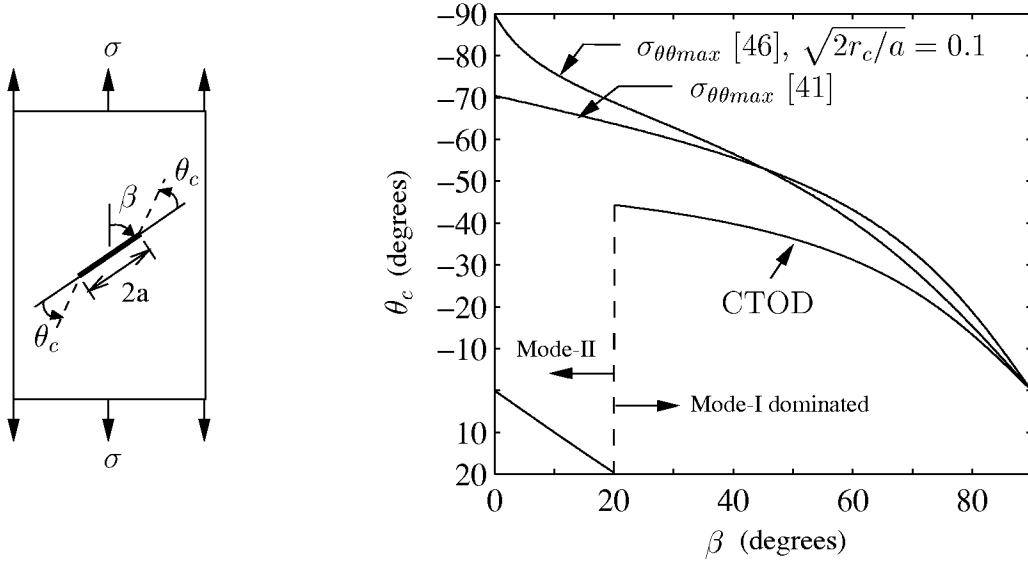


Figure 5.13: Comparison of predicted propagation angles for the angled crack problem.

main crack). By defining a local mixity  $\alpha = D_y/D_x$  of the main crack, an empirical equation to predict the crack propagation angle,  $\theta_c$ , was found:

$$\theta_c = \begin{cases} a_1 \tan^{-1}(b_1 \alpha) & \text{if } \alpha < \alpha_c \\ a_2 \cos(b_2 \alpha) \frac{\alpha}{|\alpha_c|} & \text{if } \alpha > \alpha_c \end{cases} \quad (5.33)$$

where  $\alpha_c$  is the critical local mode mixity for the transition between Mode I and Mode II type fracture and  $a_1$ ,  $b_1$ ,  $a_2$ , and  $b_2$  are the curve fitting parameters based on fracture test data. A set of parameters,  $\alpha_c = 70^\circ$ ,  $a_1 = -36.5$ ,  $b_1 = 2.2$ ,  $a_2 = 57.3$ , and  $b_2 = 1.0$  were obtained from the test data of 0.09 inch thick Arcan specimens made of 2024-T3 aluminum.

Equation (5.33) and the fitting parameters based on Arcan test data were argued to be material constants and to be applicable to other geometries with the same thickness [133]. We, however, found that this assertion may not hold for all cases. Taking the angled crack problems under LEFM for example, a substantial difference as shown in Figure 5.13 is observed between the predicted angles by the maximum tangential stress theory and those from Equation (5.33). The difference observed in Mode I dominated fracture is thought to be related to: (1) built-in orthotropy and (2) widespread plasticity in Arcan specimens. Further investigation is needed to fully justify the observation and assess the geometry independence of Equation (5.33).

Neither the HRR-type extension of the maximum tangential stress theory nor the CTOD-based directional criterion seems to be sufficient to fully characterize the direction of elastic-plastic crack growth. In this study, we will simply apply the LEFM approach to predict the direction of elastic-plastic crack growth.

## 5.5 Summary

In this chapter, theories for curvilinear crack growth in planar and thin shell structures were discussed. A well known crack growth directional criterion based on the maximum tangential stress theory was examined. Singular as well as non-singular constant stress (or  $T$ -stress) fields were included in evaluating the stress states near the crack tip.

Equation (5.17) described the predicted impending propagation angle based on the maximum tangential stress theory with the  $T$ -stress effect. Its numerical outcome on crack path instability and crack growth direction was discussed in Sections 5.3.1 and 5.3.2. This criterion will be used in Chapter 7 to predict the propagation angle for isotropic mixed-mode problems.

In Section 5.3.4, the directional theory was further extended to include the effect of material anisotropy. A simple elliptical function was used to characterize the anisotropic fracture resistance in different material orientations. The predicted propagation angle incorporating the  $T$ -stress and fracture toughness orthotropy effect was described symbolically in Equation (5.24). The effect of fracture toughness orthotropy ratio and the material orientation angle on the predicted propagation angle was shown in Figures 5.9 and 5.10. This directional criterion will be used in Chapter 7 to predict the propagation angle for orthotropic mixed-mode problems.

We then discussed possible extensions of the above directional criteria to handle both geometrically and materially nonlinear problems. For elastic deformations of arbitrary magnitude, one can evaluate the stress intensity factors and  $T$ -stress based on either the Eulerian or Lagrangian formulation. The latter is conceptually simple to be used with the powerful path independent integral. However, the Lagrangian counterparts of conservative integrals to characterize the stress intensity factors and  $T$ -stress for geometrically nonlinear shells are yet to be derived. In this study, the modified crack closure integral method and the displacement correlation method will be used to evaluate the stress intensity factors and  $T$ -stress in thin shells, respectively.

The possible extension of the maximum tangential stress criterion to predict the propagation direction of elastic-plastic crack growth was commented and critiqued. A new CTOD-based direction criterion was also examined. We concluded that neither of them seems to be sufficient to fully characterize the direction of elastic-plastic crack growth. Thus, in this study we will simply apply the LEFM approach (Equations (5.17) and (5.24)) to predict the elastic-plastic crack growth direction.

# Chapter 6

## Numerical Evaluation of $T$ -Stress

In this chapter, numerical methods for  $T$ -stress evaluation are discussed. Among all the possible methods that can be used to compute  $T$ -stress, we focus on the path independent integral method because its inherent nature allows us to evaluate the desired value in a far-field region away from the crack tip where numerical accuracy is greater. We will first put the FRANC3D/STAGS program aside and use a powerful two-dimensional hp-version finite element code [74] to fully quantify and assess the accuracy of computed  $T$ -stress using the path independent integral method. We will then discuss applicability of the FRANC3D/STAGS program in evaluating  $T$ -stress for two-dimensional as well as thin-shell problems.

### 6.1 Introduction

The second term of the elastic asymptotic stress series near a crack tip [146], often called  $T$ -stress, is known to have significant influence on crack growth direction and crack path stability [46, 103, 26]. In addition the  $T$ -stress is also known to have a strong influence on crack-tip constraint [38, 98]. To obtain an accurate  $T$ -stress for complex geometries subjected to arbitrary loading thus becomes an important task for fracture analysis assessment.

Several numerical methods have been used to evaluate the  $T$ -stress [76, 77, 67, 123, 129]. An earlier study by Larsson and Carlsson [76] determined the  $T$ -term from two finite element solutions, one with a  $K$ -field and the other with actual loading and geometry configurations. Leever and Radon [77] computed the  $T$ -stress by incorporating the eigenfunctions from Williams [146] in a variational formulation. Sham [123] used second order weight functions through a work-conjugate integral to calculate the  $T$ -term.

To compute  $T$ -stress in conjunction with finite element analyses, a path independent integral similar to the  $J$ -integral [42, 114] for stress intensity factors is highly desirable. Cardew *et al.* [16] and Kfoury [67] presented a novel  $J$ -integral type of path independent integral for computing the  $T$ -term from finite element analyses. Recently, another type of path independent integral for  $T$ -stress compu-

tation based on the Betti-Rayleigh reciprocal theorem has been proposed [129, 151]. Due to its simplicity, the Betti-Rayleigh reciprocal type of conservative integral has been widely used to solve crack and notch problems for homogeneous as well as bimaterial bodies [131, 127, 8]. As will be shown in this study, these two path independent integrals are analytically equivalent.

To our best knowledge, none of the previous studies has fully addressed the accuracy of numerical  $T$ -stress computations. Published values vary between three and five percent for identical loading and geometry configurations and the error for the computed  $T$ -stress is generally unknown. It is well known that to increase the accuracy of a finite-element computation, either the mesh has to be refined (h-version) or the polynomial degrees of the shape functions have to be increased (p-version). A combination of both strategies, referred to as the hp-version of the finite element method, is known to show exponential rates of convergence in energy norm even if the problem has singularities [6]. In our contribution we will show that path independent integrals, in conjunction with hierarchical, p- and hp-version finite element methods [141], provide a powerful tool to obtain highly accurate numerical results for  $T$ -stress. Using a novel error estimator for the  $T$ -stress, the accuracy of the computation is quantified and assessed.

### 6.1.1 Outline for Numerical Assessment of $T$ -stress Computation Using a p-version Finite Element Method

The derivations of path independent integrals for  $T$ -stress are studied in Section 6.2. Finite element implementations of equivalent domain integrals in conjunction with the hierarchical p-version finite element method are discussed in Section 6.3. To quantify the error in computing  $T$ -stress using the path independent integrals, an error estimator is proposed. Using a highly accurate hp-version finite element code [74] a benchmark example with various  $K_I$  and  $T$  imposed boundary conditions is studied in Section 6.4 with the goal being to assess the accuracy of the numerical computation of  $T$ -stress. We then compute values of  $T$ -stress for various well known fracture specimens and compare our results with values from the literature.

## 6.2 Path Independent Integral For $T$ -Stress Computation

Two types of path independent integrals for  $T$ -stress evaluation have recently been proposed. One is based on the Betti-Rayleigh reciprocal theorem [129, 151] and the other is based on Eshelby's energy momentum tensor [16, 67]. For the Betti-Rayleigh reciprocal type of conservative integral, we will detail the derivation because of its relative ambiguity in the literature. For Eshelby type integrals, we will briefly outline the formulation in Cardew *et al.* [16] and discuss their analytical

equivalence to the Betti-Rayleigh reciprocal type of conservative integral.

### 6.2.1 Construction of Path Independent Integral for $T$ -Stress Using Betti-Rayleigh Reciprocal Theorem

The Betti-Rayleigh reciprocal theorem states that “for a hyperelastic body subject to two infinitesimal systems of body and surface forces, the work done by the first system in the displacement caused by the second equals the work done by the second in the displacement caused by the first” [83]. For elastostatic problems, the body forces  $f_i$  and surface tractions  $t_i$  produce displacements  $u_i$ . The body forces  $f_i^*$  and surface tractions  $t_i^*$  produce displacements  $u_i^*$  and are called *auxiliary fields*. From the results of divergence theorem, assuming sufficient smoothness of the functions and the boundaries of the body, we can prove the Betti-Rayleigh reciprocal theorem:

$$\oint_A t_i^* u_i dA + \iiint_V f_i^* u_i dV = \oint_A t_i u_i^* dA + \iiint_V f_i u_i^* dV \quad (6.1)$$

where  $A$  is the bounding surface of the body,  $dA$  is an infinitesimal element of the surface,  $V$  is the volume of the body, and  $dV$  is an infinitesimal element of the volume. For a two-dimensional case without body forces, Equation (6.1) reduces to:

$$\oint_S (t_i^* u_i - t_i u_i^*) dS = 0 \quad (6.2)$$

where  $S$  is the bounding curve of the body and  $dS$  is an infinitesimal segment of the curve.

To construct a path independent integral for a two-dimensional elastic body with a crack using the Betti-Rayleigh reciprocal theorem, the procedure outlined by Stern *et al.* [131] is followed. First consider a contour integral along a closed path ( $C$ ,  $C_+$ ,  $C_\epsilon$ , and  $C_-$ ) as shown in Figure 6.1. From Equation (6.2), we have:

$$\begin{aligned} \oint_C (t_i^* u_i - t_i u_i^*) dC + \oint_{C_+} (t_i^* u_i - t_i u_i^*) dC_+ + \oint_{C_\epsilon} (t_i^* u_i - t_i u_i^*) dC_\epsilon \\ + \oint_{C_-} (t_i^* u_i - t_i u_i^*) dC_- = 0 \end{aligned} \quad (6.3)$$

Since  $C_+$  and  $C_-$  are traction free, we have

$$\oint_C (t_i^* u_i - t_i u_i^*) dC = \oint_{C_\epsilon} (t_i^* u_i - t_i u_i^*) dC_\epsilon \quad (6.4)$$

Equation (6.4) proves the path independence of the contour integral. With  $t_i = \sigma_{ij} n_j$  where  $\sigma_{ij}$  are components of the stress tensor and  $n_j$  are components of the



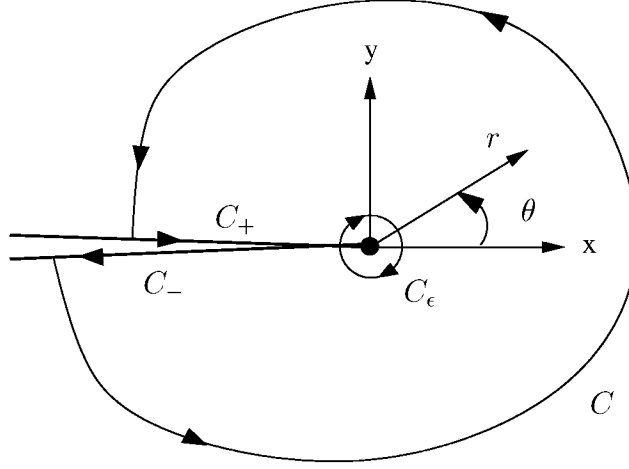


Figure 6.1: A closed contour in the neighborhood of a crack tip.

outward pointing normal vector of the contour, Equation (6.4) can be expressed as:

$$\oint_C (\sigma_{ij}^* u_i - \sigma_{ij} u_i^*) n_j dC = \oint_{C_\epsilon} (\sigma_{ij}^* u_i - \sigma_{ij} u_i^*) n_j dC_\epsilon \quad (6.5)$$

Due to its path independent nature, the integral on the left hand side of Equation (6.5) can be evaluated on a contour away from the crack tip where numerical solutions can be used for  $\sigma_{ij}$  and  $u_i$  without losing too much accuracy. The integral on the right hand side of Equation (6.5) is evaluated analytically as  $\epsilon \rightarrow 0$  [8].

Let  $(x, y)$  be the local Cartesian coordinates and  $(r, \theta)$  be the local polar coordinates centered at the crack tip. For two-dimensional elastic crack problems, Williams [146] derived a set of solutions for stresses and displacements that satisfy the equilibrium and compatibility equations near a crack tip (*cf.* Equations (5.2)–(5.8)):

$$\sigma_{ij} = \sum_{\lambda=-\infty}^{+\infty} A_\lambda r^{\frac{\lambda}{2}} f_{ij}^\lambda(\theta) \quad (6.6)$$

$$u_i = \sum_{\lambda=-\infty}^{+\infty} B_\lambda r^{\frac{\lambda}{2}+1} g_i^\lambda(\theta) \quad (6.7)$$

where  $\frac{\lambda}{2}$  is the eigenvalue of the problem and  $A_\lambda$  and  $B_\lambda$  are coefficients of the asymptotic expansions. In order to obtain coefficients of a particular order of  $\frac{\lambda}{2}$  alone, the auxiliary fields required in the reciprocal work relation in Equation (6.5) are:

$$\sigma_{ij}^* \sim r^{-\frac{\lambda}{2}-2} \quad u_i^* \sim r^{-\frac{\lambda}{2}-1} \quad (6.8)$$

The question arises how to extract the contributions of  $T$ -stress from above series expansions, without contributions from singular and other higher order terms.

Considering Equation (6.8), the idea is to choose auxiliary fields so that  $\sigma_{ij}^* \sim r^{-2}$  and  $u_i^* \sim r^{-1}$  to cancel all contributions from the first, singular terms of the expansions in Equation (6.5) to the  $T$ -stress term. The auxiliary stresses and displacements in local Cartesian coordinates are:

$$\sigma_{xx}^* = \frac{\cos 2\theta + \cos 4\theta}{2\pi r^2} \quad (6.9)$$

$$\sigma_{yy}^* = \frac{\cos 2\theta - \cos 4\theta}{2\pi r^2} \quad (6.10)$$

$$\sigma_{xy}^* = \frac{\sin 4\theta}{2\pi r^2} \quad (6.11)$$

$$u_x^* = -\frac{1}{4\pi r} \times \frac{\kappa \cos \theta + \cos 3\theta}{2G} \quad (6.12)$$

$$u_y^* = -\frac{1}{4\pi r} \times \frac{-\kappa \sin \theta + \sin 3\theta}{2G} \quad (6.13)$$

where  $G$  is the shear modulus, and  $\kappa = (3 - \nu)/(1 + \nu)$  for plane stress problems and  $\kappa = (3 - 4\nu)$  for plane strain problems.

It is clear that with such auxiliary fields, other higher order terms in stress and displacement expansions result in no contribution to the contour integral as  $r \rightarrow 0$ . With some algebraic manipulation, it is possible to show that no contribution occurs from the singular terms, and

$$T = \tilde{E} \oint_{C_\epsilon} (\sigma_{ij}^* u_i - \sigma_{ij} u_i^*) n_j dC_\epsilon \quad \text{as } \epsilon \rightarrow 0 \quad (6.14)$$

where  $\tilde{E} = E$  for plane stress problems and  $\tilde{E} = E/(1 - \nu^2)$  for plane strain problems in which  $E$  is Young's modulus.

As a result,  $T$ -stress is readily computable by combining Equations (6.5) and (6.14) with finite element analyses:

$$T = \tilde{E} \oint_C (\sigma_{ij}^* u_i^{FE} - \sigma_{ij}^{FE} u_i^*) n_j dC \quad (6.15)$$

where  $u_i^{FE}$  and  $\sigma_{ij}^{FE}$  are stresses and displacements of a finite element solution.

### 6.2.2 Construction of Path Independent Integral for $T$ -Stress Using Eshelby's Energy Momentum Tensor

Another type of path independent integral, following Eshelby, has been proposed for  $T$ -stress computations [16, 67]. The formulation uses auxiliary fields from point force loading in conjunction with finite element results. The  $T$ -stress is obtained by combining a common  $J$ -integral with a  $J$ -integral of superimposed auxiliary

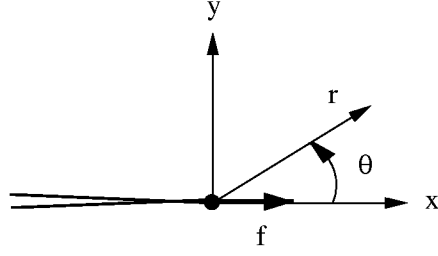


Figure 6.2: Point force applied at crack tip.

fields from the point force solutions. A brief outline of the formulation is given below.

Considering a point force at the crack tip in a infinite body (Figure 6.2), the stress fields in local Cartesian coordinates are:

$$\bar{\sigma}_{xx} = -\frac{f}{\pi r} \cos^3 \theta \quad (6.16)$$

$$\bar{\sigma}_{yy} = -\frac{f}{\pi r} \cos \theta \sin^2 \theta \quad (6.17)$$

$$\bar{\sigma}_{xy} = -\frac{f}{\pi r} \cos^2 \theta \sin \theta \quad (6.18)$$

Let  $F$  denote the two-dimensional elastic solution near the crack tip and  $\bar{F}$  the solution from the point force. The  $J$ -integral of the superimposed state of  $F$  and  $\bar{F}$  can be expressed as:

$$J(F, \bar{F}) = \oint_C \left[ \frac{1}{2} (\sigma_{ik} + \bar{\sigma}_{ik}) (e_{ik} + \bar{e}_{ik}) \delta_{xj} - (\sigma_{ij} + \bar{\sigma}_{ij}) (u_{i,x} + \bar{u}_{i,x}) \right] n_j dC \quad (6.19)$$

where  $e_{ik}$  are components of the strain tensor.

By expanding the expression, one can show that  $J(F, \bar{F})$  in Equation (6.19) is equivalent to

$$J(F, \bar{F}) = J(F) + J(\bar{F}) + J_x \quad (6.20)$$

in which  $J(F)$  is the well known  $J$ -integral for stress intensity factor computation,  $J(\bar{F})$  is the  $J$ -integral of the point force solutions, and

$$J_x = \oint_C \left[ \frac{1}{2} (\sigma_{ik} \bar{e}_{ik} + \bar{\sigma}_{ik} e_{ik}) \delta_{xj} - (\sigma_{ij} \bar{u}_{i,x} + \bar{\sigma}_{ij} u_{i,x}) \right] n_j dC \quad (6.21)$$

is the integral associated with the “cross-terms”. From the derivations in [16] and [67], we have:

$$J(\bar{F}) = 0 \quad \text{and} \quad J_x = \frac{Tf}{\widetilde{E}} \quad (6.22)$$

By rearranging Equation (6.20), we obtain a conservative integral for  $T$ -stress:

$$T = \frac{\tilde{E}}{f} [J(F, \bar{F}) - J(F)] \quad (6.23)$$

In [67], the point force solution was obtained from an additional finite element calculation. This implies that for a specific problem, two finite element computations need to be performed to obtain  $T$ -stress. In this study, we will use the analytical fields directly from the point force solution to evaluate  $T$ -stress. The displacement derivatives with respect to  $x$  and  $y$  for the point force auxiliary fields are:

$$\bar{u}_{x,x} = -\frac{f}{4\pi r} \frac{\kappa \cos \theta + \cos 3\theta}{2G} \quad (6.24)$$

$$\bar{u}_{y,x} = -\frac{f}{4\pi r} \frac{-\kappa \sin \theta + \sin 3\theta}{2G} \quad (6.25)$$

$$\bar{u}_{x,y} = -\frac{f}{\tilde{E}\pi r} (1 + \cos^2 \theta + \tilde{\nu} \cos^2 \theta) \sin \theta \quad (6.26)$$

$$\bar{u}_{y,y} = \frac{f}{\tilde{E}\pi r} (-\sin^2 \theta + \tilde{\nu} \cos^2 \theta) \cos \theta \quad (6.27)$$

and the  $T$ -stress can be readily evaluated from Equation (6.23) using a finite element solution and analytical stress and displacement derivative fields of the point force.

### 6.2.3 Analytical Equivalence between Betti's Reciprocal and Eshelby Integrals

To prove that both types of contour integrals for  $T$ -stress are analytically equivalent, we first observe that:

$$\begin{aligned} \bar{u}_{i,x} &= u_i^* \\ \bar{\sigma}_{ij,x} &= \sigma_{ij}^* \end{aligned}$$

by setting the point force equal to one. Substituting this relationship into Equation (6.14), we have:

$$\begin{aligned} \frac{T}{\tilde{E}} &= \oint_C (\sigma_{ij}^* u_i - \sigma_{ij} u_i^*) n_j dC \\ &= \oint_C (\bar{\sigma}_{ij,x} u_i) n_j dC - \oint_C (\sigma_{ij} \bar{u}_{i,x}) n_j dC \end{aligned} \quad (6.28)$$

From chain rules, we have  $(\bar{\sigma}_{ij} u_i)_{,x} = (\bar{\sigma}_{ij,x} u_i) + (\bar{\sigma}_{ij} u_{i,x})$  and Equation (6.28) becomes:

$$\frac{T}{\tilde{E}} = \oint_C (\bar{\sigma}_{ij} u_i)_{,x} n_j dC - \oint_C (\sigma_{ij} \bar{u}_{i,x}) n_j dC - \oint_C (\bar{\sigma}_{ij} u_{i,x}) n_j dC \quad (6.29)$$

By applying divergence theorem and recalling  $\sigma_{ij,j} = 0$  and  $e_{ij} = \frac{1}{2}(u_{i,j} + u_{j,i})$ , the first term in Equation (6.29) can be expressed as:

$$\begin{aligned}
\oint_C (\bar{\sigma}_{ij} u_i)_{,x} n_j dC &= \iint_A (\bar{\sigma}_{ij} u_i)_{,xj} dA \\
&= \iint_A \left( (\bar{\sigma}_{ij} u_i)_{,j} \right)_{,x} dA \\
&= \oint_C (\bar{\sigma}_{ik} e_{ik} \delta_{xj}) n_j dC \\
&= \oint_C \frac{1}{2} (\bar{\sigma}_{ik} e_{ik} + \sigma_{ik} \bar{e}_{ik}) \delta_{xj} n_j dC \quad (6.30)
\end{aligned}$$

Substituting Equation (6.30) into Equation (6.29), we then prove the analytical equivalence between Betti-Rayleigh reciprocal and Eshelby type of contour integrals.

## 6.3 $T$ -Stress Evaluation Using Finite Element Analyses

### 6.3.1 Equivalent Domain Integral

The conservative line integrals for  $T$ -stress derived above may not always be suitable for use directly with results obtained by standard finite element methods. A procedure that converts a line integral into an equivalent area (or domain) integral by means of Gauss integral theorem is usually employed. The equivalent domain integral is known to have higher accuracy in extracting the desired integral values from given standard finite element solutions [78, 7].

Following Li *et al.* [78], for cracks in homogeneous bodies, the integrals in Equations (6.15) and (6.23) can be converted into their equivalent domain integrals over a closed area  $A$ . For the Betti-Rayleigh reciprocal type of contour integral, the counterpart is given by:

$$T = \tilde{E} \iint_A (\sigma_{ij}^{FE} u_i^* - \sigma_{ij}^* u_i^{FE}) q_{,j} dA \quad (6.31)$$

For an Eshelby type contour integral, the domain integral is given by:

$$\begin{aligned}
T &= \frac{\tilde{E}}{f} [J(F, \bar{F}) - J(F)] \\
&= \frac{\tilde{E}}{f} \left( \iint_A [(\sigma_{ij}^{FE} + \bar{\sigma}_{ij})(u_{i,x}^{FE} + \bar{u}_{i,x}) - (W^{FE} + \bar{W})\delta_{xi}] q_{,j} dA \right. \\
&\quad \left. - \iint_A [\sigma_{ij}^{FE} u_{j,1}^{FE} - W^{FE} \delta_{xi}] q_{,j} dA \right) \quad (6.32)
\end{aligned}$$

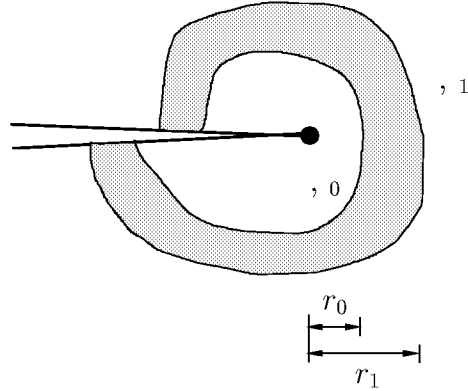


Figure 6.3: An equivalent domain integral.

where the area  $A$  is a region as illustrated in Figure 6.3 and the function  $q$  is taken to be unity on  $,_0$  and zero on  $,_1$ . To quantify our computed results, we denote  $r_0$  and  $r_1$  as the distances from the crack tip to  $,_0$  and  $,_1$  along the  $\theta = 0$  ray, respectively. The distance  $r_1$  will be used to characterize the integration domain.

### 6.3.2 Hierarchical p-version Finite Element Method

To evaluate Equations (6.31) and (6.32) we compute displacements, strains and stresses using a hierarchical p-version finite element method. A comprehensive description of the discretization properties as well as implementation details of the “p-version” can be found e.g. in [141]. We like to recall as an important property that, for problems with singularities, p-extensions converge with exponential rate if the mesh is properly refined towards the singularities.

The element formulation used to obtain the results presented in Section 6.4 restricts us to a standard, hierarchical polynomial basis for the finite element test and trial spaces. Although it is possible to introduce singular terms by the quarter-point mapping technique into hierarchical p-version formulations [109] these terms are less relevant for  $T$ -stress extraction.

The use of high order p-version elements allows domain integrals to be computed during the postprocessing step on an integration mesh that can be completely independent from the finite element mesh. Examples for two different possibilities of postprocessing meshes are shown in Figure 6.4(a) and (b). If the solution is of sufficiently high quality so that jumps in the stresses are small, it is even possible to have elements of the integration mesh reaching over more than one element of the discretization without significant loss in accuracy of the domain integral. In this case, an additional step of locating the gauss points of the integration element in the corresponding finite element would become necessary but the implementation can be integrated much easier in a CAD environment.

Numerical experiments show that it is not possible to reliably compute  $T$ -stress inside the elements directly adjacent to the crack tip. This is because, no matter

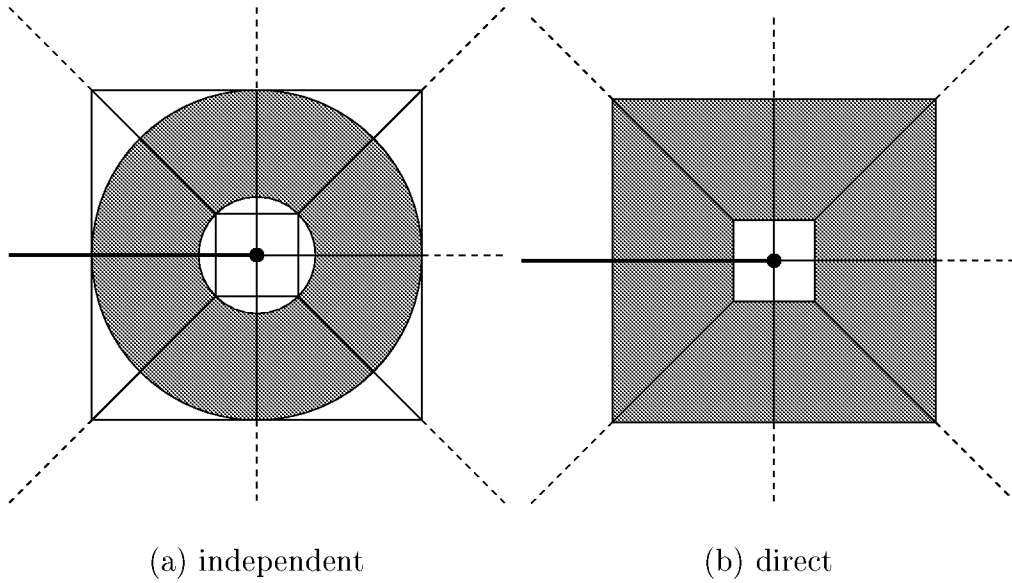


Figure 6.4: Postprocessing meshes for domain integral.

how strong the mesh refinement towards the singularity is, the solution in the elements directly adjacent to the singularity can oscillate [111]. The oscillation behavior is restricted to the crack tip elements and to a lesser degree for the first layer of elements outside the crack tip elements. If the discretization error in the remaining domain is reduced sufficiently, then path independence can be observed in the numerical results. Therefore the domain integral can always be computed in the first or second layer outside the crack tip elements.

To remove dependency of the obtained results from the error introduced by numerical integration we choose the number of integration points in each direction to be 15 for all values of  $p$ -extensions in all our computations. The additional computational cost for postprocessing of fracture parameters is orders of magnitude less than the cost of the solution process and can be neglected. With this high integration order, numerical equivalence of the Betti-Rayleigh reciprocal and Eshelby type contour integrals can be directly observed. It may finally be noted that, using high order  $p$ -elements, it is very well possible to obtain high quality results for  $T$ -stress directly from contour integrals removing the need for this kind of postprocessing completely.

### 6.3.3 Error Analysis and Accuracy Assessment

In theory, the contour integrals developed herein are path independent. The finite element approximation, however, inevitably introduces discretization error. The quality of the obtained  $J$ -integral or  $T$ -stress results does therefore depend on the location where the path independent integral has been evaluated. Thus, it is

important to quantify the error in computing  $T$ -stress using the path independent integrals and furthermore assess the accuracy of the obtained numerical results.

For a given finite element model, the difference between the exact and finite element solutions is the discretization error. Thus, taking the Betti-Rayleigh reciprocal type contour integral for example, the error for  $T$ -stress,  $e^T = |T - T^{FE}|$  at a certain integration path  $C$  is given as:

$$e^T = \tilde{E} \left| \oint_C (\sigma_{ij}^* u_i - \sigma_{ij} u_i^*) n_j dC - \oint_C (\sigma_{ij}^* u_i^{FE} - \sigma_{ij}^{FE} u_i^*) n_j dC \right|$$

Because of the different convergence rates for singular and non-singular terms in the solution, we shall observe that the discretization error is dominated mainly by the singular terms, if we extract our results in the singular-dominant zone. Thus we may postulate that the error of computed  $T$ -stress for Mode I problems (the effect of Mode II will be discussed later) in an integration domain  $r_1$  away from the crack tip is:

$$e^T \sim \tilde{e} \cdot \frac{K_I}{\sqrt{r_1}} \quad (6.33)$$

where  $\tilde{e}$  is a constant term related to the discretization error for a given discretization with a fixed polynomial degree of the shape functions. That is, the ratio of  $K_I/\sqrt{r_1}$  can be factored out in  $e^T$  similar to the asymptotic stress expansion. The relative error in  $T$ -stress

$$e_{rel}^T = \frac{|T - T^{FE}|}{T} \sim \tilde{e} \cdot \frac{K_I}{T\sqrt{r_1}} \quad (6.34)$$

scales with  $K_I/(T\sqrt{r_1})$ . From Equation (6.34), we shall anticipate that the accuracy of the computed  $T$ -stress can be improved predominately by reducing the discretization error  $\tilde{e}$ , or by increasing the size of the integration zone (which may not always be practical). The assertion that the relative error in  $T$ -stress scales with the dimensionless parameter  $K_I/(T\sqrt{r_1})$  is also supported by the following observation: geometrically similar finite element models which differ only in scale (which implies that the integration path is likewise scaled) should give numerically identical error fractions in the computed  $T$ -stress (or any local stress measurement).

We shall finally note that Equations (6.33) and (6.34) provide a powerful and useful measurement to study the accuracy of  $T$ -stress computations for finite element analyses, as will be revealed in the following numerical results. One can certainly use the property of this error estimator to calibrate and regularize the computed  $T$ -stress for other standard, low-order p finite element codes, but this is beyond our discussion in this study.



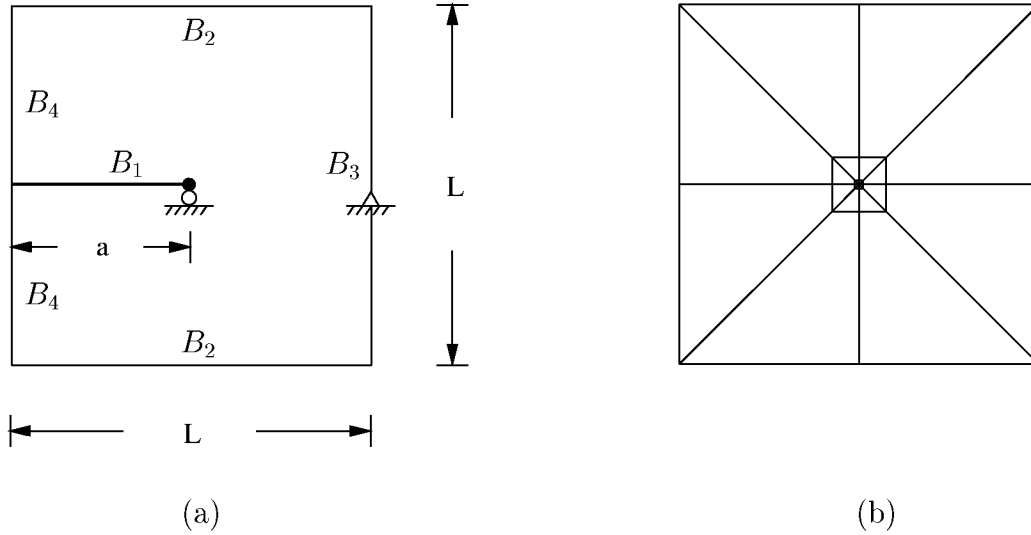


Figure 6.5: Benchmark example for  $T$ -stress computation: (a) numerical model and (b) mesh with 6 layers of refinement (only 2 visible as shown)

## 6.4 Numerical Results

### 6.4.1 A Simple Benchmark Example

In order to evaluate the accuracy of the proposed algorithm and its numerical outcome, it is desirable to compare it with an exact solution. Few exact solutions are known for the  $T$ -stress. For convenience, a problem with a simple geometry was chosen, with boundary conditions applied simulating arbitrary values of  $K_I$ ,  $K_{II}$ , and  $T$ . Since exact solutions are known, the problem may serve as a simple benchmark to study the accuracy of  $T$ -stress computations.

#### 6.4.1.1 Numerical Model

As shown in Figure 6.5(a) an edge cracked square plate with  $a/L = 0.5$  was modeled. Stresses obtained from the  $K_I$ ,  $K_{II}$ , and  $T$  related terms of the asymptotic expansion according to Equations (5.4), (5.5), and (5.6) were imposed as boundary conditions on the boundaries  $B_2$ ,  $B_3$ , and  $B_4$ , while the crack edges  $B_1$  remain traction free. Thus the model represents a variant of an internal crack in an infinite plate under remote loading, such that  $K_I$ ,  $K_{II}$ , and  $T$  can be varied independently. Because no body forces are present, the system is in equilibrium and the solution does exist. In addition to ensure uniqueness of the solution, displacement boundary conditions to prevent rigid body motions have to be prescribed (Figure 6.5(a)). A finite element mesh was constructed with six layers of refinement towards the crack tip resulting in a total of 52 elements (Figure 6.5(b)). The mesh was geometrically refined towards the crack tip with a progression factor of 0.15 as recommended in [140].

### 6.4.1.2 Numerical Results and Discussion

For three different load combinations  $K_I/T = 0.1$ ,  $K_I/T = 1.0$  and  $K_I/T = 10.0$  uniform p-extensions were performed, *i.e.* the polynomial degree  $p$  was changed for all elements uniformly between 1 and 11. The largest discretization with  $p = 11$  had 6169 degrees of freedom. In the postprocessing step of all computations the discretization error in energy norm  $\|e\|$ , the error in  $K_I$  and the error in  $T$  were computed.

The first observation to be made from the results is that the  $T$ -stress values computed from Betti-Rayleigh reciprocal and Eshelby type integrals coincide for all computations and all degrees of  $p$  up to machine accuracy. The equivalence proven in Section 6.2.3 is therefore also visible in the numerical results, if the integration order for the domain integral is sufficiently high.

In Table 6.1 values for the  $J$ -domain integral,  $K_I$ , and  $T$ -stress, computed on four different integration domains are tabulated. The domains are coincident with the first to the fourth layer of elements surrounding the crack tip elements. The load parameter  $K_I/T$  was 1.0 and the polynomial degree of the elements was  $p = 6$  corresponding to 1899 degrees of freedom. Since the discretization error is virtually non-existent for this case, path independence of  $K_I$  obtained from  $J$  as well as the  $T$ -stress term can be observed.

In Figure 6.6(a)–(c) convergence curves of computed  $T$ -stress values are shown for various  $K_I/T$  combinations. In each figure the error in  $T$ -stress computed on the first layer ( $L1$ ,  $r_1 = 7.59375 \times 10^{-5}$ ) and the second layer ( $L2$ ,  $r_1 = 5.0625 \times 10^{-4}$ ) of elements outside the crack tip is plotted over the number of degrees of freedom. Each mark indicates a polynomial degree  $p$ . As an indication of the global convergence behavior of the solution, the error in energy norm is also plotted for all load combinations. While the energy norm curves show the typical *S-shape* (*i.e.* exponential convergence rates until  $p$  equals the number of refinement layers), the curves for the  $T$ -stress show exponential convergence rates throughout the entire  $p$ -range. It is further observed that, for constant  $r_1$ , the relative error in  $T$ -stress increases with  $K_I/T$  but, as apparent in Table 6.2, the convergence rate is exactly the same for all loading values as we shall expect from Equation (6.34). Finally it is also observed that curves for computation of  $T$ -stress on the second layer outside the crack tip elements are slightly smoother, especially for low orders of  $p$ , indicating that oscillatory behavior of the solution is restricted to the crack tip and first layer of elements.

Table 6.2 summarizes the computed errors of  $K_I$ ,  $T$  and the energy norm on the first layer of elements away from the crack tip for all three  $K_I/T$  ratios. From these values it becomes apparent that the relative error in  $K_I$  is independent of  $K_I/T$ . The convergence rate of the relative error in energy norm calculated at  $p = 4$  and  $p = 8$  from

$$\beta = \frac{\log\left(\frac{\|e_8\|}{\|e_4\|}\right)}{\log\left(\frac{N_8}{N_4}\right)}$$

Table 6.1: Numerical Path Independence of  $J$ ,  $K_I$ , and  $T$  for  $p = 6$  and  $K_I/T = 1$  for Benchmark Example

Path	$r_1$	$J$ -domain	$K_I$	$T$
4	$2.25 \times 10^{-2}$	0.91012	1.0001	0.9997
3	$3.375 \times 10^{-3}$	0.91019	1.0001	0.9993
2	$5.0625 \times 10^{-4}$	0.91026	1.0001	0.9980
1	$7.59375 \times 10^{-5}$	0.91032	1.0002	0.9942

\*plane strain problems with  $E = 1.0$  and  $\nu = 0.3$

is  $\beta = -2.15$  for  $K_I/T = 1$  which is about the same as  $\beta = -2.2$  for  $K/T = 10$ .

We further evaluated the model with various values of  $K_I$ ,  $T$ , and  $r_1$  for various  $p$ -extensions to obtain the results plotted in Figure 6.7. Both the order of  $p$  and  $K_I/(T\sqrt{r_1})$  are seen to have a significant effect on the accuracy of the solution. The results are expected from Equation (6.34), since the relative error in  $T$ -stress is proportional to the discretization error  $\tilde{e}$  and the dimensionless parameter  $K_I/(T\sqrt{r_1})$ . We finally note that with  $p = 11$ , a relative error in the calculated  $T$ -stress approaching  $1 \times 10^{-6} \%$  is achieved.

In the process of simulations, various  $K_{II}/K_I$  ratios were also evaluated, and the effect of  $K_{II}$  was found to be negligible for values up to  $K_{II}/K_I = 100$ . Thus the effect of  $K_{II}$  was not given further consideration in this study.

From the above we observe that for problems where  $T$ -stress is small compared to  $K_I$ , it is more difficult to accurately evaluate. Perhaps most significantly, the above exercise identifies the conditions under which we may with confidence calculate  $T$ -stress with very high accuracy.

## 6.4.2 Fracture Specimens

In this section, the numerical results for various fracture specimens are evaluated. This serves two purposes: one is to demonstrate that the convergence and accuracy of computed  $T$ -stress can be observed easily with the  $p$ -extensions, and the other is to compare our results for various fracture specimen configurations with numerical values from the literature. We detail our results for double cantilever beam (DCB) specimens due to its practical importance in obtaining an accurate  $T$ -stress to characterize crack turning behavior [103]. For other fracture specimens, we tabulate our computed  $T$ -stress for comparison.

### 6.4.2.1 Double Cantilever Beam (DCB) Specimen

DCB fracture specimens are known to have large positive  $T$ -stress that may cause crack path instability under pure Mode I conditions [46, 26]. In order to compare

Table 6.2: Relative Error of  $K_I$  and  $T$  Computed at Integration Domain on First Layer Away From Crack Tip and Relative Error in Energy Norm for Benchmark Example

$r_1 = 7.59375 \times 10^{-5}, K_I/T = 1/10$				
p	DOFs	relative error (%)		
		$K_I$	$T$	$  e  $
4	919	0.456	0.7693	0.0781
8	3295	$4.3810 \times 10^{-4}$	$2.7548 \times 10^{-3}$	0.004
11	6169	$8.1660 \times 10^{-5}$	$3.0 \times 10^{-5}$	0.002

$r_1 = 7.59375 \times 10^{-5}, K_I/T = 1/1$				
p	DOFs	relative error (%)		
		$K_I$	$T$	$  e  $
4	919	0.456	7.693	0.656
8	3295	$4.3810 \times 10^{-4}$	$2.7548 \times 10^{-2}$	0.042
11	6169	$8.1650 \times 10^{-5}$	$2.9995 \times 10^{-4}$	0.022

$r_1 = 7.59375 \times 10^{-5}, K_I/T = 10/1$				
p	DOFs	relative error (%)		
		$K_I$	$T$	$  e  $
4	919	0.456	76.93	1.4675
8	3295	$4.3810 \times 10^{-4}$	0.27548	0.073
11	6169	$8.1660 \times 10^{-5}$	$2.996 \times 10^{-3}$	0.046

\*results are independent of the length units associated with  $r_1$  and  $K_I/T$

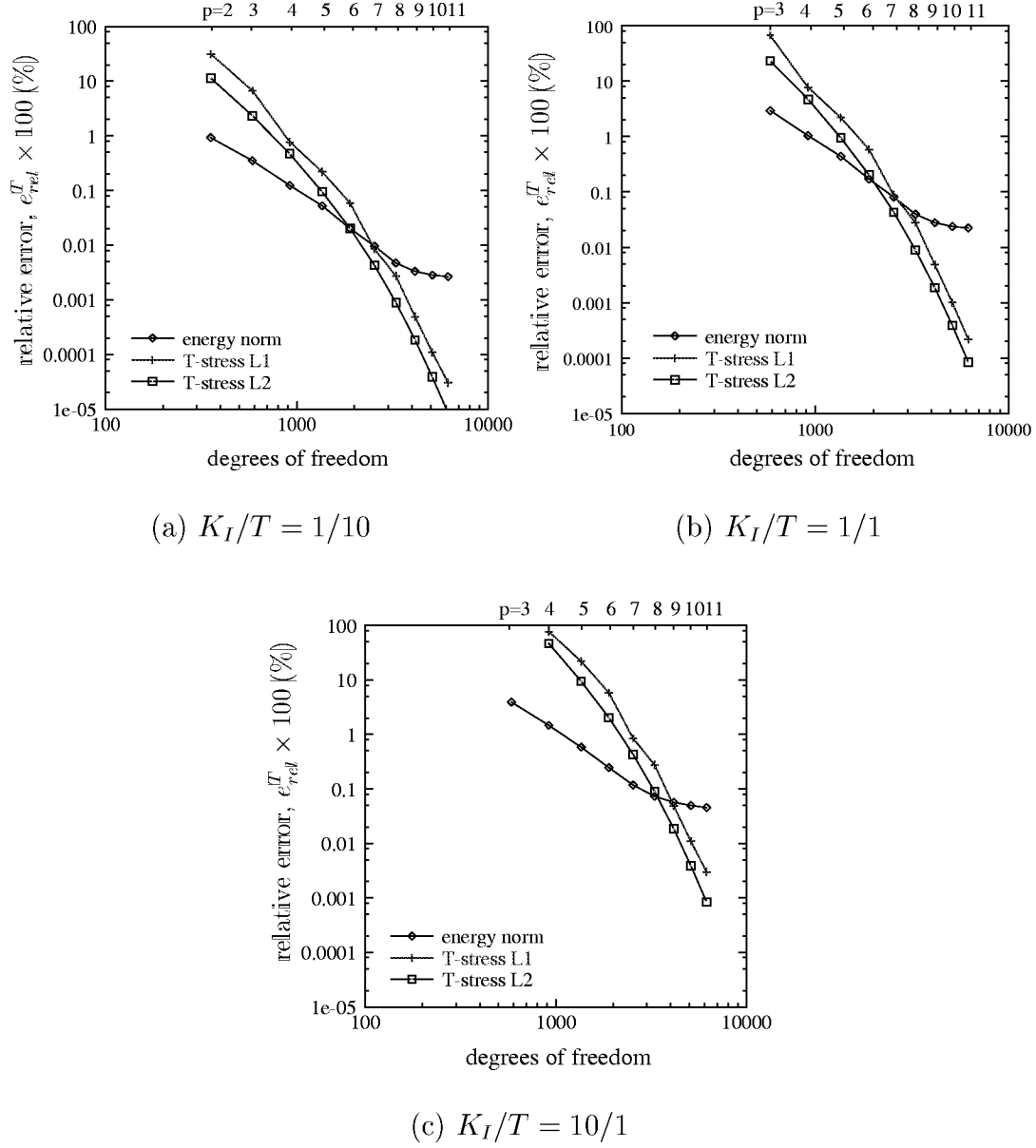


Figure 6.6: Convergence of  $T$ -stress and energy norm for the benchmark example.  $T$ -stress values are computed on the first layer ( $L1$ ,  $r_1 = 7.59375 \times 10^{-5}$ ) and the second layer ( $L2$ ,  $r_1 = 5.0625 \times 10^{-4}$ ) of elements outside the crack tip.

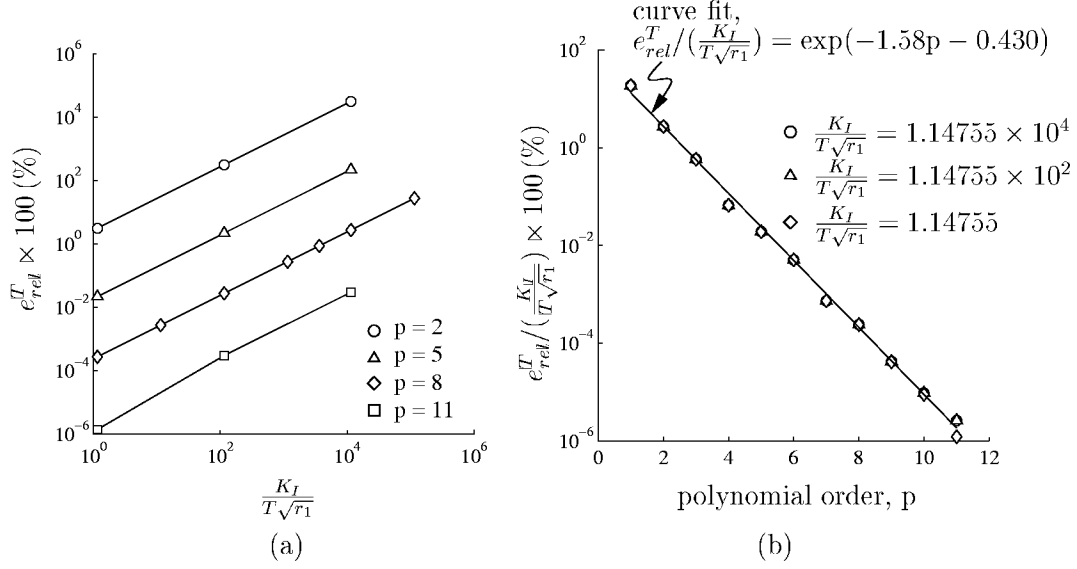


Figure 6.7: Accuracy assessment with p-extension for the benchmark example: (a) the relative error of calculated  $T$ -stress,  $e_{rel}^T$ , versus dimensionless parameter  $K_I/(T\sqrt{r_1})$ , and (b) the ratio of  $e_{rel}^T$  over  $K_I/(T\sqrt{r_1})$  versus the polynomial degree of the shape functions,  $p$ .

numerically computed  $T$ -stress values to those found in the literature, a DCB configuration shown in Figure 6.8(a) with  $h/w = 0.2$  and  $a/w = 0.5$  was modeled. Again a finite element mesh with six layers of refinement towards the crack tip was constructed, as shown in Figure 6.8(b). To eliminate any influence of perturbations from point forces the load was introduced as distributed forces along one half of the hole edges.

With the mesh fixed, a p-extension was performed, *i.e.*  $p$  was increased between  $1 \leq p \leq 11$ . The discretization at  $p = 11$  had 9277 degrees of freedom and, because no analytical solutions are available for this specimen, it was used as a reference solution.  $K_I$  and  $T$  were computed in two different domains corresponding to the first and second layer of elements away from the crack tip with  $r_1/a = 2.025 \times 10^{-4}$  and  $r_1/a = 1.35 \times 10^{-3}$ . We note that the value of the error parameter  $K_I/(T\sqrt{r_1})$  for the integration domain at the first layer is 42.2; thus the relative error of the reference solution is estimated to be on the order of  $10^{-5} \%$  based on Figure 6.7.

The convergence of the computed normalized  $K_I$  and  $T$ -stress values can be observed in Figure 6.9 and Figure 6.10, respectively, where for each polynomial degree from  $p = 3$  to  $p = 8$ ,  $K_I$  and  $T$ -stress computed on the two integration domains are plotted. For engineering accuracy, *i.e.* to obtain a relative error of 1 percent in  $T$ -stress, a degree of  $p = 6$  corresponding to 2917 degrees of freedom is necessary. Again path independence of the computed integrals can be observed from  $p = 5$  and up.

To compare our results with values from different sources published in the literature, a normalized stress biaxial parameter  $B$  defined in [77] is introduced

Table 6.3: Computed Values of  $K_I$ ,  $T$ , and  $B$  for the DCB Specimen

DCB ( $a/w = 0.5$ , $h/w = 0.2$ )			
SOURCES	$\frac{K_I}{\sigma\sqrt{\pi a}}$	$\frac{T}{\sigma}$	$B = \frac{T\sqrt{\pi a}}{K_I}$
Present ( $p = 11$ )	3.9225	11.5745	2.9508
Leevers and Radon [77]	-	-	2.942
Cardew <i>et al.</i> [16]	-	-	2.829
Kfouri [67]	-	-	2.956
Fett [45]	3.9307	11.5304	2.933

where

$$B = \frac{T\sqrt{\pi a}}{K_I} \quad (6.35)$$

Table 6.3 summarizes the normalized stress intensity factor  $K_I/(\sigma\sqrt{\pi a})$ , the normalized  $T$ -stress, and  $B$  with  $p = 11$  as well as computed values from [77, 16, 67, 45]. A difference of up to 4.2% in the results for  $B$  is observed in comparison with the sources from the literature.

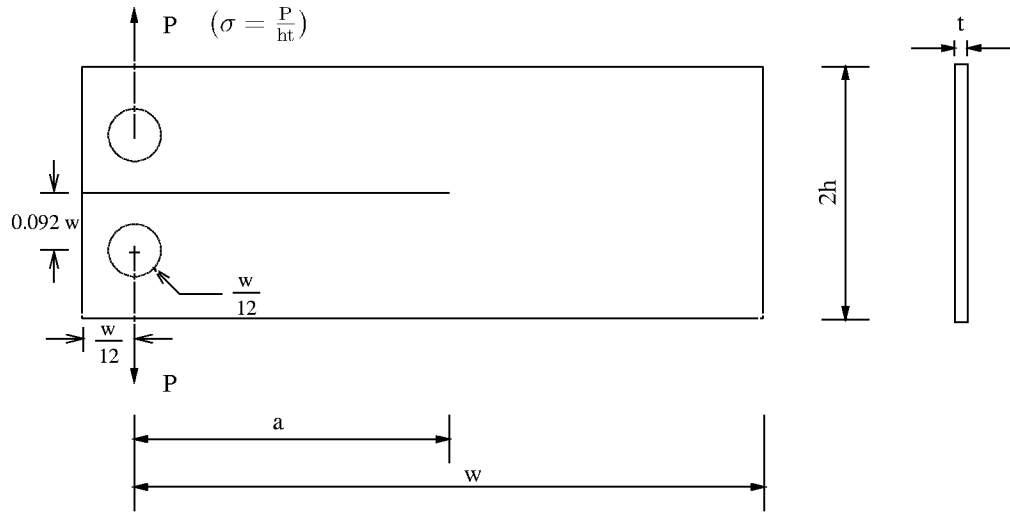
#### 6.4.2.2 $T$ -stress for Various Fracture Specimen Configurations

Computed  $T$ -stress in various fracture specimen configurations including middle crack tension specimen (MT) and single edge notch specimen subjected to tension (SENT) and pure bending (SENB) as shown in Figure 6.11 was evaluated. All the meshes were constructed with six layers of refinement towards the crack tip and a progression factor of 0.15.

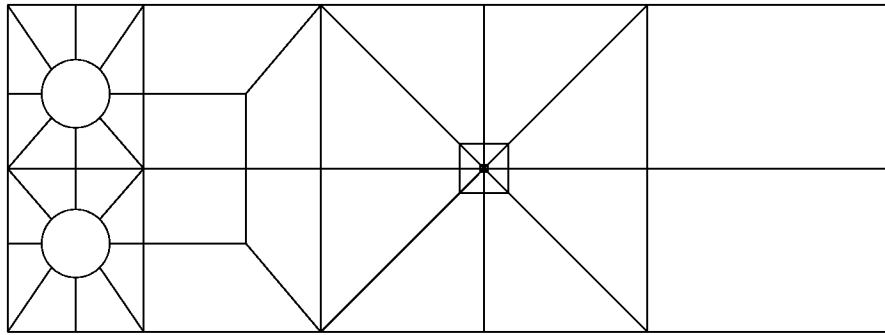
Table 6.4 summarizes our computed results for  $K_I$ ,  $T$ -stress, and  $B$ . The results are compared with values from different sources published in the literature.

#### 6.4.3 Discussion: Numerical Assessment of $T$ -stress Computation Using a p-version Finite Element Method

Throughout the numerical examples, we have demonstrated that using the path independent integrals with hierarchical, p- and hp-version finite element methods proves to be a powerful tool to obtain highly accurate numerical results for  $T$ -stress. The convergence and accuracy of computed  $T$ -stress values are observed easily and confidently with the p-extensions in the benchmark example of known exact solutions, and the error correlates reliably with the error estimator,  $K_I/\sqrt{r_1}$ . It is thus inferred that the results presented for the fracture specimen geometries are of comparable accuracy to the benchmark at equal values of  $K_I/\sqrt{r_1}$ , and are thus numerically exact to the significant digits given in the tables.



(a)



(b)

Figure 6.8: (a) Double cantilever beam (DCB) specimen configuration, and (b) a  $hp$ -version finite element model for DCB specimen with 6 layer refinement (only 2 visible).



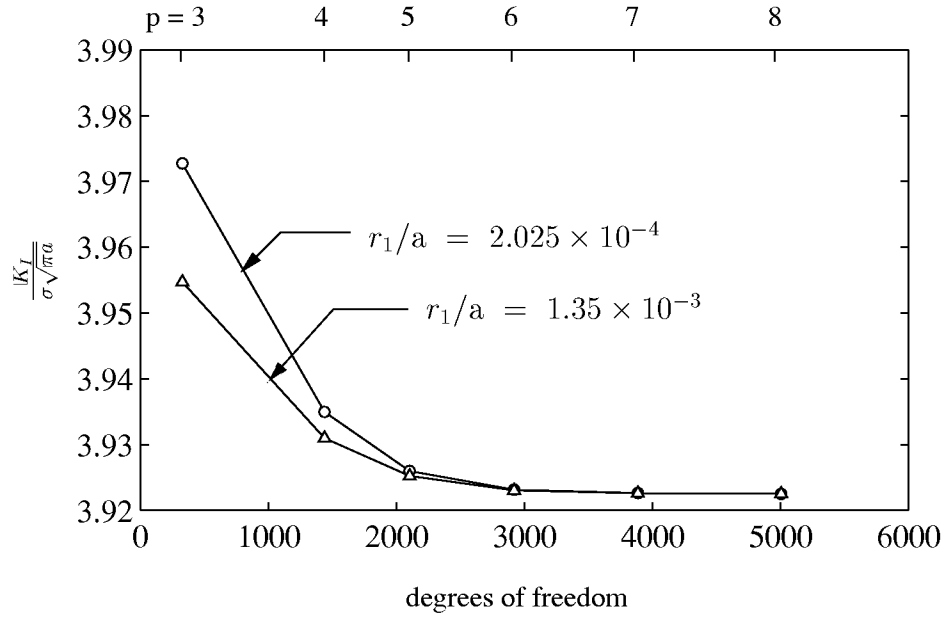


Figure 6.9: Convergence of normalized  $K_I$  for p-extension for the DCB specimen.

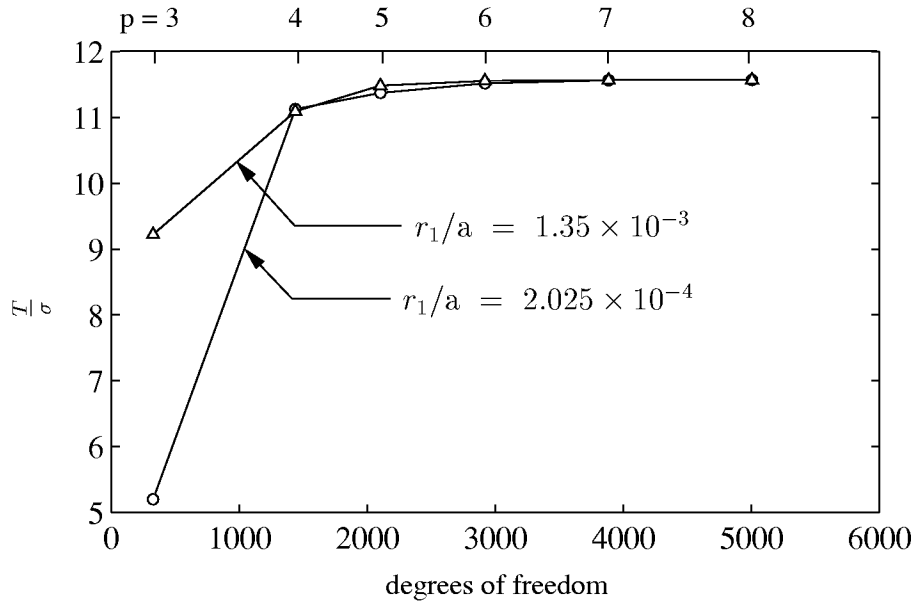


Figure 6.10: Convergence of normalized  $T$ -stress for p-extension for the DCB specimen.

Table 6.4: Computed Values of  $K_I$ ,  $T$ , and  $B$  for MT, SENT, and SENB Specimens

SOURCES	$\frac{K_I}{\sigma\sqrt{\pi a}}$	$\frac{T}{\sigma}$	$B = \frac{T\sqrt{\pi a}}{K_I}$
MT ( $2a/w = 0.3$ , $h/w = 1.0$ )			
Present ( $p = 11$ )	1.1232	-1.15536	-1.0286
Leevers and Radon [77]	-	-	-1.0255
Cardew <i>et al.</i> [16]	-	-	-1.026
Fett [45]	-	-1.1557	-1.028
Isida [61]	1.123	-	-
SENT ( $a/w = 0.3$ , $h/w = 12$ )			
Present ( $p = 11$ )	1.6598	-0.61033	-0.36771
Sham [123]	1.6570	-0.61425	-0.37070
SENT ( $a/w = 0.5$ , $h/w = 12$ )			
Present ( $p = 11$ )	2.8246	-0.42168	-0.14929
Sham [123]	2.8210	-0.43142	-0.15293
SENB ( $a/w = 0.3$ , $h/w = 12$ )			
Present ( $p = 11$ )	1.1241	-0.079177	-0.070436
Sham [123]	1.1220	-0.082404	-0.073444
SENB ( $a/w = 0.5$ , $h/w = 12$ )			
Present ( $p = 11$ )	1.4972	0.39749	0.26549
Sham [123]	1.4951	0.39112	0.26160

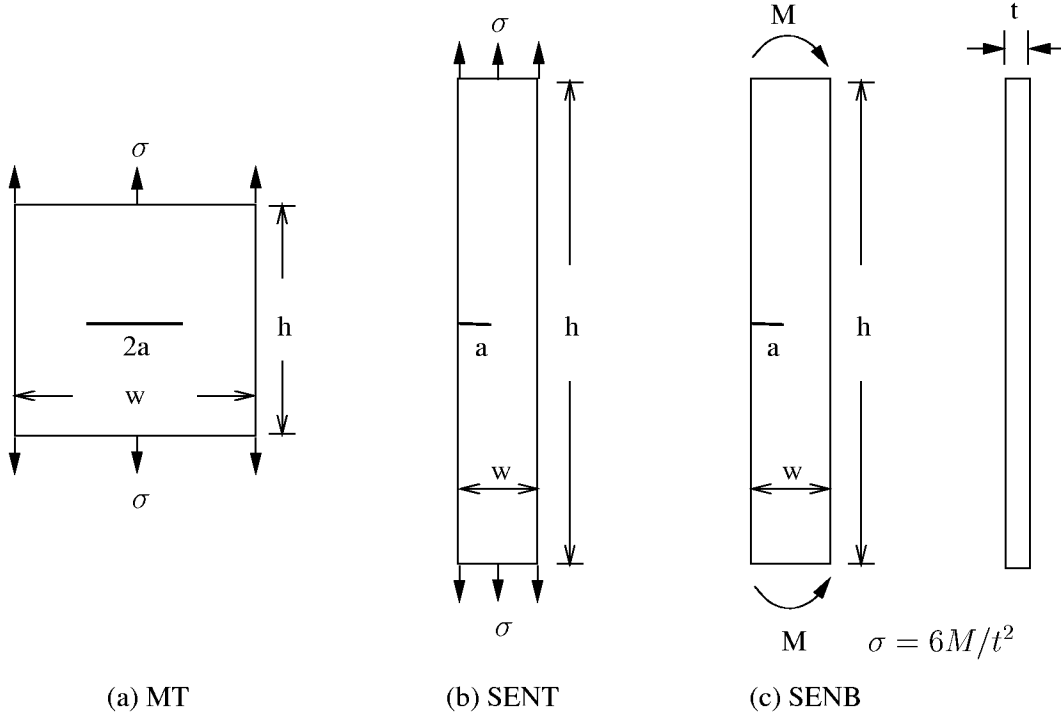


Figure 6.11: Various fracture specimen configurations used for  $T$ -stress computation.

## 6.5 FRANC3D/STAGS Results

Both the Betti-Rayleigh reciprocal and Eshelby types of domain integrals were also implemented in the FRANC3D/STAGS software program. We note that the polynomial degree of shape functions for the quadrilateral shell element used in FRANC3D/STAGS is the lowest, *i.e.*,  $p = 1$ . Thus, to obtain an acceptable accuracy for  $T$ -stress, we need to introduce a highly focused mesh near the crack tip and/or evaluate the domain integral sufficiently away from the crack tip.

### 6.5.1 Two-Dimensional Problems

The DCB specimen was studied using FRANC3D/STAGS. An all-quadrilateral element meshing algorithm developed by Potyondy *et al.* [107] was used to generate a graded mesh with a high mesh density near the crack tip and coarser away from the crack tip. Figure 6.12 shows a graded finite element mesh with a crack tip template. Computed values of  $K_I$  and  $T$  evaluated at the third layer away from the crack tip ( $r_1/a = 0.02$ ) are within 0.8 and 1.2% of the reference solutions in Table 6.3, respectively.

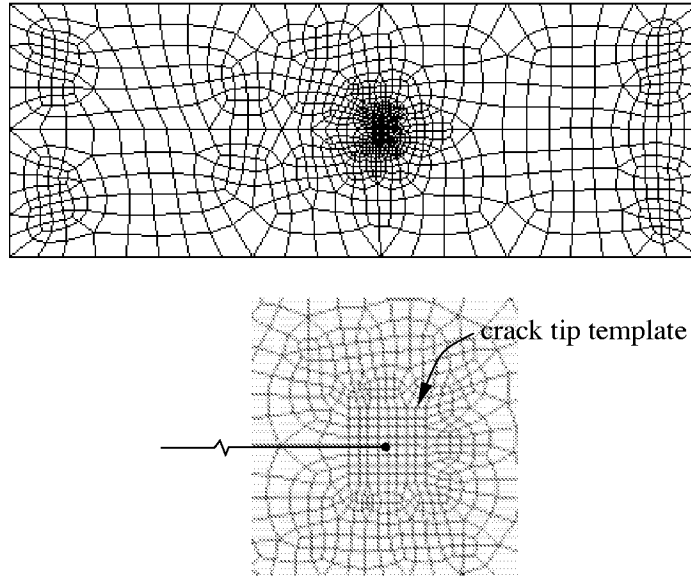


Figure 6.12: A focused finite element mesh used in FRANC3D/STAGS.

### 6.5.2 Thin Shell Problems

The methods developed herein are mainly for two-dimensional linear elastic problems. Further study is needed to derive its Lagrangian counterpart for shell structures subjected to large displacements and rotations.

## 6.6 Summary

Two types of path independent integrals for  $T$ -stress computations, one based on the Betti-Rayleigh reciprocal theorem and the other based on Eshelby's energy momentum tensor were studied. Analytical as well as numerical equivalence between the two integrals was found. To quantify and assess the accuracy of computed values, a novel error estimator for  $T$ -stress was proposed. Specifically, it was found that the error of the computed  $T$ -stress is proportional to the ratio of stress intensity factor divided by the square root of the characteristic dimension of the integration domain where the path independent integral is evaluated. Using a highly accurate hierarchical p- and hp-version finite element code, the convergence and accuracy of computed values were observed easily and confidently, and the error of the computed  $T$ -stress correlated reliably with the proposed error estimator. We conclude that the path independent integrals, in conjunction with hierarchical, p- and hp-version finite element methods, provide a powerful tool to obtain highly accurate numerical results for  $T$ -stress.

We then evaluated numerical results using the FRANC3D/STAGS program. Because the polynomial degree of the shape functions of the shell elements was the lowest (*i.e.*,  $p = 1$ ), a highly focused mesh near the crack tip and a remote inte-

gration path were needed to extract the  $T$ -stress from the finite element solutions without losing too much accuracy. Numerical results showed that the errors in  $T$ -stress for DCB specimens could be kept well below 2% using FRANC3D/STAGS.

# Chapter 7

## Curvilinear Crack Growth Simulations

Curvilinear crack growth in coupon tests and in full-scale curved panel tests are analyzed in this chapter. Crack growth direction is predicted using the directional criteria developed in Chapter 5. The predicted crack trajectories are compared with those observed in the tests.

### 7.1 Curvilinear Crack Growth Simulations For DCB Fracture Specimens

Simulations of crack growth in double cantilever beam (DCB) fracture specimens were performed. The predicted crack trajectories were compared with the experimental measurements. Among all the possible parameters that could affect the crack trajectory prediction, only  $T$ -stress,  $r_c$ , fracture toughness orthotropy, and the length of the crack growth increment were examined.

#### 7.1.1 Description of Experiment

DCB specimens made of 0.09 inch thick, 2024-T3 aluminum alloy were tested at the NASA Langley Research Center in cooperation with the McDonnell Douglas Company (now Boeing). A brief description of the tests is presented below. More information about the fracture tests can be found in [103, 101, 104].

The dimensions and material properties of the test specimens are shown in Figure 7.1. Stable crack growth in the L-T and T-L orientation under a monotonically increasing load was conducted. Fatigue crack growth in the L-T orientation under a low stress level of cyclic loading was performed. The test matrix is summarized in Table 7.1. Only one test per configuration was performed.

The final cracked configurations in the L-T orientation are shown in Figure 7.2. The crack path observed in stable crack growth was different from that in fatigue crack propagation. For specimens under stable tearing, the crack turned sharply

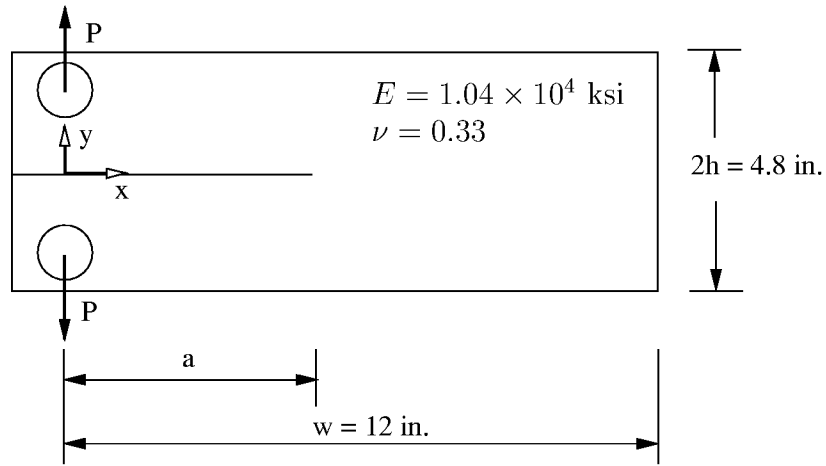


Figure 7.1: The DCB specimen configuration.

Table 7.1: Test Matrix for DCB Specimens

Specimen ID	Initial Crack (in.)	Type of Crack Growth
2024LT-4	5.507	stable tearing
2024TL-5	5.47	stable tearing
2024LT-6	5.104	fatigue crack growth

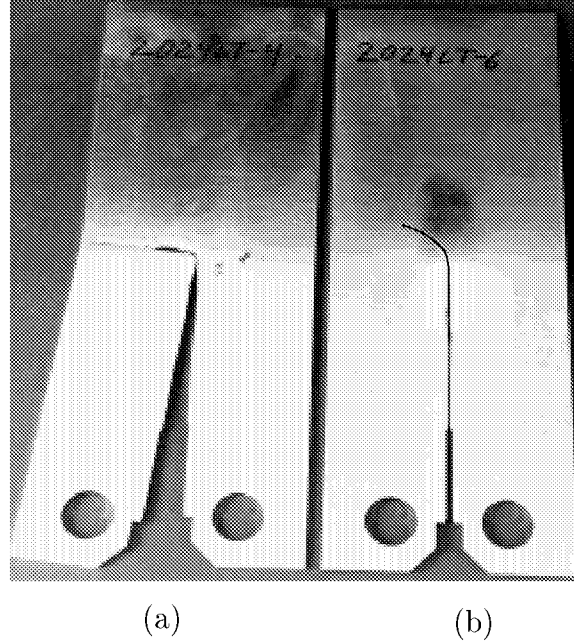


Figure 7.2: (a) Stable tearing (2024LT-4) and (b) fatigue crack growth (2024LT-6) in the L-T orientation observed in DCB specimens (after [101]).

away from its initial crack tip. For specimens subjected to fatigue loading, a much smoother crack path was observed.

### 7.1.2 Description of Simulation

Curvilinear crack growth analyses were conducted using the FRANC3D/STAGS software program. As described in Section 1.3, to simulate crack growth where the crack trajectory is not known *a priori*, continual updating of the geometry is required. The procedure of simulating crack growth consists of the following steps [106, 108]:

- step 1:** generate a STAGS finite element model from FRANC3D.
- step 2:** obtain the equilibrium state by executing the STAGS code.
- step 3:** compute the fracture parameters and determine the direction of crack growth.
- step 4:** decide the amount of crack growth extension and propagate the crack.

The process is repeated until a suitable termination condition is reached. The crack growth alters the geometric model in FRANC3D and leads to localized mesh deletion. The deletion region is remeshed automatically using an all-quadrilateral element meshing algorithm [107].



Stress intensity factors,  $K_I$  and  $K_{II}$ , were computed using the equivalent domain  $J$  integral with the mode-separation method [15].  $T$ -stress was computed using the equivalent domain integral method derived from the Betti-Rayleigh reciprocal theorem (Equation (6.15)). Several integration paths about the crack tip were evaluated to assure the accuracy of the computations. The propagation angle was predicted based on the maximum tangential stress theory developed in Chapter 5, that is, Equations (5.17) and (5.24) for the isotropic and orthotropic media, respectively. We assumed that both fatigue and stable crack growth in the DCB specimens can be analyzed using linear elastic fracture mechanics (LEFM). This assumption may not hold for stable crack growth. We will further discuss this issue in Section 7.3.

### 7.1.3 Numerical Results

#### 7.1.3.1 Effect of $T$ -stress and $r_c$

The specimens under stable crack growth were analyzed first. The crack was grown in 0.2 inch increments. Crack growth direction was predicted by the isotropic directional criterion, *i.e.*, Equation (5.17). Figure 7.3 depicts four predicted crack trajectories with various magnitudes of  $r_c$  and the experimental measurements. Figure 7.4 shows the computed deformed shapes and the corresponding finite element meshes used in curvilinear crack growth simulations. Predicted and measured results shown in Figure 7.3 indicate that:

1. The predicted crack path for  $r_c = 0$  coincides with the straight line ahead of the initial crack. For this special case, we note that the directional criterion reduces to the Erdogan and Sih's criterion [41].
2. For  $r_c = 0.05$  inch, the predicted crack path initially follows a zigzag along the straight path, but deviates from it at about 1.6 inches of crack extension.
3. For  $r_c \geq 0.06$  inch, predicted crack paths turn sharply away from the initial crack tip.
4. The case with  $r_c = 0.09$  inch best correlates the experimental data and numerical results for stable tearing.
5. Notable difference between the measured crack paths in the L-T and T-L orientations are observed.

Similar trends were observed for fatigue crack growth. Figure 7.5 plots three predicted crack trajectories with various magnitudes of  $r_c$  and the experimental measurements. The case with  $r_c = 0.06$  inch best correlates the experimental data and numerical results for fatigue crack growth.

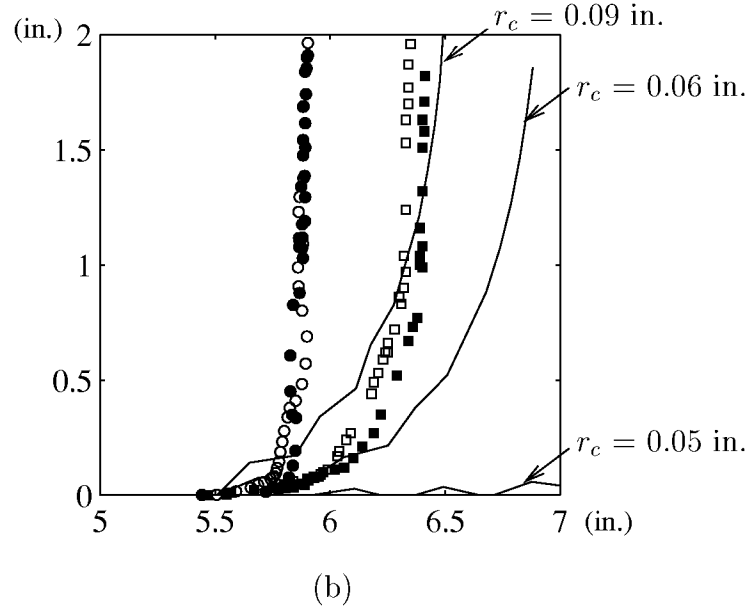
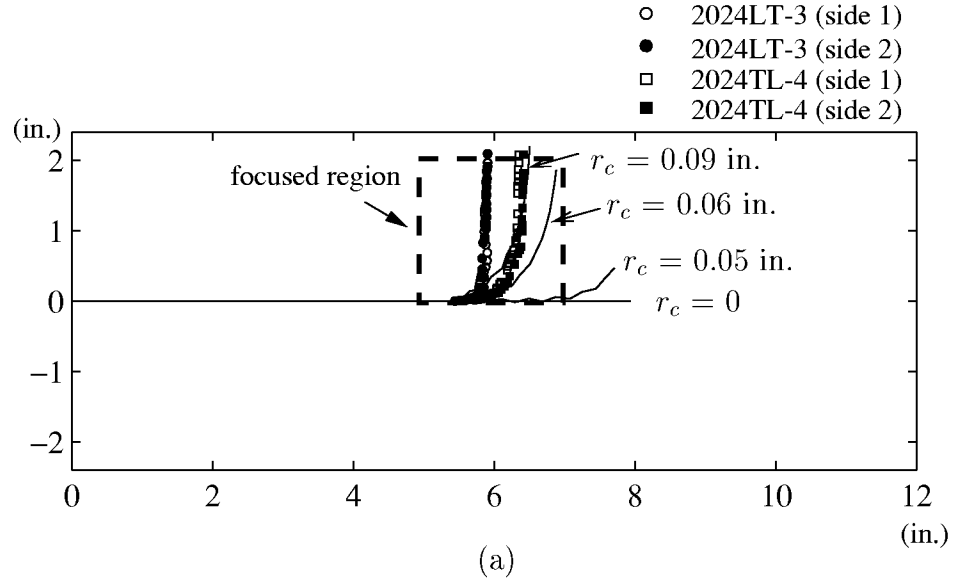
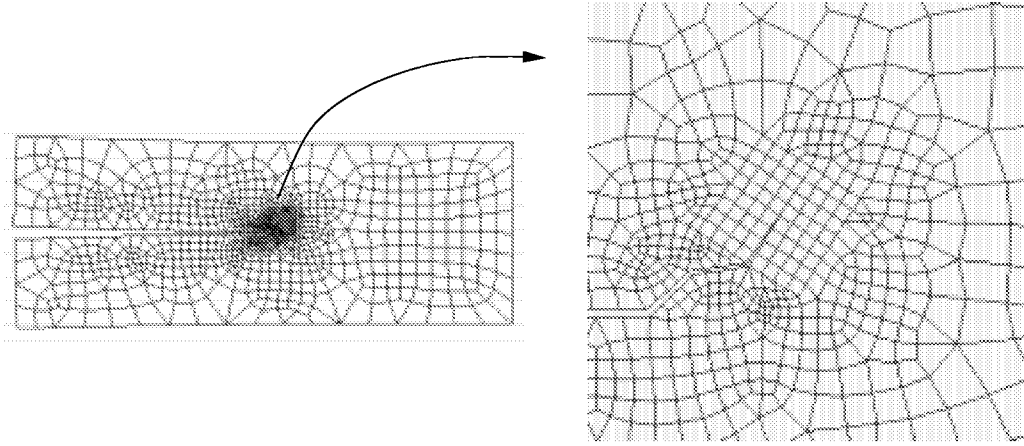
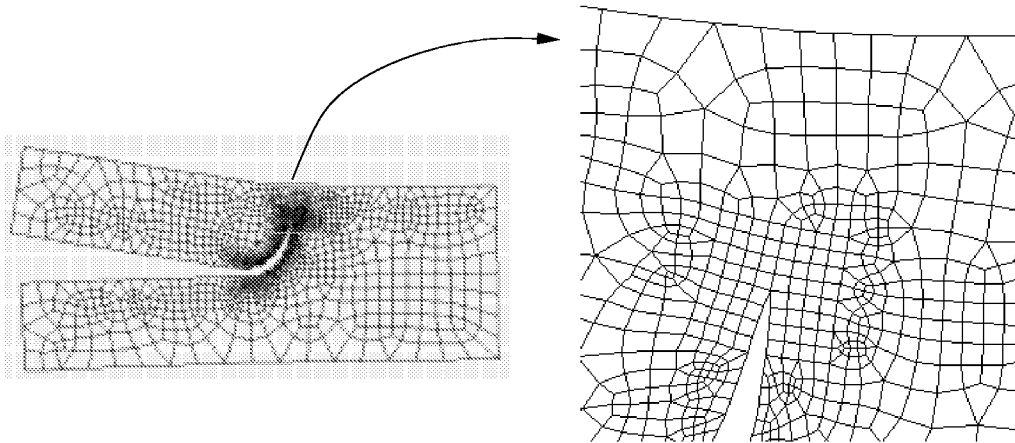


Figure 7.3: Predicted and measured crack trajectories for DCB specimen under stable crack growth: (a) overall crack trajectories, and (b) crack paths in the focused region (Equation (5.17) with various magnitudes of  $r_c$ ;  $\Delta a = 0.2$  in.).



(a)  $\Delta a = 0.6$  inch



(b)  $\Delta a = 2.0$  inch

Figure 7.4: Computed deformed shapes and the corresponding finite element meshes used in the curvilinear crack growth simulations in DCB specimens (isotropic case with  $r_c = 0.09$  inch).

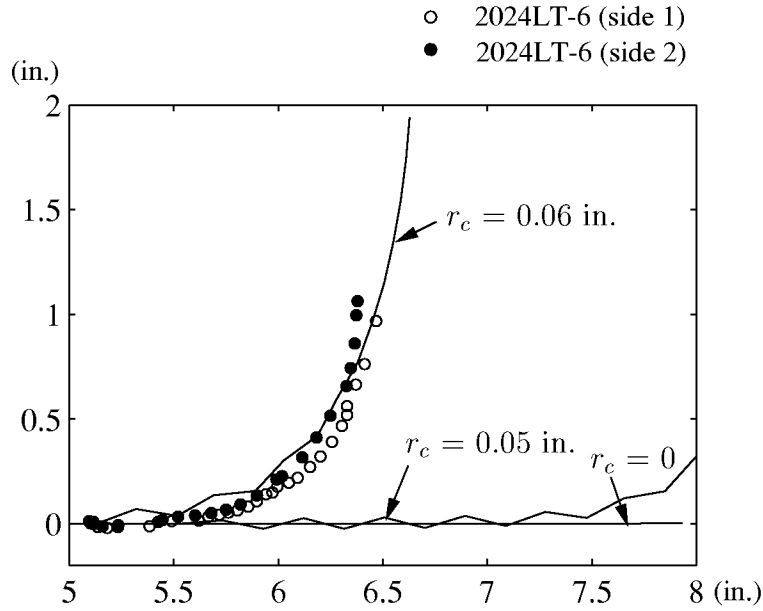


Figure 7.5: Predicted and measured crack trajectories for DCB specimen under fatigue crack growth (Equation (5.17) with various magnitudes of  $r_c$ ;  $\Delta a = 0.2$  in.).

### 7.1.3.2 Length of Crack Growth Increment

For LEFM problems, no adaptive scheme is currently implemented to control the length of curvilinear crack growth increment. Instead, during the simulation process, the analyst needs to decide and specify the amount of crack extension at the crack tip. To investigate possible effects of the crack growth increment on crack trajectory prediction, the crack growth simulation was performed again with  $\Delta a = 0.1$  inch for  $r_c = 0.09$  inch. The length of crack growth increment has a minor effect on the crack trajectory prediction as shown in Figure 7.6.

### 7.1.3.3 Fracture Toughness Orthotropy

From the laboratory observation, the specimen in the L-T orientation turned sharper than that in the T-L orientation under stable tearing. This is thought to be related to the possible difference between the fracture resistance along the transverse (T) direction compared to that along the longitudinal (L) direction. In subsequent analyses, a simple elliptical function presented in Section 5.3.4 was used to incorporate the effect of fracture orthotropy. The fracture toughness was assumed to be 10% higher in the T than in the L direction. As shown in Figure 7.7, the predicted crack trajectory in the L-T orientation agrees better with the experimental measurements than the isotropic prediction. However, the predicted trajectory in the T-L orientation deviates from the observed crack path.

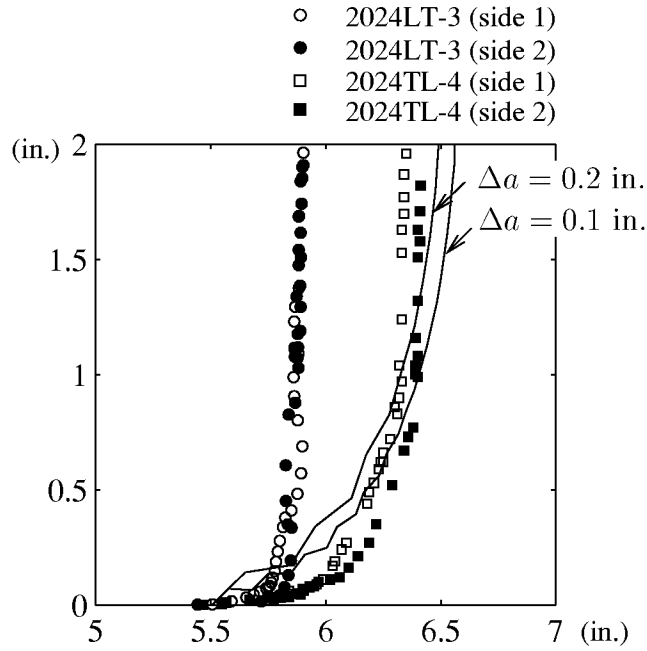


Figure 7.6: Predicted and measured crack trajectories for DCB specimen under stable crack growth: effect of the length of crack growth increment (Equation (5.17) with  $r_c = 0.09$  inch).

#### 7.1.4 Concluding Remarks for Curvilinear Crack Growth Simulation in DCB Specimen

Curvilinear crack growth in thin, metallic DCB specimens was studied. For this specific configuration, cracks showed a tendency to turn away from the initial crack tip under pure Mode I conditions. The crack growth directional criterion, incorporating the  $T$ -stress effect, was capable of capturing the essence of crack turning under such circumstance. The predicted results were in good agreement with the experimental measurements.

The fracture toughness orthotropy was introduced to explain the difference between the measured crack paths in the L-T and T-L orientations. The orthotropic directional criterion showed some promise to correlate the experimental data, but some disagreement between predicted and measured results was observed for the specimen in the T-L orientation. One possible explanation is that the magnitude of  $r_c$  along the T direction may be different than that along the L direction. Incorporating different magnitudes of  $r_c$  along T and L directions could certainly provide better correlation with experimental results. But additional tests and analyses need to be conducted to justify this assertion.

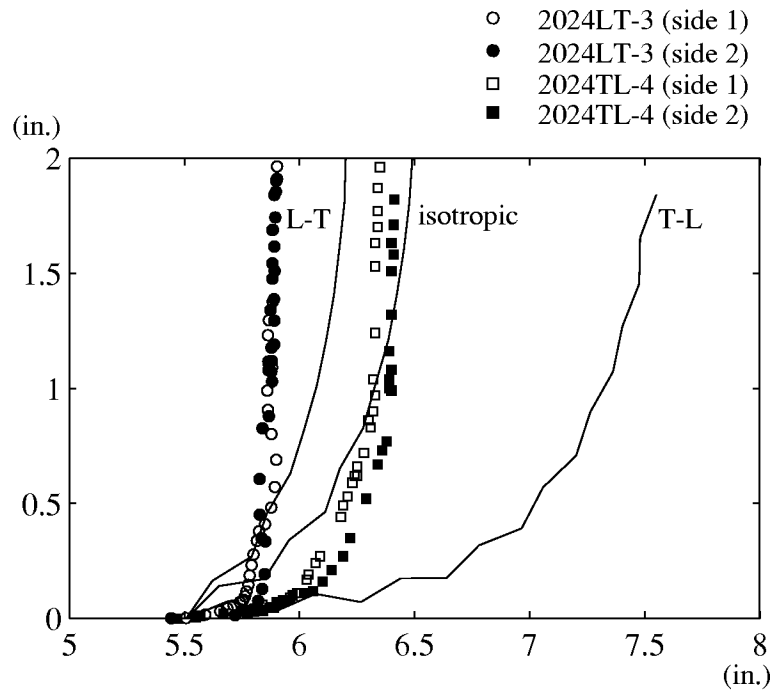


Figure 7.7: Predicted and measured crack trajectories for DCB specimen under stable crack growth: effect of the fracture toughness orthotropy (Equation (5.24) with  $r_c = 0.09$  inch;  $\frac{K_c(T)}{K_c(L)} = 1.1$ ;  $\Delta a = 0.2$  in.).

Material: Skin and tear strap, 2024-T3 clad,  $E=10,500$  ksi,  $\nu=0.33$ ;  
stringer and frame, 7075-T6 clad,  $E=10,700$  ksi,  $\nu=0.33$ ;

Radius: 74 inches

Skin: 0.036 in. thick

Tear strap: 0.036 in. thick

Stringer: 0.028-in.-thick hat section  
9.25-in. spacing

Frame: 0.040-in.-thick Z-section  
20-in spacing

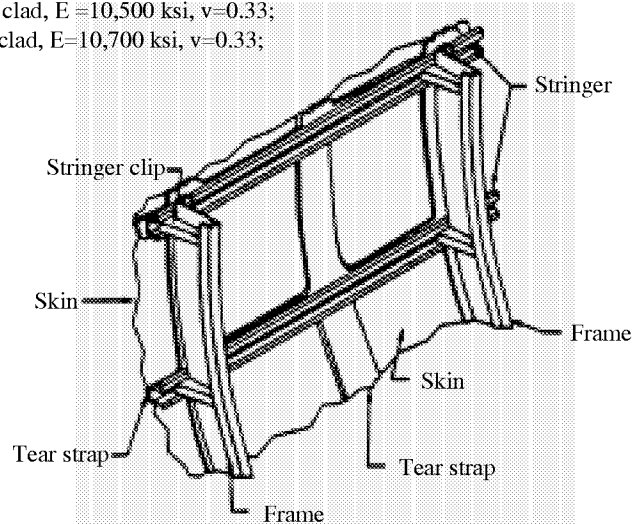


Figure 7.8: Structural features of a narrow body fuselage panel (modified after [85]).

## 7.2 Curvilinear Crack Growth Simulations For Fuselage Structures

Simulations of curvilinear crack growth in a generic narrow body fuselage panel were performed. The predicted crack trajectories were compared with the measured values from a full-scale pressurization test. The problem demonstrates the applicability of the direction criteria developed herein for predicting curvilinear crack growth in fuselage structures.

### 7.2.1 Description of Experiment

A narrow body fuselage panel with tear straps, stringers, stringer clips, and frames was tested by the Boeing Commercial Airplane Group. Skins and tear straps were made of 0.036 inch thick, 2024-T3 clad aluminum alloy. Stringers, frames, and stringer clips were made of 7075-T6 clad aluminum alloy. The tear straps were hot-bonded to the skins at midbay and at each frame station. The structural features of the test panel are shown in Figure 7.8. More information about panel dimensions can be found in [106, 48].

The panel had a 5.0 inch initial saw cut in the T-L orientation centered on the midbay tear strap and just above the stringer tear strap. The saw cut went completely through both the skin and midbay tear strap. The panel was inserted into a test fixture with a radius of curvature of 74 inches to match narrow body airplanes. A cyclic pressure of 7.8 psi was applied to propagate the crack. During the test, the positions of the crack tips were recorded. The detailed test data can be found in [106].

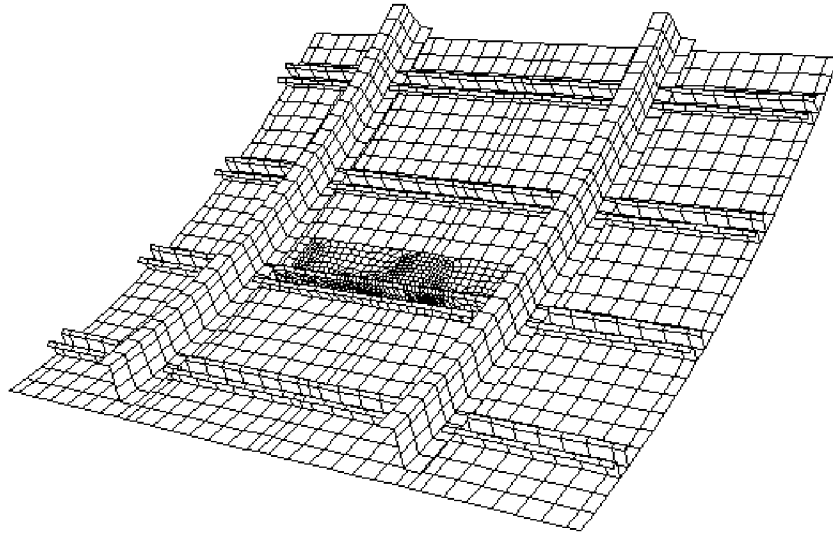


Figure 7.9: Finite element model for the narrow body fuselage panel.

### 7.2.2 Numerical Model

The entire curvilinear crack growth simulation consists of more than 20 inches of crack extension. As a result, using a global-local hierarchical modeling approach could require continual updating of the boundary conditions from the preceding model in the hierarchy due to the crack growth. This would increase efforts substantially in performing the numerical analyses. For this specific problem, only internal pressure was applied to the structure, thus a simple numerical model using symmetric boundary conditions might suffice to simulate the panel test.

In this study, a 4-stringer-bay wide and 2-frame-bay long panel was analyzed. All structural components including skins, stringers, and frames were modeled by quadrilateral shell elements. Each node of the shell element has six degrees of freedom. A typical finite element mesh used in the simulation is shown in Figure 7.9.

Geometrically nonlinear analyses were performed. Pressure loading was applied on the skin of the shell model. Symmetric boundary conditions were imposed on all the boundary edges of the model to simulate a cylinder-like fuselage structure. Uniform axial expansion was allowed at one longitudinal end. On this boundary edge, an axial force equal to  $(PR/2) \cdot L$  was assigned where  $P$  is the applied pressure,  $R$  is the radius of the panel, and  $L$  is the arc-length of the edge.

### 7.2.3 Fracture Parameter Evaluation

Deformation and stress fields near the crack tip were used to compute fracture parameters for crack growth simulations. The modified crack closure integral method



was used to compute the membrane and bending stress intensity factors ( $K_I$ ,  $K_{II}$ ,  $k_1$ ,  $k_2$ ) [106, 142]. The crack growth directional criteria, Equations (5.17) and (5.24) for the isotropic and orthotropic media, were used to predict the propagation angle in thin shell structures.

The equivalent domain integral method for  $T$ -stress developed in Chapter 6 is only valid for two-dimensional problems. The derivation of its counterpart for shell structures subjected to large displacements and rotations is not yet available. Instead, a simple displacement correlation method was used to evaluate the  $T$ -stress [69, 134, 104].

## 7.2.4 Numerical Results

### 7.2.4.1 Effect of $T$ -stress and $r_c$

The effect of  $T$ -stress and  $r_c$  on crack trajectory prediction was studied first. Crack growth direction was predicted by the isotropic directional criterion (Equation (5.17)). Figure 7.10 plots the predicted crack trajectories with  $r_c = 0$  and  $r_c = 0.09$  inch as well as the experimental measurements. Figure 7.11 shows the computed deformed shapes during curvilinear crack growth. Bulging caused by the applied pressure is observed. Moreover, severe flapping is predicted as the crack turns. Figure 7.12 shows the computed stress intensity factors and  $T$ -stress versus the half crack extension at the right crack tip. The sign conventions of stress intensity factors follow those in [106]. Predicted results suggest:

1. The  $T$ -stress has a very mild influence on the early crack trajectory prediction because of its small magnitude. But as the crack approaches the tear strap,  $T$ -stress increases and plays an important role in the crack turning prediction. For the case with  $r_c = 0.09$  inch, a sharp turning caused by  $T$ -stress is predicted as the crack approaches the tear strap.
2. The computed fracture parameters for  $r_c = 0$  and  $r_c = 0.09$  inch are comparable at the early stage of curvilinear crack growth. However, sharp turning as the crack approaches the tear strap alters the deformation and stress fields. This drastically changes the computed values of fracture parameters.
3. Predicted crack paths from both numerical simulations at the right and left crack tips are almost symmetric about the midbay, but the measured crack paths are not. This observation gives a preliminary indication of the experimental scatter that might occur in the panel test.

### 7.2.4.2 Effect of Fracture Toughness Orthotropy

The predicted crack growth trajectories depicted in Figure 7.10 are comparable to the experimental measurements, but with some discrepancy. The disagreement

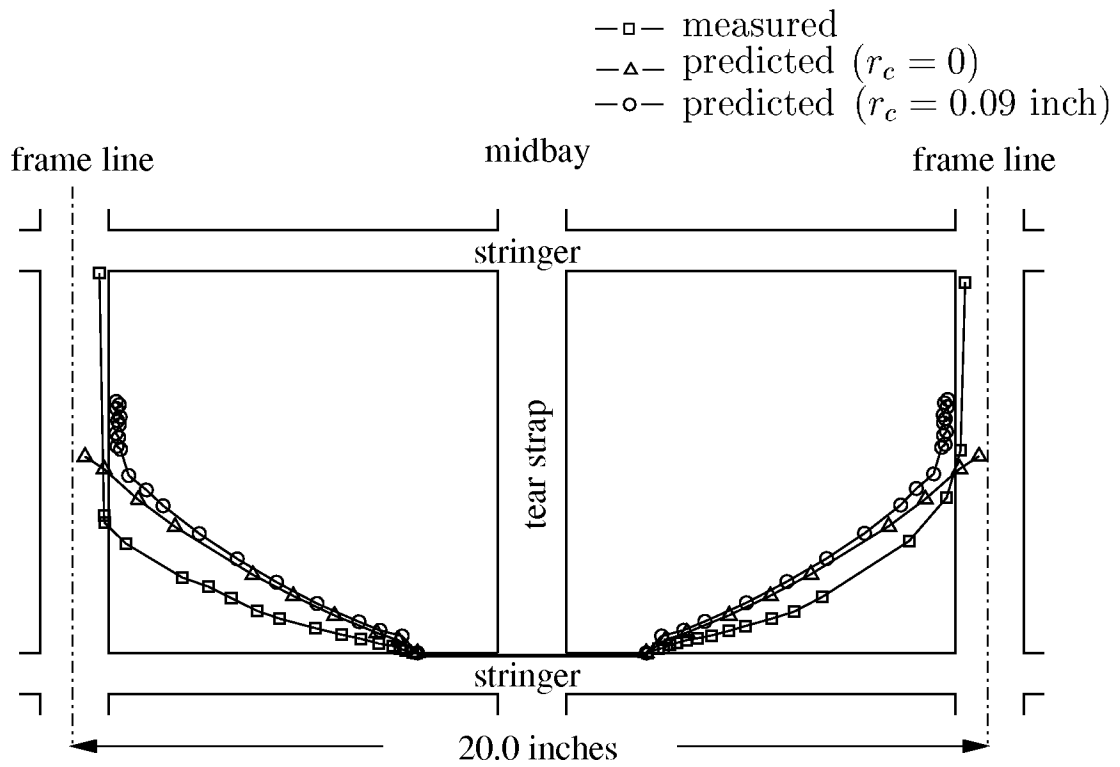


Figure 7.10: Comparisons between predicted and measured crack trajectories (isotropic directional criterion with various magnitudes of  $r_c$ ).

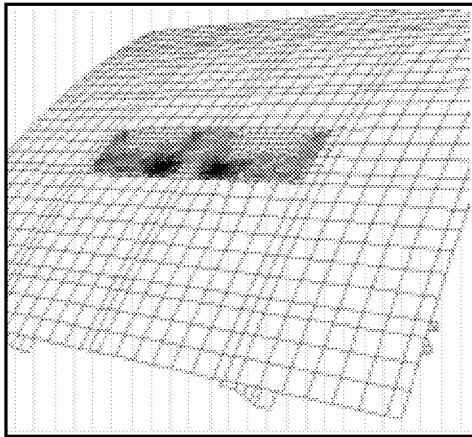
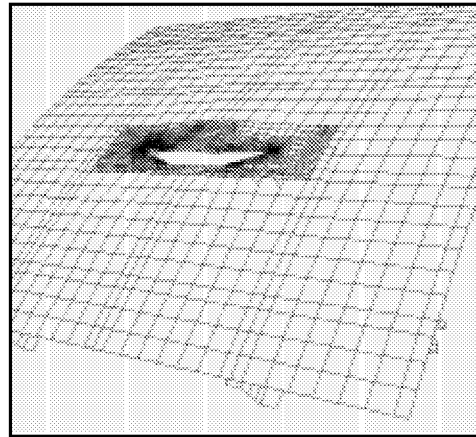
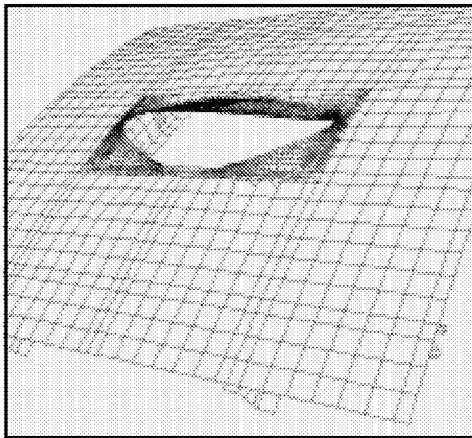
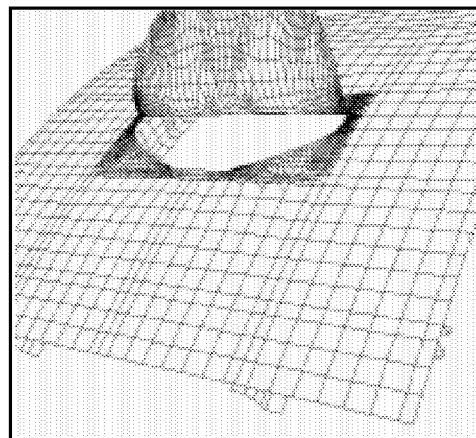
(a)  $a = 5.0$  in.(b)  $a = 12.0$  in.(c)  $a = 21.8$  in.(d)  $a = 23.6$  in.

Figure 7.11: Computed deformed shapes during curvilinear crack growth (isotropic case with  $r_c = 0.09$  inch, magnification factor = 2.0).

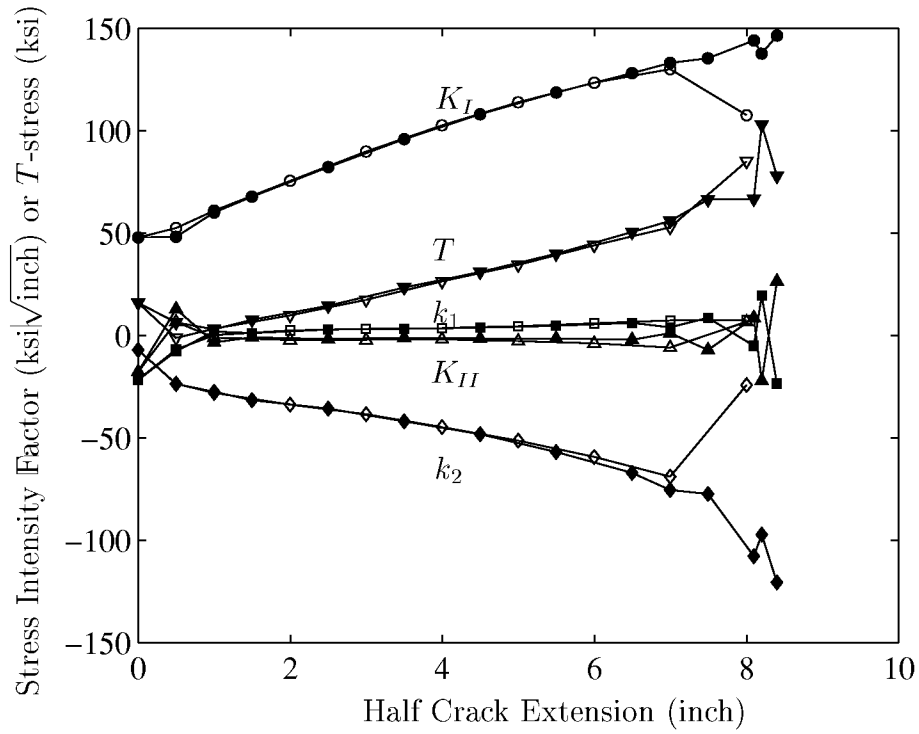


Figure 7.12: Computed stress intensity factors and  $T$ -stress versus half crack extension. The hollow and solid markers denote the computed fracture parameters for the isotropic case with  $r_c = 0$  and  $r_c = 0.09$  inch, respectively.

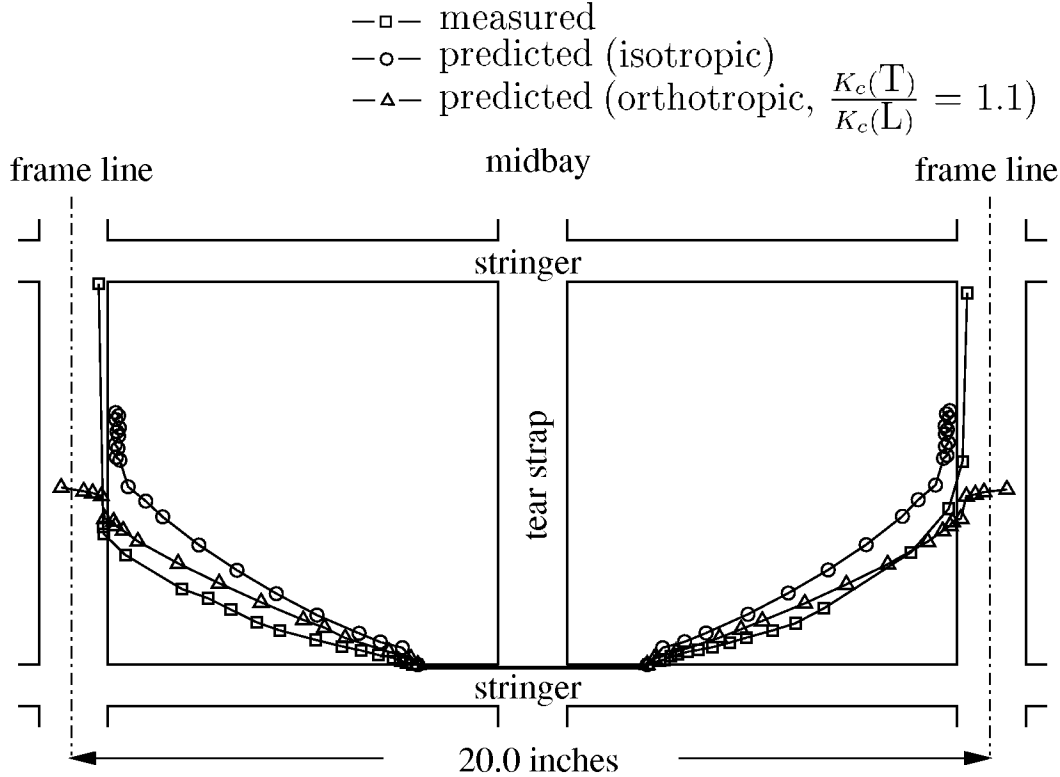


Figure 7.13: Comparisons between predicted and measured crack trajectories (isotropic and orthotropic cases with  $r_c = 0.09$  inch).

during early stages of crack growth might be related to the fracture toughness orthotropy of the fuselage skins.

In subsequent analyses, the orthotropic directional criterion, *i.e.*, Equation (5.24), was used to predict the propagation angle. From the coupon test results, the fracture toughness for this material and thickness was about  $100 \text{ ksi}\sqrt{\text{inch}}$  in the L direction and  $105\text{--}120 \text{ ksi}\sqrt{\text{inch}}$  in the T direction [106]. Thus, the fracture toughness was assumed to be 10% higher in the T than in the L direction. The predicted crack trajectories with  $r_c = 0.09$  inch were compared with those from the isotropic prediction and experimental measurements. As shown in Figure 7.13, during early stages of crack growth, the predicted trajectories for the orthotropic case agree better with the experimental measurements than the isotropic case. Crack growth simulation with fracture orthotropy also predicts crack turning as the crack approaches the tear strap. Yet, when the crack grows further into the tear strap region, the inclusion of fracture orthotropy adversely alters the crack path prediction and does not predict flapping as observed in the panel test.

Several possible reasons may explain why the current methodology including the fracture toughness orthotropy does not predict the desired flapping and should be examined in future research:

1. Characteristic feature of fracture orthotropy in the tear strap region—The

material orientation in the tear strap differs from that in the skin (*i.e.*, the transverse direction in the tear strap is along the longitudinal direction of the skin and vice versa). As a result, the material characteristics in this overlapped region may behave like a quasi-isotropic material with less fracture toughness orthotropy.

2. Occurrence of debonding between the skin and tear strap—In the current model, we assume that the skin and tear strap are perfectly bonded. However, as the crack grows into this region, the adhesive bond between the skin and tear strap is likely to fail. This inevitably alters the local crack tip stress fields and would consequently affect the crack growth behavior.
3. Thin-shell representation of three-dimensional behavior—The thin-shell approximation does not capture all the three-dimensional complexities of the problem in the vicinity of the tear strap, particularly in the crack tip region. Further study on three-dimensional crack growth simulations is needed to quantify the three-dimensional effect on crack turning prediction.
4. Sources of error from the computed fracture parameters—Accurate stress intensity factor and  $T$ -stress evaluations in this region are crucial to predict crack turning. Current crack growth simulations use a low-order polynomial degree of shape functions for thin-shell finite element analyses and use a displacement correlation method to extract the  $T$ -stress term from the finite element solutions. Further study using adaptive and higher order shell finite element analyses would improve the accuracy of numerical computation. Other numerical methods, for example, path independent integrals for geometrically nonlinear shells would also improve the accuracy of fracture parameter evaluations.
5. Validity of the LEFM approach—The crack growth directional criterion and its subsequent curvilinear crack growth simulations explicitly assume that the crack is grown under small scale yielding conditions. Yet, as the length of the fatigue crack extends to a sufficient amount, stable tearing and extensive plasticity are likely to occur. The active plastic zone and accumulated plastic wake due to stable tearing would likely affect the crack growth prediction.
6. Validity of the magnitude of  $r_c$ —In the current study, the parameter  $r_c$  is assumed to be a constant magnitude during the entire curvilinear crack growth simulations. Also the same constant magnitude of  $r_c$  is used in the T and L directions. The magnitude of  $r_c$  used in the current simulation (0.09 inch) is mainly based on the predicted results that best correlate the crack trajectories observed in the DCB tests and the isotropic results that predict crack flapping in the current fuselage model. Further study on the appropriate experimental methods and numerical simulations for determining the magnitude of  $r_c$  is needed to validate the current approach.

### 7.2.5 Comparisons with Previous Studies

Potyondy *et al.* [106, 108] and Chen *et al.* [21] have reported numerical simulations for this problem previously. Both studies analyzed early curvilinear crack growth but did not address the issue of sharp turning as the crack approaches the tear strap. It is, nevertheless, of interest to compare these results with the current prediction. This serves two purposes: one is to assess the accuracy of the simulation through comparisons with independent numerical simulations and the other is to show alternate modeling representations that may affect the crack trajectory prediction.

In Potyondy *et al.* [106, 108] and Chen *et al.* [21], a global-local hierarchical modeling approach was used to model the panel test. Three hierarchical modeling levels were employed, comprised of a global shell model, a 6x6 bay stiffened panel model, and a 2x2 bay stiffened panel model. Crack growth was only performed in the 2x2 bay model, the lowest level in the hierarchy. The kinematic boundary conditions on the 2x2 bay model were not updated during crack growth. Also, the boundary conditions applied to the global shell model corresponded with an open cylinder. Thus, the longitudinal stress in this numerical model is expected to be less than that in the test fixture, since the test fixture is a closed cylinder.

The directional criterion used in Potyondy *et al.* and Chen *et al.* corresponds to the Erdogan and Sih directional criterion [41], *i.e.*, Equation (5.18); thus comparisons are made with the isotropic prediction with  $r_c = 0$ . Figure 7.14 shows the predicted crack growth trajectories from previous and current studies as well as experimental measurements. We note that the initial crack location in Potyondy's simulations was modeled at 0.45 inch away from the intersection of the skin and stringer due to limitations in the previous version of the FRANC3D program. Figures 7.15 and 7.16 show the computed stress intensity factors at the right crack tip in comparison with [21] and [106, 108], respectively. From these results, we conclude:

- The applied axial force used to model the longitudinal stress caused by a closed cylinder has little influence on the computed stress intensity factors. This can be seen from the computed values shown in Figure 7.15 at zero crack extension; two numerical simulations at this stage basically represent the same boundary conditions and crack configuration except an axial force was applied in the current model.
- The fact that the kinematic boundary conditions were not altered during crack growth in the previous studies has a mild affect on the crack trajectory prediction and stress intensity factor computation. In the previous studies, the kinematic boundary conditions used in the lowest level in the hierarchy were obtained from a global model with an initial 5.0 inch crack. We can certainly conclude that the driving force for this case would be less than the one with updated boundary conditions as the crack grows. This is properly reflected on the computed  $K_I$  values shown both in Figures 7.15 and 7.16.

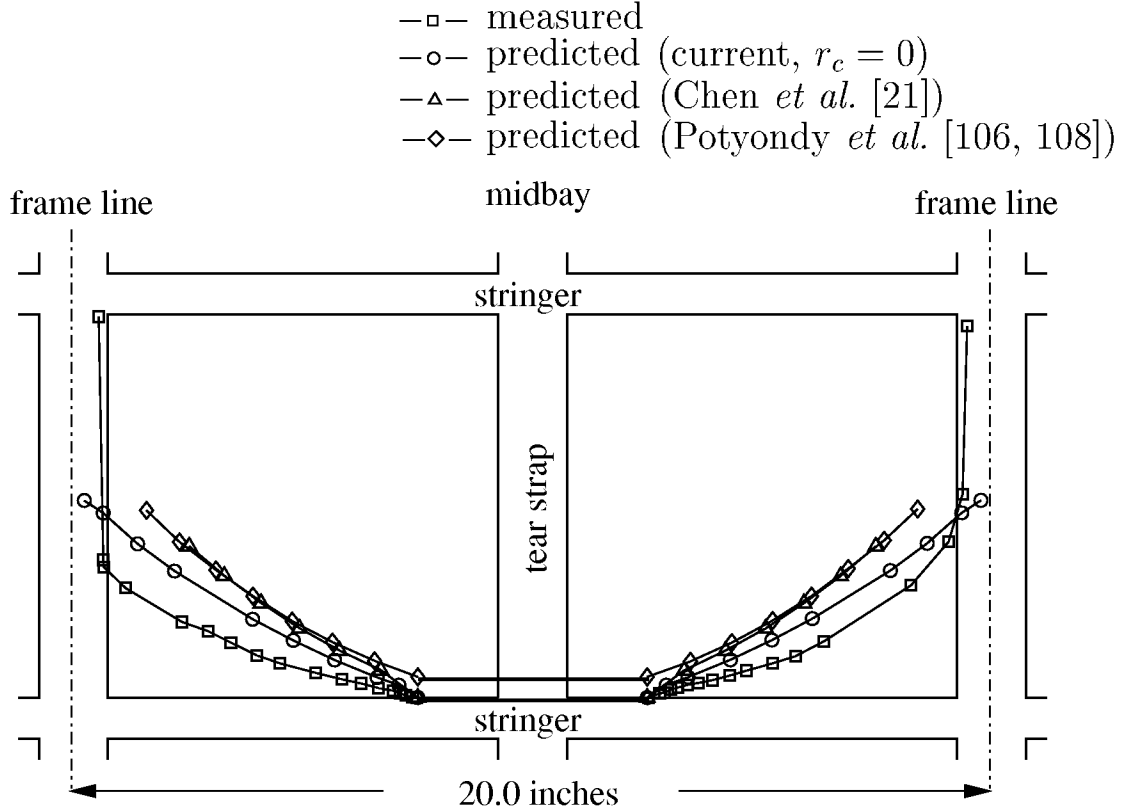


Figure 7.14: Comparisons between predicted and measured crack trajectories (isotropic directional criterion with various magnitudes of  $r_c$ ).

The issue seems to have little effect on the computed values of  $K_{II}$ , since they remain more or less the same for all cases. This leads to a lower ratio of  $K_{II}/K_I$  in the current model with updated boundary conditions. As a result, more shallow crack trajectories are predicted in the present study. Nevertheless, the computed fracture parameters are comparable with previous results; thus, a similar fatigue life is anticipated.

### 7.2.6 Concluding Remarks for Curvilinear Crack Growth Simulation in Narrow Body Fuselage Panel

Curvilinear crack growth in a generic narrow body fuselage was studied. Comparisons with experimental measurements suggest that the fracture toughness orthotropy plays an important role in predicting the early crack growth trajectories. The subsequent crack growth after the initial crack deflection followed a trajectory where the local stress states are of a Mode I type. Thus, like crack growth in DCB specimens, crack turning and flapping as the crack approaches the tear strap is highly related to the  $T$ -stress.



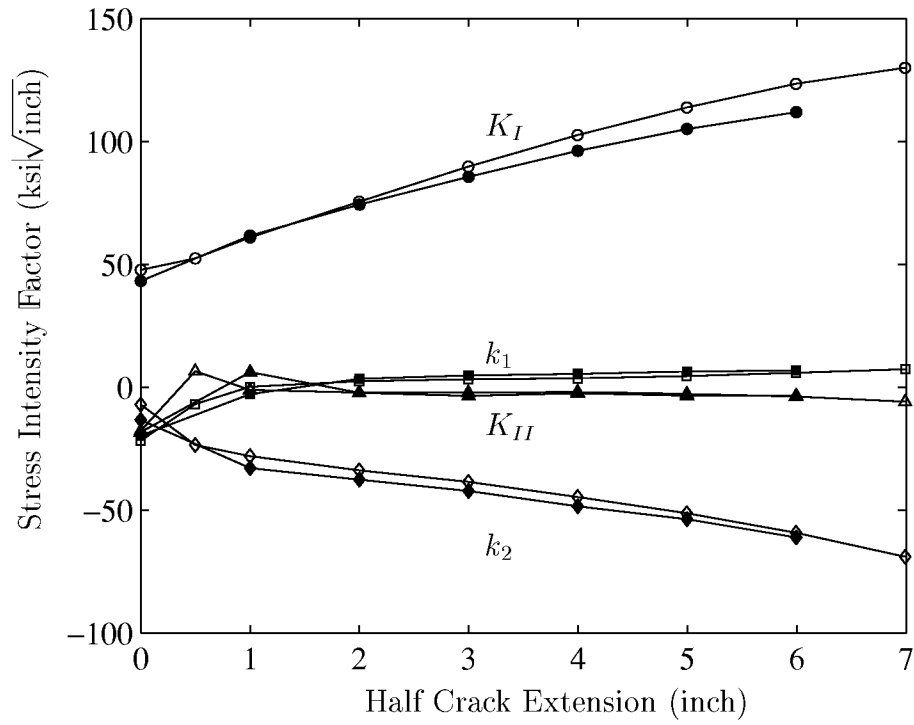


Figure 7.15: Computed stress intensity factors versus half crack extension. The hollow and solid markers denote the computed stress intensity factors from the current isotropic prediction with  $r_c = 0$  and those from Chen *et al.* [21], respectively.

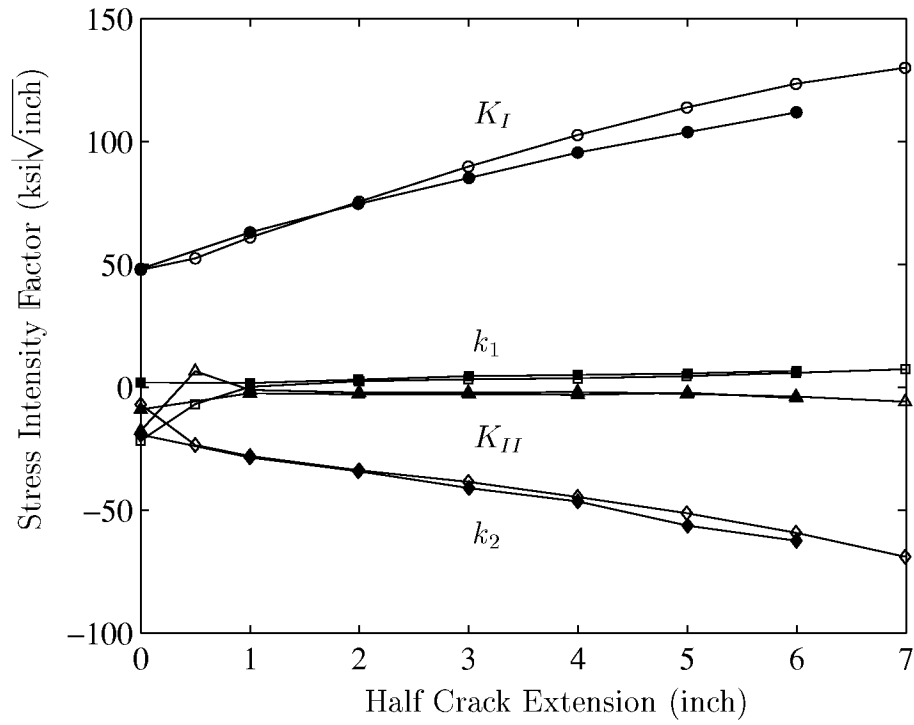


Figure 7.16: Computed stress intensity factors versus half crack extension. The hollow and solid markers denote the computed stress intensity factors from the current isotropic prediction with  $r_c = 0$  and those from Potyondy *et al.* [106, 108], respectively.

The predicted results based on the proposed methodology show the potential to characterize curvilinear crack growth, but further studies as discussed in Section 7.2.4.2 need to be conducted to fully assess its applicability as part of a damage tolerance methodology.

### 7.3 Discussion: Elastic-Plastic Curvilinear Crack Growth and Residual Strength Prediction

The above curvilinear crack growth simulations explicitly assume that the crack is grown under small scale yielding conditions. To simulate elastic-plastic curvilinear crack growth, one can use the predicted curvilinear crack path as the predefined crack path and stable crack growth and residual strength analyses can be performed accordingly. The procedure was used in Chen *et al.* [21, 20] to study the trajectory effect on residual strength prediction.

A more rigorous approach is to use a directional criterion based on the current elastic-plastic states at crack tips directly. A procedure for mapping the state variables from one finite element mesh to another is then performed as the crack propagates. A plane stress, non-self-similar elastic-plastic crack growth simulation based on the CTOD directional criterion discussed in Section 5.4.2 in conjunction with the CTOA crack growth criterion has recently been implemented [62]. The predicted results are comparable to those observed in the Arcan fracture tests. Future work is needed to assess the applicability of the mapping algorithm and direction criterion to fuselage structures under stable tearing.

### 7.4 Summary

The directional criteria developed in Chapter 5 were used to predict curvilinear crack growth in coupon tests and in full-scale fuselage panel tests. The predicted trajectories were in good agreement with those observed in the tests.

The influence of various parameters on the crack trajectory prediction was studied. Both  $T$ -stress and fracture orthotropy were found to be essential to predict the observed paths. The proposed methodology shows its potential to predict crack turning and flapping that can be used as part of a damage tolerance methodology.

## Chapter 8

# Summary, Conclusions, and Recommendations for Future Work

This chapter summarizes the contributions of this thesis, draws conclusions, and where appropriate, provides recommendations for future work.

This dissertation begins with a description of aging aircraft problems faced by the aircraft community. Aging of aircraft may significantly reduce structural integrity and residual strength below an acceptable level. This concern serves as the primary motivation for the dissertation. The objective is to develop an accurate structural analysis methodology and a useful and usable software tool for predicting the structural integrity and residual strength of pressurized, thin-shell structures.

Background material related to structural integrity of aircraft fuselages and effective simulations of arbitrary crack growth is discussed in Chapter 1. This serves as a departing point to study simulations of fracturing processes in thin-shell structures. The dissertation is then divided into two parts to facilitate the discussion. Chapters 2 through 4 deal with the crack tip opening angle (CTOA) fracture criterion obtained from coupon tests to the prediction of fracture behavior and residual strength of built-up aircraft fuselages. Chapters 5 through 7 discuss relevant issues for crack trajectory prediction methodologies to improve structural integrity of airframes. Summaries, conclusions, and recommendations for future work of each part are presented below.

## 8.1 Part One: Elastic-Plastic Crack Growth Simulation and Residual Strength Prediction

### 8.1.1 Chapter 2: Theory for CTOA-Driven Elastic-Plastic Crack Growth and Residual Strength Analysis

Various fracture mechanics methods for simulating elastic-plastic crack growth and predicting residual strength of thin-sheet metallic structures are reviewed and critiqued in Chapter 2. The fracture analysis methods include linear elastic fracture mechanics (LEFM) and elastic plastic fracture mechanics (EPFM) versions of  $K_R$ ,  $G_R$ ,  $J_R$ ,  $\delta_R$ ,  $T_R^*$ , and CTOA using two-dimensional and three-dimensional analyses. Among the methods, the CTOA fracture criterion with three-dimensional elastic-plastic analyses is found to be superior because of its relative independence of the geometry of the structure, the length of the crack, and the presence of multiple cracks. Elastic-plastic crack growth, link-up of multiple cracks, and residual strength analyses using the CTOA fracture criterion are discussed.

### 8.1.2 Chapter 3: Residual Strength Analysis of a Flat Panel with Self-Similar Elastic-Plastic Crack Growth

In Chapter 3, numerical simulations of flat panel tests are conducted by using thin-shell finite element analyses. The CTOA fracture criterion is used to characterize elastic-plastic crack growth. Two sets of fracture tests are simulated: one with a single crack but different widths and the other with multiple cracks.

Predicted results of the flat panel simulations with a single crack show two distinct failure phenomena. For small specimens, plastic zones reach the free boundary and the limit load is attained due to net section yielding. For large specimens, plastic zones are well confined by the elastic region and residual strength is reached due to fracture instability. Results of predicted residual strength are comparable to experimental measurements. Yet as the width of the panel increases, the relative difference between experimental measurements and numerical predictions increases. This discrepancy is associated with the three-dimensional nature of the stresses around the crack tip, a result of constraint effects due to the finite thickness of the panels. A plane strain core concept is proposed to incorporate the three-dimensional constraint effects into two-dimensional as well as thin shell analyses. Predicted results with the plane strain core follow those of three-dimensional analyses and experimental measurements for small and large panels.

Predicted residual strength of small flat panels with multiple cracks agrees well with experimental measurements. A loss of residual strength due to the presence of multiple small cracks is observed.

### 8.1.3 Chapter 4: Residual Strength Analysis of Fuselage Structures with Self-Similar Crack Growth

Chapter 4 examines the feasibility and validity of the analysis methodology to predict residual strength of pressurized fuselage structures that are subjected to widespread fatigue damage (WFD). The first part of the chapter uses a relatively simple built-up configuration to examine the effect of lead crack sizes, multi-site damage (MSD), and material thinning due to corrosion damage. Predicted results indicate a 21.8 to 28.0% loss of residual strength due to the presence of small MSD. Coupling of MSD and corrosion damage leads to the most severe damage scenario.

The second part of the chapter describes analyses of fuselage panels tested in a wide body, pressure test fixture. The objective is to validate the analysis methodology by direct comparison of numerical and experimental results. A global-local hierarchical modeling strategy is used to analyze the panel tests. This modeling strategy allows one to obtain sufficient accuracy of computed values with reasonable computer resources.

Predicted stress distributions in the vicinity of the lap joint are compared with strain gage readings. Major results from the strain gage comparison are:

- For global and local models of about the same coarse mesh density, the predicted results converge quickly and agree with experimental measurements.
- Results with a much higher mesh density that is suitable for stable crack growth analysis disagree with the rest of the numerical predictions and experimental measurements. The discrepancy is related to the idealized representation of the two-noded spring element for the rivet connection. The problem is effectively overcome by generating distributed connections between the two-noded spring element and the surrounding shell elements.

Elastic-plastic crack growth analyses using the CTOA fracture criterion are conducted. Numerical results for the case with and without MSD are compared to experimental observations. Two key factors are found to be crucial for accurate prediction of stable crack growth and residual strength of the wide body panel tests. One is to incorporate the residual plastic deformation left by the fatigue crack growth, and the other is to consider the failure of other structural elements during stable crack growth. The specific highlights are:

- The residual plastic deformation or the plastic wake from fatigue crack growth has a strong effect on stable crack initiation but a mild effect on residual strength prediction. Neglecting plastic wake effect leads to a totally erroneous prediction of the early stable crack growth.
- The breakage of the inner tear strap, categorized as possible failure of other structural elements during stable crack growth, is crucial to residual strength prediction. For all the analyses conducted, the occurrence of the broken tear strap reduces the predicted residual strength by 24% to 30%.

Both observed and predicted results of the wide body panel tests again show substantial reduction of residual strength due to the occurrence of MSD.

#### 8.1.4 Recommendations for Future Work

For cracks in a pressurized fuselage, the out-of-plane deformation or bulging at the crack edges is an essential characteristic feature of the displacement fields. The current analysis methodology assumes that the same critical CTOA determined from flat panel tests with guide plates suffices to characterize the fracturing processes. To fully justify this assumption, laboratory tests that generate the out-of-plane deformation during stable crack growth need to be conducted<sup>1</sup>. Numerical simulations of these laboratory tests using geometrically and materially nonlinear thin-shell and three-dimensional crack growth analyses will shed new light on the possible invariance of the CTOA fracture criterion to crack bulging.

Constraint effects due to finite thickness of the panels are currently incorporated into thin-shell finite element analyses by an *ad-hoc* fashion, that is, using a plane strain core concept along the tearing crack path. Fully three-dimensional analyses or *mixed* thin-shell and three-dimensional analyses can automatically capture the three-dimensional constraint effect and eliminate the need for the plane strain core. A *mixed* model consisting of thin shell and three-dimensional idealizations as illustrated in Figure 8.1 seems to be a very attractive approach. Using this approach, fracture behavior around the crack tip region can be described accurately by three-dimensional analyses while thin shell idealizations may apply to the remote regions where the through thickness effect can be ignored.

The current model does not faithfully represent crack growth in the vicinity of rivets. Distributed connections may be adequate to represent load transfer through the rivets, but may not have sufficient accuracy to characterize fracturing processes. Further laboratory fracture tests and analyses of various lap-jointed configurations need to be conducted to quantify its effect on stable crack growth and residual strength prediction.

The current analysis procedures of incorporating the residual plastic deformation for stable tearing do not include the effect of crack face contact. This leads to a much higher crack-opening pressure in comparison with 2D plane stress results and laboratory observations. Further study is needed to quantify its effect on residual strength prediction.

Widespread fatigue damage (WFD) has two subsets: multi-site damage (MSD) and multi-element damage (MED). The effect of MSD on residual strength can be analyzed and accurately predicted by the current methodology. The MED is yet to be explored rigorously. Also, the similar scenario including static or dynamic failure of other structural elements during stable crack growth needs further investigation. A proper mechanism to initiate and propagate damage in other structural elements

---

<sup>1</sup>The MT specimen with the width larger than 24 inch but without guide plates seem to be a plausible candidate.

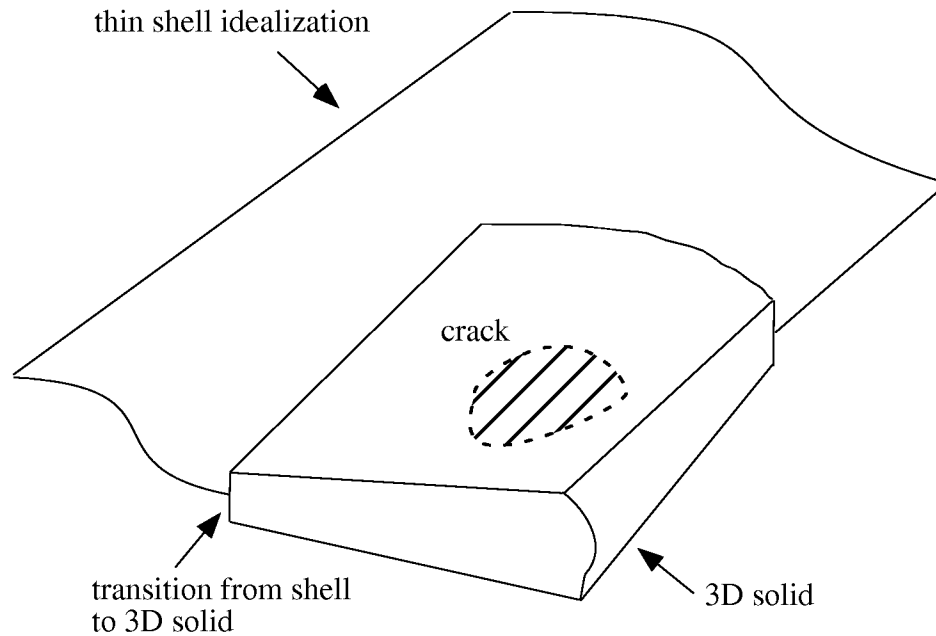


Figure 8.1: Illustration of *mixed modeling* of thin shell and 3D solids.

needs to be included in stable crack growth analyses.

Material thinning due to corrosion damage that may occur in aging aircraft is modeled through a uniform thickness reduction over the skin at the lap joint. More detailed analyses are needed to assess its applicability in characterizing corrosion damage.

Finally, the methodology developed herein is mainly for thin-sheet metallic structures. Its applicability to thick, heavily loaded structures (for example, wings) or to different materials (for example, composites) is yet to be determined.

## 8.2 Part Two: Curvilinear Crack Growth Simulation

### 8.2.1 Chapter 5: Theory for Curvilinear Crack Growth in Planar and Thin Shell Structures

This chapter begins with the motivation for using the crack turning phenomenon to improve the structural integrity of fuselage structures. To predict a crack trajectory that is not known *a priori*, a criterion for predicting the crack propagation direction is required.

The maximum tangential stress theory is used as a starting point to evaluate the direction of crack growth. Full stress and displacement fields in two-dimensions and asymptotic fields in thin plates subjected to bending are outlined.

The crack growth direction criterion based on the two-dimensional, linear elas-



tic crack tip fields is assumed to be sufficient to handle thin shell problems under the LEFM conditions. Singular as well as non-singular constant stress fields are included in evaluating the tangential stress near the crack tip. A directional criterion based on the maximum tangential stress up to the order of the  $T$ -stress term is derived. The specific highlights include:

- The predicted propagation angle is determined based on  $r_c$ ,  $K_I$ ,  $K_{II}$ , and  $T$ . A predicted propagation angle diagram is presented using a non-dimensional parameter  $\bar{T}$  where  $\bar{T} \equiv (8T\sqrt{2\pi r_c})/(3K_I)$ .
- Under pure Mode-I and positive  $T$ -stress conditions, the crack path instability will occur when  $r_c > (9K_I^2)/(128\pi T^2)$ .
- Under general mixed-mode conditions, the criterion predicts a bigger propagation angle under positive  $T$ -stress and a smaller angle under negative  $T$ -stress. The criterion reduces to the Erdogan and Sih criterion when  $T = 0$  or  $r_c = 0$ .

The criterion is then extended to include the effect of fracture toughness orthotropy. A simple elliptical function is used to characterize the anisotropic fracture resistance in different material orientations. The effect of fracture toughness orthotropy ratio and the material orientation angle on the predicted propagation angle is examined.

The rest of the chapter examines possible extensions of the current crack growth direction criterion to handle geometrically and materially nonlinear problems.

For elastic deformations of arbitrary magnitude, the extensions rely on finding the Lagrangian counterparts of conservative integrals, well-defined under elastic states with infinitesimal deformations, in the context of finite elastic deformations. The fracture parameters are then related to these conservative integrals.

For elastic-plastic problems two directional criteria are examined: one based on the HRR fields and the other based on the crack tip opening displacement (CTOD) concept. The study concludes that neither the HRR type extension of the maximum tangential stress theory nor the CTOD based directional criterion is currently sufficient to fully characterize the direction of elastic-plastic crack growth.

### 8.2.2 Chapter 6: Numerical Evaluation of $T$ -Stress

Numerical methods to obtain accurate  $T$ -stress for two-dimensional as well as thin shell problems are the main theme of Chapter 6. The specific highlights are:

- Two types of path independent integrals for  $T$ -stress evaluations are presented: one based on the Betti-Rayleigh reciprocal theorem and the other on Eshelby's energy momentum tensor. The analytical and numerical equivalence between the two is found.

- A novel error estimator for  $T$ -stress is proposed to quantify and assess the accuracy of computed values. Specifically, it is found that the error of the computed  $T$ -stress is proportional to the ratio of stress intensity factor divided by the square root of the characteristic dimension of the integration domain where the path independent integral is evaluated.
- Numerical accuracy in evaluating  $T$ -stress using the path independent integral method is assessed by highly accurate two-dimensional p- and hp-version adaptive finite element analyses.

### 8.2.3 Chapter 7: Curvilinear Crack Growth Simulations

Chapter 7 analyzes curvilinear crack growth in double cantilever beam (DCB) specimens and in full-scale narrow body fuselage panel tests. The specific highlights for curvilinear crack growth in the DCB specimens are:

- Observations in the fracture tests indicate that the crack tends to turn away from its initial crack tip under pure Mode I conditions. The crack growth directional criterion, incorporating the  $T$ -stress effect, is capable of capturing the essence of crack turning under such circumstance. The predicted results with  $r_c = 0.09$  inch best correlate the experimental data for stable tearing. The predicted results with  $r_c = 0.06$  inch best correlate the experimental data for fatigue crack growth.
- The fracture toughness orthotropy is introduced to explain the difference between the measured crack paths in the L-T and T-L orientations. The orthotropic directional criterion shows a promising nature to correlate the experimental data.

The specific highlights for curvilinear crack growth in the full-scale narrow body fuselage panel tests are:

- $T$ -stress has a very mild influence on the early crack trajectory prediction because of its small magnitude. But as the crack approaches the tear strap,  $T$ -stress increases and plays an important role in the crack turning prediction. For the case with  $r_c = 0.09$  inch, a sharp turning caused by  $T$ -stress is predicted as the crack approaches the tear strap.
- The fracture toughness orthotropy has a strong effect on the early crack trajectory prediction. The predicted crack trajectory, with 10% higher fracture toughness in the T than in the L direction of propagation, agrees well with that from the experimental measurements, before the crack approaches the tear strap.

### 8.2.4 Recommendations for Future Work

The current methodology assumes that the maximum tangential stress directional criterion developed under the two-dimensional, LEFM framework can be directly applied to thin shell problems. Further crack trajectory study of fracture coupon tests and full-scale fuselage panel tests is needed to fully justify the assumption.

A rigorous elastic-plastic directional criterion for non-self-similar stable crack growth simulations is yet to be found. A procedure that maps the state variables from one finite element mesh to another as the crack propagates is yet to be implemented into the FRANC3D/STAGS software program.

Accurate stress intensity factor and  $T$ -stress evaluations as the crack approaches the tear straps are crucial to predict the crack turning. In the current study, the convergence study was conducted to ensure the accuracy of fracture parameter evaluations. Further study on adaptive and higher order shell finite element analyses may help to improve the accuracy of numerical computation. Other numerical methods, for example, path independent integrals for geometrically nonlinear shells may also help to improve the accuracy of fracture parameter evaluations.

The physical meaning of the parameter  $r_c$  is yet to be found and the appropriate experimental method to measure  $r_c$  is yet to be determined. Further understanding of fracture behavior at the meso- or micro-scale may shed new light on  $r_c$ , and furthermore, the crack growth directional criterion.

# Bibliography

- [1] B. E. Amstutz, M. A. Sutton, D. S. Dawicke, and J.C. Newman, Jr. An Experimental Study of CTOD for Mode I/ II Stable Crack Growth in Thin 2024-T3 Aluminum Specimens. In *Fracture Mechanics: 26th Volume, ASTM STP 1256, Philadelphia*, pages 256–271, 1995.
- [2] H. Anderson. Finite Element Representation of Stable Crack Growth. *International Journal of Fracture*, 21:337–356, 1973.
- [3] ASTM. Standard Practice for *R*-Curve Determination. *ASTM E561-94, Annual Book of ASTM Standard*, 03.01:489–501, 1997.
- [4] S. N. Atluri. *Structural Integrity & Durability*. Tech Science Press, Georgia, U.S.A., 1997.
- [5] AWST. Aging Aircraft Issue Presents Major Challenge to Industry. *Aviation Week & Space Technology*, pages 42–95, July 24 1989.
- [6] I. Babuška and B.A. Szabó. On the Rates of Convergence of the Finite Element Method. *International Journal for Numerical Methods in Engineering*, 18:323–341, 1982.
- [7] L. Banks-Sills. Application of the Finite Element Method to Linear Elastic Fracture Mechanics. *Applied Mechanic Reviews*, 44:447–461, 1991.
- [8] L. Banks-Sills. A Conservative Integral for Determining Stress Intensity Factors of a Bimaterial Strip. *International Journal of Fracture*, 86:385–398, 1997.
- [9] J. M. Barsom and S. T. Rolfe. *Fracture and Fatigue Control in Structures*. Prentice-Hall, Inc., Englewood, New Jersey, 1987.
- [10] J. M. Bloom. An Evaluation of Fracture Analysis Methods. In *Elastic-Plastic Fracture Mechanics Technology, ASTM STP 896, Philadelphia*, pages 114–127, 1985.
- [11] G. E. Bockrath and J. B. Glassco. *Theory of Ductile Fracture*, November 1981. California State University Report No. ME 81-400, Long Beach, CA.

- [12] T. J. Boone, P. A. Wawrzynek, and A. R. Ingraffea. Finite Element Modeling of Fracture Propagation in Orthotropic Materials. *Engineering Fracture Mechanics*, 26(2):185–201, 1987.
- [13] D. Broek, D. Y. Jeong, and T. P. Forte. Testing and Analysis of Flat and Curved Panels with Multiple Cracks. In *Proceedings of the FAA-NASA Sixth International Conference on the Continued Airworthiness of Aircraft Structures*, pages 85–98, Atlantic City, New Jersey, 1994.
- [14] M. B. Buczek and C. T. Herakovich. A Normal Stress Criterion for Crack Extension Direction in Orthotropic Composite Materials. *Journal of Composite Materials*, 19:544–553, 1985.
- [15] H. D. Bui. Associated Path Independent  $J$ -Integrals for Separating Mixed Modes. *Journal of the Mechanics and Physics of Solids*, 31:439–448, 1983.
- [16] G. E. Cardew, M. R. Goldthorpe, I. C. Howard, and A. P. Kfoury. On the Elastic T-term. In *Fundamentals of deformation and fracture : Eshelby memorial symposium*, 1985.
- [17] B. J. Carter, C.-S. Chen, P. A. Wawrzynek, and A. R. Ingraffea. A Topology-Based System for Modeling 3D Crack Growth in Solid and Shell Structures. In *Proceedings of the Ninth International Congress on Fracture, ICF9*, pages 1923–1934, Sydney, Australia, 1997. Elsevier Science Publishers.
- [18] B. J. Carter, P. A. Wawrzynek, and A. R. Ingraffea. Automated 3D Crack Growth Simulation. Submitted for publication, International Journal for Numerical Methods in Engineering, 1998.
- [19] C.-S. Chen. *Crack Growth Simulation and Residual Strength Prediction in Thin Shell Structures*. Ph.D. Thesis, Cornell University, January 1999.
- [20] C.-S. Chen, P. A. Wawrzynek, and A. R. Ingraffea. Simulation of Stable Tearing and Residual Strength Prediction with Applications to Aircraft Fuselages. In *Proceedings of the FAA-NASA Symposium on Continued Airworthiness of Aircraft Structures*, pages 605–618, 1996.
- [21] C.-S. Chen, P. A. Wawrzynek, and A. R. Ingraffea. Methodology for Fatigue Crack Growth and Residual Strength Prediction with Applications to Aircraft Fuselages. *Computational Mechanics*, 19:527–532, 1997.
- [22] C.-S. Chen, P. A. Wawrzynek, and A. R. Ingraffea. Recent Advances in Numerical Simulation of Stable Crack Growth and Residual Strength Prediction. In *the Sixth East Asia-Pacific Conference on Structural Engineering & Construction*, pages 1773–1778, 1997.

- [23] C.-S. Chen, P. A. Wawrzynek, and A. R. Ingraffea. Elastic-Plastic Crack Growth Simulation and Residual Strength Prediction of Thin Plates with Single and Multiple Cracks. In *Fatigue and Fracture Mechanics: 29th Volume, ASTM STP 1332*, 1998 (in press).
- [24] D. Cope. Corrosion Damage Assessment Framework: Corrosion/Fatigue Effects on Structural Integrity. Technical Report D500-13008-1, The Boeing Defense and Space Group, 1998.
- [25] D. Cope. Private Communication. The Boeing Defense and Space Group, 1998.
- [26] B. Cotterell and J. R. Rice. Slightly Curved or Kinked Cracks. *International Journal of Fracture*, 16:155–169, 1980.
- [27] D. S. Dawicke. Residual Strength Predictions Using a Crack Tip Opening Angle Criterion. In *Proceedings of the FAA-NASA Symposium on the Continued Airworthiness of Aircraft Structures*, pages 555–566, Atlanta, Georgia, 1996.
- [28] D. S. Dawicke and J. C. Newman, Jr. Evaluation of Various Fracture Parameters for Predictions of Residual Strength in Sheets with Multi-Site Damage. Submitted for publication, the first joint DoD/FAA/NASA Conference on Aging Aircraft, Ogden, Utah, July 1997.
- [29] D. S. Dawicke and J. C. Newman, Jr. Residual Strength Predictions for Multiple Site Damage Cracking Using a Three-Dimensional Analysis and a CTOA Criterion. In *Fatigue and Fracture Mechanics: 29th Volume, ASTM STP 1332*, 1998 (in press).
- [30] D. S. Dawicke, J. C. Newman, Jr., M. A. Sutton, and B. E. Amstutz. Influence of Crack History on the Stable Tearing Behavior of a Thin-Sheet Material with Multiple Cracks. In *Proceedings of the FAA-NASA Sixth International Conference on the Continued Airworthiness of Aircraft Structures*, pages 193–212, Atlantic City, New Jersey, 1994.
- [31] D. S. Dawicke, J.C. Newman, Jr., and C. A. Bigelow. Three-Dimensional CTOA and Constraint Effects During Stable Tearing in a Thin-Sheet Material. In *Fracture Mechanics: 26th Volume, ASTM STP 1256, Philadelphia*, pages 223–242, 1995.
- [32] D. S. Dawicke, R. S. Piascik, and M. L. Boone. Effects of Mixed Mode I/II Loading and Grain Orientation on Crack Initiation and Stable Tearing in 2024-T3 Aluminum. In *Fracture Mechanics: 27th Volume, ASTM STP 1296, Philadelphia*, pages 105–125, 1997.

- [33] D. S. Dawicke, R. S. Piascik, and J. C. Newman, Jr. Prediction of Stable Tearing and Fracture of a 2000-Series Aluminum Alloy Plate Using a CTOA Criterion. In *Fracture Mechanics: 27th Volume, ASTM STP 1296, Philadelphia*, pages 90–104, 1997.
- [34] D. S. Dawicke and M. A. Sutton. CTOA and Crack-tunneling Measurements in Thin Sheet 2024-T3 Aluminum Alloy. *Experimental Mechanics*, 34:357–368, 1994.
- [35] D. S. Dawicke, M. A. Sutton, J. C. Newman, Jr., and C. A. Bigelow. Measurement and Analysis of Critical CTOA for an Aluminum Alloy Sheet. In *Fracture Mechanics: 25th Volume, ASTM STP 1220, Philadelphia*, pages 358–379, 1995.
- [36] A. U. de Koning. A Contribution to the Analysis of Quasi Static Crack Growth in Steel Materials. In *Fracture 1977, Proceedings of the 4th International Conference on Fracture*, volume 3, pages 25–31, 1977.
- [37] R. deWit. A Review of Generalized Failure Criteria Based on the Plastic Yield Strip Model. In *Fracture Mechanics: 14th Symposium, ASTM STP 791, Philadelphia*, volume 1, pages 124–150, 1983.
- [38] Z.-Z. Du and J. W. Hancock. The Effect of Non-Singular Stresses on Crack-Tip Constraint. *Journal of the Mechanics and Physics of Solids*, 39(4):555–567, 1991.
- [39] W. Elber. Fatigue Crack Closure Under Cyclic Tension. *Engineering Fracture Mechanics*, 2:37–45, 1970.
- [40] W. Elber. The Significance of Fatigue Crack Closure. In *Damage Tolerance in Aircraft Structures, ASTM STP 486, Philadelphia*, pages 230–242, 1971.
- [41] F. Erdogan and G. C. Sih. On the Crack Extension of Plates under Plane Loading and Transverse Shear. *Journal of Basic Engineering*, 85(4):519–527, 1963.
- [42] J. D. Eshelby. The Force on an Elastic Singularity. *Phil. Trans. Roy. Soc.*, A244:87–112, 1951.
- [43] J. D. Eshelby. Energy Relations and the Energy Momentum Tensor in Continuum Mechanics. In M. F. Kanninen, W. F. Alder, A. R. Rosenfield, and R. I. Jaffee, editors, *Inelastic behavior of solids*, pages 77–115, 1970.
- [44] B. Farahmand, G. Bockrath, and J. Glassco. *Fatigue and Fracture Mechanics of High Risk Parts: application of LEFM & FMDM theory*. Chapman & Hall, New York, 1997.

- [45] T Fett. A Compendium of T-stress Solutions. Technical Report FZKA 6057, Institut für Materialforschung, February 1998.
- [46] I. Finnie and A. Saith. A Note on the Angled Crack Problem and the Directional Stability of Cracks. *International Journal of Fracture*, 9:484–486, 1973.
- [47] R. G. Forman, V. Shivakumar, and J. C. Newman, Jr. Fatigue crack growth computer program: NASGRO Version 3.0. Technical Report JSC-22267A, Johnson Space Center, 1998.
- [48] The Cornell Fracture Group. FRANC3D Version 1.14 Thin Shell Tutorial Guide (DRAFT). Online. Available [www.cfg.cornell.edu](http://www.cfg.cornell.edu), 1998.
- [49] M. L. Gruber, C. J. Mazur, K. E. Wilkins, and R. E. Worden. Investigation of Fuselage Structure Subject to Widespread Fatigue Damage. Technical Report DOT/FAA/AR-95/47, FAA, February 1996.
- [50] M. L. Gruber, K. E. Wilkins, and R. E. Worden. Investigation of Fuselage Structure Subject to Widespread Fatigue Damage. In *Proceedings of the FAA-NASA Symposium on the Continued Airworthiness of Aircraft Structures*, pages 439–460, Atlanta, Georgia, 1996.
- [51] N. Hallbäck. The Influence of Finite Geometry and Material Properties on Mixed-Mode I/II Fracture of Aluminum. *International Journal of Fracture*, 87:151–188, 1997.
- [52] C. E. Harris. NASA Airframe Structural Integrity Program. In *Structural Integrity of Aging Airplanes*, pages 141–152. Springer-Verlag, 1991.
- [53] C. E. Harris, J.H. Starnes, Jr., and J.C. Newman, Jr. Development of Advanced Structural Analysis Methodologies for Predicting Widespread Fatigue Damage in Aircraft Structures. In *Proceedings of the FAA-NASA Sixth International Conference on the Continued Airworthiness of Aircraft Structures*, pages 139–164, Atlantic City, New Jersey, 1994.
- [54] C. E. Harris, J.H. Starnes, Jr., and J.C. Newman, Jr. Analytical Methodology for Predicting the Onset of Predicting Widespread Fatigue Damage in Fuselage Structure. In *Proceedings of the FAA-NASA Symposium on the Continued Airworthiness of Aircraft Structures*, pages 63–88, Atlanta, Georgia, 1996.
- [55] D. Hellman and K. H. Schwalbe. On the Experimental Determination of CTOD Based R-Curves. In *Proceedings of the Conference on Crack Tip Opening Displacement in Elastic-Plastic Fracture Mechanics*, pages 115–132. Springer-Verlag, 1986.



- [56] C. L. Hom and R. M. McMeeking. Large Crack Tip Opening in Thin Elastic-Plastic Sheets. *International Journal of Fracture*, 45:103–122, 1990.
- [57] C. Y. Hui and A. T. Zehnder. A Theory for the Fracture of Thin Plates Subjected to Bending and Twisting Moments. *International Journal of Fracture*, 61:211–229, 1993.
- [58] M. A. Hussain, S. L. Pu, and J. H. Underwood. Strain Energy Release Rate for a Crack Under Combined Mode I and Mode II. In *Fracture Analysis, ASTM STP 560, Philadelphia*, pages 2–28, 1974.
- [59] J. W. Hutchinson. Plastic Stress and Strain Fields at a Crack Tip. *Journal of the Mechanics of Physics and Solids*, 16:337–347, 1968.
- [60] J. W. Hutchinson. Singular Behaviour at the End of a Tensile Crack Tip in Hardening Material. *Journal of the Mechanics of Physics and Solids*, 16:13–31, 1968.
- [61] M. Isida. Effect of Width and Length on Stress Intensity Factors of Internally Cracked Plates Under Various Boundary Conditions. *International Journal of Fracture*, 7:301–316, 1971.
- [62] M. James. *A Plane Stress Finite Element Model For Elastic-Plastic Mode I/II Crack Growth*. Ph.D. Thesis, Kansas State University, 1998.
- [63] M. F. Kanninen. The Analysis of Stable Crack Growth in Type 304 Stainless Steel. In *Proceedings of the International Conference of Fracture*, pages 1759–1768, 1980.
- [64] M. F. Kanninen and C. H. Popelar. *Advanced Fracture Mechanics*. Oxford University Press, New York, 1985.
- [65] M. F. Kanninen, C. H. Popelar, and Broek D. A Critical Survey on the Application of Plastic Fracture Mechanics to Nuclear Pressure Vessels and Piping. *Nuclear Engineering and Design*, 67:27–55, 1981.
- [66] M. F. Kanninen, E. F. Rybicki, R. B. Stonesifer, Broek D., A. R. Rosenfield, C. W. Marschall, and G. T. Hahn. Elastic-Plastic Fracture Mechanics for Two-Dimensional Stable Crack Growth and Instability Problems. In *Elastic-Plastic Fracture Mechanics, ASTM STP 668, Philadelphia*, pages 121–150, 1979.
- [67] A. P. Kfouri. Some Evaluations of the Elastic  $T$ -term using Eshelby's Method. *International Journal of Fracture*, 30:301–315, 1986.
- [68] A. P. Kfouri. Crack Extension under Mixed-Mode Loading in an Anisotropic Mode-Asymmetric Material in Respect of Resistance to Fracture. *Fatigue Fract. Engng. Mater. Struct.*, 19(1):27–38, 1996.

- [69] H.A.J. Knops. *Numerical Simulation of Crack Growth in Pressurized Fuselages*. Ph.D. Thesis, Delft University of Technology, September 1994.
- [70] J. K. Knowles and E. Sternberg. On a Class of Conservation Laws in Linearized and Finite Elastostatics. *Archive for Rational Mechanics and Analysis*, 44(3):187–211, 1972.
- [71] M. Kosai and A. S. Kobayashi. Axial Crack Propagation and Arrest in Pressurized Fuselage. In *Structural Integrity of Aging Airplanes*, pages 225–239, 1991.
- [72] M. Kosai, A. S. Kobayashi, and M. Ramulu. Tear Strap in Airplane Fuselage. In *Proceedings of the International Workshop on Structural Integrity of Aging Airplanes*, pages 443–457, 1992.
- [73] M. Kosai, A. Shimamoto, C.-T. Yu, S. I. Walker, A. S. Kobayashi, and P. Tan. Axial Crack Propagation and Arrest in Pressurized Fuselage. In *Proceedings of the FAA-NASA Sixth International Conference on the Continued Airworthiness of Aircraft Structures*, pages 375–392, Atlantic City, New Jersey, 1994.
- [74] R. Krause. *Multiscale Computations With a Combined H- and P-version of the Finite-element Method*. Ph.D. Thesis, Universität Dortmund, 1996.
- [75] V. Kumar, M. D. German, and C. F. Shih. *An Engineering Approach for Elastic-Plastic Fracture Analysis*, July 1981. EPRI NP-1931, Project 1287-1, Topical Report.
- [76] S. G. Larsson and A. J. Carlsson. Influence of Non-Singular Stress Terms and Specimen Geometry on Small-Scale Yielding at Crack Tips in Elastic-Plastic Materials. *Journal of the Mechanics and Physics of Solids*, 21:263–277, 1973.
- [77] P. S. Leevers and J. C. Radon. Inherent Stress Biaxiality in Various Fracture Specimen. *International Journal of Fracture*, 19:311–325, 1982.
- [78] F. Z. Li, C. F. Shih, and A. Needleman. A Comparison of Method for Calculating Energy Release Rates. *Engineering Fracture Mechanics*, 21:405–421, 1985.
- [79] D. E. McCabe and K. H. Schwalbe. Prediction of Instability Using the  $K_R$ -Curve Approach. In *Elastic-Plastic Fracture Mechanics Technology, ASTM STP 896, Philadelphia*, pages 99–113, 1985.
- [80] T. M. Maccagno and J. F. Knott. The Low Temperature Brittle Fracture Behaviour of Steel in Mixed Modes I and II. *Engineering Fracture Mechanics*, 38:111–128, 1991.

- [81] B. D. Macdonald. Fracture Prediction Based on Plastic Stress Singularity Strength. *Theoretical and Applied Fracture Mechanics*, 1:169–180, 1984.
- [82] J. R. Maclin. Performance of Fuselage Pressure Structure. In *1991 International Conference on Aging Aircraft and Structural Airworthiness*, pages 67–74. NASA Conference Publication 3160, 1991.
- [83] J. E. Marsden and T. J. R. Hughes. *Mathematical Foundations of Elasticity*. Prentice-Hall, Inc., Englewood Cliffs, N.J., 1983.
- [84] K. K. Mathur, A. Needleman, and V. Tvergaard. Three Dimensional Analysis of Dynamic Ductile Crack Growth in a Thin Plate. *Journal of the Mechanics and Physics of Solids*, 44:439–464, 1996.
- [85] M. Miller, K. N. Kaelber, and R. E. Worden. Finite-Element Analysis of Pressure Vessel Panels. In *Proceedings of the International Workshop on Structural Integrity of Aging Airplanes*, 1992.
- [86] R. Narasimhan, A. J. Rosakis, and J. F. Hall. A Finite Element Study of Stable Crack Growth under Plane Stress Conditions: Part I-Elastic-Perfectly Plastic Solids . *Journal of Applied Mechanics*, 54:838–845, 1987.
- [87] J. C. Newman, Jr. Fracture Analysis of Surface and Through Cracked Sheet and Plates. *Engineering Fracture Mechanics*, 5:667–689, 1973.
- [88] J. C. Newman, Jr. *Finite-Element Analysis of Fatigue Crack Propagation—Including the Effects of Crack Closure*. Ph.D. Thesis, Virginia Polytechnic Institute, 1974.
- [89] J. C. Newman, Jr. A Finite-Element Analysis of Fatigue Crack Closure. In *Mechanics of Crack Growth, ASTM STP 590, Philadelphia*, pages 281–301, 1976.
- [90] J. C. Newman, Jr. An Elastic-Plastic Finite Element Analysis of Crack Initiation, Stable Crack Growth, and Instability. In *Fracture Mechanics: Fifteenth Symposium, ASTM STP 833, Philadelphia*, pages 93–117, 1984.
- [91] J. C. Newman, Jr. An Evaluation of Fracture Analysis Methods. In *Elastic-Plastic Fracture Mechanics Technology, ASTM STP 896, Philadelphia*, pages 5–96, 1985.
- [92] J. C. Newman, Jr., B. C. Booth, and K. N. Shivakumar. An Elastic-Plastic Finite-Element Analysis of the  $J$ -Resistance Curve Using a CTOD Criterion. In *Fracture Mechanics: Eighteenth Symposium, ASTM STP 945, Philadelphia*, pages 665–685, 1988.

- [93] J. C. Newman, Jr., D. S. Dawicke, and C. A. Bigelow. Finite-Element Analysis and Fracture Simulation in Thin-Sheet Aluminum Alloy. In *Proceedings of the International Workshop on Structural Integrity of Aging Airplanes*, 1992.
- [94] J. C. Newman, Jr., D. S. Dawicke, M. A. Sutton, and C. A. Bigelow. A Fracture Criterion For Widespread Cracking in Thin-Sheet Aluminum Alloys. In *International Committee on Aeronautical Fatigue, 17th Symposium, Stockholm, Sweden*, 1993.
- [95] J.C. Newman, Jr. and C. E. Harris. Fracture Mechanics Research at NASA Related to the Aging Commercial Transport Fleet. In *1991 International Conference on Aging Aircraft and Structural Airworthiness*, pages 75–91. NASA Conference Publication 3160, 1991.
- [96] B. Nour-Omid and C. C. Rankin. Finite Rotation Analysis and Consistent Linearization Using Projectors. *Computer Methods in Applied Mechanics and Engineering*, 93:353–384, 1991.
- [97] NTSB. *Aloha Airlines, Flight 243. Boeing 737-200, N73711, Near Maui, Hawaii, April 28, 1988*, June 1989. National Transportation Safety Board, Aircraft Accident Report, NTSB/AAR-89/03.
- [98] N. P. O'Dowd, C. F. Shih, and R. H. Dodds, Jr. The Role of Geometry and Crack Growth on Constraint and Implications for Ductile/Brittle Fracture. In *Constraint Effects in Fracture Theory and Applications: Second Volume, ASTM STP 1244*, pages 134–159, 1995.
- [99] U.S. Department of Transportation. Damage Tolerance Assessment Handbook. Technical Report DOT-VNTSC-FAA-93-13.I, Federal Aviation Administration, 1993.
- [100] Pawliska P., H. A. Richard, and P. Diekmann. The Behaviour of Cracks in Elastic-Plastic Materials under Plane Normal and Shear Loading. *International Journal of Fracture*, 62:43–54, 1993.
- [101] R. G. Pettit. Evaluation of Integrally Stiffened Fuselage Concepts. Presented in Aeromat '97, Williamsburg, VA, May 1997.
- [102] R. G. Pettit. Private Communication. The McDonnell Douglas (now Boeing) Commercial Airplane Group, 1998.
- [103] R. G. Pettit, J. C. Newman, Jr., and M. S. Domack. Crack Turning Damage Tolerance Approach for Integrally Stiffened Structure. In *19th ICAF Symposium, Edinburgh, Scotland*, June 1997.

- [104] R. G. Pettit, J. J. Wang, and C. Toh. Integral Airframe Structure Program. Final Report, NASA Contract NAS1-20014, Task 34, The Boeing Company (in preparation), September 1998.
- [105] R. S. Piascik, S. A. Willard, and M. Miller. The Characterization of Widespread Fatigue Damage in Fuselage Structure. In *FAA/NASA International Symposium on Advanced Structural Integrity Methods for Airframe Durability and Damage Tolerance*, pages 563–580, Langley Research Center, Hampton, Virginia, 1994.
- [106] D. O. Potyondy. *A Methodology for Simulation of Curvilinear Crack Growth in Pressurized Shells*. Ph.D. Thesis, Cornell University, August 1993.
- [107] D. O. Potyondy, P. A. Wawrzynek, and A. R. Ingraffea. An Algorithm to Generate Quadrilateral or Triangular Element Surface Meshes in Arbitrary Domains with Applications to Crack Propagation. *International Journal for Numerical Methods in Engineering*, 38:2677–2701, 1995.
- [108] D. O. Potyondy, P. A. Wawrzynek, and A. R. Ingraffea. Discrete Crack Growth Analysis Methodology for Through Cracks in Pressurized Fuselage Structures. *International Journal for Numerical Methods in Engineering*, 38:1611–1633, 1995.
- [109] P. Rahulkumar, S. Saigal, and S. Yunus. Singular p-version Finite Elements for Stress Intensity Factor Computations. *International Journal for Numerical Methods in Engineering*, 40:1091–1114, 1997.
- [110] M. Ramulu and A. S. Kobayashi. Dynamic Crack Turning—A Photoelastic Evaluation. *Experimental Mechanics*, 23:1–9, 1983.
- [111] E. Rank, R. Krause, and K. Preusch. On the Accuracy of P-version Elements for the Reissner-Mindlin Plate Problem. *International Journal for Numerical Methods in Engineering*, 43:51–67, 1998.
- [112] C. C. Rankin and F. A. Brogan. *The Computational Structural Mechanics Testbed Structural Element Processor ES5: STAGS Shell Element*, 1991. NASA CR-4358.
- [113] C. C. Rankin, F. A. Brogan, W. A. Loden, and H. D. Cabiness. *STAGS User Manual Version 2.4*. Lockheed Martin Missiles & Space Co., Inc., Advanced Technology Center, 1997.
- [114] J. R. Rice. A Path Independent Integral and the Approximate Analysis of Strain Concentration by Notches and Cracks. *Journal of Applied Mechanics*, 35:379–386, 1968.

- [115] J. R. Rice. Elastic-Plastic Models for Stable Crack Growth. In *Mechanics and Mechanisms of Crack Growth*, May, M. J. ed., British Steel Corp. Physical Metallurgy Center Publication, Sheffield, England, pages 14–39, 1975.
- [116] J. R. Rice. Mechanics of Quasi-Static Crack Growth. In *IEEE Journal of Solid-State Circuits, Proceedings of the US National Congress of Applied Mechanics*, pages 191–216, 1979.
- [117] J. R. Rice. Elastic-Plastic Crack Growth. In *Mechanics of Solids*, pages 539–562. Pergamon Press, Oxford, 1982.
- [118] J. R. Rice, W. J. Drugan, and T.-L. Sham. Elastic-Plastic Analysis of Growing Cracks. In *Fracture Mechanics: Twelfth Conference, ASTM STP 700, Philadelphia*, pages 189–221, 1980.
- [119] J. R. Rice, R. M. McMeeking, D. M. Parks, and E. P. Sorensen. Recent Finite Element Studies in Plasticity and Fracture Mechanics. *Computer Methods in Applied Mechanics and Engineering*, 17/18:411–442, 1979.
- [120] J. R. Rice and G. F. Rosengren. Plane Strain Deformation near a Crack Tip in a Power Law Hardening Material. *Journal of the Mechanics of Physics and Solids*, 16:1–12, 1968.
- [121] J. R. Rice and E. P. Sorensen. Continuing Crack-Tip Deformation and Fracture for Plane-Strain Crack Growth in Elastic-Plastic Solids. *Journal of the Mechanics and Physics of Solids*, 26:163–186, 1978.
- [122] E. Riks. Some Computational Aspects of the Stability Analysis of Nonlinear Structures. *Computer Methods in Applied Mechanics and Engineering*, 47:219–259, 1984.
- [123] T.-L. Sham. The Determination of the Elastic  $T$ -term Using Higher Order Weight Functions. *International Journal of Fracture*, 48:81–102, 1991.
- [124] C. F. Shih. Small-Scale Yielding Analysis of Mixed Mode Plane-Strain Crack Problems. In *Fracture Analysis, ASTM STP 560, Philadelphia*, pages 187–210, 1974.
- [125] C. F. Shih, B. Moran, and T. Nakamura. Energy Release Rate Along a Three-Dimensional Crack Front in a Thermally Stressed Body. *International Journal of Fracture*, 30:79–102, 1986.
- [126] G. C. Sih. Strain-Energy-Density Factor Applied to Mixed-Mode Crack Problems. *International Journal of Fracture*, 10:305–321, 1974.
- [127] G. B. Sinclair, M. Okajima, and J. H. Griffin. Path Independent Integrals for Computing Stress Intensity Factors at Sharp Notches in Elastic Plates. *International Journal for Numerical Methods in Engineering*, 20:999–1008, 1984.

- [128] R. Singh, J. H. Park, and S. N. Atluri. Growth of Multiple Cracks and Their Linkup in a Fuselage Lap Joint. *AIAA Journal*, 32(11):2260–2268, 1994.
- [129] J. Sladek, V. Sladek, and P. Fedelinski. Contour Integrals for Mixed-Mode Crack Analysis: Effect of Nonsingular Terms. *Theoretical and Applied Fracture Mechanics*, 27:115–127, 1997.
- [130] J. H. Starnes, Jr., C. A. Rose, R. D. Young, and C. C. Rankin. Effects of Combined Loads on the Nonlinear Response of Stiffened Shells with Long Cracks. In *19th ICAF Symposium, Edinburgh, Scotland*, pages 967–978, 1997.
- [131] M. Stern, E. B. Becker, and R. S. Dunham. A Contour Integral Computation of Mixed-Mode Stress Intensity Factors. *International Journal of Fracture*, 12:359–368, 1976.
- [132] R. Streit and I. Finnie. An Experimental Investigation of Crack-path Directional Stability. *Experimental Mechanics*, 20:17–23, 1980.
- [133] M. A. Sutton, X. Deng, F. Ma, and J. C. Newman, Jr. A mixed-mode i/ii fracture criterion and its application in crack growth predictions. Submitted for publication, the second joint NASA/DoD/FAA Conference on Aging Aircraft, Williamsburg, Virginia, 1998.
- [134] M. A. Sutton, W. Zhao, M. L. Boone, Reynolds A. P., and D. S. Dawicke. Prediction of crack growth direction for mode i/ii loading using small-scale yielding and void initiation/growth concepts. *International Journal of Fracture*, 83:275–290, 1997.
- [135] T. Swift. Fracture Analysis of Adhesively Bonded Cracked Panels. *Journal of Engineering Materials and Technology*, 100:10–15, 1978.
- [136] T. Swift. Fracture Analysis of Stiffened Structure. In *Damage Tolerance of Metallic Structures: Analysis Methods and Application, ASTM STP 842, Philadelphia*, pages 69–107, 1984.
- [137] T. Swift. Damage Tolerance in Pressurized Fuselages. In *11th Plantema Memorial Lecture, 14th Symposium of the ICAF, Ottawa, Canada*, pages 1–77, 1987.
- [138] T. Swift. Damage Tolerance Capability. In *Specialist' Conference on Fatigue of Aircraft Materials*, pages 351–387, Delft University of Technology, Delft, The Netherlands, 1992.
- [139] T. Swift. Widespread Fatigue Damage Monitoring - Issues and Concerns. In *FAA/NASA International Symposium on Advanced Structural Integrity Methods for Airframe Durability and Damage Tolerance*, pages 829–870, Langley Research Center, Hampton, Virginia, 1994.

- [140] B. A. Szabó. Mesh Design for the p-version of the Finite Element Method. *Computer Methods in Applied Mechanics and Engineering*, 55:181–197, 1986.
- [141] B.A. Szabó and I. Babuška. *Finite Element Analysis*. John Wiley & Sons, Inc., 1991.
- [142] M. J. Viz, D. O. Potyondy, A. T. Zehnder, C.C Rankin, and E. Riks. Computation of Membrane and Bending Stress Intensity Factors for Thin, Cracked Plate. *International Journal of Fracture*, 72:21–38, 1995.
- [143] P. A. Wawrzynek. *Discrete Modeling of Crack Propagation: Theoretical Aspects and Implementation Issues in Two and Three Dimensions*. Ph.D. Thesis, Cornell University, August 1991.
- [144] A. A. Wells. Unstable Crack Propagation in Metals: Cleavage and Fast Fracture. In *Proceedings of the Cranfield Crack Propagation Symposium*, volume 1, pages 210–230, 1961.
- [145] J. G. Williams and P. D. Ewing. Fracture under Complex Stress—The Angled Crack Problem. *International Journal of Fracture*, 8(4):441–446, 1972.
- [146] M. L. Williams. On the Stress Distribution at the Base of a Stationary Crack. *Journal of Applied Mechanics*, 24:109–114, 1957.
- [147] M. L. Williams. The Bending Stress Distribution at the Base of a Stationary Crack. *Journal of Applied Mechanics*, 28:78–82, 1961.
- [148] F. J. Witt. The Equivalent Energy Method: An Engineering Approach to Fracture. *Engineering Fracture Mechanics*, 14:171–187, 1980.
- [149] J. F. Yau, S. S. Wang, and H. T. Corten. A Mixed-Mode Crack Analysis of Isotropic Solids using Conservation Laws of Elasticity. *Journal of Applied Mechanics*, 47:335–341, 1980.
- [150] R. D. Young, C. A. Rose, C. G. Dávila, and J. H. Starnes, Jr. Crack Growth and Residual Strength Characteristics of Selected Flat Stiffened Aluminum Panels. Submitted for publication, the first joint DoD/FAA/NASA Conference on Aging Aircraft, Ogden, Utah, July 1997.
- [151] F. G. Yuan and S. Yang. The Application of Fracture Mechanics to Stitched Warp-knit Fabric Composites. In *39th AIAA/ASME/ASCE/AHS/ASC structures, structural dynamics, and materials conference, Long Beach, CA*, April 1998.
- [152] K.J.J.M. Zaal. A Survey of Crack Path Stability Criteria and Their Application to Crack Flapping Phenomena in Stiffened Structures. Technical Report LR-681, Faculty of Aerospace Engineering, Delft University of Technology, The Netherlands, September 1992.



REPORT DOCUMENTATION PAGE			Form Approved OMB No. 07704-0188	
Public reporting burden for this collection of information is estimated to average 1 hour per response, including the time for reviewing instructions, searching existing data sources, gathering and maintaining the data needed, and completing and reviewing the collection of information. Send comments regarding this burden estimate or any other aspect of this collection of information, including suggestions for reducing this burden, to Washington Headquarters Services, Directorate for Information Operations and Reports, 1215 Jefferson Davis Highway, Suite 1204, Arlington, VA 22202-4302, and to the Office of Management and Budget, Paperwork Reduction Project (0704-0188), Washington, DC 20503.				
1. AGENCY USE ONLY (Leave blank)	2. REPORT DATE March 1999	3. REPORT TYPE AND DATES COVERED Contractor Report		
4. TITLE AND SUBTITLE Crack Growth Simulation and Residual Strength Prediction in Airplane Fuselages		5. FUNDING NUMBERS WU 538-02-10-01 NAG1-1184		
6. AUTHOR(S) Chuin-Shan Chen, Paul A. Wawrzynek, and Anthony R. Ingraffea				
7. PERFORMING ORGANIZATION NAME(S) AND ADDRESS(ES) Cornell University School of Civil and Environmental Engineering Ithaca, NY 14853		8. PERFORMING ORGANIZATION REPORT NUMBER		
9. SPONSORING/MONITORING AGENCY NAME(S) AND ADDRESS(ES)  National Aeronautics and Space Administration Langley Research Center Hampton, VA 23681-2199		10. SPONSORING/MONITORING AGENCY REPORT NUMBER  NASA/CR-1999-209115		
11. SUPPLEMENTARY NOTES Final Report, NASA Grant NAG1-1184 from Professor Anthony R. Ingraffea Langley Technical Monitor: James C. Newman, Jr.				
12a. DISTRIBUTION/AVAILABILITY STATEMENT  Unclassified-Unlimited Subject Category 24 Availability: NASA CASI (301) 621-0390		12b. DISTRIBUTION CODE		
13. ABSTRACT (Maximum 200 words) The objectives were to create a capability to simulate curvilinear crack growth and ductile tearing in aircraft fuselages subjected to widespread fatigue damage and to validate with tests. Analysis methodology and software program (FRANC3D/STAGS) developed herein allows engineers to maintain aging aircraft economically, while insuring continuous airworthiness, and to design more damage-tolerant aircraft for the next generation. Simulations of crack growth in fuselages were described. The crack tip opening angle (CTOA) fracture criterion, obtained from laboratory tests, was used to predict fracture behavior of fuselage panel tests. Geometrically nonlinear, elastic-plastic, thin shell finite element crack growth analyses were conducted. Comparisons of stress distributions, multiple stable crack growth history, and residual strength between measured and predicted results were made to assess the validity of the methodology. Incorporation of residual plastic deformations and tear strap failure was essential for accurate residual strength predictions. Issue related to predicting crack trajectory in fuselages were also discussed. A directional criterion, including T-stress and fracture toughness orthotropy, was developed. Curvilinear crack growth was simulated in coupon and fuselage panel tests. Both T-stress and fracture toughness orthotropy were essential to predict the observed crack paths. Flapping of fuselages were predicted. Measured and predicted results agreed reasonable well.				
14. SUBJECT TERMS Fuselage; Fracture; Plasticity; Cracks; FRANC3D; STAGS; Residual strength; Finite-element method; CTOA			15. NUMBER OF PAGES 189	
			16. PRICE CODE A09	
17. SECURITY CLASSIFICATION OF REPORT Unclassified	18. SECURITY CLASSIFICATION OF THIS PAGE Unclassified	19. SECURITY CLASSIFICATION OF ABSTRACT Unclassified	20. LIMITATION OF ABSTRACT UL	